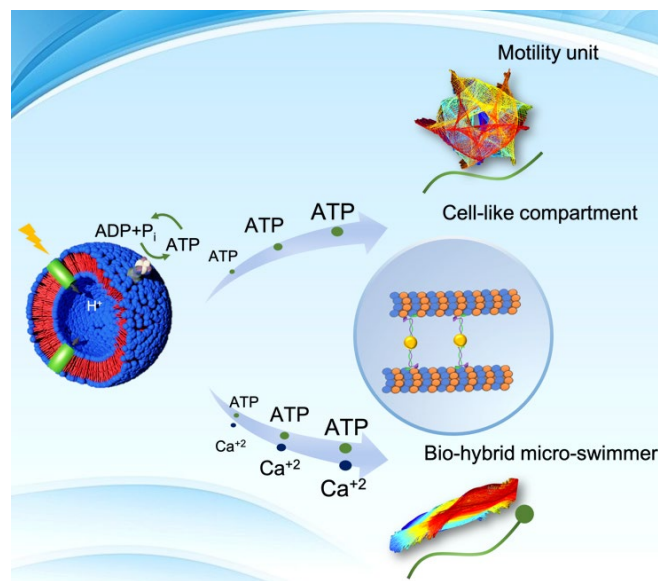


Integration of a Light-switchable ATP Regeneration System with Motility Modules: Toward Building an Artificial Cell and a Bio-hybrid Micro-swimmer

Integration eines durch Licht schaltbaren ATP-Regenerationssystems mit Motilitätsmodulen: Auf dem Weg zu einer künstlichen Zelle und einem Bio-hybriden Mikro-Schwimmer



Dissertation

zur Erlangung des akademischen Grades

Doktoringenieur (Dr.-Ing.)

von M.Sc. Raheel Ahmad

geb.am 17.04.1989 in Faisalabad, Pakistan

genehmigt durch die Fakultät für Verfahrens- und Systemtechnik der Otto-von-Guericke Universität Magdeburg

Promotionskommission:

Prof. Dr. rer. nat. habil. Dieter Schinzer (Vorsitz)

Prof. Dr.-Ing. habil. Kai Sundmacher (Gutachter)

Prof. Dr. Seraphine V. Wegner (Gutachter)

Prof. Dr. Ghulam Destgeer (Gutachter)

eingereicht am: 25. Februar 2022

Promotionskolloquium am: 23. Mai 2022

Supervisor at the MPI for Dynamics and Self-Organization (MPIDS)

Dr. Azam Gholami

Laboratory for Fluid Physics, Pattern Formation and Biocomplexity

Max Planck Institute for Dynamics and Self-Organization, Am Faßberg 17, 37077

Göttingen, Germany.

Email: azam.gholami@ds.mpg.de; Tel: +49 551 5176 301

I like to think of synthetic biology as liquid alchemy, only instead of transmuting precious metals, you're synthesizing new biological functionality inside very small channels. It's called microfluidics.

Neri Oxman.

Abstract

The reconstruction of cellular functions in a cell-like compartment is a current area of research in synthetic biology. Mimicking biological processes such as metabolism, growth and sensing is of prime importance, but achieving motility and directed movement is also challenging in the context of biomedical applications. To address these challenges, we have integrated an efficient light-driven ATP regeneration system with two types of motility modules. First, we reactivated isolated and demembrated flagella of *Chlamydomonas reinhardtii* (*C. reinhardtii*) with an artificial ATP regeneration module that allows us to control propulsion and beating frequency in response to light stimulation. Second, we constructed an artificial cell-like compartment by encapsulating microtubules with a force-generating molecular motors and light-switchable photosynthetic vesicles, in which we investigated motor-driven contraction of the filamentous network in response to optical stimuli.

We have also constructed a bio-hybrid micro-swimmer by attaching a synthetic cargo with isolated axonemes from *C. reinhardtii*. First, we investigated the motion of the axoneme, which has an asymmetric waveform and is known to involve the superposition of a static component, a dynamic wave component travelling from base to the tip and higher harmonics. We report that calcium plays an important role in reshaping the axonemal waveform by affecting the static component and find that calcium concentrations above 0.03 mM trigger a transition from asymmetric to symmetric swimming trajectories. We performed principal component analysis, from which we conclude that shape of the axoneme can be reconstructed with high accuracy when the first four leading eigenmodes are taken into account. Next, considering the calcium switching mechanism, we built an axonemally-driven micro-swimmers that consumes ATP for directional transport of cargo at a speed of 20 $\mu\text{m}/\text{sec}$, comparable to the speed of human sperm *in vivo*.

In addition to experimental studies, our analytical and numerical analysis reveals the existence of a counter-intuitive propulsion regime in which the velocity of the axonemally-driven cargo increases with the size of the bead. We also investigate the effect of bead-axoneme attachment geometry (symmetric versus asymmetric) on the swimming dynamics and show that the sideways attachment of the axoneme to the bead can also contribute to the rotational

velocity of the micro-swimmers. This discovered mechanism could find applications in the design of an artificial micro-swimmers for targeted drug delivery.

Zusammenfassung

Die Rekonstruktion zellulärer Funktionen in einem zellähnlichen Kompartiment ist ein aktuelles Forschungsgebiet der synthetischen Biologie. Die Nachahmung biologischer Prozesse wie Stoffwechsel, Wachstum und Sensorik ist von größter Bedeutung, aber auch die Erzielung von Motilität und gerichteter Bewegung ist im Zusammenhang mit biomedizinischen Anwendungen eine Herausforderung. Um diese Herausforderungen zu meistern, haben wir ein effizientes, lichtgetriebenes ATP-Regenerierungssystem mit zwei Arten von Motilitätssystemen integriert. Erstens haben wir isolierte und demembranierte Geißeln von *Chlamydomonas reinhardtii* (*C. reinhardtii*) mit einem künstlichen ATP-Regenerationsmodul reaktiviert, das es uns ermöglicht, Antrieb und Schlagfrequenz als Reaktion auf Lichtstimulation zu steuern. Zweitens haben wir ein künstliches zellähnliches Kompartiment konstruiert, indem wir Mikrotubuli mit einem krafterzeugenden molekularen Motorprotein und lichtschtbaren photosynthetischen Vesikeln eingekapselt haben, in denen wir die motorgetriebene Kontraktion des filamentösen Netzwerks als Reaktion auf optische Reize untersucht haben. Wir haben auch einen Bio-Hybrid-Mikroschwimmer konstruiert, indem wir eine synthetische Fracht mit isolierten Axonemen von *C. reinhardtii* verbunden haben. Zunächst untersuchten wir die Bewegung des Axonems, die eine asymmetrische Wellenform aufweist und bekanntermaßen aus der Überlagerung einer statischen Komponente, einer dynamischen Wellenkomponente, die sich von der Basis zur Spitze bewegt, und höheren Harmonischen besteht. Wir berichten, dass Kalzium eine wichtige Rolle bei der Umformung der axonemalen Wellenform spielt, indem es die statische Komponente beeinflusst, und stellen fest, dass Kalziumkonzentrationen über 0,03 mM einen Übergang von einer asymmetrischen zu einer symmetrischen Schwimmtrajektorie auslösen. Wir führten eine Hauptkomponentenanalyse durch, aus der wir schließen konnten, dass die Form des Axonems mit hoher Genauigkeit rekonstruiert werden kann, wenn die ersten vier führenden Eigenmoden berücksichtigt werden. Dann bauten wir unter Berücksichtigung des Kalzium-Schaltmechanismus einen axonemal angetriebenen Mikroschwimmer, der ATP für den gerichteten Transport der Ladung

mit einer Geschwindigkeit von $20 \mu\text{m/s}$ verbraucht, vergleichbar mit der Geschwindigkeit menschlicher Spermien in vivo.

Zusätzlich zu den experimentellen Studien zeigt unsere analytische und numerische Analyse die Existenz eines kontra-intuitiven Antriebsregimes, in dem die Geschwindigkeit der axonemal angetriebenen Fracht mit der Größe der Perle zunimmt. Wir untersuchen auch die Auswirkung der Geometrie der Befestigung von Perle und Axonem (symmetrisch oder asymmetrisch) auf die Schwimmdynamik und zeigen, dass die seitliche Befestigung des Axonems an der Perle ebenfalls zur Rotationsgeschwindigkeit des Mikroschwimmers beitragen kann. Dieser entdeckte Mechanismus könnte bei der Entwicklung eines künstlichen Mikroschwimmers für die gezielte Verabreichung von Medikamenten Anwendung finden.

Table of Contents

Abstract.....	i
Zusammenfassung.....	iii
Table of Contents	v
Chapter 1 Introduction	1
1.1 Motivation	1
1.2 Background	3
1.2.1 Types of cells and their constituent components	3
1.2.2 <i>C. reinhardtii</i> as a eukaryotic photosynthetic model organism	4
1.2.3 <i>C. reinhardtii</i> cell cycle	5
1.3 Biological micro-swimmers	6
1.3.1 Types of a flagellated micro-swimmers.....	6
1.3.2 The flow field of a flagellated micro-swimmers	7
1.4 Components of flagella and their functions.....	9
1.4.1 The internal architecture of flagella	9
1.5 Microtubules and molecular motor proteins: building blocks of an axoneme	11
1.5.1 Microtubules structure and their function.....	11
1.5.2 Type of molecular motor proteins and their function	12
1.6 ATP: a source of energy for cellular functions	17
1.6.1 ATP energy cycle	19
1.7 Synthetic biology and artificial energy regeneration systems	20
1.7.1 Building a cell motility assay	21
1.7.2 Bottom-up synthetic biology for ATP energy functional module	21
1.8 Bottom-up synthetic biology for building an artificial cell	26
1.9 The objectives of this thesis.....	27
Chapter 2 Materials and Methods.....	30
2.1 Chemicals and Materials.....	30
2.2 Expression, Isolation and characterization of his-tagged ATP Synthase	31
2.2.1 <i>E. coli</i> cell culture cultivation	31
2.2.2 Isolation and purification of EF ₀ F ₁	31
2.2.3 SDS-PAGE analysis.....	32
2.2.4 Determination of ATP synthase concentration	32
2.2.5 Preparation of liposomes by dialysis method for ATP synthase reconstitution	33
2.2.6 Turnover of ATP synthase	33
2.3 Bacteriorhodopsin expression, isolation and characterization	34
2.3.1 Halobacterium salinarium cell cultivation	34
2.3.2 Isolation of Bacteriorhodopsin	34
2.3.3 Calculation of bR concentration	35

2.3.4	Solubilization of bR patches.....	36
2.4	Preparation of lipid vesicles by an extrusion method and coreconstitution of EF_oF₁-ATP Synthase and bR.....	36
2.4.1	Preparation of small unilamellar lipid vesicles by extrusion method	36
2.4.2	Reconstitution of bR into lipid vesicles and its pumping efficiency	37
2.4.3	Determination of bR orientation by proteolytic assay	39
2.5	Preparation and characterization of light-driven ATP functional module	39
2.5.1	Preparation of lipid vesicles for coreconstitution of ATP synthase and bR	39
2.5.2	Light-driven ATP production by coreconstituted vesicles.....	41
2.6	Preparation of growth media and agar tube for <i>C. reinhardtii</i> and cells cultivation.....	42
2.6.1	Preparation of growth media	42
2.6.2	Preparation of agar tube	42
2.6.3	Cultivation of <i>C. reinhardtii</i> cells.....	43
2.6.4	Calculation of cell density	44
2.7	Isolation and reactivation of demembrated flagella.....	45
2.7.1	Isolation of axoneme	45
2.7.2	Preparation of reaction chamber for reactivation of axonemes	45
2.7.3	Reactivation of <i>C. reinhardtii</i> isolated axonemes.....	46
2.7.4	Bead-attached axonemes and reactivation with and without calcium	46
2.8	Axoneme contour tracking	47
2.9	Principal component analysis	48
2.10	Preparation of motile bundle solution.....	49
2.11	Fabrication of droplet microfluidic and millifluidic devices	50
2.11.1	Fabrication of droplet microfluidic.....	50
2.11.2	Fabrication of millifluidic	51
2.12	Encapsulation of MTs/Kinesin-1 network assembled with photosynthetic vesicles.....	51
2.13	MTs/Kinesin-1 network assembled with ATP functional module in millifluidic device.....	52
2.14	Light-triggered glucose consumption	52
Chapter 3	Light-Powered Reactivation of Flagella and Contraction of Microtubule Networks: Toward Building an Artificial Cell	54
3.1	Results.....	55
3.1.1	Light-driven energy module	55
3.1.2	Integration of energy module with motility module.....	58
3.2	Light-driven contraction of MTs/Kinesin-1 network.....	67
3.3	Discussion	71
Chapter 4	Waveform of Free, Hinged and Clamped Axonemes Isolated from <i>C. reinhardtii</i>: Influence of Calcium	77
4.1	Results.....	78
4.1.1	Illustration of the motion.....	78
4.1.2	Principal component analysis of the curvature waves demonstrates the existence of the back-propagating waves in free axonemes	81

4.1.3	Implication for the motion of free axonemes: an analytical study	84
4.1.4	Calcium reduces the static curvature of the free axonemes	84
4.1.5	Hinged and clamped boundary conditions	87
4.2	Discussion	90
Chapter 5	Bio-hybrid Micro-swimmers Propelled by Flagella Isolated from <i>C. reinhardtii</i>.....	94
5.1	Results.....	95
5.1.1	Overview of the results: two modes of propulsion.....	96
5.1.2	Analytical approximations of rotational and translational velocities of an axonemal-propelled bead	101
5.1.3	Analysis with the experimental waveform	102
5.2	Conclusions.....	105
Chapter 6	Conclusions and Outlook	109
A. 1	Buffer, Media and Solutions	113
A. 1.1	List of chemicals and materials.....	119
A. 1.2	List of equipment	121
A. 2	Supporting Information	122
Nomenclature.....		163
References		167
List of Figures		184
List of Tables.....		186

Chapter 1 Introduction

1.1 Motivation

Cilia and flagella are hair-like appendages that protrude from the surface of many cell types and function as a fundamental unit of motion³, converting chemical energy into mechanical work in the form of oscillatory beating motion.^{3,4} Whereas, non-motile primary cilia transduce a multitude of sensory stimuli, including a chemical concentration of growth factors, hormones, osmolarity, light intensity and fluid flow.⁵ The beating of motile cilia generates a directional flow, and this is a subject of great interest. Typical examples are mucociliary clearance in mammalian airways to protect the respiratory system from harmful inhaled materials^{6,7}, transport of cerebrospinal fluid in the brains of mammals⁸, transport of the egg to the uterus⁹, left-right asymmetry in the embryonic node¹⁰, or propulsion of microorganisms such as paramecium, spermatozoa, or the unicellular biflagellate algae *C. reinhardtii*. Besides, sperm, which is known to play an important role in the origin of life, is propelled by a single flagellum, and its motility is not only important for the cargo transport, but also for the straight swimming of the sperm cell to fertilize an egg cell.¹¹

To study the beating pattern of flagella, *C. reinhardtii* seems to be a promising candidate because of its structural similarity to the motile cilia. It is classified as a eukaryotic cell and is found in temperate soil habitats, and has two flagella attached with the basal body.¹² The internal structure of flagella, known as axoneme, has a highly conserved cylindrical architecture^{13, 14}. To date, many structural components of the axoneme have been discovered¹³⁻¹⁵ among which microtubules (MTs) and the dynein molecular motors are the most important significant.¹⁶ Axonemal dyneins are highly specific to ATP as a substrate.¹⁷ In the presence of ATP, the molecular dynein motors generate internal stresses to slide adjacent MTs relative to each other, resulting in bending motion. On the other hand, MTs are one of the cytoskeletal filaments, which together with actin and intermediate filaments, provide shape and motility in eukaryotic cells and play a crucial role in the formation of various cellular

structures, such as the dynamic asters found in mitotic and meiotic spindles.¹⁸ Encapsulation of cytoskeletal filaments and purified motors¹⁹ is a powerful tool to study the influence of geometrical confinement on self-organization of motor-driven filamentous network in cell-like compartments²⁰. Both types of motility modules require energy in the form of ATP. ATP is also a common chemical energy source for many different motility mechanisms found in nature. Therefore, an ATP regeneration module is required for a self-sustained motility. In this context, bottom-up synthetic biology provided the road map to constructing an artificial ATP energy regeneration system capable of delivering on-demand energy to mimic cellular and life-like processes.^{19, 21} Therefore, we tested the possibility to integrate a light-switchable ATP regeneration system with a motility module, namely axonemes isolated from *C. reinhardtii*. We used light to reactivate axonemes and controlled their beat frequency as a function of illumination time. Further, toward building an artificial cell, we co-encapsulated the light-to-ATP energy module with polymerized MTs and kinesin-1 molecular motors to generate active stresses in a confined cell-like compartment.

In addition, bio-hybrid micro-swimmers constructed by integration of a biological entity with a synthetic cargo^{22, 23} are the subject of growing interest in the field of targeted drug delivery or assisted fertilization *in vivo*²⁴. It is known that, in comparison to the existing synthetic non-biological micro-motors, biological motors are orders of magnitude more efficient in the conversion of chemical energy into mechanical work.²⁵

In this PhD project, using isolated and demembranated flagella from *C. reinhardtii*, we have built efficient axonemally-driven micro-swimmers that consume ATP to propel micron-sized beads. To achieve directional cargo transport, we used calcium ions²⁶ to change the axonemal waveform inducing a transition from circular to a straight swimming trajectory.²⁷

1.2 Background

1.2.1 Types of cells and their constituent components

In biology, a cell is a membrane-bound entity that comprises fundamental molecules of life.²⁸⁻
³⁰ The interior of the cell is divided into several compartments called organelles, each surrounded by its own membrane. The nucleus is one of the major organelle that contain the genetic information necessary for cell growth and reproduction. Mitochondria are one of the main building blocks of a cell and provide the energy needed by the cell to survive. Lysosome help to digest excreted and unwanted materials within the cell.³¹ The internal organization of the cell is maintained by Golgi apparatus and endoplasmic reticulum by synthesizing selected molecules and directing them to the proper location.

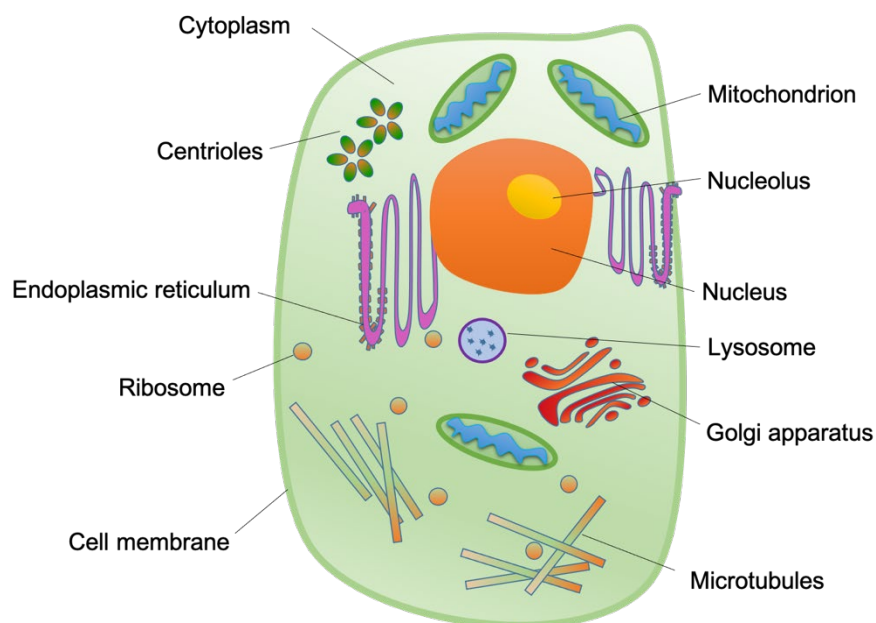


Figure 1.1: A structure of a eukaryotic cell. See text for the explanation of components and their function. Based on Payne et al.^[31]

The space between the organelles in the cytoplasm is called cytosol, which itself is responsible for cellular biosynthesis. The cytosol contains fibrous molecules that constitute the cytoskeleton, which allow organelles to move within the cell and provide the mechanism by which cells can move.³² The cytoskeleton also helps the cell to maintain its shape and structure. A schematic illustration of a typical eukaryotic cell is shown in Figure 1.1. Cells that contain

membrane-bound organelles are classified as eukaryotes, while cells that do not contain membrane-bound organelles are prokaryotes (Figure 1.2)³³⁻³⁵. However, all cells share many similarities in biochemical and cellular functions. In this thesis, *C. reinhardtii* (eukaryote) is used as a model organism.

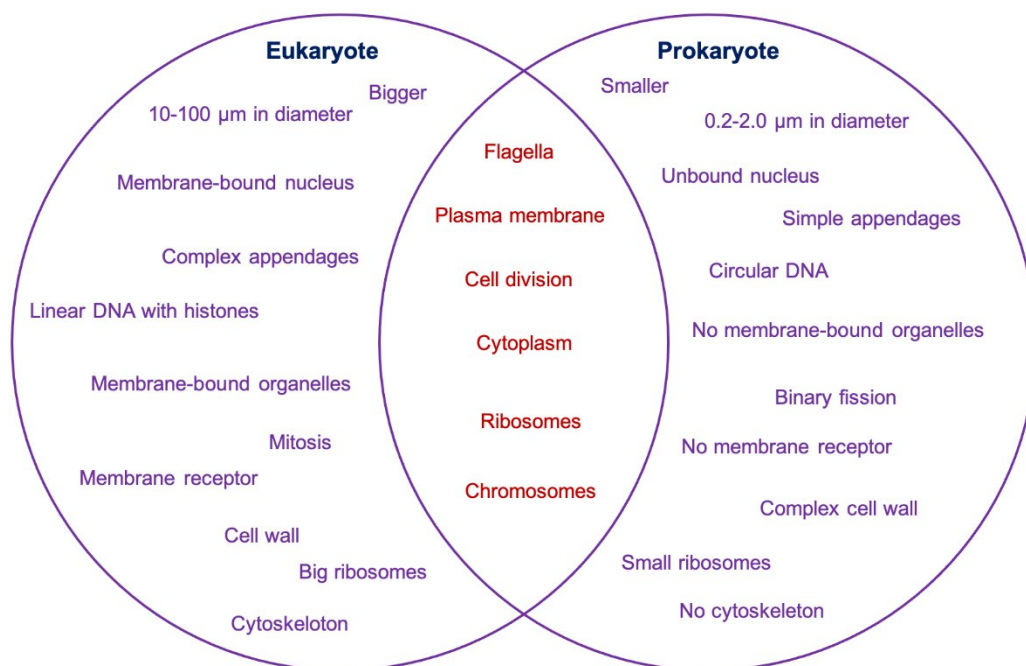


Figure 1.2: Difference between eukaryotic and prokaryotic cells. The intersection area (text in red color) shows the common cellular components of both cell types. Based on Favor et al.^[35]

1.2.2 *C. reinhardtii* as a eukaryotic photosynthetic model organism

C. reinhardtii is a single-celled green alga found in soil. *C. reinhardtii* came into consideration as a model organism in mid of 20th century and its fundamental cellular functions such as photosynthesis, structure, function and motility were revealed thereof.³⁶ *C. reinhardtii* found as a haploid organism (which is an organism having a single set of unpaired chromosomes), grown rapidly in axenic culture. In addition, *C. reinhardtii* can grow photoautotrophically or in acetate media in the dark (heterotrophically).³⁷ *C. reinhardtii* is oval in shape (~10 μm in length and ~4 μm in width) and has two whip-like appendages called flagella.³⁸ The active beating of flagella drives fluid flow at the cell surface and propels the cell body through the fluid.

1.2.3 *C. reinhardtii* cell cycle

The cell cycle^{12, 39} of *C. reinhardtii* is a sequence of events that leads to the duplication of all cell components and ultimately to division into a daughter cell. Most organisms divide by fission, but some algae including *C. reinhardtii* divide by multiple fission to produce 2^n daughter cells,

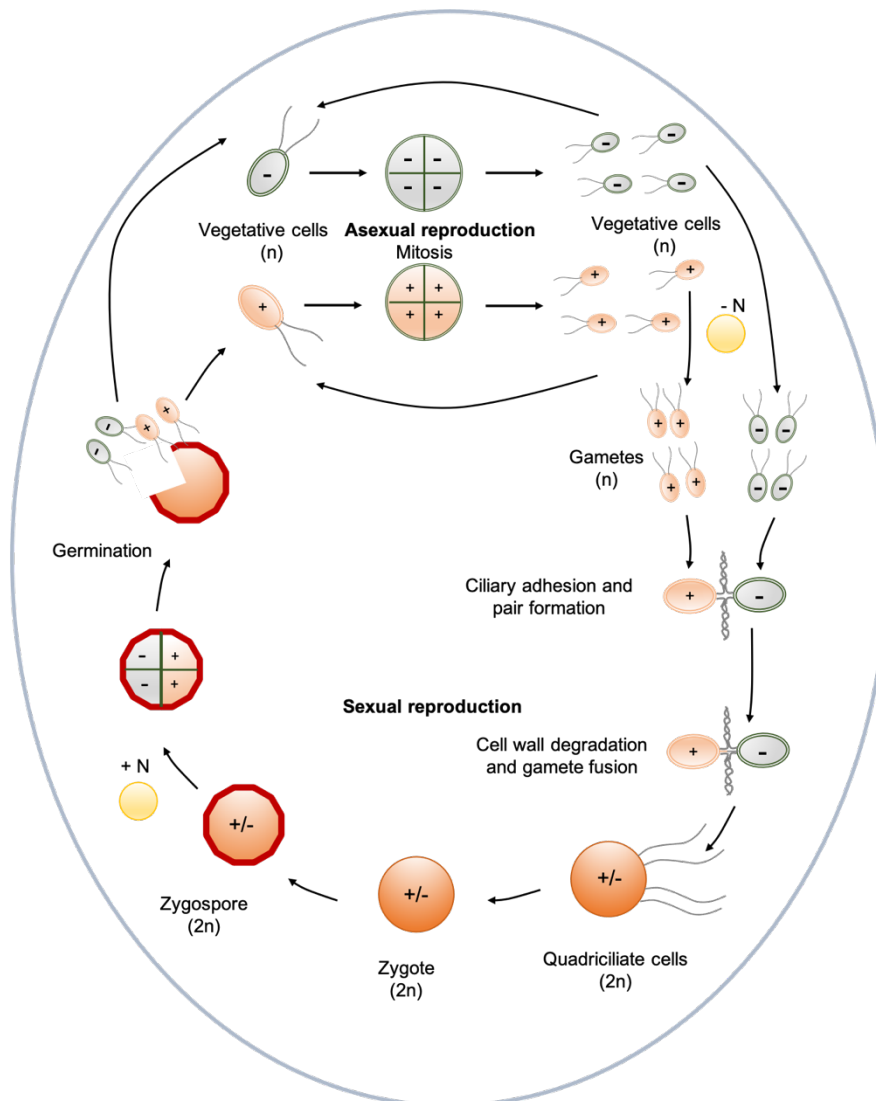


Figure 1.3: Life cycle of *C. reinhardtii*. See text for explanation. Based on Sasso et al. ^[12]

where n is the number of cell divisions.⁴⁰ There are two types of cell division, asexual and sexual (Figure 1.3). In asexual production, the zoospore loses its motility and divides mitotically into 4 to 8 biflagellate cells. These biflagellate cells grow to daughter cells after detachment from the

cell wall. On the other hand, sexual production consists of four stages: Gametogenesis, zygote formation, zygote maturation (zygospore formation) and meiosis (zygospore germination). In response to the mixing of gametes of opposite mating (mt +/-), flagellar adhesion triggers the cell-cell fusion (zygote formation). Then, the cell cycle enters into the dormant stage, also known as the resistance life form where zygotes will develop into zygospores. Under appropriate environmental conditions, the resting zygote is stimulated to germinate to generate new haploid cells (mt +/-). Eventually, four haploid daughter cells are released by hatching from the cell wall of the zygospores cells.

1.3 Biological micro-swimmers

In general, cells that have cilia and flagella on their surface can perform two types of functions, cells propulsion and fluid flow.^{41, 42} Common examples of cilia-based fluid transport are found in the cerebral ventricles inside the brain and in the mucus over the respiratory tract of mammals. Another interesting example is the cilia in the ventral node of mouse embryos, which are known to play an important role in vertebrate development by breaking left-right symmetry. In addition, the collective behaviors of cilia increase the speed and sensitivity of olfactory receptors in the nose of zebrafish embryos. Paramecium and Volvox are known model organisms for the study of ciliary carpets. Moreover, in Paramecium, the cell surface is covered with hundreds of cilia, while in Volvox there are two other types, the shell type and the germ type. In the shell type, the cilia cover the cell surface, while in the germ type, the flagella are found inside the cell. In both types, the cilia serve not only to transport fluid but also propel the microorganism.

1.3.1 Types of a flagellated micro-swimmers

Microorganisms that have few cilia or flagella are classified as self-propelled species, the most common examples are sperm cells and the unicellular green algae *C. reinhardtii*. Table 1.1 shows the types of flagellated micro-swimmers.^{41, 43-46} The sperm cell is composed of a head, midpiece and tail (single flagella) (Figure 1.4)^{47, 48}. The flagella perform a whip-like motion similar to the traveling wave, propagating from the cell body to the tail. The beating of sperm flagellum is known to be in-plane, while a small out-of-plane beating component results in a

spiral trajectory that supports the mechanism of chemotaxis. The sperm cell waveform is typically sinusoidal and follows a symmetrical beating pattern.^{41, 49-51}

In contrast to sperm cells, *C. reinhardtii* has two flagella and beats in a breast stroke-like manner. The beating pattern of each flagellum is similar to sperm cell, but the mean curvature is larger. The motion of *C. reinhardtii* flagella is characterized by two phases, power and recovery stroke.

Table 1.1: Types of flagellated micro-swimmers.

Types of specie	Number of flagella	Length (μm)
<i>C. reinhardtii</i>	2	~ 12
Bull sperm	1	~ 60
Sea urchin	1	~ 30
Trypanosoma	1	~ 30
Anopheles sperm	1	Highly variable

In the power stroke, the flagella move from front to back, accelerating the cell body in the direction of the swimming motion. Whereas, in the recovery stroke, the flagella move in the opposite direction, from back to front, and slide close to the cell surface, covering half the distance compared to the forward swimming motion. The small out-of-plane component results in a helical swimming motion that allows *C. reinhardtii* to perform phototaxis.⁵² This feature is due to the eyespot on the surface of the cell body which contains a light-sensitive protein sensor that triggers swimming toward or away from light in a spiral swimming path. When *C. reinhardtii* swims forward, the direction of swimming changes due to the skipping of a stroke by one of the flagella, resulting in an asymmetric stroke pattern.⁴⁹

1.3.2 The flow field of a flagellated micro-swimmers

As described by Purcell et al.⁵³, a micro-swimmer swims at a low Reynolds number where viscous forces dominate over inertia. Under no external torque or force condition, the micro-swimmer swims freely, and therefore total force or torque acting on the swimmer vanishes.⁵⁴ Thus, far-field hydrodynamics, where the distances from the swimmer are much larger than its

size, can be well described by a force dipole. This was confirmed experimentally by Drescher et al.⁵⁵ for *E. coli* as a model micro-swimmer. In addition, Hu et al.⁵⁶, performed simulation to verify the experimental findings of Drescher et al.⁵⁵

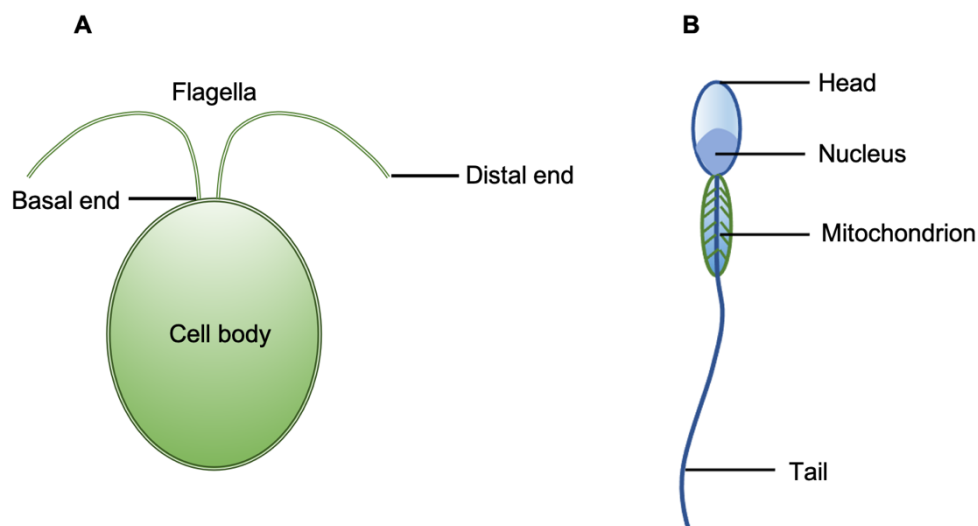


Figure 1.4: Schematic illustration of flagellated micro-swimmers. A) *C. reinhardtii* with two flagella, based on Salome et al.^[48]. B) Sperm cell with single flagellum, based on Turner et al.^[47] See text for explanation.

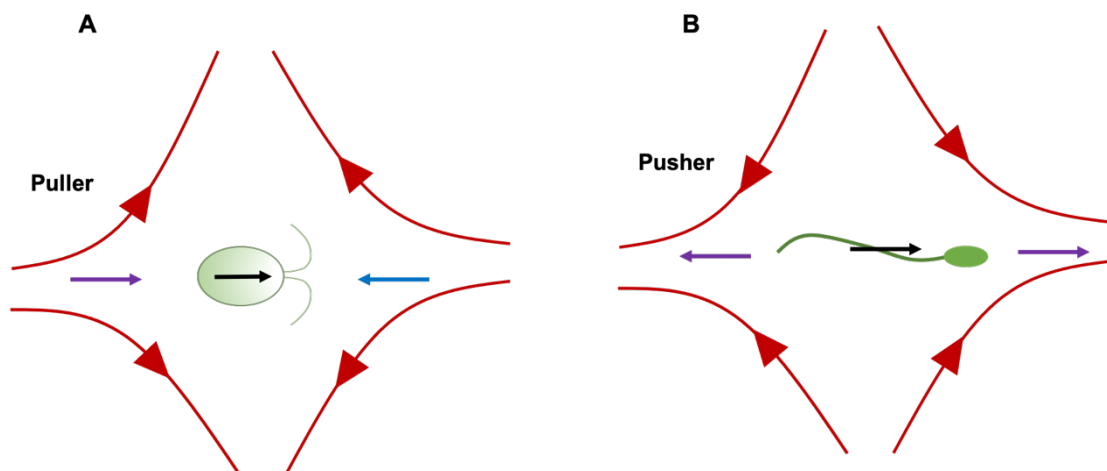


Figure 1.5: Schematic illustration of puller and pusher type micro-swimmers. The micro-swimmer and the surrounding mean flow field is shown in green color and red color, respectively. A) *C. reinhardtii* is a typical representative of puller type micro-swimmer because its mean swimming direction (black arrow) is perpendicular to the mean outflow direction. B) The sperm cell is a typical pusher type micro-swimmer with outflow direction is the same as the swimming direction. Based on Brown et al.^[57]

The flow field of *C. reinhardtii* can well be described by three stokeslets.⁴⁹ Based on the sign of hydrodynamic force dipole, micro-swimmer can be classified as a pusher or puller^{49, 57} (Figure

1.5). In a pusher micro-swimmer, the motor is located in the back (e.g. sperm) and the passive body is dragged along by the surrounding fluid, creating an inward fluid flow^{49, 58} (Figure 1.5A). In a puller micro-swimmer, the motor is in the front (e.g. *C. reinhardtii*) and the passive drag of the body together with the fluid behind it, creates an outward fluid flow^{49, 58} (Figure 1.5B).

1.4 Components of flagella and their functions

1.4.1 The internal architecture of flagella

Flagella are highly conserved organelles composed of an MTs-based structure called axoneme, covered by a plasma membrane (Figure 1.6A).⁵⁹⁻⁶¹ Nine MTs doublet (MTDs), each formed of a complete A-microtubule and an incomplete B-microtubule, are cylindrically arranged around a central pair of singlet MTs (Figure 1.6B).

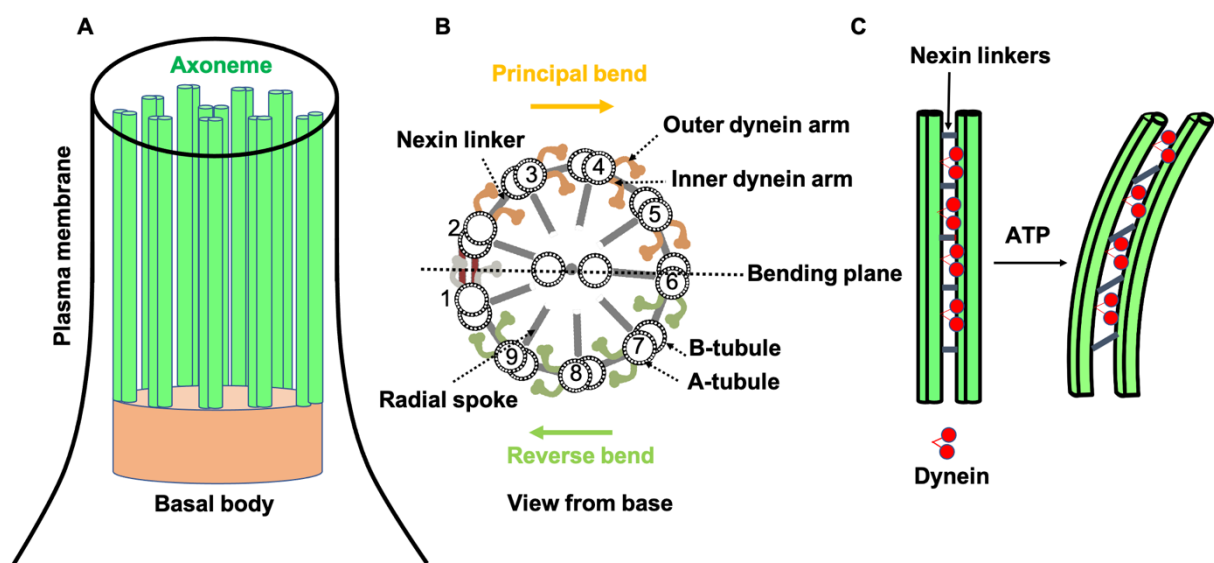


Figure 1.6: Structure of cilia/flagella. A) Cilia/flagella have a cylindrical architecture composed of axoneme, plasma membrane and basal body. B) Axoneme has a MTs-based structure formed of nine MTDs at the periphery and two MTs singlets at the center, which are associated with protein complexes such as radial spokes, inner dynein arm, outer dynein arm and nexin linkers. There is mechanical feedback from the bending on the regulation of dynein activity, which switches the activity of dyneins on the opposite side of the central pair MTs. C) In the presence of nexin proteins which cross-link the neighboring doublets, MTs are not free to slide and active forces generated by dynein molecular motors bend the cilium/flagellum. Nexin linkers play an important role to convert the action of dynein motors in microtubule bending, and radial spokes ensure that dyneins work together in a highly coordinated manner to generate a regular wave pattern. Based on Santos et al.^[59]

Nexin linkers play an important role to convert the action of dynein motors in MTs bending (Figure 1.6C). The diameter of an axoneme is around 200 nm, and the adjacent MTDs are spaced 30 nm away from each other.^{62, 63}

To date, more than 250 constituent proteins have been found to contribute to the highly ordered and precisely assembled structure of axoneme.¹⁵ The MTDs and the dynein molecular motors are known to be the most important components of axonemes.^{14,64} The arrangement of A and B-tubule to adjacent sets of tubules gives radial polarity.⁶¹ Figure 1.7 shows the arrangement of nexin-dynein regulatory complex (N-DRC), distribution of ODAs and IDAs and the radial spokes (RS). Three RS (S1, S2, S3) with evolutionally conserved spacing are present in most species, but only S3 is present in *C. reinhardtii*.⁶⁵ Each segment contains four ODAs and seven IDAs. The ODAs and IDAs are positioned outer side of the A-tubule and towards the inside of the axoneme, respectively. Each segment includes three RS arranged toward the central pair and spaced 96 nm apart.⁶⁶ Calmodulin, a calcium-responsive protein, has been shown to present at the interface of RS1 and IDAa. Calcium can cause a conformational change in calmodulin that can directly alter the flagella waveform (from an asymmetric to a symmetric waveform) by affecting the interaction between RS1 and IDAa⁶⁷ or by affecting the calmodulin-like subunit (LC4) of ODA⁶⁸. The ends of axonemes are called the basal end and distal tip.^{41, 69} The axoneme is anchored at the basal end, from where it nucleate from a centriole, a MTs-based organelle⁷⁰ (Figure 1.6A). The basal end consists of three sets of nine microtubule triplets with 0.5-0.75 μm in length. Each microtubule (MT) consists of an A-tubule, a B-tubule and an additional partial tubule C. In the transition zone (the so-called stellate structure), as a result of flagella excision and regrowth, the drastic change in the flagella structure leads to a 12% reduction in the diameter of the transition zone and a 42% reduction in the distance between A-tubule and outer cylinder. However, the diameter of the basal body and the rearrangement of the MTs are not affected significantly during the transition phase.⁷⁰ As reported in the literature⁷⁰, after 5 min of excision, the flagella structure comes to its original shape, and the axoneme starts to regrow due to the termination of the C-tubule.⁷¹ In contrast, at the distal tip ($\sim 1 \mu\text{m}$ long region), outer doublets fall off and the central structure remained covered by the plasma membrane. As shown in Figure 1.6B, the parallel structure of MTs gives longitudinal

polarity, whereas the dynein molecular motor gives radial polarity. The combination of both polarities makes axonemes a chiral structure.

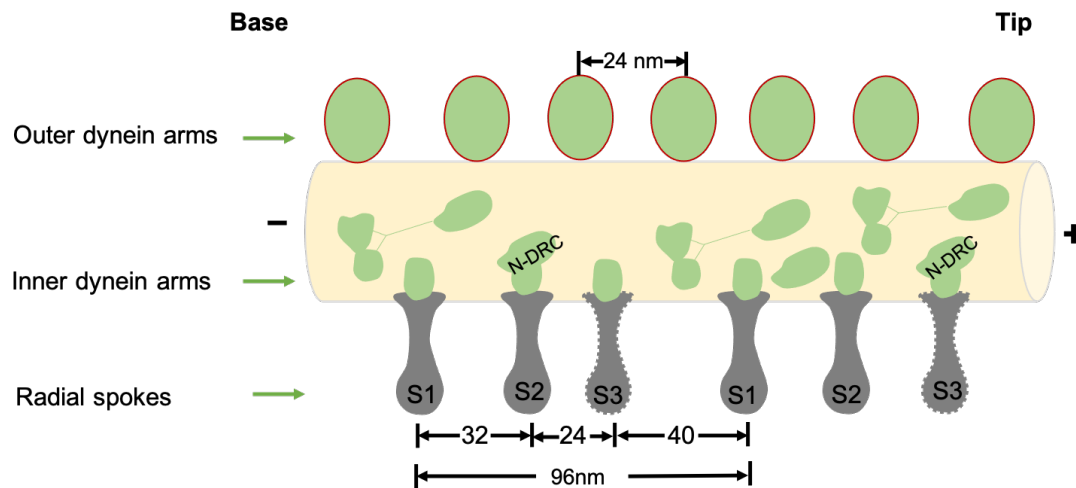


Figure 1.7: An arrangement and interconnectivity of axonemal motors and regulators. The distance between two ODA is 24 nm, whereas, three radial spokes (RS1-RS3) maintain a distance of 96 nm. N-DRC provides a nucleotide-independent linkage that connects adjacent MTDs and acts to resist sliding. Based on Heck et al. [66]

1.5 Microtubules and molecular motor proteins: building blocks of an axoneme

1.5.1 Microtubules structure and their function

MTs are hollow polymer cylinders made up of molecular units called tubulin which are composed of a heterodimer subunit (α and β tubulin). MTs perform the scaffold-like functions in a eukaryotic cell.⁷² Figure 1.8 shows the schematic representation of MTs and their dimer. The outer and inner diameter of MTs is ~ 25 and ~ 15 nm, respectively, while, MTs can grow up to tens of micrometers, giving them a high dynamic range.^{73, 74} MTs are one of the cytoskeletal filaments which together with actin and intermediate filaments provide shape and motility to eukaryotic cells and also involved in the formation of various cellular structures such as the dynamic asters.⁷⁵⁻⁷⁷ A typical MT consists of 13 protofilaments in a well-organized hollow tubular arrangement. Tubulin has GTPase activity and guanosine triphosphate (GTP) incorporated in β -tubulin (GTP- β) is rapidly hydrolysed to guanosine diphosphate (GDP), leading to conformational changes in tubulin network. As a result, depolymerization of MTs

occurs, and this process is called a catastrophe.⁷⁸ In contrast, α -tubulin, which binds with GTP is neither hydrolyzed nor exchanged.⁷⁹

The loss of GDP bound tubulin at the growing part is called GTP-cap⁷⁸ which helps to prevent depolymerization and this process is known as a rescue.⁸⁰ This switching mechanism between catastrophe and rescue phases is termed dynamic instability. The GTP-cap model and its experimental evidence are widely supported in the literature.^{78, 81-83} MTs have an intrinsic polarity because the two ends have different types of tubulins and both have different affinities to binding GTP, resulting in a faster-growing plus end and a slower-growing minus end.¹⁸ In *C. reinhardtii* axoneme, MTs doublet consists of complete A-tubule (13 protofilaments) and incomplete B-tubule (10 protofilaments). Compared to single MT, the MTDs have almost three times bending stiffness, which is due to the additional material of the B-tubule and the molecular machinery.⁴¹

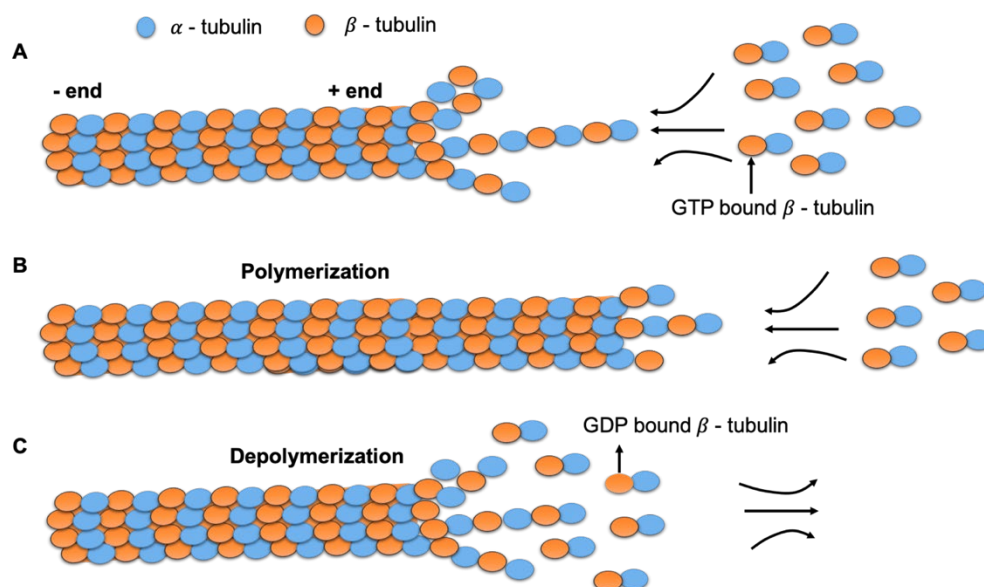


Figure 1.8: MTs polymerization and depolymerization. A) Initiation of MTs polymerization by GTP hydrolysis. B) Growth of of MTs at the plus end. C) Depolymerization of MTs and loss of GDP bound tubulin. Based on Horio et al.^[78]

1.5.2 Type of molecular motor proteins and their function

Proteins associated with the cytoskeleton are known as motor proteins. Motor proteins move along the cytoskeleton using a unique mechanochemical cycle to convert chemical energy drives from ATP hydrolysis into mechanical work.⁸⁴ The thermomechanical cycle consists of

filament binding, conformational change, filament release, conformational relaxation and filament rebinding. The motor protein and the associated cargo move one step along the length of filament (usually cover a few nm distance). The direction of movement and identity of cargo is determined by motor head and tail, respectively.⁸⁵ Motor proteins are categorized into three sub-classes: Myosin, dynein and kinesin. The first-ever motor protein, myosin, was discovered in the early 1940s⁸⁶ by Szent-Györgyi and the co-workers. Two decades later, dynein was discovered by Gibbons and the co-workers in 1963⁸⁷ and the third type of motor protein, kinesin, was discovered by Brady and Valle and their co-workers in 1985.^{85, 88} Myosin is known as muscle protein and responsible for force generation during muscle contraction, whereas dynein (–end-directed, retrograde transport) and kinesin (+end-directed, anterograde transport) moves along the MTs. The discussion of the myosin motors protein is beyond the scope of this thesis. Therefore, the focus will be on the dynein and kinesin motors protein.⁸⁵

1.5.2.1 Dynein motor protein: cytoplasmic and axonemal

Dynein is an MTs-based molecular motor protein which acts as a nanomachines driving the molecular mechanism at a cellular level. The crystal structure of cytoplasmic dynein reveals that it consists of a heavy chain (HC), intermediate chain (IC), light intermediate chain (LIC) and light chain (LC).⁸⁹ The HC is responsible for ATPase activity and others are supporting components. Cytoplasmic dyneins are a source of power generation during intracellular transport, whereas axonemal dyneins reside on MTs and are responsible for the beating of cilia/flagella. The motor domain of all dynein (approx. 300 kDa) consists of a ring of six different ATPase (AAA+), also known as AAA1-AAA6^{89,90} (Figure 1.9A). The first four domains AAA1-4 are capable of binding ATP, and the AAA1 domain is connected to the linker domain (AAA1-linker), which is responsible for force generation to drive cyclic displacement. The AAA1-linker domain connects the tail region and also interacts with cargo (in the case of cytoplasmic dynein) or MTs (in the case of axonemal dynein). In between the AAA4-AAA5 domain, there exists a coiled stalk 10 nm long known as the MTs binding domain (MTBD). This domain is of great interest because it is located opposite the force-generating AAA1 domain, suggesting that the ring can support a moment.⁹¹

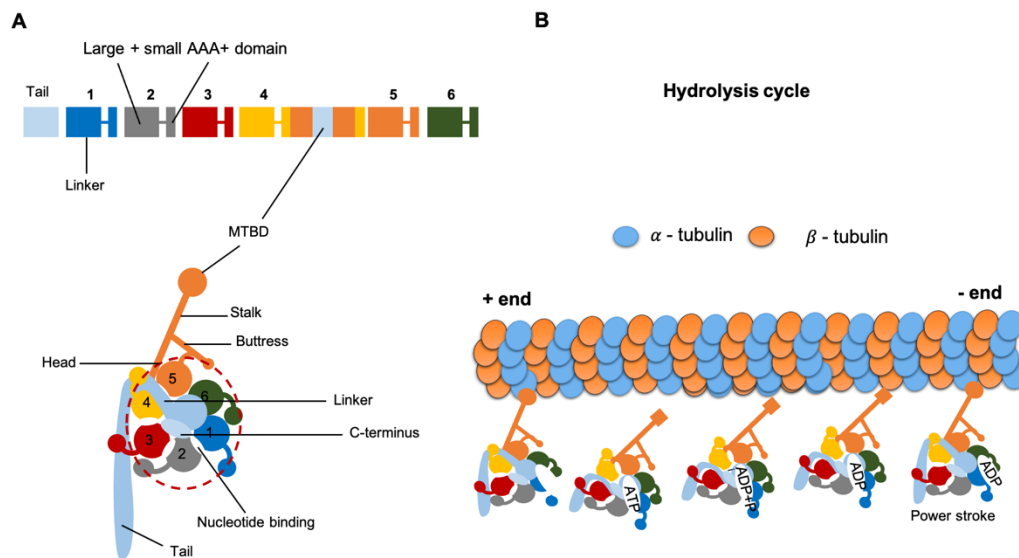


Figure 1.9: Structure of dynein molecular motor. A) Schematic illustration of dynein molecular motor and its constituent components. B) Power stroke of dynein motor by ATP hydrolysis. Based on Schmidt et al. [72]

1.5.2.2 A hydrolysis cycle of dynein molecular motor

In the absence of ATP, MTBD is strongly linked with MTs through its N-terminus and follows a straight conformation⁸⁵, as shown in Figure 1.9B. When ATP binds to the AAA1 domain, MTBD loses its connection with N-terminus, resulting in bending deformation in the structure and establishes a connection with AAA2/AAA3 domain. After ATP hydrolysis⁷², the dynein motor reconnects with MTs and undergoes a power stroke. As a result of power stroke, the linker undergoes a conformational change from bending to a straight configuration and produces a force for cargo movement. After the power stroke, the N-terminus of AAA1 comes in the proximity of AAA4 and returns the linker to its original position (AAA5), which significantly depends on the release of ADP, the resetting of ATP and the ATP hydrolysis cycle.⁸⁵

1.5.2.3 Types of dynein molecular motors in *C. reinhardtii* isolated axoneme

To date, fourteen different kinds of dynein motor domains have been found to contribute to the beating of the axoneme.^{41, 85} Dyneins are divided into two subclasses, ODAs and IDAs, located on the outer side and inner side of the A-tubule, respectively (see Figure 1.6B). In the last decades, many subclasses of dyneins in wild and mutant types of *C. reinhardtii* have been discovered and are well known in the literature.^{41, 92-94}

1.5.2.4 Asymmetric distribution of dynein molecular motors and cross-linkers

The IDAs and ODAs in an axoneme repeat every 96 nm⁶¹. Each turn has been shown to involve four ODAs, seven IDAs, two radial spokes and the N-DRC complex. Bui et al.⁹⁵ found asymmetry in the radial and longitudinal distribution of dynein motor. Further, Pigino et al.⁹⁶ found an asymmetric distribution of the nexin linker. Furthermore, Yagi et al.⁹⁷ demonstrated that minor dynein (DHC3, DHC4 and DHC11) exists at the proximal end of the axoneme. As shown in Figure 1.6B, the MTDs connected by different linkers e.g. MTDs 1-2 are connected with bridge-type static linkers with a length of 8 nm, whereas, nexin is connected at a distance of 96 nm in each repeat. The N-DRC complex is shown to be an elastic element with nonlinear stiffness that restricts the sliding of individual MTDs onto adjacent ones. Hoops et al.⁹⁸ found another unique asymmetry, a break-like protein structure in the lumen of the B-tubule of the MTDs at the position of 1,5 and 6, which also restricts the sliding of MTDs on the adjacent. The asymmetric distribution of cross-linkers also contributes to the bending deformation of the axoneme.⁹⁸ The main contribution comes from the sets of MTDs at the position of 1,9 and 5,6.⁹⁸

1.5.2.4.1 The waveform of *C. reinhardtii* flagella

To describe bending propagation, Brokaw et al.^{99, 100} presented a curvature control model by performing a computer simulation and compared it with the experimental waveform of sea urchin. Lindemann et al.¹⁰¹ reported the geometric control model, later known as the T-force control model showing that the arrangement of MTDs and motor proteins acts as a clutch. Later, Riedel-Kruse et al.¹⁰² described a sliding control model which shows that a motor regulation is proportional to the local sliding displacement, and this model showed good agreement with the experimental bending pattern of an intact bull sperm cell. In addition, the bending deformation of an axoneme can be represented by the curvature. The curvature indicates how much the axonemal structure is locally curved and thus represents a combination of material properties and local bending forces.^{27, 41} In this thesis, we calculated the bending deformation of the axoneme by calculating the curvature, see Chapter 2, section 2.8. First, we tracked the axoneme using the gradient vector flow (GVF) technique^{103, 104} to compute $\theta(s, t)$ and defined the curvature $\kappa(s)$ as, $\kappa(s) = d\theta(s)/ds$, where $\theta(s)$ is the angle

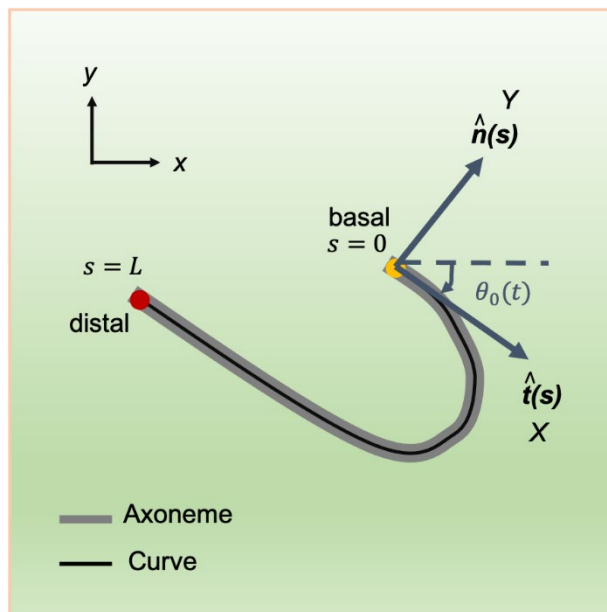


Figure 1.10: Schematic illustration of an instantaneous shape of an axoneme. Tangent vector $\hat{\mathbf{t}}(s)$ at $s = 0$ defines the X-direction and the corresponding normal vector $\hat{\mathbf{n}}(s)$ defines the Y-direction of the swimmer fixed frame.

between tangent vector at counter length (s) and x -axis at each point (Figure 1.10). To quantify the static curvature, we translate and rotate the axonemal configurations such that the basal end ($s = 0$) is at the origin of the coordinate system and the tangent vector at $s = 0$ is oriented in the x -direction (Figure 1.10). Further, principal component analysis (PCA) is performed to reconstruct the shape of an axoneme as described by Stephens et al.¹⁰⁵ for *C. elegans* (see Chapter 2, section 2.9).

1.5.2.5 Kinesin motor protein and its stepping mechanism

Kinesin is a molecular motor protein that is involved in the anterograde transport of cargo on MTs using ATP as an energy source.⁸⁴ Kinesin belongs to the superfamily proteins and is divided into fourteen different groups, kinesin-1 to 14.¹⁰⁶ The first twelve kinesin families (Kinesin1-12)¹⁰⁷ are known as N-domain kinesin (N-kinesin) because they have conserved motor domain that is a minimal domain required for motility. N-kinesin is motile and carries cargo towards the positive end of the MTs surface. Kinesin 13¹⁰⁸ has its motor domain in the middle of MTs and is involved in depolymerization instead of moving along the surface. Kinesin 14¹⁰⁹ known

as C-terminus motor protein, has its motor domain at C-region and moves the attached cargo to the minus end.

In this work, we used kinesin-1 motors protein with polymerized MTs to perform an *in vitro* motility assay. Therefore, the structure of kinesin-1 and the mechanism of cargo transport are briefly described here. Kinesin-1 was first discovered in the form of a heterotetramer for the transport of cargo at the cellular level.^{110, 111} The heterotetramer consists of two heavy (HC, molecular mass: 110-120 kDa) and light chains (LC, molecular mass: 60-70 kDa) (Figure 1.11A). The two identical HC have N-terminus globular domains which bind to MTs and dimerize to form a parallel coiled-coil stalk.^{112, 113} This stalk is elongated and connected to the C-terminus, which is a domain for cargo attachment.^{114, 115} The stepping and ATP hydrolysis mechanisms of kinesin-1 are different as compared to dynein because it contains two heads of HC. Each head has a tightly bound ADP. During the interaction of heads with MTs, heads start to coordinate effectively with each other, resulting in the rapid release of ADP (Figure 1.11B). At the leading head (head in red color in Figure 1.11B), the binding of ATP leads to a conformation change in the neck docks and causes a trailing head (head in blue color in Figure 1.11C) to swing forward by 180° toward the (+) end, known as a force-generating step. The next leading head binds quickly with the tubulin subunit and releases ADP (Figure 1.11D), and kinesin-1 attached cargo moves one step along the MTs. The new trailing head (head in red color in Figure 1.11E) hydrolyzes and releases P_i which diffuses away and the trailing head begins to detach from MTs (head in red color in Figure 1.11E). Again, ATP binds to the leading head (head in blue color in Figure 1.11E) and repeats the cycle. Kinesin-1 walks in hand- over-hand manner and each head covers 16 nm distance in one repetition, while leading to trailing head cover 8 nm.¹¹⁴

1.6 ATP: a source of energy for cellular functions

Adenosine triphosphate (ATP) was first discovered by Karl Lohman in 1929¹¹⁶ and termed as a source of energy in bacteria, fungi, plants and humans.¹¹⁷ ATP consists of an adenine base attached to a ribose sugar, which is linked to three phosphate group by phosphoanhydride bond. This bond is highly unstable and releases a significant amount of energy (~36 KJ/mol)¹¹⁸ as a result of ATP hydrolysis. This energy powers all reactions inside the cell. Conversely, ATP

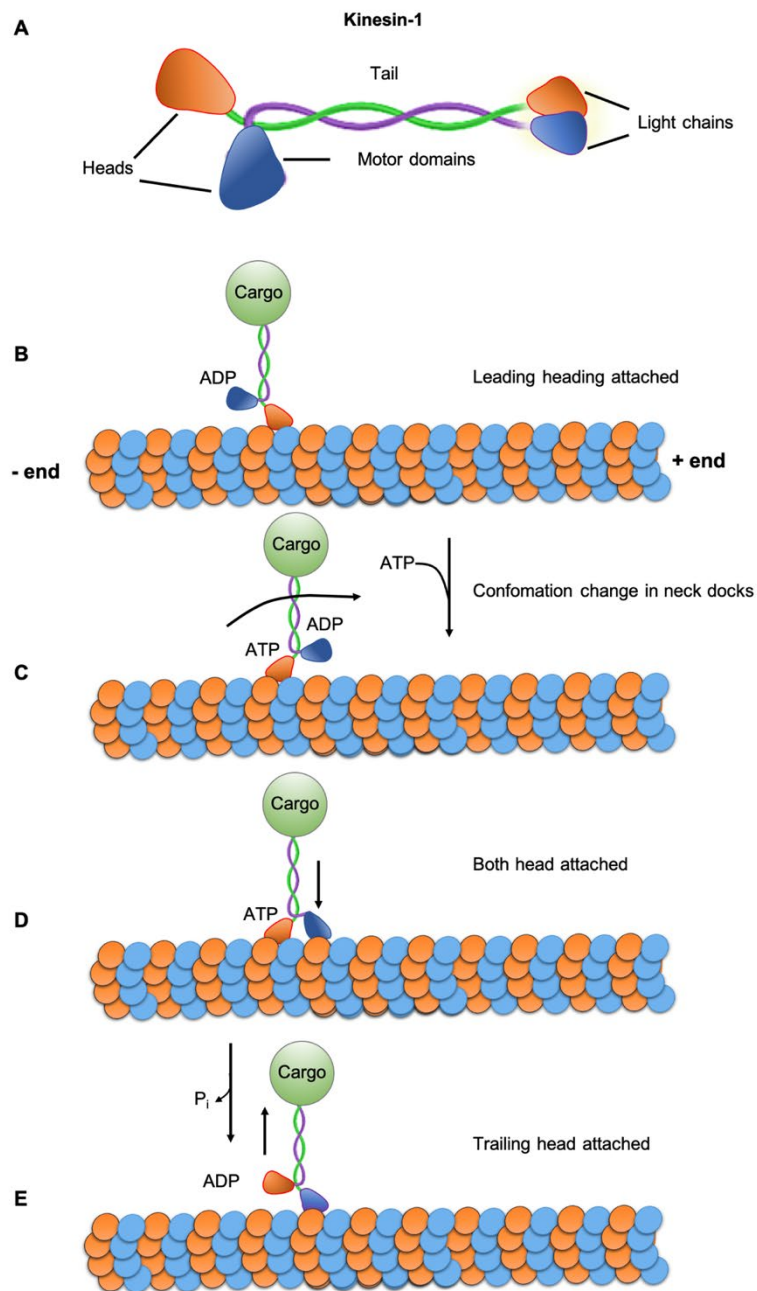


Figure 1.11: A schematic illustration of kinesin-1 motor protein, its constituent components and stepping mechanism for cargo transport. Based on Kawaguchi et al.^[115]

is regenerated from ADP and inorganic phosphate (P_i) molecules (Figure 1.12). *In vivo*, ATP is produced in different species by the different mechanisms e.g. (i) in plants and cyanobacteria,¹¹⁹ by the photophosphorylation, (ii) in cells, by the cellular respiration¹¹⁹, (iii) in some yeast or bacteria¹¹⁹ by fermentation.

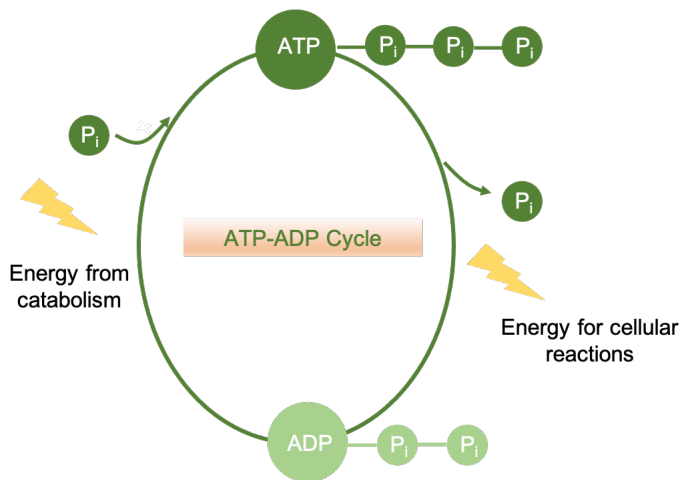


Figure 1.12: Schematic illustration of ATP-ADP energy cycle. See text for explanation. Based on Langen et al.^[116]

1.6.1 ATP energy cycle

In general, glucose is the major source of cellular metabolism in eukaryotic metabolic pathways, which break down into three sequential processes (Figure 1.13) within the mitochondrion.¹¹⁸⁻¹²¹ (I) Glycolysis: This reaction occurs in the cytoplasm where it is converted into two pyruvates at the expense of two ATP molecules. At the end of glycolysis, two molecules of ATP and nicotinamide adenine dinucleotide (NADH) are produced. The NADH molecules serve as electron carriers for other cellular reactions. (II) Tricarboxylic acid cycle (TCA or Krebs cycle), the pyruvates formed at the end of the first cycle enter the mitochondrion where they are converted to acetyl-CoA (a two-carbon energy carrier) and carbon dioxide (CO₂). Subsequently, acetyl-CoA enters the citric acid cycle, the second main energy process, which involves eight steps and generates three more NADH molecules and two flavin adenine dinucleotide (FADH₂) and GTP molecules. (III) Oxidative phosphorylation, in which electrons from FADH₂ and NADH cross the protein complex and generate a proton gradient across the mitochondrial membrane. The cells use the energy of this proton gradient and synthesize three additional ATP molecules. The combination of citric acid and oxidative phosphorylation cycle yields about 15 times more energy than a single glucose molecule. The ATP produced in the mitochondrion is regenerated by the energy shuttle¹²² located between the intermembrane space and the cytosol.

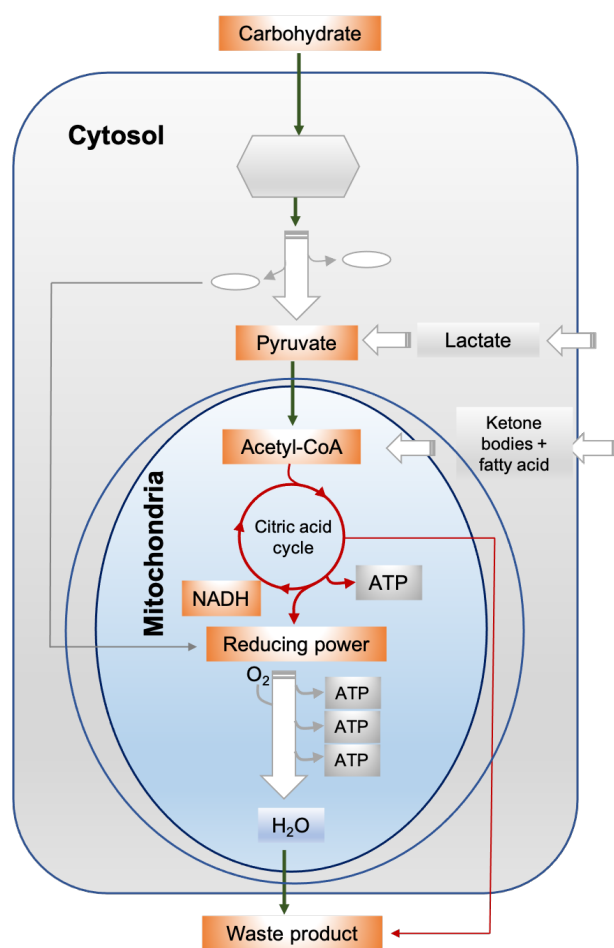


Figure 1.13: An ATP energy transduction cycle. See text for explanation. Based on Demetrius et al. ^[121]

1.7 Synthetic biology and artificial energy regeneration systems

A cell is composed of various components interconnected with each other to carry out a biological function. *In vivo*, understanding each cellular function is difficult because of self-complexity. Therefore, *in vitro* study seems a promising platform to study the function, properties and behaviors of each cellular component. The concept of *in vitro* study is the basis for new research fields such as genetic engineering and synthetic biology. Genetic engineering permits us to manipulate the genomic sequence of various organisms to redesign and construct the model-driven conception of new genetically-modified organisms or cells. Synthetic biology, on the other hand, provides the opportunity to reconstruct the biological components by applying engineering principles that mimic the natural system. Synthetic biology is itself a diverse field but can be classified into two main areas, (i) bottom-up synthetic

biology, which has potential application in creating truly *De novo* artificial life-like structure, and (ii) top-down synthetic biology, allows us to design metabolic and signaling pathways. In a top-down approach, the host cell can be used to extract cofactor, metabolites, transcription pathways and other existing components but this holds the drawback of crosstalk between the endogenous system and the introduced synthetic system.¹²³

1.7.1 Building a cell motility assay

A motility assay is a schematic study of extracting the motility components of the cell and supplying energy from external environment. The first *in vitro* motility assay was performed by Kron et al.¹²⁴ in 1986 to study the actin and myosin contraction. Subsequently, the motility of axonemes and MTs were studied in detail.^{19, 125-129} In these studies, purified ATP was supplied externally to enable motor proteins to perform mechanical work. Therefore, energy transduction is a crucial step in the assembly of a motility unit. In addition, ATP regeneration by enzymatic cyclic reaction of creatine kinase (CK) and phosphocreatine (PCr) has been used in some studies,^{130, 131} but cost, on-demand synthesis, high volumetric productivity, stability and lack of robustness limit its use. Therefore, bottom-up synthetic biology is emerging as a potential area of interest for ATP energy regeneration systems.¹³¹

1.7.2 Bottom-up synthetic biology for ATP energy functional module

In a biological cell, cellular functions such as metabolism, cell division and motility are energy dependent and are supplied in the form of ATP. When studying cell motility, ATP as a source of energy without regeneration limits the analysis to gain deep insights into molecular mechanisms.¹³¹ To overcome this limitation, a system in which ATP energy is regenerated in a controllable manner is needed. This can be done by incorporating biological components responsible for ATP synthesis *in vivo* and coupling them with an artificial system that can maintain the functions of energy regeneration in an artificial environment. Figure 1.14 illustrates the three important components for the construction of an artificial ATP regeneration system: (i) a compartment that mimics the cell membrane, (ii) isolated and purified functional proteins from biological cells, and (iii) integration of the first two

components to build a functional module and optimize its performance under different reaction conditions.

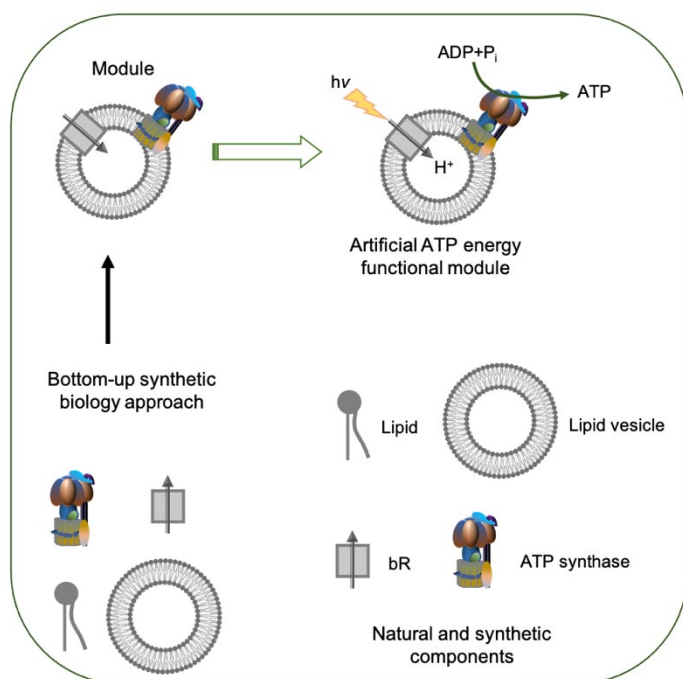


Figure 1.14: Bottom-up construction of an artificial ATP regeneration system. See text for explanation.

The ATP functional module can be of different types, such as metabolic or energy conversion^{118, 132}. The optimization of these modules can be accomplished by performing the simulations, and by modeling a system that is capable of predicting system behavior for further improvements in reconstitution.

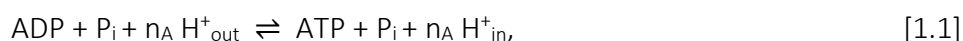
1.7.2.1 Light-to-ATP energy system

To date, many ATP regeneration systems have been reported, but a combination of ATP synthase with a photoswitchable proton pump has attracted more attention because it is less complex as compared to other systems, such as oxidative photophosphorylation.¹³¹⁻¹³⁴ The driving force for the construction of an artificial ATP regeneration system was the chemiosmosis theory proposed by Peter Mitchell in 1961.¹³⁵ This theory stated that ATP synthase is driven by proton motive force (PMF) generated by proton gradient over the

membrane. Based on this theory, Racker and coworker.¹³⁶ built a system by coreconstitution of ATP synthase and bR into lipid vesicles. Subsequently, several types of light-driven ATP regeneration systems have been reported based on lipid compositions (natural or synthetic)^{132-140 141, 142}, types of ATP synthase¹³⁸⁻¹⁴¹ and by varying the ATP synthase/bR ratio^{132-140 141, 142}. In this thesis, the light-driven ATP module (see Figure 1.14) is built in collaboration with the research group of Dr. Tanja Vidaković-Koch and Prof. Kai Sundmacher (MPI Magdeburg) using EF_oF₁-ATP synthase and bacteriorhodopsin (bR). Therefore, these two components are explained in the following section.

1.7.2.1.1 EF_oF₁-ATP synthase

F-type ATP synthase is a membrane-bound enzyme which is involved in ATP synthesis. In bacteria, such as *E. coli*, it is located in the mitochondria and is also known as EF_oF₁-ATP synthase.¹⁴³ EF_oF₁-ATP synthase uses the electrochemical gradient generated by the difference in the proton concentration on either side of the membrane to drive ATP synthesis from ADP and inorganic phosphate (P_i). The synthesis of ATP is energetically unfavorable. The general form of the reaction¹³⁴ is as follows:



where $n_A \sim 3-4$ is the number of protons. The ATP synthase consists of two major components, F_o and F₁. The F_o consists of α_3 , β_3 , γ , δ and ϵ subunits, and it is hydrophilic in nature (Figure 1.15). The three pairs of $\alpha\beta$ ($\alpha_3\beta_3$) have a hexagonal structure and six distinct binding domains, three of which are catalytically active. The subunit γ stalk in the F₁-ATP synthase is responsible for ATP synthesis in combination with δ and ϵ subunits. The mechanism of ATP synthesis by a conformational change in the enzyme through the γ -stalk was postulated by Paul Boyer in 1960¹⁴⁴ and he discovered that the active sites of the β -subunits cycles between three states, loose, tight and open^{120, 144} (Figure 1.16). In a loose state, ADP and P_i enter into the cycle and cause a conformational change in the structure. (II) Due to the conformational change, ADP

and P_i come very close to each other and bring the active site into a tight state. (III) The synthesized ATP is released, and at the same moment ADP and P_i enter into the loop.

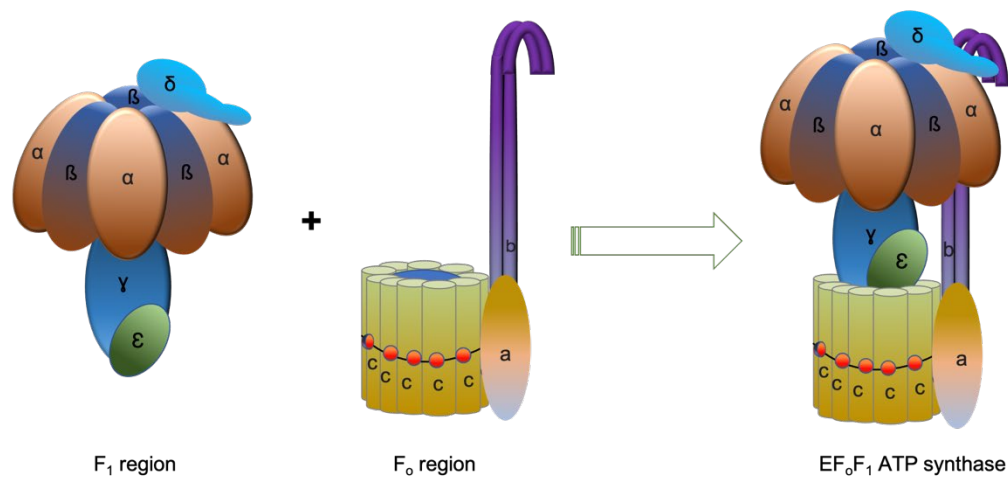


Figure 1.15: A schematic illustration of bacterial EF_0F_1 -ATP synthase and its subunits. Based on Matsui et al. ^[143]

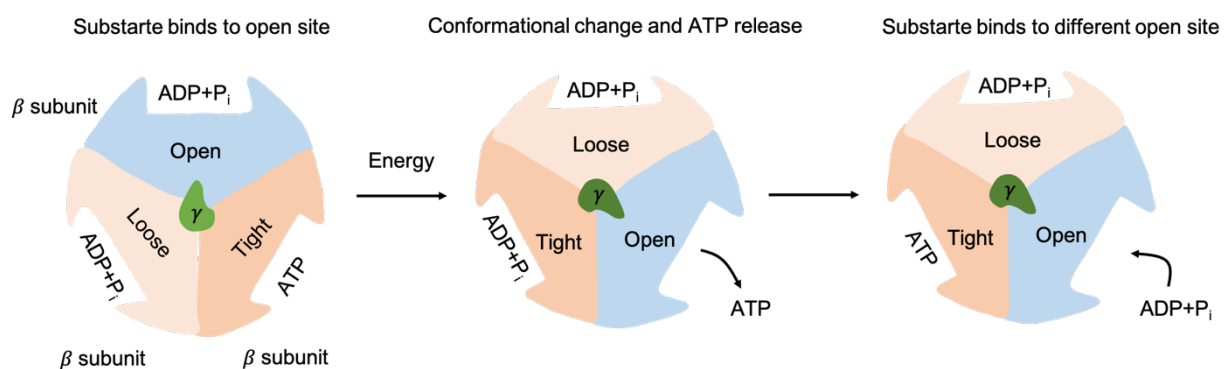


Figure 1.16: A schematic illustration of Boyer's binding change mechanism of EF_0F_1 -ATP synthase. Based on Neupane et al. ^[120]

1.7.2.1.2 Bacteriorhodopsin

Bacteriorhodopsin (bR) is the major photosynthetic protein of the archaeon *Halobacterium salinarum*. It functions as a light-gated proton ion pump with seven transmembrane helices. bR is located in the center of the retinal chromophore, which is covalently bound to Lys216 by a retinal Schiff base (RSB) and absorbs green light (~ 570 nm). Upon illumination, the retinal

chromophore captures light energy as photons and use it to moves protons from the cytoplasm to the extracellular space. This movement of a proton across the membrane is due to the

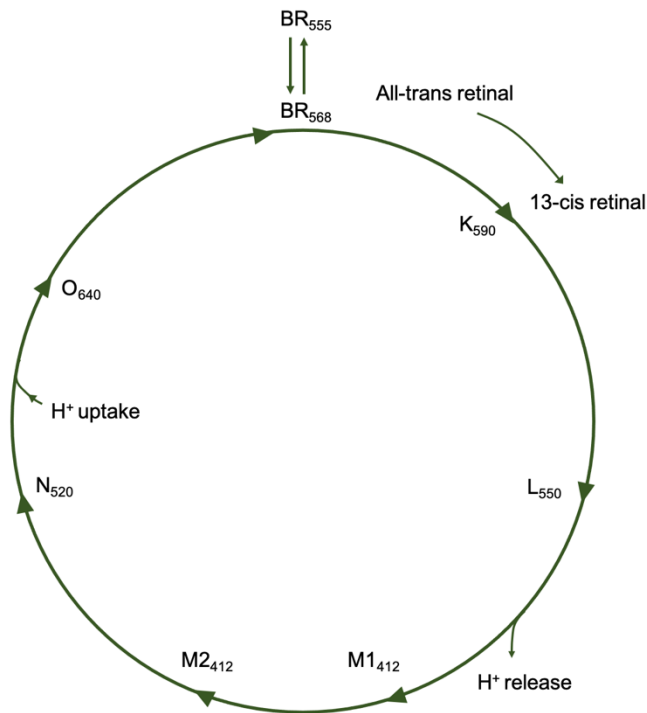


Figure 1.17: An overview of a bR photo-cycle. Based on Friedrich et al. ^[145]

isomerization of the chromophore from the all-trans to the 13-cis conformation. The bR photocycle¹⁴⁵ consists of several time-dependent intermediate states (Figure 1.17). Hirai et al.¹⁴⁶ reported that an illumination period of 1 ms is required for the change of protein conformation in the cytoplasmic region. In the dark state, 65% of the retinal chromophore is in the 13-cis conformation. Under light illumination, BR₅₆₈ transitions to an excited state (K₅₉₀) and all chromophores isomerize to a 13-cis configuration. In the K₅₉₀ intermediate state, the chromophore is not fully isomerized and remains highly strained. Upon degradation, this short-lived state transitions to a relaxed state (L₅₅₀), and as a result RSB donates its proton to aspartate D85, leading to a blue shift in absorbance at ~ 412 nm (M1₄₁₂). As a result, a proton is donated to the extracellular phase and the direction of the helix is realigned at M1₄₁₂, and RSB is deprotonated by penetrating water (N₅₂₀). In addition, a proton is transferred to the releasing group (O₆₄₀). The photocycle is then completed by the recovery of the all-trans

configuration (BR568), and release the proton due to thermal relaxation at D85. Note that the numbers in the index correspond to the maximum absorption wavelength.

1.8 Bottom-up synthetic biology for building an artificial cell

Bottom-up synthetic biology is an intriguing but challenging way to unravel the complexity of cellular function. Considerable attention has been paid to constructing artificial cells by assembling the biological components with a synthetic system. With this approach, system properties and reaction conditions can be better controlled than with a top-down approach. Thus, the bottom-up approach not only offers the possibility of constructing a system that mimics origins of life properties, but also the possibility of constructing nano-bio-machines such as molecular switches^{131, 147}, DNA nanorobots¹⁴⁸ and molecular motor¹⁴⁹ for cargo delivery. Further, droplet microfluidics at the interface of synthetic biology provides the platform to encapsulate the active biological module in a controllable manner. Recently, Bao et al.¹⁵⁰ synthesized giant unilamellar vesicles (GUVs) and investigated the lyotropic nematic crystal properties. Subsequently, Bacher et al.¹⁵¹ applied the droplet microfluidics technique to study translocation-reaction cascades. Shetty et al.¹⁵² combined droplet microfluidics with a synthetic bottom-up approach to study directed signaling cascades between compartments. In recent reviews,^{153, 154} authors summarize the application of droplet microfluidics at the interface of biology.

1.9 The objectives of this thesis

The aim of this thesis is divided into three parts:

- (1) We demonstrate the feasibility, biocompatibility and efficiency of a light-switchable ATP regeneration energy system with motility modules (Figure 1.18). First, we integrate the light-switched ATP module with *C. reinhardtii* isolated axonemes to control the beating frequency in response to light. Next, toward the construction of an artificial cell, we build an *in vitro* motility assay by encapsulating MTs assembled with the force-generating kinesin-1 motors and the energy module using droplet microfluidics, and study the dynamics of a contractile filament network in a cell-like compartment.

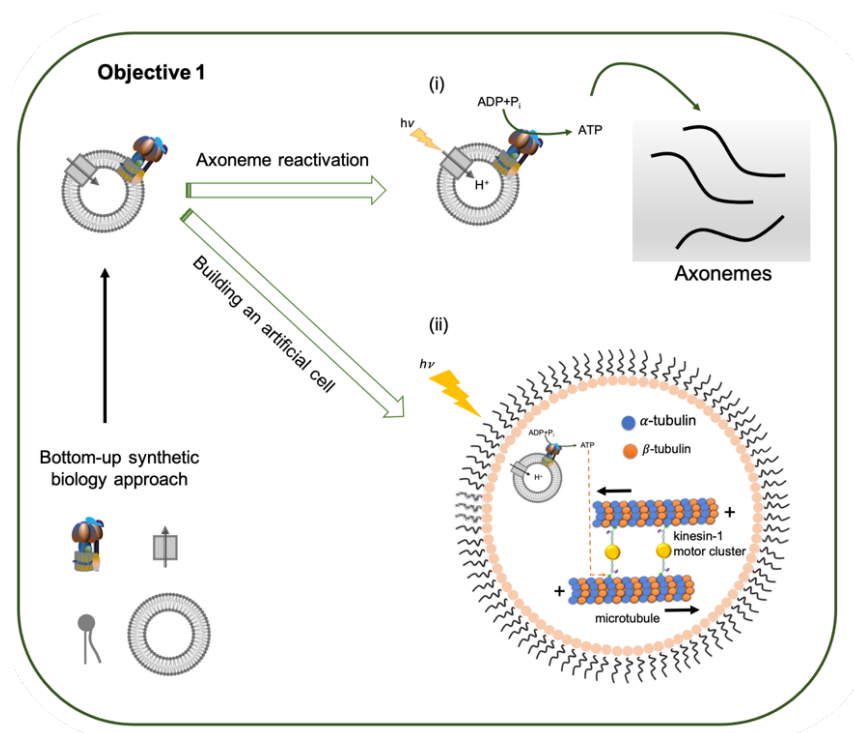


Figure 1.18: Integration of light-switchable ATP regeneration module with two types of motility modules. (I) Reactivation of axonemes. (II) Encapsulation of MTs assembled force-generating kinesin-1 motors and energy functional module.

- (2) We assess the viability of *C. reinhardtii* isolated axoneme as an ATP-driven micro-swimmers (Figure 1.9). We analyze the waveform of the axoneme and investigate how the individual wave components change in response to chemical stimuli (such as calcium ions).

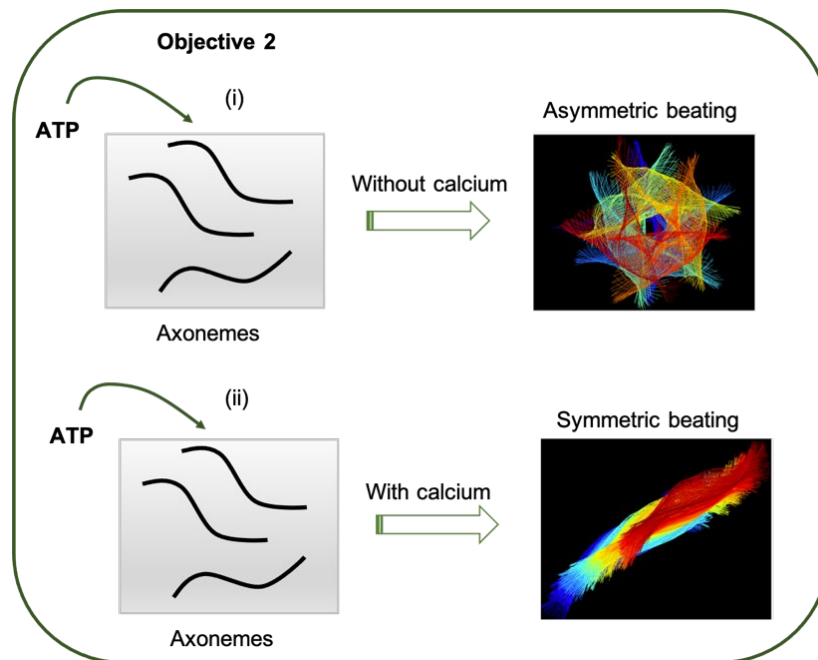


Figure 1.19: *C. reinhardtii* isolated axonemes as an ATP-driven micro-swimmer and effect of calcium ion on its waveform. (I) Asymmetric waveform of an *C. reinhardtii* isolated axoneme. (II) Calcium triggers a transition from asymmetric to a symmetric waveform.

- (3) We construct an ATP-driven bio-actuator by attaching micron-sized cargo to the *C. reinhardtii* axonemes (Figure 1.20). We study the waveform of the bio-hybrid micro-swimmers, the effect of the mode of attachment of the beads (asymmetric vs symmetric) to the axonemes and the size of the cargo on the swimming speed. In addition, the effect of chemical stimuli (calcium ions) on the flagellar waveform, switching from asymmetric to symmetric, is considered for targeted drug delivery applications.

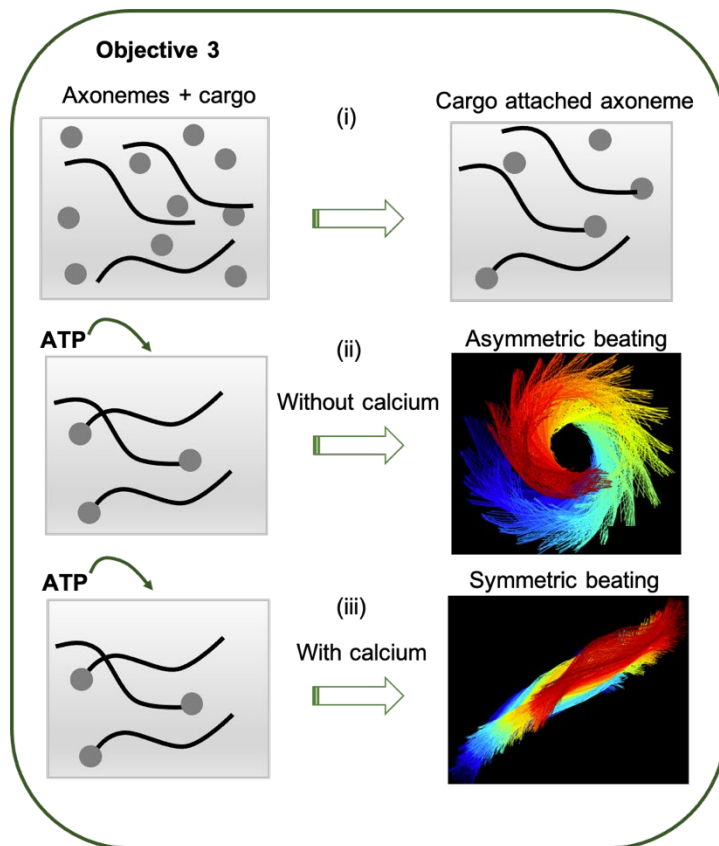


Figure 1.20: Construction of a bio-hybrid micro-swimmer. (I) Cargo attached to *C. reinhardtii* isolated axonemes. (II) Asymmetric waveform of an axoneme in the absence of calcium. (III) Calcium-induced transition in the swimming trajectory of micro-swimmer, switching from asymmetric to symmetric waveform.

Chapter 2 Materials and Methods

Sections, 2.2.6, 2.4.2, 2.4.3, 2.5.1.1, 2.5.1.3, 2.5.2, and 2.6-2.11 are adapted from:

[1] **Raheel Ahmad***, Christin Kleineberg*, Vahid Nasirimarekani, Yu-Jung Su, Samira Goli Pozveh, Albert J Bae, Kai Sundmacher, Eberhard Bodenschatz, Isabella Guido, Tanja Vidaković-Koch and Azam Gholami, "Light-Powered Reactivation of Flagella and Contraction of Microtubule Networks: Toward Building an Artificial Cell", *ACS Synthetic Biology (Featured on Front Cover)*, 2021, 10, 1490-1504. (*Equal contribution).

Raheel Ahmad contributions: Isolation of flagella, integration of ATP energy module with flagella, experiments with pure commercial ATP, fabrication of microfluidic device, experiments with MTs/kinesin-1, data analysis, writing, discussion and revision.

[2] **Raheel Ahmad**, Albert J Bae, Yu-Jung Su, Samira Goli Pozveh, Alain Pumir, Eberhard Bodenschatz and Azam Gholami, "Bio-hybrid Micro-swimmers Propelled by Flagella Isolated from *C. reinhardtii*", *Soft Matter*, *Accepted*, 2022.

Raheel Ahmad contributions: Isolation of flagella, experiments with calcium and beads, data analysis, discussion and revision.

[3] Azam Gholami, **Raheel Ahmad**, Albert J bae, Alain Pumir and Eberhard Bodenschatz, "Waveform of Free, Hinged and Clamped Axonemes Isolated from *C. reinhardtii*: Influence of Calcium", *New Journal of Physics*, 2022, 24, 053025.

Raheel Ahmad contributions: Isolation of flagella, experiments with calcium, data analysis, discussion and revision.

2.1 Chemicals and Materials

C. reinhardtii wild type (strain 11- 32b) was provided by Göttingen Algae Collection (SAG). Lipid (L- α -phosphatidylcholine (Soy-PC)) was purchased from Avanti Polar Lipids (Alabama, USA). Luciferin/Luciferase reagent CLSII from Roche was purchased from Merck (Darmstadt, Germany) and prepared a 10X solution. Ultra-pure ADP was purchased from Cell Technology (Hayward, USA). Film masks for microfluidic and millifluidic devices were purchased from Micro Lithography Service (Essex, UK). Soft photolithography was performed in the cleanroom at Göttingen Microfluidics Facility (Max Planck Institute for Dynamics and Self-organization, Göttingen, Germany) and PDMS devices were fabricated in the wet lab. All buffers and

solutions were prepared in double distilled water (ddH₂O) using the arium® pro-VF ultrapure water system. A detailed list of all chemicals and types of equipment can be found in Appendix A. 1.1 and A. 1.2, respectively.

2.2 Expression, Isolation and characterization of his-tagged ATP Synthase

His-tagged *E. coli* F₀F₁-ATP synthase (EF₀F₁) was expressed from the plasmid pBWU13-βHis in the *E. coli* strain DK8 (ΔuncBEFHAGDC) as described by Ishmukhametov et al.¹⁵⁵ with slight modifications in the protocol. These experiments were performed by the research groups of Dr. Tanja Vidaković-Koch and Prof. Kai Sundmacher (MPI Magdeburg), therefore, explained here briefly for readership. The plasmid pBWU13-βHis introduced a hexahistidine tag at the amino-terminus of the β subunit of the ATP synthase and used for efficient purification using Ni-NTA affinity chromatography.

2.2.1 *E. coli* cell culture cultivation

Cells were grown in Lysogeny broth (LB) medium (Appendix, Table A. 1) supplemented with ampicillin (100 μg/mL) and tetracycline (20 μg/mL) under continuous shaking for 4.5 hr at 37 °C. The cells were collected by centrifugation at 7,700 X g for 15 min at 4 °C. The optical density of the collected cells was measured to ~2. The wet bacterial cells (4-5 g) were harvested from a 1-litre LB medium. The collected cell pellets were frozen in liquid nitrogen and stored at –80°C for further use.

2.2.2 Isolation and purification of EF₀F₁

The cell pellets from –80°C were thawed at ambient temperature and resuspended in a French press buffer supplemented with a spade point tip of phenylmethylsulphonyl fluoride (PMSF) and Dnase (Appendix, Table A. 2). The suspension was subjected to the French press procedure¹⁵⁵ at 16,000 psi pressure. The drops were collected in liquid nitrogen and stored at –80°C. Further, cells were thawed and added 500 μL of PMSF. Unbroken cells were separated by centrifugation at 25,000 X g for 15 min at 4°C. Next, all isolation steps were performed at 4°C using an ice bath. The supernatant containing membranes was ultracentrifuged at 184,000 X g for 1 hr and the pellet was resuspended in an extraction buffer (Appendix, Table A. 3). A

four milliliter of extraction buffer was used for 1 g of membrane protein and the sample was put on a shaker at medium speed for 90 min. Afterwards, the sample was ultracentrifuged at 200,000 X g for 60 min. The supernatant was collected and applied to the Ni-NTA column, which was preequilibrated with the same buffer. The flow rate of the sample was adjusted to 250 $\mu\text{L}/\text{min}$. To remove other contaminations, the resin was flushed with 20 mL of extraction buffer. Finally, EF_oF₁ was eluted with 5 mL of extraction buffer supplemented with 150 mM imidazole at the flow rate of 250 $\mu\text{L}/\text{min}$. The eluted fraction was frozen in liquid nitrogen and stored at -80°C for further use.

2.2.3 SDS-PAGE analysis

The purity of isolated his-tagged ATP synthase was by confirmed sodium dodecyl sulphate – polyacrylamide gel electrophoresis (SDS-PAGE) .¹⁵⁶ Gel was prepared in a Bio-Rad gel apparatus with 4% of a stack and 13% of a running composition. The samples were loaded with 5 μL of gel sample buffer (Appendix, Table A. 4) and incubated at 90°C for 20 min. The electrophoresis was carried out with the current value of 20 mA and 40 mA in the stacking and running gel section, respectively, for 1 hr at room temperature. A five microliter of pre-stained protein ladder (PageRule™, ThermoFisher Scientific) was used as a gel band reference. Afterwards, the running gel was stained with coomassie brilliant blue R-250 dye and placed in a staining solution (Appendix, Table A. 5) followed by heating at 600 W for 20 sec in a microwave oven. Finally, the gel was decolorized in a decolorizing solution (Appendix, Table A. 6) for 15 min, until the band had the desired intensity.

2.2.4 Determination of ATP synthase concentration

The concentration of purified ATP synthase was determined by the Beer-Lambert law, see Eq. 2.1¹³⁴. The absorbance at 280 nm (A_{280}) was measured with spectrophotometry (specord 50 plus). The extinction coefficient of ATP synthase at 280 min is $\epsilon_{280} = 340,000 \text{ M}^{-1}\text{cm}^{-1}$. The cuvette with a path length of $d = 1 \text{ cm}$ was used for measurements. Extraction buffer (Appendix, Table A. 3) was used as a reference sample.

$$C_{EF_oF_1} = \frac{A_{280}}{\epsilon_{280} \cdot d} \quad [2.1]$$

2.2.5 Preparation of liposomes by dialysis method for ATP synthase reconstitution

Liposomes were prepared by dialysis as described by Fischer et al.¹⁵⁷ 6.8 mL of soy-PC in chloroform (25 g/L) and 3.6 mL of phosphoric acid (2.5 g/L) were mixed thoroughly. The solvent was removed in a rotary evaporator with a nitrogen stream. The evaporator was placed in a water bath and the temperature and pressure were 40°C and 20 mbar, respectively. The dried lipids were resuspended in 10 mL of liposome sonication buffer (Appendix, Table A. 7) and sonicated three times for 30 sec in an ice bath, to make multilamellar to unilamellar vesicles. To avoid overheating of the vesicles, the time between each sonication step was maintained to 30 sec. Further, lipid vesicles were stored overnight at – 20°C. Finally, the lipid vesicles were defrosted and dialyzed in dialysis buffer (Appendix, Table A. 8) at 30°C for 5 hr. The liposomes had a final lipid concentration of 16 g/L. The liposomes were frozen in liquid nitrogen and stored at – 80 °C for further use. The E_oF₁-ATP synthase was reconstituted into preformed liposomes with slight modification in the protocol as described by Fischer et al.¹⁵⁷. A hundred microliter of liposomes were mixed with 0.5 µL of MgCl₂ (1 M), 78 µL of reconstitution buffer (Appendix, Table A. 9) and 0.1 µM of ATP synthase (final concentration). The theoretical ratio of ATP synthase to liposomes was 1 (ATP synthase: liposomes, 1:1). A sixteen microliter of Triton X-100 with a final concentration of 0.8% was added to the above solution and vortex to partially destabilize the liposomes. Further, the mixture was incubated under gentle shaking at room temperature for 15 min. For removal of detergent, 80 mg of wet SM-2 Bio-Beads were added to the above solution and incubated at room temperature for 60 min.

2.2.6 Turnover of ATP synthase

The activity of ATP synthase was confirmed by energizing the proteoliposomes in an acid-base transition experiment as previously described by Schmidt and Gräber.¹⁵⁷ A one milliliter of basic medium buffer (Appendix, Table A. 10) was mixed with 6 µL (10X) concentration of luciferin/luciferase reagent and 1 µL of 9.5 mM ultrapure ADP. A baseline was recorded using Luminometer (Glomax 20/20). Further, 20 µL of proteoliposomes were mixed with 90 µL of acidic medium buffer (Appendix, Table A. 11) and incubated at room temperature for 3 min followed by the addition of ADP (0.1 µM) and 2 µL of valinomycin (10 mM). The reaction was started by the addition of 100 µL of the above prepared acidic proteoliposomes solution into

the basic buffer and ATP synthesis was measured for 150 sec. The detected luminescence signal was used to calculate the change in ATP concentration (C_{ATP}) and the catalytic constant (k_{cat}) of ATP synthesis (Figure 2.1). After each measurement 10 μL of ATP (7.8 μM) was added threefold to normalize the luminescence signal (Figure 2.1). The initial reaction velocity (V_0 , nMs^{-1}) is calculated from the slope of the line while k_{cat} is obtained by dividing the V_0 by the enzyme concentration $[E]$. The ATPase was reconstituted in 0.8% Triton X-100, and electrical potential difference ($\Delta\psi$) was measured to 143 mv.

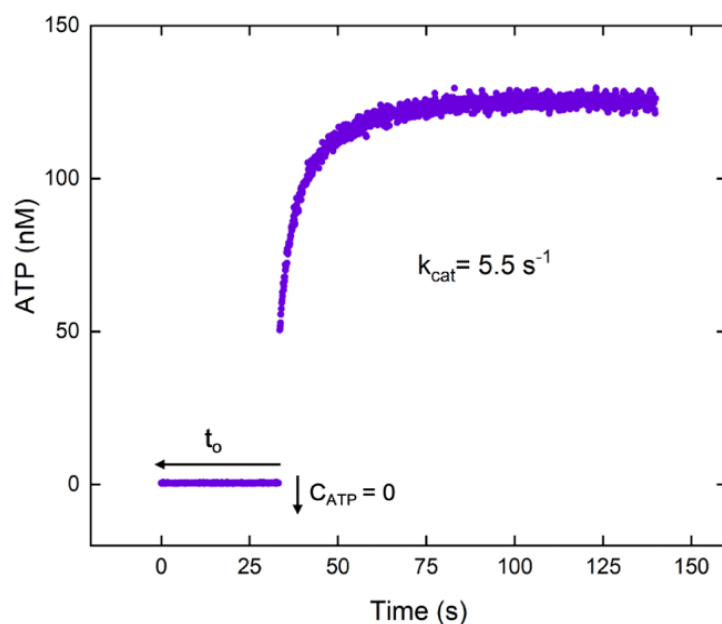


Figure 2.1: Turnover (k_{cat}) of ATP synthase determined by acid-base transition experiment. Measurements were performed by Dr. Christin Kleineberg, MPI Magdeburg.

2.3 Bacteriorhodopsin expression, isolation and characterization

2.3.1 Halobacterium salinarium cell cultivation

Cells were cultivated in a Halobacterium salinarium culture medium (Appendix, Table A. 12) under continuous illumination and shaking at 200 rpm for 90 hr at 39°C.

2.3.2 Isolation of Bacteriorhodopsin

Bacteriorhodopsin (bR) was isolated from Halobacterium salinarum (strain S9) as described by

Oesterhelt et al.¹⁵⁸ Cultivation and isolation experiments were performed by the research groups of Dr. Tanja Vidaković-Koch and Prof. Kai Sundmacher (MPI Magdeburg), therefore, explained here briefly for readership. Cells were grown in a 10-liter of volume and harvested by centrifugation at 13,000 X g for 15 min. Further, pellets were resuspended in 250 mL of membrane resuspension buffer (Appendix, Table A. 13). For cell lysis, 2-liter of 0.1 M NaCl was added to the above suspension and incubated overnight at room temperature. The lysate was centrifuged at 40,000 X g for 40 min and removed the red fragments from the supernatant. The purple pellet was collected and resuspended in 300 mL of 0.1 M NaCl and centrifuged under the same conditions. The washing step was continued until all material in the solution settled down and the supernatant appeared colorless. The pellet was collected and resuspended in deionized water and washed several times. Finally, the pellet was taken up to 6-10 mL in water and layered over a 30-50% sucrose density gradient with 2 mL of 60% sucrose bottom cushion, and ultracentrifuged at 100,000 X g for 17 hr. The purple solution was equilibrated at a density of 1.18 g/cm³ and collected by centrifugation at 50,000 X g for 30 min.

2.3.3 Calculation of bR concentration

The concentration of bR was calculated using the absorbance at 560 nm (A_{560}).¹⁵⁹

$$C_{bR} = \frac{A_{560}}{\epsilon_{560} \cdot d}, \quad [2.2]$$

where C_{bR} is the concentration of bR, ϵ_{560} is the extinction coefficient of bR at 560 nm (54,000 M⁻¹cm⁻¹), d is the path length (1 cm) of cuvette. The bR was diluted in Milli-Q water with volume ratio of 1:20 (v/v). Milli-Q water was set as a blank. The absorbance of bR was measured by UV-vis spectrometry (Specord 50 plus) using the scanning range of 280-800 nm. The absorption ratio of A_{560} and A_{280} was used to calculate the purity of isolated bR.¹⁵⁹

$$\text{Purity (\%)} = \frac{A_{560}/A_{280}}{0.5}. \quad [2.3]$$

2.3.4 Solubilization of bR patches

Solubilization of bR was performed in detergent (Triton X-100) as described by Meyer et al.¹⁶⁰ The molar ratio of Triton to bR was taken to 68. First, the volume of Triton was calculated using the Eqs 2.4-2.7. The calculated amount of the detergent was added and the suspension was sonicated for 10 min and followed by stirring for four days at 4°C in the dark. Finally, membrane pellets were collected by ultracentrifugation at 400,000 X g for 30 min.

$$n_{bR} = c_{bR} \cdot V_{bR}, \quad [2.4]$$

$$n_{Triton} = n_{bR} \cdot 68, \quad [2.5]$$

$$V_{Triton} = \frac{n_{Triton}}{C_{Triton}}, \quad [2.6]$$

$$V_{Triton} = \frac{A_{560} \cdot V_{bR} \cdot 68}{\epsilon_{560} \cdot d \cdot C_{Triton}}, \quad [2.7]$$

where n_{bR} is the molar amount of bR, V_{bR} is the volume of bR, n_{Triton} is the molar amount of Triton, C_{Triton} is the concentration of Triton (10% = 0.16 mol/L).

2.4 Preparation of lipid vesicles by an extrusion method and coreconstitution of EF₀F₁-ATP Synthase and bR

2.4.1 Preparation of small unilamellar lipid vesicles by extrusion method

Lipid vesicles were synthesized by film rehydration method (see Figure 2.2) and followed by a size extrusion using polycarbonate membrane (PC, 100 nm pore size). Ten milligrams of dissolved lipid (soy-PC) were taken in a glass vial and the solvent was removed using a gentle stream of nitrogen and kept rotating the glass vial. Thin lipid films were rehydrated in HMDEKP buffer (Appendix, Table A. 14) to a final lipid concentration of 10 mg/mL by vortexing, until lipid films dissolved. For pyranine (8-Hydroxypyrene-1,3,6-trisulfonic acid) encapsulation experiments, 10 mM of pyranine was added in the rehydration step. Further, multilamellar vesicles obtained in the previous step were transformed into unilamellar vesicles by subjecting five freeze–thaw cycles. Each cycle comprised of freezing the solution in liquid nitrogen followed by thawing in a 35°C water bath and vortexing for 30 sec. To get small unilamellar

vesicles, the suspensions were extruded using Avanti Mini-Extruder 11 times through a PC membrane.

2.4.2 Reconstitution of bR into lipid vesicles and its pumping efficiency

A hundred microliter of preformed lipid vesicles were mixed with 80 μ L (6 mg/mL) of bR in the form of patches. To partially solubilize the vesicles, Triton X-100 (0.8%) was added followed by vortexing. The sample was incubated in dark for 15 min at room temperature under gentle shaking. Afterwards, the detergent was removed by adding SM-2 Bio-Beads (80 mg) to the above solution and incubated for 60 min under constant shaking at room temperature in dark. For the pumping efficiency experiment, pyranine (10 mM) was added in the aqueous phase and non-encapsulated dye was removed using gel filtration (pre-packed G25 size exclusion column, PD Mini TrapTM G-25, GE Healthcare). The reconstitution efficiency of bR (bR_{eff}) was

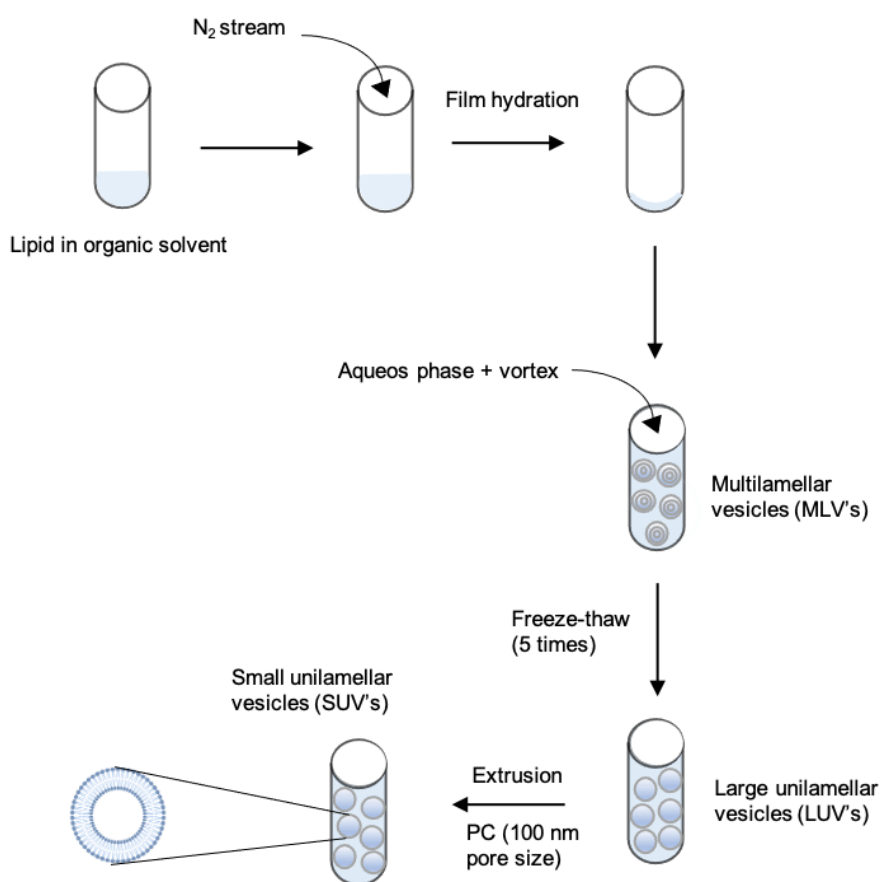


Figure 2.2 : Schematic illustration of lipid vesicles preparation by extrusion method.

calculated from the absorbance at A_{560} before and after gel filtration using Eqs. 2.8-2.10. The dilution of bR was determined by the volume applied to column (V_{before}) and the volume collected (V_{after}) by elution.

$$bR_{eff} = \frac{C_{bR,after}}{C_{bR,before}}, \quad [2.8]$$

$$C_{bR,after} = \frac{A_{560,before}}{\varepsilon_{560} \cdot d}, \quad [2.9]$$

$$C_{bR,before} = \frac{A_{560,after}}{\varepsilon_{560} \cdot d} \cdot \frac{V_{before}}{V_{after}}, \quad [2.10]$$

$$bR_{eff} = \frac{A_{560,after}}{A_{560,before}} \cdot \frac{V_{after}}{V_{before}}, \quad [2.11]$$

where $C_{bR,after}$ is the concentration of bR after gel filtration, $C_{bR,before}$ is the concentration of bR before gel filtration. To avoid the formation of a potential gradient that counteracts the generated pH gradient, valinomycin (0.1 μ M) was added to the solution. The sample was equilibrated by placing it in the dark for 1 hr and measurement was started by illumination with a 50 W green LED lamp (SMD RGB, V-TAC). The absorbance changes at 450 nm (A_{450}) and 405 nm (A_{405}) were monitored over 10 min using a spectrometer (QEPRO, Ocean Optics).

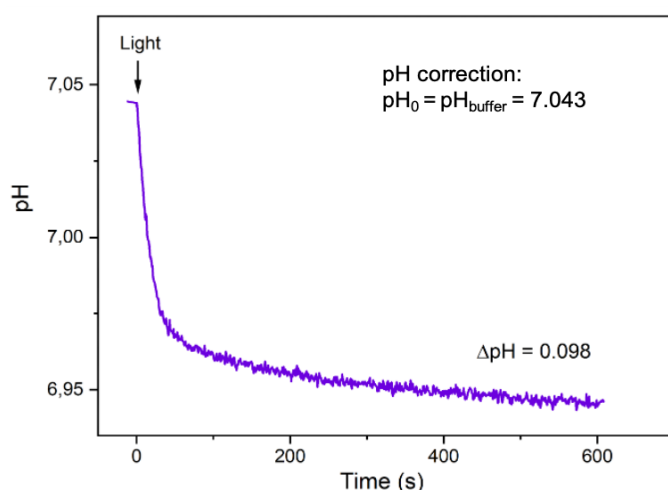


Figure 2.3: Proton pumping of bR measured by encapsulation of pH sensitive dye (pyranine) in lipid vesicles. Measurements were performed by Dr. Christin Kleineberg, MPI Magdeburg.

The pH value was calculated by the absorbance ratio of A_{450} (deprotonated) and A_{405} (protonated) (Figure 2.3) using the calibration curve.¹³⁴ The starting pH (pH_0) was corrected to the pH of the buffer solution (pH_{buffer}).

2.4.3 Determination of bR orientation by proteolytic assay

Orientation of bR in reconstituted vesicles was determined by proteolytic cleavage as described by Gerber et al.¹⁶¹ Proteinase K (Roche) was added to a final concentration of 2.5 mg/mL. After incubation at 37°C for 2 hr, the reaction was stopped by adding protease inhibitor PMSF (10 mM). The reaction product was cooled down on the ice for 30 min. Further, the reaction product was analyzed by running an SDS-PAGE (4-20% Tris-HCl Criterion Precast Gels (Bio-Rad)). A twenty microliter of each sample was supplemented with 5 μ L of gel sample buffer (Table A. 4) and incubated at 90 °C for 5 min. A ten microliter of each sample was loaded on the gel, and a current value of 100-150 mA was applied for 40 min in the gel chamber pre-filled with Laemmli buffer (Appendix, Table A. 15). A five microliter of protein ladder (PageRuler™ Prestained Protein Ladder) was used as a reference. The gel was placed in a staining solution (Appendix, Table A. 5) and incubated for 60 min on a shaker. Finally, the gel was placed in a decolorizing solution (Appendix, Table A. 6) till the bands had the desired intensity.

2.5 Preparation and characterization of light-driven ATP functional module

2.5.1 Preparation of lipid vesicles for coreconstitution of ATP synthase and bR

Lipid vesicles were synthesized by the extrusion method as described in section 2.4 without pyranine encapsulation.

2.5.1.1 Determination of vesicle size by dynamic light scattering (DLS)

The size distribution profile and monodispersity were determined by dynamic light scattering (DLS) using a Zetasizer Nano ZS (Malvern, Worcestershire, UK) with a 633 nm helium-neon laser and back-scattering detection. A two microliter of vesicles were diluted in 1 mL of HMDEKP buffer and samples were measured at a fixed scattering angle ($\theta = 173^\circ$) at 25°C. All reported

values are based on the average of three measurements. Each measurement consisted of 3X5 runs with 70 sec durations.

2.5.1.2 Calculation of the lipid concentration

The concentration of the lipids per vesicles¹⁶² was calculated as:

$$N_{tot} = \frac{4\pi\left[\left(\frac{d}{2}\right)^2 + \left(\frac{d}{2}-l\right)^2\right]}{A_{pc}}, \quad [2.12]$$

where d is the diameter of vesicles, l is the thickness of the bilayer (~ 5 nm), A_{pc} is the lipid surface area (0.71 nm^2)¹⁶². The number of lipids in 150 nm size vesicles is around 3.7×10^5 . The number of vesicles per milliliter ($N_{vesicles}/mL$) was calculated using the following equations¹³⁴,

$$N_{vesicles} = \frac{C_{Lipids} \cdot N_A}{N_{tot} \cdot 1000}, \quad [2.13]$$

where, N_A is the Avogadro number ($6.022 \times 10^{23} \text{ mol}^{-1}$), C_{Lipids} is the mass concentration of lipids, M_{pc} is the molar mass of PC (775 g/mol).

2.5.1.3 Coreconstitution of EF₀F₁-ATP Synthase and bR

A hundred microliter of preformed lipid vesicles were mixed with 0.1 μM EF₀F₁-ATP synthase and 9.9 μM bR (in patches form) aiming for a theoretical ratio of 1 ATP synthase and 96 bR molecules per vesicle. Triton X-100 (0.8%) was added under vortexing to partially solubilize the vesicles followed by incubation in the dark for 15 min. To remove the detergent, 80 mg of wet SM-2 Bio-Beads were added to the solution and incubated in dark under gentle shaking for 60 min. The number of the proteins (EF₀F₁-ATP synthase ($N_{EF_0F_1}$)) and bR (N_{bR}) were calculated as¹³⁴,

$$N_{bR} = C_{bR} \cdot N_A, \quad [2.14]$$

$$N_{EF_0F_1} = C_{EF_0F_1} \cdot N_A. \quad [2.15]$$

The number of proteins/vesicles can be obtained by dividing $N_{bR}/N_{vesicles}$ or $N_{EF_0F_1}/N_{vesicles}$.

2.5.2 Light-driven ATP production by coreconstituted vesicles

For measurement of light-driven ATP production, ATP functional module was prepared with 25 μL of coreconstituted vesicles diluted in 250 μL of HMDEKP buffer (Appendix, Table A. 14) supplemented with 10 μL of ultra pure ADP (7.8 mM) and 5 μL of sodium phosphate (5 mM). The reaction was started by illumination with a 50W green LED lamp or a 5W microscope light. A twenty-five microliter of volume was taken from the reaction mixture and the reaction was stopped by adding the same volume of trichloroacetic acid (TCA, 40 g/L). The ATP concentration was measured with the luciferin/luciferase assay and calibrated by the addition of 10 μL ATP (7.8 μM) after each measurement.

2.5.2.1 Calculation of ATP concentration

The amount of ATP produced was calculated from the luminescence signal¹³⁴ as,

$$C_{syn} = \frac{I_S - (I_B \frac{V_0}{V_1})}{I_C - (I_S \frac{V_1}{V_2})} \cdot \frac{C_C \cdot V_C}{V_2} \cdot \frac{V_1}{V_S} \cdot \frac{V_{TCA}}{V_{syn}} \quad [2.16]$$

Where C_{syn} is the concentration of ATP, I_B is the background luminescence intensity, I_S is the intensity of the sample, I_C is the calibration intensity, V_0 is the volume of luciferase (200 μL), V_1 is the volume of luciferase + sample volume (220 μL), V_2 is the volume of luciferase + sample volume + calibration volume (230 μL), C_C is the concentration of ATP for calibration (7.8 μM), V_C is the Volume of calibration (10 μL), V_S is the volume of a sample (20 μL), V_{syn} is the volume of a sample for stopping the reaction (25 μL), V_{TCA} is the volume of the sample when stopping the reaction + volume of TCA (50 μL).

2.6 Preparation of growth media and agar tube for *C. reinhardtii* and cells cultivation

2.6.1 Preparation of growth media

Cells were grown in tris acetate phosphate (TAP) with excess phosphate (TAP+P) medium.⁴¹ In this culture media, phosphate concentration was four times higher as compared to TAP medium¹⁶³ which facilitated the cells to grow for a longer time. TAP+P (1-liter) was prepared by mixing salt solution (Appendix, Table A. 16), potassium phosphate solution (Appendix, Table A. 17) and Hunter's trace element (Appendix, Table A. 18). First, Hunter's trace element solution was prepared as described in the literature¹⁶³. Upon mixing the components as described in Table A. 18, the color of the solution turns green. The solution was heated to a boil until all components appeared dissolved. Afterwards, lowered the solution temperature to 70°C and added 85 mL of hot KOH (20%) into the solution. Cooled down the solution to room temperature and fill the flask volume up to one liter. The solution appeared clear green and pH was measured to ~6.5. Stopper the flask for air passage and left the solution at room temperature for two weeks, and the flask was swirled once a day. A few days later, the solution should turn purple and leave rust-brown precipitate. Note that if no precipitate form and the solution remain green, adjust the pH to 6.5 using either KOH or HCl as needed. Finally, after the rust-brown precipitate was formed, the solution was filtered with two-layer Whatman-1 filter paper and the filtration step was repeated until getting a clear solution.

Finally, the stock solution of TAP+P media was prepared by mixing the above-prepared solutions (Appendix, Table A. 19) except glacial acetic acid and filled the flask to one liter. Titrate the solution with glacial acetic acid to pH 7, and mixed vigorously until the solution turned clear. Autoclaved the TAP+P at 121°C for 20 min and the stock solution was stored at 4°C for further use.

2.6.2 Preparation of agar tube

Agar tubes were prepared by dissolving agar (1.5%, w/v) in TAP+P medium and autoclaved the mixture at 121°C for 20 min. The solution was cooled down to ~ 60°C and poured the solution (~20 mL) into the agar tube followed by tilting the tube for a few seconds to make it stiff, and

left the tube open for 2 hr at room temperature. Finally, the agar tubes were stored at 4°C for further use. All steps were performed under a sterile bench.

2.6.3 Cultivation of *C. reinhardtii* cells

Cells were grown in 12 hr/12 hr day-night cycle¹²⁵ in a custom-made laboratory setup (Figure 2.4) using a 1000 mL Erlenmeyer flasks. Each time two flasks were filled with 500 mL of TAP+P culture media and taken *C. reinhardtii* culture from an agar tube using inoculating loop and mixed it thoroughly.

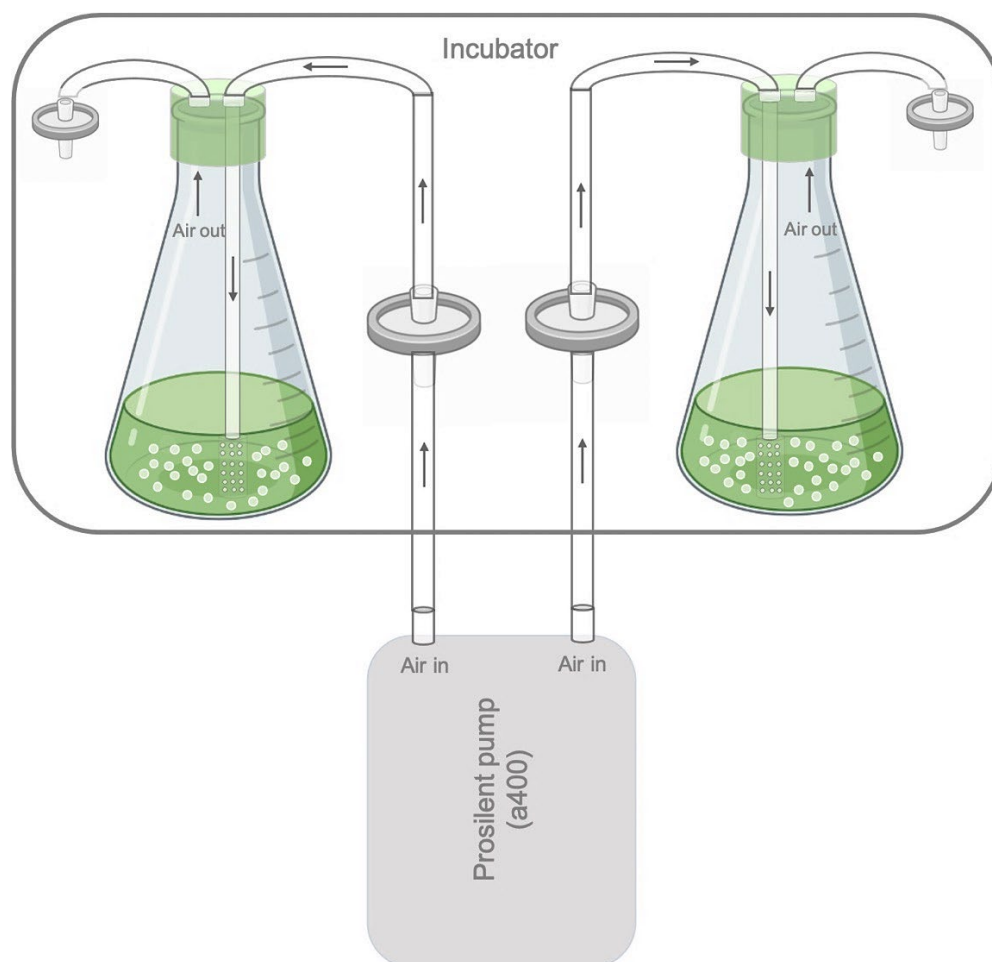


Figure 2.4: Schematic illustration of a setup for *C. reinhardtii* cells cultivation.

Flasks were closed with a rubber stopper which has two holes. Micro filter candles (Duran® Micro filter candle with narrow tube, 125aD, porosity 2) were fixed into one hole for uniform distribution of filtered air coming from the air pump (Prosilent a400) with a flow rate of 100

L/min, whereas, the other was fixed with micro filter (Minisart® High Flow with Polyethersulfon) for filtered air out. The flasks were mounted on an incubator and cells were grown under gentle shaking (100 rpm) at 25°C. Two LED lights (LMH2 4000 lm, LED module) were mounted on an incubator and connected with an automatic switch to make it on/off mode.

2.6.4 Calculation of cell density

To obtain the calibration curve, cell density was monitored by extracting the sample every twelve hours and measured the absorbance at 750 nm (A_{750}) using a spectrophotometer (SmartSpec Plus Spectrophotometer). The absorbance (A_{750}) is proportional to the number of cells⁴¹. The cells were allowed to grow to a late exponential phase $\sim 8 \times 10^6$ cells/mL and this concentration was reached in 72 hr (Figure 2.5A).

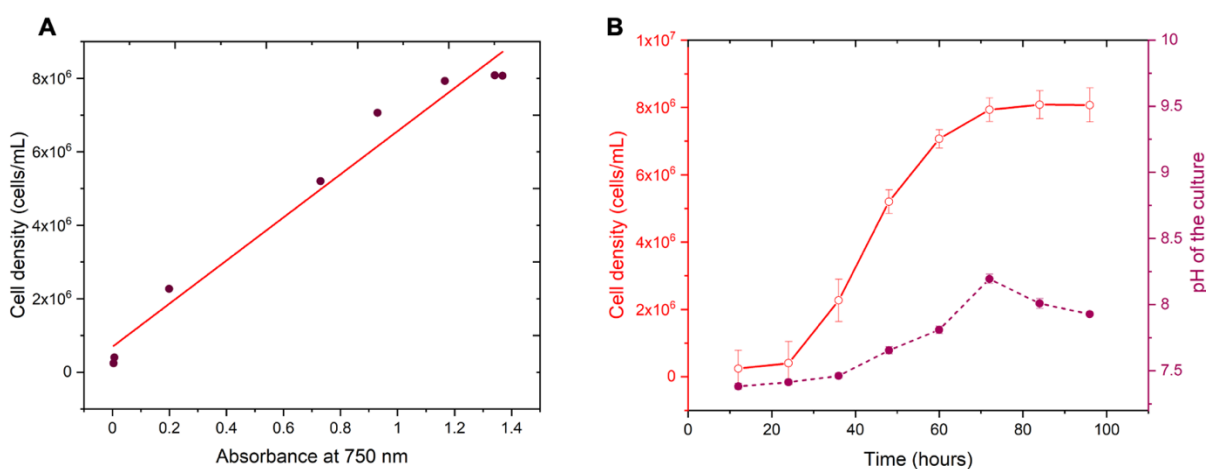


Figure 2.5: The growth rate of *C. reinhardtii*. A) Calibration curve for the measurements of cell density using absorbance at 750 nm (A_{750}). The extinction coefficient of the wild type cell is $5.8 \pm 0.4 \times 10^6$ cells/(OD.mL.cm), slope \pm 95% confidence interval of least square fit was used to determine the cell density. B) Growth curve for 12 hr day/night cycle (red line) and change in the pH value of the cell culture (purple line).

Further, the number of cells was accounted using Neubauer hemocytometer (Figure 2.5B). As the cell metabolize, the concentration of acetate in the growth phase increases, resulting in an increase in the pH value of the cell culture⁴¹ (Figure 2.5B). In total, 10^9 cells were used to isolate the axonemes.

2.7 Isolation and reactivation of demembrated flagella

2.7.1 Isolation of axoneme

Axonemes were isolated by the dibucaine method with slight modification in the protocol as described in the literature^{125, 164}. The cell culture solution was filled in 50 mL tubes (Falcon 50mL Conical Centrifuge Tubes) and centrifuged at 2000 rpm for 5 min. The supernatant was removed and the pellet was dissolved by gentle shaking in 10 mL of HEPES (10 mM). To increase the concentration of cells, 10 mL of solution from each tube was mixed and filled the tubes up to 45 mL. The centrifugation and resuspension steps were performed three times. After the third cycle, the supernatant was removed and 20 mL of HMDS 4% buffer (Appendix, Table A. 20) was added. Afterwards, 2 mL of dibucaine (25 mM) was quickly added using a 2 mL pipette and triturate seven times, and filled the tubes up to 40 mL with HMDS-EGTA 4% buffer (Appendix Table A. 21). The solution was centrifuged at 1800 X g for 5 min and the supernatant was collected. The flagella were purified in a sucrose cushion by adding 9 mL of HMDS 25% buffer (Appendix, Table A. 22) at the bottom of the tube with a syringe (20 mL syringe and B. Braun Sterican® 21G x 4 3/4"; 0,80 x 120 mm needle) followed by centrifugation at 2800 rpm for 10 min. The supernatant was collected and ultra-centrifuged at 24,000 X g for 40 min. Further, the supernatant was removed and a whitish pellet of flagella at the bottom of the tube was gently dissolved in HMDEK+Pefabloc buffer (Appendix, Table A. 23) using an inoculation loop. To demembrate the flagella, non-ionic surfactant (NP-40) with a 1:9 volume ratio (NP-40: flagella, v/v) was added followed by incubation for 30 min at 4°C in an ice bath. Finally, the demembrated flagella (axonemes) were collected by centrifugation at 14,000 rpm for 20 min and dissolved the pellet in 100 µL of HMDEKP + Pefabloc buffer (Appendix, Table A. 24). Finally, the collected axonemes were distributed in 5 µL aliquots and stored at –80°C for further use.

2.7.2 Preparation of reaction chamber for reactivation of axonemes

A reaction chamber for reactivation of axoneme was built using a glass slide (24 mm × 60 mm, Menzel Gläser, Germany) and 100 µm double-sided tape. The glass slide was coated with

casein (2 mg/mL in HMDEKP reactivation buffer (Appendix, Table A. 14)). To close the chamber, a cover slip (18 X 18 mm # 1, Deckgläser) was used.

2.7.3 Reactivation of *C. reinhardtii* isolated axonemes

2.7.3.1 Reactivation with pure commercial ATP

To reactivate the axonemes with pure commercial ATP, different concentrations of ATP were added to the HMDEKP buffer (Appendix, Table A. 14).

2.7.3.2 Reactivation with light-driven ATP functional module

Light-driven ATP module was prepared by mixing coreconstituted vesicles with ADP (1.6 mM) and sodium phosphate (5 mM). The solution was preshined under microscope light 5W or 50W LED lamp at different time points and mixed immediately with thawed axonemes (from -80°C). The volume ratio of ATP module to axoneme (9:1, v/v) was fixed for all experiments. In all experiments, the activity of axonemes was found to $\geq 90\%$.

2.7.3.3 Reactivation of axoneme supplemented with calcium

In axoneme reactivation experiments with ATP and calcium, different concentrations of ATP were used with fixed calcium concentration and vice versa. Whereas, in reactivation experiments with a light-driven ATP module, the ATP module was prepared in the same manner as described in section 2.7.3.2, supplemented with different concentrations of calcium according to the experiments.

2.7.4 Bead-attached axonemes and reactivation with and without calcium

For axoneme-bead experiments, 1 μm polystyrene (PS) particles (Fluoresbrite® YG Microspheres, Polysciences) were used. One hundred microliters of PS particles were taken from the stock solution and diluted to 1 mL with HMEDEKP buffer (Appendix, Table A. 14 supplemented with 0.01% SDS). The PS particles were washed twice in 1 mL of the same buffer by centrifugation at 14,000 rpm for 5 min. Before use, PS particles were sonicated for 5 min. One microliter of PS beads was mixed with 2 μL of axonemes by gentle pipetting and incubated

for 20 min at room temperature. For experiments with calcium, different concentrations of calcium were used in the HMDEKP reactivation buffer.

2.8 Axoneme contour tracking

We imaged reactivated axonemes using phase-contrast microscopy (100X objective, imaging frequency of 1000 fps). To increase the signal-to-noise ratio, we first inverted phase-contrast images and then subtracted the mean intensity of the time series. This background-subtraction method increased the signal-to-noise ratio by a factor of 3^{41} . Next, we applied a Gaussian filter to smooth the images. Tracking of axonemes is done using the gradient vector flow (GVF) technique.^{103, 104} Tracking of an axoneme is performed under the framework of a snake or active contour model by defining the curve $\mathbf{r}(s) = [x(s), y(s)]$, where s is the contour length, that can move under the influence of internal and external force field in a spatial domain. The internal and external force derives from the curve and image data, respectively. The internal forces hold the curve together (elasticity forces) and keep it from bending too much (bending forces) whereas, external forces pull it toward the contour.^{103, 104} The external force for active contour is called gradient vector flow (GVF) field, which are dense vector fields derived from images by minimizing an energy function.^{103, 104}

For the first frame, we select a region of interest that should contain only one actively beating axoneme. Then, we initialize the snake by drawing a line polygon along the contour of the axoneme in the first frame (Figure 2.6). This polygon is interpolated at N equally spaced points and used as a starting parameter for the snake. The GVF is calculated using the GVF regularization coefficient $\mu = 0.1$ with 20 iterations. The snake is then deformed according to the GVF where we have adapted the original algorithm by Xu and Prince for open boundary conditions. We obtain positions of N points along the contour length s of the filament so that $s = 0$ is the basal end and $s = L$ is the distal side, where L is the total contour length of the filament (see chapter 1, Figure 1.10). The position of axoneme at s_i and time point t is by $\mathbf{r}(s, t) = (x(s_i, t), y(s_i, t))$. Furthermore, to estimate the systematic error of our tracking algorithm, we generated artificial filaments with known values of mean curvature and used the GVF algorithm to determine the curvature from the tracking algorithm. As shown in Appendix, Figure A.2.21, the measured values systematically deviate from the real values at small mean

curvatures, but provide a much better estimate when the mean curvature is larger. In other words, our algorithm has a smaller systematic error (less than 4%) for curved filaments with dimensionless mean curvature C_0 larger than 0.3.

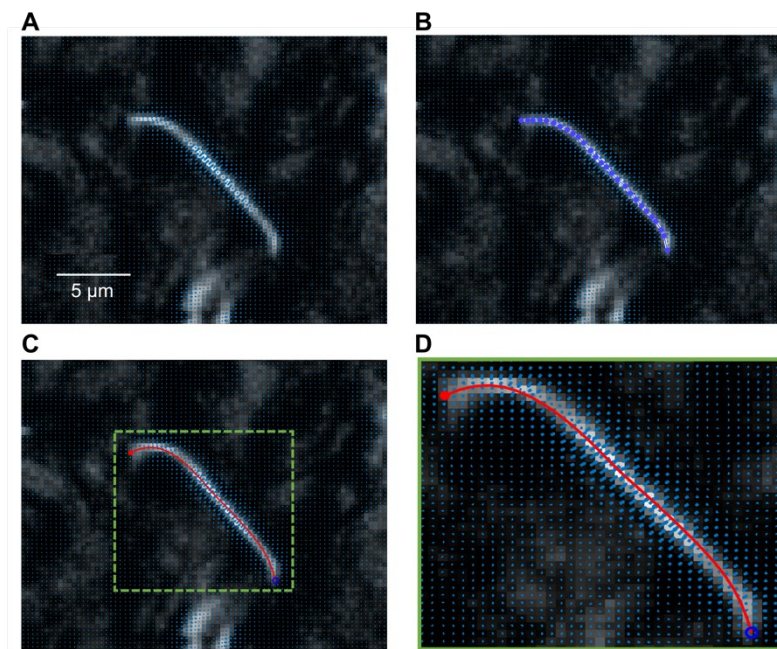


Figure 2.6: Axoneme contour tracking. A) Gradient vector flow of single active axoneme. B) The initial selection of a polygon for the first frame which deforms according to the gradient vector flow shown in blue arrows. C) The final tracked shape of an axoneme. D) A zoomed-in image of the area shown by a green dashed box in panel C. The tracking algorithm yields a discrete approximation of the axoneme's contour represented by a set of $N = 30$ positions $\mathbf{r}(s, t) = (x(s_i, t), y(s_i, t))$, $i = 1, \dots, N$.

2.9 Principal component analysis

This analysis is based on the method introduced by Stephens et al.¹⁰⁵ to characterize the waveforms in *C. elegans*. We describe the shape of the flagellum by its unit tangent vector $\mathbf{t}(s)$ and the unit normal vector $\mathbf{n}(s)$ at distance s along the contour¹⁶⁵. Instantaneous deformation of flagellum is described by curvature $\kappa(s, t)$, using the Frenet-Serret formulas¹⁰⁵

$$\frac{d\mathbf{r}(s)}{ds} = \mathbf{t}(s) \quad \text{and} \quad \frac{d\mathbf{t}(s)}{ds} = \kappa(s)\mathbf{n}(s) \quad [2.17]$$

Let us define $\theta(s)$ to be the angle between the tangent vector at contour length s and the x -axis, then $\kappa(s) = d\theta(s)/ds$. For shape analysis, we translate and rotate each flagellum such that basal end is at $(0,0)$ and the orientation of tangent vector at $s = 0$ is along x -axis, i.e. $\theta(s = 0, t) = 0$. Following Stephens et al.,¹⁰⁵ we performed principal mode analysis by calculating the covariance matrix of mean-subtracted angles $\theta_m(s, t) = \theta(s, t) - \langle \theta(s, t) \rangle_t$, defined as $\theta_{Cov}(s, s') = \langle (\theta_m(s, t) - \langle \theta_m \rangle)(\theta_m(s', t) - \langle \theta_m \rangle) \rangle$, where $\langle \theta_m \rangle$ is the spatial average of $\theta_m(s, t)$ at a given time t . The eigen values λ_n and corresponding eigen vectors M_n of the covariance matrix are given by $\sum_{s'} \theta_{Cov}(s, s') M_n(s') = \lambda_n(t) M_n(s)$. We show that superposition of four eigenvectors corresponding to four largest eigenvalues can describe the flagellum's shape with high accuracy.

$$\theta(s, t) - \langle \theta(s, t) \rangle_t \approx \sum_{n=1}^4 a_n(t) M_n(s). \quad [2.18]$$

Here the four variables $a_1(t), \dots, a_4(t)$ are the amplitudes of motion along different principal components and are given by $a_n(t) = \sum_s M_n(s) \theta_m(s, t)$. The fractional variance of flagellum's shape capture by n eigenvectors is calculated as $\sigma_k^2 = \sum_{i=1}^n \lambda_i / \sigma^2$ where $\sigma^2 = \sum_i^N \lambda_i$. Here N is the total number of eigen vectors. Chapter 4, Figure 4.4G shows that already two modes capture 98.52% and four modes capture 99.85% of the total variance. Considering reactivated axonemes as an example of a self-sustained biological oscillator, it is possible to define a phase which facilitates quantitative analysis. To present instantaneous state of an oscillator, we consider the stable limit cycle that forms in $a_1 - a_2$ plane, and define phase as a monotonically increasing function $\phi(t)$ (Chapter 3, Figure 3.10B,F). For a given limit cycle, phase ϕ rotates uniformly in the phase space such that $d\phi/dt = 2\pi f_0$, where f_0 is the autonomous beating frequency of axoneme (Chapter 3, Figure 3.10F). MATLAB code for principal component analysis is developed by Dr. Azam Gholami, MPI Göttingen.

2.10 Preparation of motile bundle solution

The motile bundle solution was obtained by mixing taxol-stabilized MTs and an active mixture (AM) containing molecular motors Kinesin-1 clustered in multimotors configuration using streptavidin-biotin affinity interaction. Kinesin 401 was purified as previously published¹⁶⁶,

¹⁶⁷and the kinesin-streptavidin complexes were prepared by mixing 0.2 mg/mL kinesin 401, 0.9 mM dithiothreitol (DTT), 0.1 mg/mL streptavidin dissolved in M2B (Appendix, Table A. 25) and incubated on ice for 15 min. The AM was obtained by mixing 2.4 mM trolox, 16.6 μ L 3% PEG, 5.5 μ L M2B, 3.25 μ L DTT (10 mM), the oxygen scavenger (0.2 mg/ml glucose oxidase (Sigma G2133), 0.05 mg/ml catalase (Sigma C40)) and 0.5 mg/mL glucose and 4 μ L kinesin1-streptavidin clusters. The MTs polymerization mixture was prepared by mixing 27 μ M porcine brain tubulin (1:5 labeled tubulin) in M2B with 5 mM $MgCl_2$, 1 mM GTP, 50% DMSO and 0.3% PEG. This solution is kept in the oven for 30 minutes by 37 °C and diluted up to 200 μ L with M2B and 7 μ M taxol. The final mixture was prepared by mixing polymerized MTs, AM and light-driven ATP module in different amounts depending on the experimental set up.

2.11 Fabrication of droplet microfluidic and millifluidic devices

2.11.1 Fabrication of droplet microfluidic

A schematic illustration of the microfluidic device for droplet formation is shown in chapter 3, Figure 3.13A. The device was designed using DraftSight (DraftSight® 2D CAD Drafting and 3D Design Software). Polydimethylsiloxane (PDMS) microchannel was fabricated using conventional soft lithography. A thin layer of SU-8 3010 photoresists (MicroChem, Newton, MA) was spin coated on Si-wafer and patterned via ultraviolet exposure through a film mask. The device has two different heights, therefore, SU-8 coatings and UV exposures were performed two times. For first the layer (17 μ m height), a red color section in (Chapter 3, Figure 3.13A), SU-8 3010 was spin coated at 1700 rpm for 30 sec and followed by soft baked at 95 °C for 11 min. Afterwards, the wafer was exposed to UV light (mask aligner, UV-KUB 3, France) for 5 sec (200 mJ/cm²) and proceeded to post-exposure baked (PEB) at 95 °C for 4 min. For the second layer (13 μ m height), the same photoresist was spin coated at 2500 rpm for 30 sec and soft baked at 95 °C for 4 min followed by UV exposure under same conditions as for the first layer. Further, PEB was performed at 95 °C for 2 min. Finally, the wafer was immersed in a photoresist developer (mr-DEV 600) to remove excess photoresist and make the pattern visible. The wafer was rinsed with isopropanol followed by Milli-Q water and dried in N₂ air. To fabricate the device, PDMS and the curing agent (SYLGARD 184 Silicone Elastomer) were thoroughly mixed with a 10:1 weight ratio (w/w) and poured onto the patterned silicon wafer

followed by degassing to remove air bubbles under vacuum pressure. After removing the bubbles and baking at 75 °C for 45 min, the PDMS was peeled off from the Si-substrate and the microchannels were cut into appropriate size. After punching the inlet and outlet ports, PDMS microchannel was oxygen plasma-bonded (PDC 002, Harrick Plasma, Ithaca, USA) to the glass slide (24 mm X 60 mm, Menzel Gläser, Germany) at power and pressure of 200 W and 200 mTorr, respectively for 30 sec. To strengthen the bonding, the device was heated at 75 °C in an oven for at least 2 min. The height and width of the observation chamber were 13 µm and 120 µm, respectively. Diameter of pillars and pillar to pillar distance inside the observation chamber was 30 and 150 µm, respectively. Microchannel was coated with Novec™ 1720, 3M™ (Electronic grade coating) at 120 °C for 1 hr to make it hydrophobic.

2.11.2 Fabrication of millifluidic

A millifluidic device (straight channel assembly) was fabricated by conventional soft photolithography. The height of the device was fixed to 100 µm, therefore, a single layer of SU-8 100 photoresist was spin coated on silicon wafer at 2900 rpm for 30 sec and followed the same steps as described in the previous section. The height, width and length of the millifluidic channel were 1.5, 0.1 and 30 mm, respectively.

2.12 Encapsulation of MTs/Kinesin-1 network assembled with photosynthetic vesicles

The feasibility of the proposed concept, toward building an artificial cell, was demonstrated by encapsulation (water-in-oil droplets, w/o) of MTs/kinesin-1 mixed with preilluminated ATP module by droplet microfluidic technique. Sample containing the MTs/kinesin-1 and 45 min preilluminated ATP module with volume ratio of 1:20 v/v (ATP module:MTs mixture) was pumped into inner-inlets (aqueous phase 1 and 2), while oil phase (FluoSurf 2% in HFE 7500 or FC40) was pumped into outer-inlet. Micro syringe pumps (CETONI BASE 120 with neMESYS pumps, Germany) and glass syringes (Hamilton, USA) were used to inject the aqueous and oil phases. Aqueous phases merged with oil phase at T-junction and generated droplets in a continuous mode of device operation (see Chapter 3, Figure 3.13A). Solution of MTs/kinesin-1 and ATP module encapsulated continuously inside water-in-oil droplets at T-junction in a

stabilized manner (see Chapter 3, Figure 3.13B) and passed from red to green area of the channel where the height of the microchannel is reduced to 13 μm to flatten the droplets, which helps in microscopy (see Chapter 3, Figure 3.13C). Further, droplets were entrapped between pillars in observation chamber by applying the pressure at top layer which aided in blocking the forward flow (see Chapter 3, Figure 3.13D). Inside observation chamber entrapped encapsulated MTs/kinesin-1/ATP module were imaged by epifluorescence microscope to observe contraction of filamentous network. The size of droplets was measured to $50 \pm 20 \mu\text{m}$.

2.13 MTs/Kinesin-1 network assembled with ATP functional module in millifluidic device

To validate the concept of light-driven ATP production in a continuous light illuminated area and corresponding MTs network contraction, straight channel millifluidic device was used. A 3D volume of the device was filled MTs/kinesin-1 and 45 min pre-illuminated ATP module and closed the both ends (inlet and outlet) of channel using silicone. The light illuminated region is marked with red dashed line circle and non-illuminated region marked with red dashed line rectangle (see Chapter 3, Figure 3.14).

2.14 Light-triggered glucose consumption

For measurement of light-triggered glucose consumption (see Chapter 3, Figure 3.15A), a solution containing the ATP module was supplemented with ADP, P_i , glucose and hexokinase. As a control, a solution containing only the ATP module, ADP and P_i was run in parallel. The reaction was started by illumination and samples were taken each 5 min from the reaction mixture. The reaction was stopped by the addition of TCA. The ATP concentration of the sample and the control was calculated and the reaction rates were determined by linear regression (see Chapter 3, Figure 3.15B). The suspension containing the ATP module, hexokinase and glucose (ATP module + hexokinase + glucose) showed barely the ATP production (0.01 nM/min). All ATP is constantly consumed by hexokinase to convert glucose in glucose-6-phosphate. This result confirmed that concentration of hexokinase was chosen high enough and consequentially the glucose consumption reaction was not the limiting step. In contrast,

the control sample (ATP module) verified that the ATP module was working as expected, and produced 58.6 nM ATP per min. The glucose concentration was determined using a highly sensitive glucose assay, which allows the detection of glucose by measuring the fluorescence intensity. Therefore, a standard curve relating glucose concentration and fluorescence signal was taken according to the manufacturers protocol.¹³⁴ The glucose concentration over time is shown in Chapter 3, Figure 3.15C. The glucose concentration at $t = 0$ agrees well with the glucose concentration added to the solution (10 μM), confirms that the glucose assay is working with the high sensitivity. The concentration of glucose was decreasing over time with a consumption rate of -69.4 nM glucose per min. This rate is slightly higher (18%) compared to the detected ATP production rate because ATP synthase is product inhibited by ATP itself.¹⁶⁸ Thus, higher turnover rates are anticipated when ATP is constantly removed from the system.

Results and Discussions

Chapter 3 Light-Powered Reactivation of Flagella and Contraction of Microtubule Networks: Toward Building an Artificial Cell

Chapter 3 is adapted from:

Raheel Ahmad*, Christin Kleineberg*, Vahid Nasirimarekani, Yu-Jung Su, Samira Goli Pozveh, Albert Bae, Kai Sundmacher, Eberhard Bodenschatz, Isabella Guido, Tanja Vidaković-Koch and Azam Gholami, "Light-Powered Reactivation of Flagella and Contraction of Microtubule Networks: Toward Building an Artificial Cell", *ACS Synthetic Biology (Featured on Front Cover)*, 2021, 10, 1490-1504. (*Equal contribution).

Raheel Ahmad contributions: Isolation of flagella, integration of ATP energy module with flagella, experiments with pure commercial ATP and MTs/kinesin-1, fabrication of microfluidic device, data analysis, writing, discussion and revision.

In this work, we tested a possibility to integrate the energy module with two different motility modules. First, we integrated the light-switchable bottom-up assembled ATP regeneration module with a motility functional unit which was isolated from green algae *C. reinhardtii*. The combination of these two modules leads to an artificial system where energy of light is converted into mechanical work in a self-sustained manner. Next, we coencapsulated the light-to-ATP energy module with MTs and kinesin-1 molecular motors to generate active stresses in confined cell-like compartments. We observed controlled motor-driven contraction of filamentous network upon light stimulation, indicating the efficiency of the artificial photosynthetic module in providing self-sufficient energy. This integrated system is potentially applicable in ATP-dependent motility assays, which aim to reconstitute motor-driven motion and force generation inside a synthetic cell, with the challenging goal of achieving a light controllable switch between the motile and immotile states of an artificial cell.

3.1 Results

3.1.1 Light-driven energy module

We engineered light-switchable photosynthetic liposomes (~150 nm in diameter) as energy modules to generate ATP under illumination. To convert light into ATP, we coreconstituted two purified transmembrane proteins, namely, bacteriorhodopsin (bR) from halobacterium

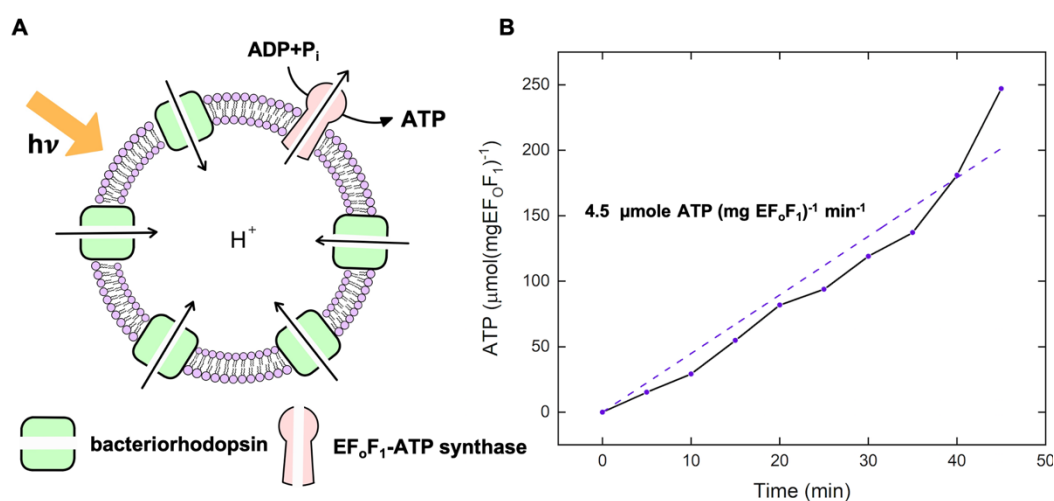


Figure 3.1: Light-driven ATP production. A) Schematic representation of light-driven ATP synthesis in lipid vesicles. EF_oF_1 ATP synthase uses the electrochemical gradient generated by bacteriorhodopsin to synthesize ATP from ADP and P_i . B) Measurement of light-driven ATP production over time. The maximal rate of $4.5 \mu\text{mol ATP} (\text{mg}EF_oF_1)^{-1}\text{min}^{-1}$ is determined by linear regression. Experiments were performed at room temperature with the HMDEKP buffer as the inner solution (30 mM HEPES-KOH, 5 mM $MgSO_4$, 1 mM DTT, 1 mM EGTA, 50 mM potassium acetate, 1% (w/v) PEG, pH = 7.4). The same outer solution was adjusted with 5 mM NaH_2PO_4 , 2 mM $MgCl_2$, 1 mM DTT and 810 μM ADP. $[P_i] = 5 \text{ mM}$, $[\text{lipid}] = 0.022 \text{ mg/mL}$, $[EF_oF_1] = 2.6 \text{ nM}$, $[bR] = 160 \text{ nM}$ and $\Delta\Psi = 143 \text{ mV}$ is the membrane potential (the outer potential minus the inner potential). Proteins were reconstituted with 0.8% Triton.

salinarum and EF_oF_1 -ATP synthase from *E. coli*. Upon illumination, bR pumps proton into the vesicles interior, establishing a proton motive force that drives ATP synthase to catalyze the conversion of ADP to ATP (Figure 3.1A). Both enzymes are isolated according to the procedures earlier described by Ishmukhametov et al.¹⁵⁵ and Oesterhelt et al.¹⁵⁸ Their purity is checked by SDS-PAGE (Figure 3.2). bR is reconstituted in the form of membrane patches to avoid material loss during solubilization. Recently, it was shown that¹⁴² the usage of monomeric, detergent-solubilized bR for reconstitution is also possible and will lead to a functional ATP regeneration module. However, an almost uniform orientation of bR in phosphatidylcholine (PC) liposomes could only be achieved when using bR in the form of membrane patches (Figure 3.3). Both

enzymes are coreconstituted into preformed PC unilamellar vesicles using Triton X-100 as detergent, similar to the method described by Fischer and Gräber¹⁶⁹ for ATP synthase reconstitution. Liposomes are prepared using the extrusion method. The size of vesicles before and after reconstitution is checked using DLS.

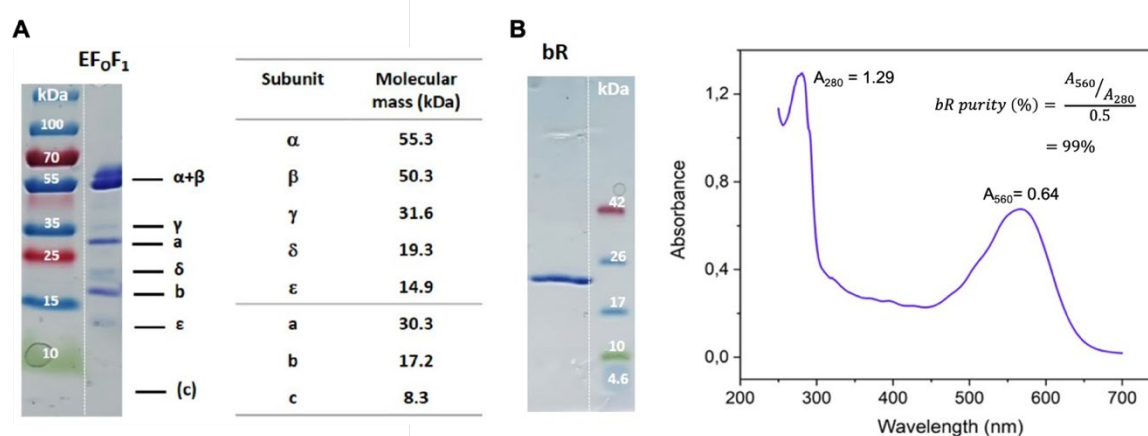


Figure 3.2: SDS-PAGE of purified proteins. A) Coomassie-stained SDS-PAGE of purified EF_0F_1 ATP synthase and molecular masses of EF_0F_1 subunits. B) Coomassie-stained SDS-PAGE of purified bR with the corresponding absorbance spectrum. Measurements were performed by Dr. Christin Kleineberg, MPI Magdeburg.

DLS data confirm an average vesicle diameter of ~ 150 nm (Figure 3.4). Separate assays for each transmembrane protein further prove their functionality. bR proton pumping and intravesicular acidification is detected using pyranine as an internal probe (see Chapter 2, Figure 2.3). The activity of ATP synthase is determined in an acid–base transition experiment (see Chapter 2, Figure 2.1). ATP production in the coreconstituted module under illumination is measured using the luciferin/luciferase assay (Figure 3.1B). The achieved maximal rate of $4.5 \mu\text{mol ATP (mg}EF_0F_1)^{-1}\text{min}^{-1}$ is high compared to the literature work. An overview of different light-driven and chemically driven ATP regeneration modules and their ATP production rates can be found in the ref.¹³² We mainly attribute this comparably high efficiency of ATP production to the increased amount of bR reconstituted in our system, aiming for a theoretical ratio of 1 ATP synthase and 96 bR molecules per liposome with an almost uniform direction. In most of the literature work^{132, 138, 170-172} significantly lower bR concentrations were used for

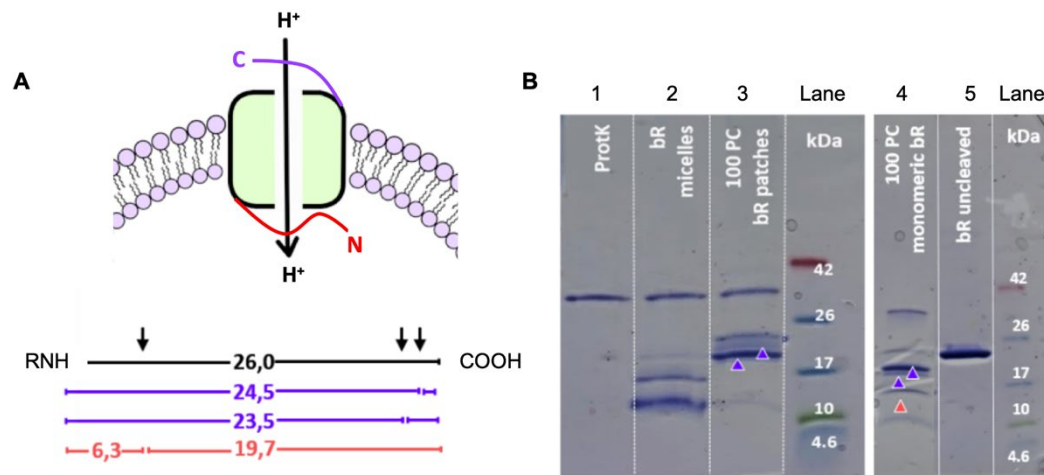


Figure 3.3: Proteolytic cleavage of reconstituted bR with proteinase K (ProtK) shows mixed orientation for monomeric bR and almost uniform orientation (with the C-terminus outwards) for bR patches. A) Expected sizes of proteolytic fragments for ProtK digestion of bR when the N-terminus (orange values) or C-terminus (violet values) is exposed to the bulk solution. B) SDS-PAGE analysis of the digestion products. Lane 1: band specific for ProtK enzyme only; lane 2: digestion product of not reconstituted bR; lane 3: digest pattern for PC vesicles containing bR patches; lane 4: digest pattern for PC vesicles containing monomeric bR; lane 5: undigested bR in PC lipid vesicles. Measurements were performed by Dr. Christin Kleineberg, MPI Magdeburg.

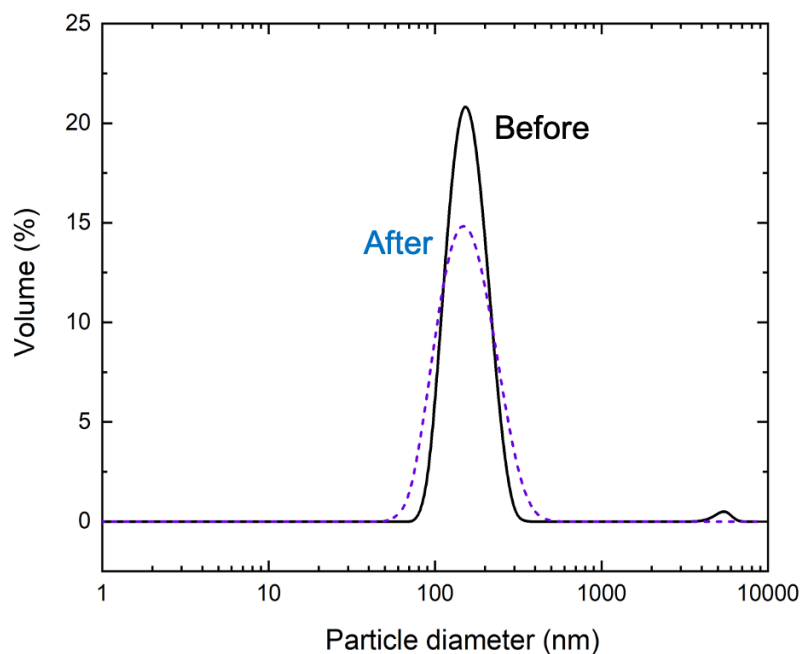


Figure 3.4: Size distribution of vesicles before (before) and after reconstitution and removal of detergent using Bio-Beads (after).

coreconstitution. Only Racker and Stoeckenius¹³⁶ as well as Choi and Montemagno¹⁴¹ applied bR concentrations of similar magnitude. Moreover, we found out that the vesicle preparation method has significant impact on the performance of the ATP module. Using dialysis liposomes instead of vesicles produced by extrusion, led to roughly a 50% decrease in activity. Furthermore, dithiothreitol (DTT) has a positive effect on the ATP production rates. Only 43% of activity remained in the absence of DTT (Figure 3.5). DTT is known to prevent oxidation and thus to preserve proteins in their functional form. In addition, DTT can contribute to changes in membrane potential, as shown in the ref¹⁷³. Finally, all experiments have been done with ultra pure ADP (>99.9%). Commonly offered ADP salt is highly contaminated with ATP (>2%). Due to the high ADP concentration in the present measurements (1.6 mM), this would lead to a high ATP concentration at the beginning of the experiments, which could compromise the activity of ATP energy module.

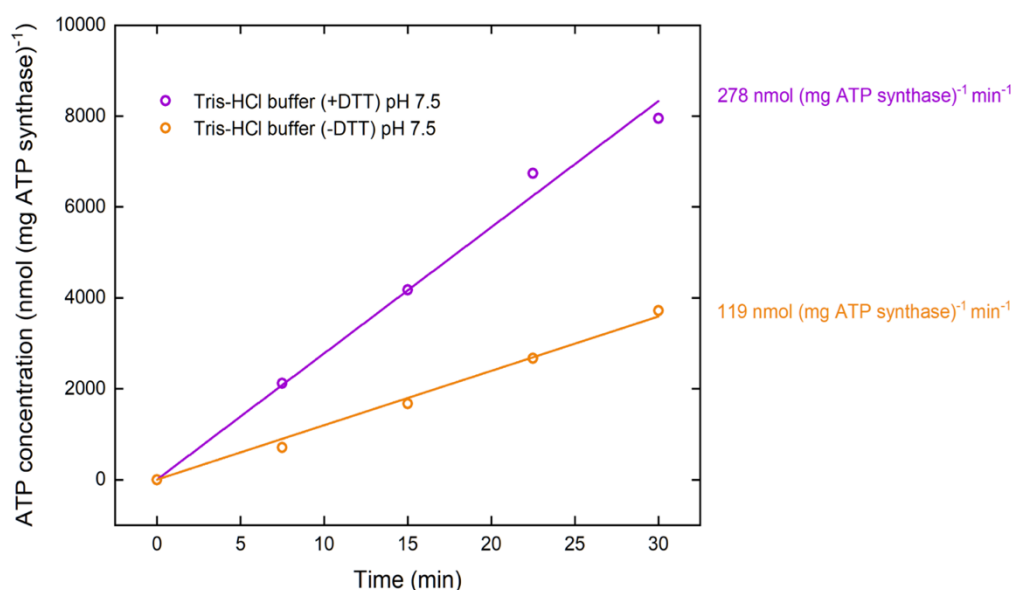


Figure 3.5: ATP production in Tris-HCl buffer in the presence (+DTT) and absence of DTT (-DTT). The activity was determined by linear regression. Measurements were performed with [ADP]= 300 μ M, [P_i]= 5 mM, [lipid]= 0.022 mg/mL, [EF_oF₁] = 1.3 nM, [bR]= 88 nM, $\Delta\Psi$ = 143 mV at room temperature. Proteins were reconstituted in 0.8 % Triton. Measurements were performed by Dr. Christin Kleineberg, MPI Magdeburg.

3.1.2 Integration of energy module with motility module

3.1.2.1 Reactivation of axonemes with pure ATP

In this part, we aim to integrate the light-driven energy module with the motility module, namely, the flagella isolated from green algae *C. reinhardtii*⁴¹ (see Figure 3.6A,B). In the first step, we characterized the activity of the isolated flagella (~10 μm in length) using commercially available pure ATP.⁴¹ Upon mixing ATP with demembrated flagella (axonemes), ATP powers dynein molecular motors that convert chemical energy into mechanical work by sliding adjacent MTDs relative to each other, see Chapter 1, Figure 1.1. However, due to mechanical constraints, MTDs cannot slide freely. Instead, sliding is converted into rhythmic bending deformations that propagate along the contour length of axonemes at a frequency that depends on ATP concentration (Figure 3.6C–E). We did not observe beating activity for ATP concentrations below the critical value of $[\text{ATP}]_{\text{critical}} = 60 \mu\text{M}$,^{41, 174} suggesting that a minimum number of active molecular motors are required to generate rhythmic motion in axonemes. The critical beat frequency was $f_{\text{critical}} \sim 14.6 \text{ Hz}$. Above $[\text{ATP}]_{\text{critical}} = 60 \mu\text{M}$, the beat frequency increases with $[\text{ATP}]$ following modified Michaelis–Menten kinetics, which predicts a plateau with a linear onset at small values of $[\text{ATP}]$: $f = f_{\text{critical}} + f_{\text{max}} ([\text{ATP}] - [\text{ATP}_{\text{critical}}]) / (K_m + ([\text{ATP}] - [\text{ATP}_{\text{critical}}]))$, with $f_{\text{max}} = 73.75 \text{ Hz}$ and $K_m = 298.5 \text{ Hz}$.^{41, 175}

Axonemes consume ATP and beat at a frequency that decays over time until they stop beating (Figure 3.6F). The rate of ATP consumption depends on both ATP and axoneme concentration. In our experiments, we estimate to have 6×10^5 axonemes in 10 μL of reactivation solution. At an ATP concentration of 1 mM, axonemes stop beating after 32 min, resulting in an estimated ATP consumption rate of 0.31 nmol/min. Assuming that all 6×10^5 axonemes in the chamber are active and consume ATP, we calculate that 5×10^5 ATP molecules/sec are consumed by a single axoneme. Given the mean beat frequency of 50 Hz, we estimate that $\sim 10^5$ ATP molecules are consumed in one beating cycle.¹⁷⁶ This averaged consumption rate estimated from our experimental data is comparable to the bulk measurements in the sea urchin sperm¹⁷⁷ but lower than the value of 2.3×10^5 ATP/beat measured at the single-axoneme level by Chen et al.¹⁷⁶ This discrepancy can probably be related to the assumption that 100% of axonemes are reactivated, which is not the case even under ideal experimental conditions. Normally, the isolation and demembration process results in a mixed population of active, nonactive, and fragmented axonemes and a 100% reactivation is never achieved.

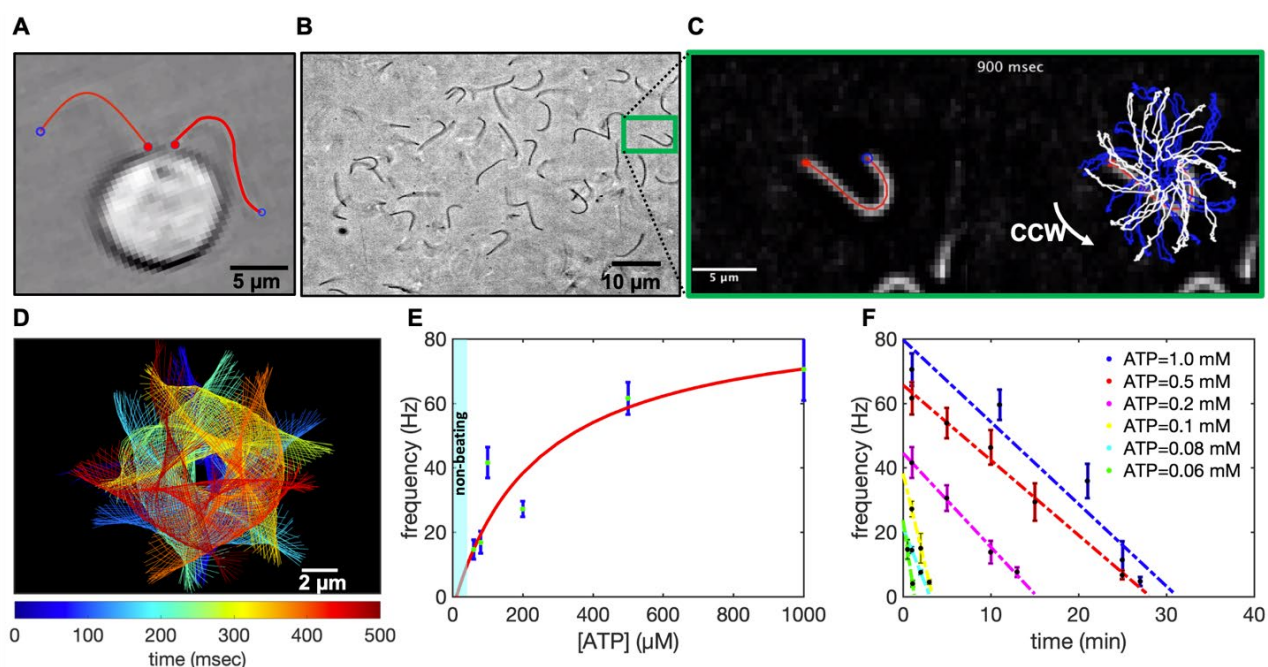


Figure 3.6: Experiments with pure commercial ATP. A) Snapshot of a *C. reinhardtii* cell with its two flagella. B) Isolated and demembrated flagella are reactivated with pure ATP. C) Swimming trajectory of an exemplary axoneme beating at 18 Hz with $[ATP] = 80 \mu M$. D) Color-coded time projection of the axoneme in panel C shows the circular swimming path. E) Mean beat frequency as a function of ATP concentration. Solid red line is a least-square fit to the modified Michaelis–Menten relation. The minimum ATP concentration required to observe axonemal beating was $[ATP]_{critical} = 60 \mu M$. F) Beat frequency decays over time at a rate that depends on ATP concentration. In the presence of 1 mM ATP (blue line) in a 10 μL volume, axonemes beat for 32 min at a decreasing beating frequency that allows us to estimate the averaged ATP consumption rate of 0.31 nmol/min. This rate depends on ATP concentration and decreases to 0.25 nmol/min for $[ATP] = 0.1$ mM (yellow line). Error bars are mean \pm standard deviation ($N = 7$).

Therefore, single-flagellar experiments, such as those performed by Chen et al.¹⁷⁵ are more accurate in determining ATP consumption rates.

3.1.2.2 Reactivation of axonemes with light

Next, we combined the light-driven ATP generation module with isolated and demembrated axonemes, as schematically shown in Figure 3.7A. We first illuminated the energy module for various time intervals between 0 to 45 min before mixing the functionalized vesicles with axonemes. Higher ATP concentrations are produced by illuminating the energy module for longer periods. While illumination with a 5W microscope light generates up to 213 μM ATP, a 50W white light LED lamp produces up to 330 μM ATP after 45 min of illumination (Figure 3.7B, C). Synthesized ATP reactivates axonemes at a frequency that depends on $[ATP]$. The mean beat frequency as a function of $[ATP]$ follows the Michaelis–Menten kinetics scaling with

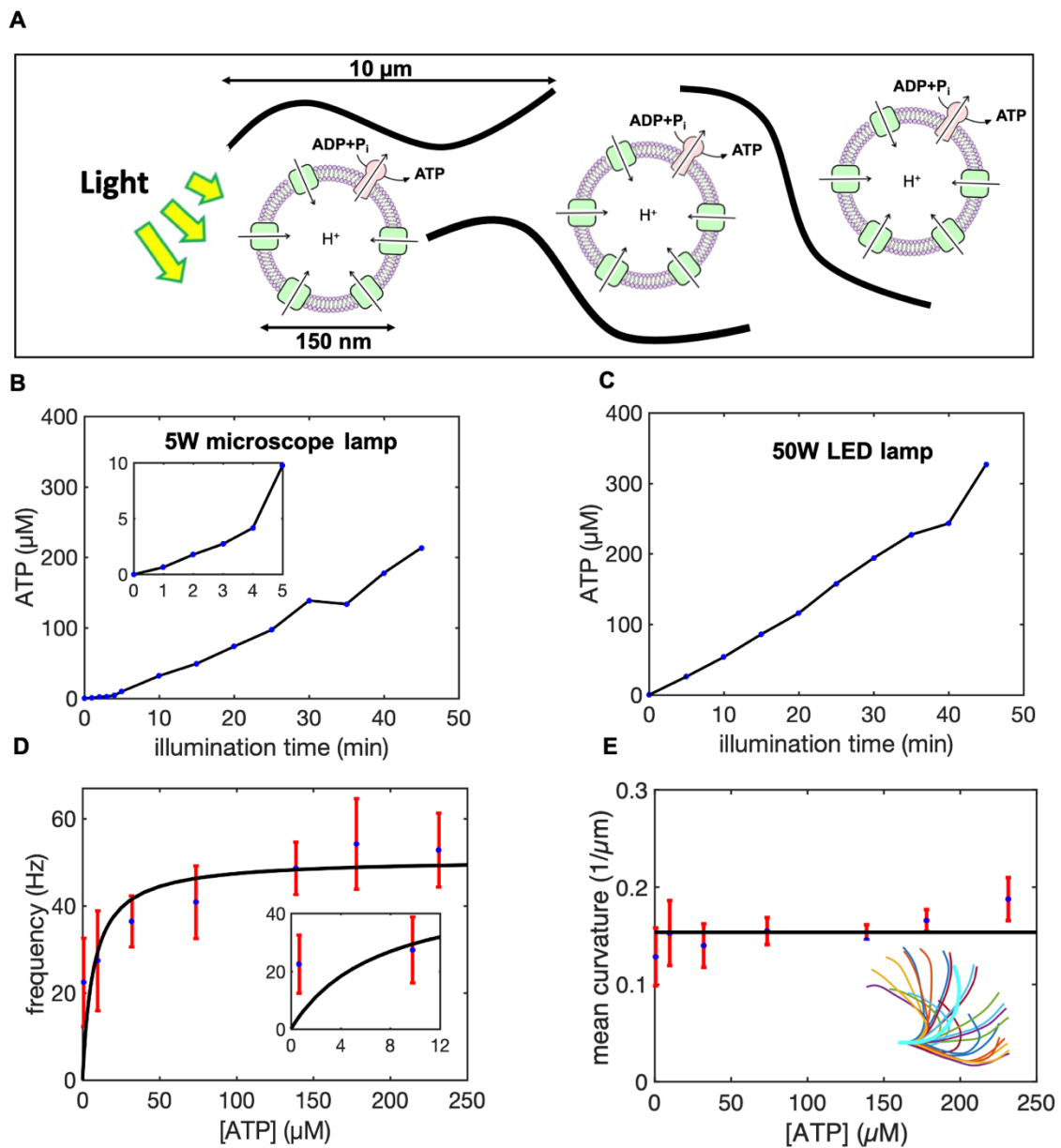


Figure 3.7: Integration of the motility module with the light-switchable energy module. A) Schematic presentation of isolated flagella mixed with energy module. B) Functionalized liposomes are illuminated for different times, generating ATP concentrations up to 213 μM under illumination with a 5W microscope lamp. C) Higher ATP concentrations up to 330 μM was produced under illumination with a 50W LED lamp. Both light sources are located 25 cm away from the sample. Inset shows ATP production in the time interval 0 to 5 min of illumination. D) Axonemes beat faster at higher ATP concentrations produced by longer illumination of energy module under microscope light. Inset shows that axonemes beat even at small ATP concentrations below 10 μM . E) Static curvature of the axonemes, defined as the curvature of the mean shape averaged over one beating cycle (arc-shaped filament with cyan color), does not significantly depend on ATP concentration. The black line shows a linear fit with the offset of $\sim 0.16 \mu\text{m}^{-1}$ and slope of zero. For each data point in panels D and E, frequencies of 10 axonemes are measured to calculate the mean and standard deviation.

$f_{max} = 50.80$ Hz and $K_m = 7.14$ μ M (Figure 3.7D). Interestingly, we observed that illumination with the microscope light for 1 min, corresponding to 1 μ M ATP, was sufficient to reactivate axonemes at a beat frequency of around 22 Hz. This is rather surprising because the minimum critical ATP concentration required to reactivate axonemes in our pure ATP experiments was 60 μ M (Figure 3.6E). We attribute this discrepancy to several factors: (1) In the vicinity of axonemes, ATP is constantly synthesized and subsequently consumed by dynein molecular motors. ATP is known to inhibit the activity of ATP synthase and local consumption of ATP by axonemes can enhance the rate of ATP production. Therefore, the ATP concentration in the presence of axonemes might be slightly higher. (2) Functionalized vesicles may accumulate/adhere to the demembrated axonemes resulting in higher ATP concentrations around them. Our experiments with fluorescently labeled vesicles did not confirm any significant accumulation of vesicles along the entire contour length of axonemes, but we occasionally observed attachment of vesicles to a part of axonemes. (3) The last but most important factor is ADP. In contrast to the experiments with pure ATP, experimental system with axonemes and energy module contains a significant amount of ADP (1.6 mM). According to the literature,^{1, 178, 179} ADP can bind to noncatalytic sites of dynein motors, enhancing the overall energy efficiency of chemical to mechanical energy transformation (Figure 3.8A,B). In fact, the activating role of ADP in the regulation of on-off switching of dynein arms in flagellar motility has been the subject of several studies in the past years.¹⁸⁰⁻¹⁸² To confirm the activating effect of ADP, we repeated our pure ATP experiments with 1.6 mM ADP. Remarkably, we observed reactivation of axonemes even at a very low ATP concentration of 0.1 μ M (Figure 3.8C). Furthermore, in the presence of ADP, ATP consumption rate was much lower. This is shown in Figure 5D for the fixed ATP concentration of 60 μ M with 1.6 mM ADP, where in comparison to the experiment without ADP, axonemes beat at higher frequencies and for a longer period of time. ATP consumed by axonemes is replenished by the continuous microscope illumination while we image the sample, establishing an energy production-consumption cycle. Once the microscope light is turned off, the time required for the synthesized ATP to be hydrolyzed depends on both ATP and axoneme concentrations. Exemplary, in a 10 μ L solution with 6×10^5 axonemes, 60 μ M ATP which is produced in a 10 min

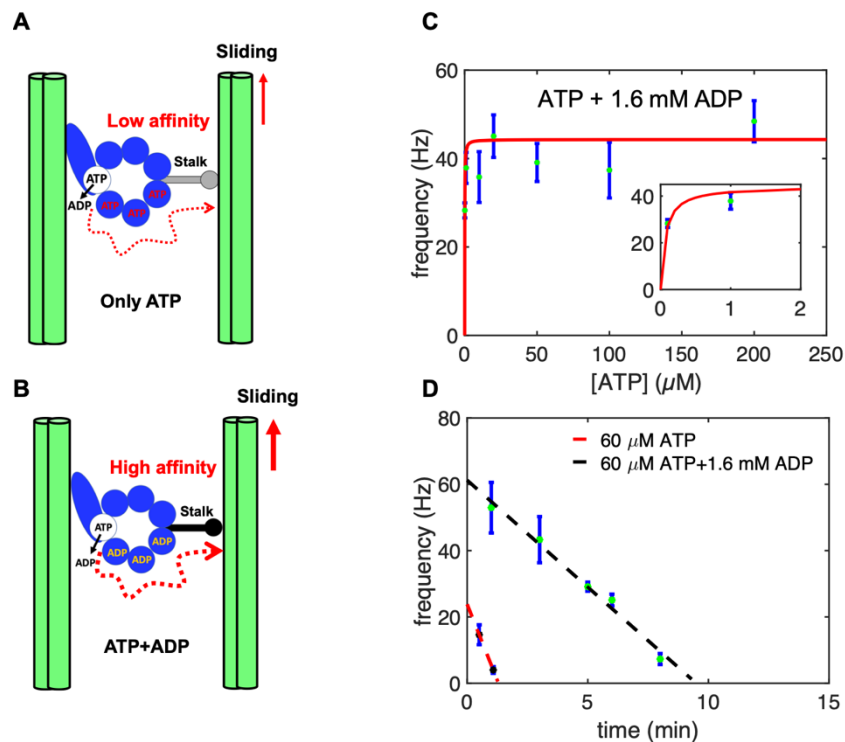


Figure 3.8: Activating role of ADP. A,B) A hypothetical mechanism introduced in the refs^{1,2} illustrating the regulatory effect of ADP on the binding affinity of dynein to the B-subtubule of the outer MTDs. Hence, in the presence of ADP which binds to a noncatalytic site, dynein is more efficient in generating the sliding force. C) Pure ATP experiments supplemented with 1.6 mM ADP confirm the activating role of ADP at low ATP concentrations. Note that axonemes are reactivated even at a very low ATP concentration of 0.1 μM . D) Comparison of two sets of experiments with and without ADP at fixed ATP concentration of 60 μM . While without ADP, axonemes stop beating after 2 min, with 1.6 mM ADP, axonemes beat with higher frequencies and are active for a longer time.

preilluminated energy module, will be consumed in ~ 10 min. This is consistent with Figure 3.8D with 60 μM commercial ATP and 1.6 mM ADP. Once ATP is depleted, turning on the microscope light for 1 min generates ~ 1 μM ATP, which is sufficient to reactivate axonemes but at a lower frequency of ~ 20 Hz. Figure 3.9A–C shows exemplary oscillatory motion of an axoneme in response to ATP generated by the light-driven energy module which is preilluminated with the microscope light for 45 min. We observed bending deformations propagating at a frequency of up to 72 Hz from the basal end toward the distal tip (Figure 3.9D,E). To analyze the oscillatory motion of axonemes, we first tracked the filaments using

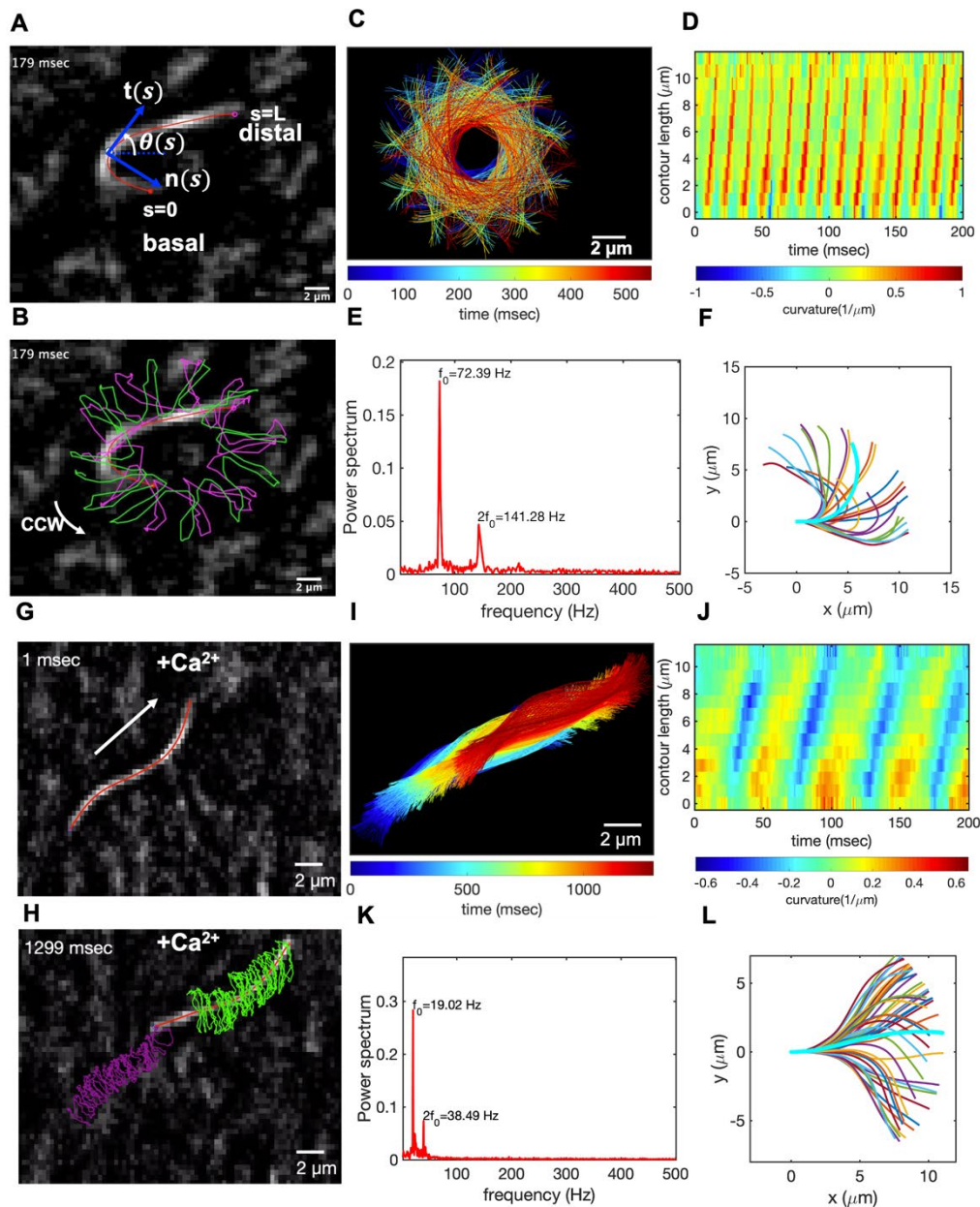


Figure 3.9: Light-driven reactivation of axonemes with and without calcium. A) An actively beating axoneme fueled by $213 \mu\text{M}$ ATP produced upon illumination of energy module for 45 min by microscope light. B) As axoneme beats with frequency of 72 Hz, it rotates CCW with slower frequency of 2 Hz. Magenta and green trajectories show the trace of basal and distal ends, respectively. C) Color-coded time projections of the beating axoneme showing the circular swimming path. D) Curvature waves propagate along the contour. E) Power spectrum of curvature waves shows dominant peaks at $f_0 = 72$ Hz and at second harmonic $2f_0$. F) Configurations of the axoneme at different time points are translated and rotated such that the basal end is at $(0,0)$ and the orientation of the tangle vector at the basal end is in the \hat{x} direction. Static curvature of this axoneme is $\sim 0.2 \mu\text{m}^{-1}$. G–L) A separate experiment with 1 mM CaCl_2 which reduces the static curvature of the axoneme to $0.01 \mu\text{m}^{-1}$ (compare filaments with cyan color in panels F and L). Thus, the axoneme swims in a straight trajectory (compare panels C and I) utilizing $\sim 1 \mu\text{M}$ ATP synthesized by energy of microscope light without 45 min preillumination step. At such a low ATP concentration, axoneme beats at a slower frequency of 19 Hz.

the GVF technique^{103, 104} (see Chapter 2, section 2.8) 2.8 and quantified the curvature waves using the Frenet-Serret equations in a plane:¹⁰⁵

$$\frac{d\mathbf{r}(s)}{ds} = \mathbf{t}(s) \quad \text{and} \quad \frac{d\mathbf{t}(s)}{ds} = \kappa(s)\mathbf{n}(s) \quad [3.1]$$

Here $\mathbf{t}(s)$ is the unit tangent vector to the axoneme, $\mathbf{n}(s)$ is the unit normal vector and $\kappa(s)$ is the curvature (see Figure 3.9A). We define $\theta(s)$ as the angle between the tangent vector at contour length s and the x -axis, then $\kappa(s) = d\theta(s)/ds$, which is plotted in Figure 3.9D. Furthermore, considering reactivated axonemes as an example of a self-sustained biological oscillator, it is possible to perform a principal mode analysis¹⁰⁵ and define a phase which facilitates a quantitative dynamic analysis of axonemal shape (Figure 3.10). Finally, to characterize the mean shape of axonemes, which is a circular arc (the filament in cyan color in Figure 3.9F), we translated and rotated configurations of an actively beating axoneme such that the basal end defined as $s = 0$ is at position (0,0) and the tangent vector at the basal end is orientated in the x -direction (Figure 3.9F). Figure 3.7E illustrates that curvature of the mean shape of axonemes does not depend significantly on ATP concentration.⁴¹ This static curvature ($\sim 0.16 \mu\text{m}^{-1}$), which leads to an asymmetric waveform and causes a circular swimming trajectory of axonemes (Figure 3.9B,C), is comparable to the values obtained in our pure ATP experiments with and without ADP (see Figure 3.11) and can be reduced by adding calcium ions to the reactivation buffer.¹⁸³ Calcium ions are known to play a crucial role in shaping and controlling flagellar waveforms.^{26, 183} A calcium-responsive protein at the interface between RS1 and IDAa is calmodulin (see Chapter 1, Figure 1.6B and Figure 5 in the ref⁴¹). Electron cryotomography (cryo-EM) data⁶⁷ show that the structure of calmodulin undergoes a Ca^{2+} dependent conformational change, which could affect the RS1-IDAa interaction, therefore modulating the flagellar beat from an asymmetric to a symmetric waveform. Figure 3.9G–L

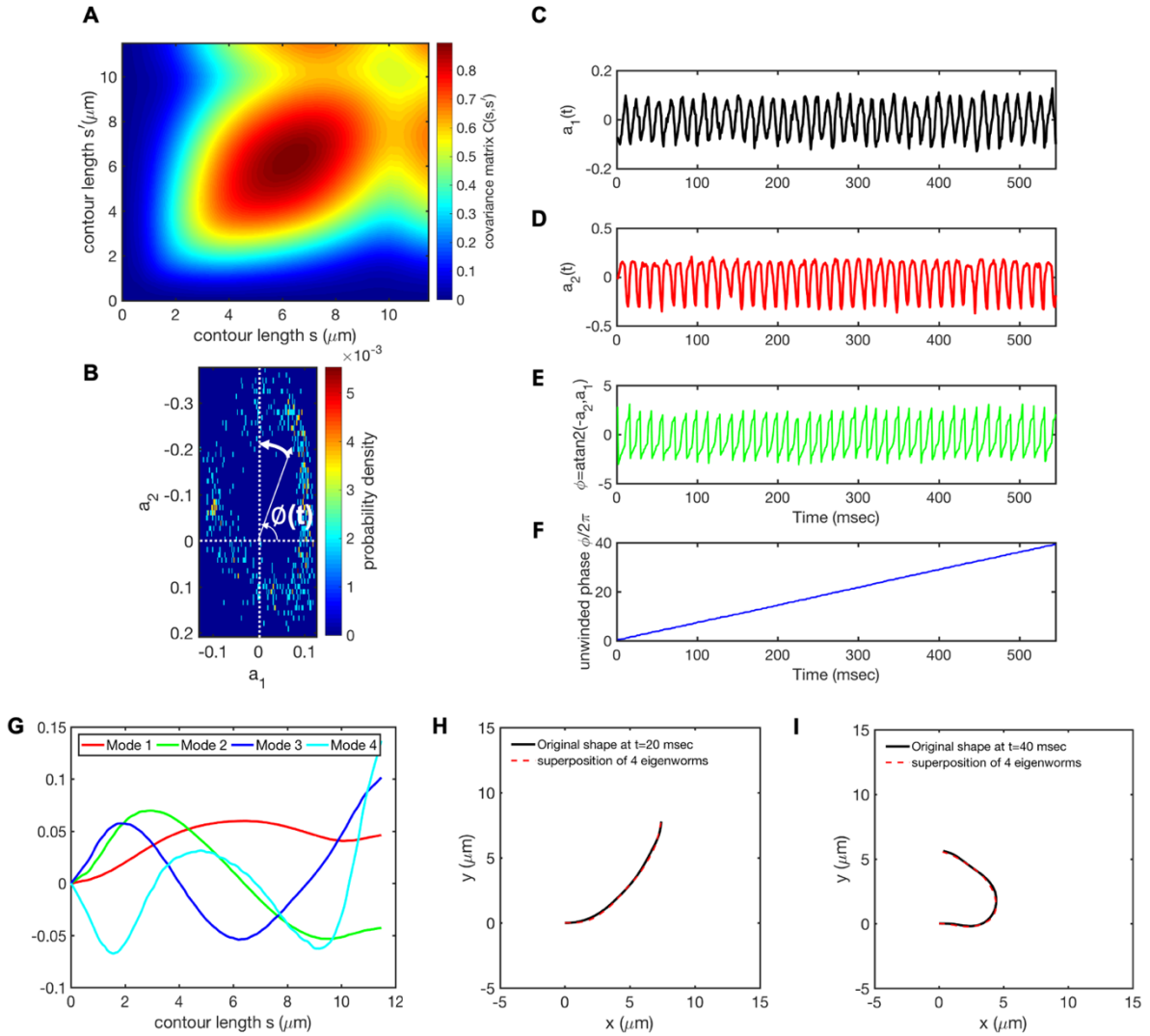


Figure 3.10: Mode analysis of the reactivated axoneme presented in Figure 3.9A-F. A) The covariance matrix $C(s, s')$ of fluctuations in angle $\theta(s, t)$. B) The probability distribution of the first two shape amplitudes $p(a_1(t), a_2(t))$. The phase angle of the axoneme as an oscillator is defined as $\phi = \text{atan2}(-a_2(t), a_1(t))$. C-D) Time evolution of the first two dominant shape amplitudes $a_1(t)$ and $a_2(t)$ showing regular oscillations at frequency of 72 Hz. E-F) We observe a linear growth in dynamics of $\phi(t)$, indicating steady rotation in $a_1 - a_2$ plane presented in part B. Note that $d\phi/dt = 2\pi f_0$ where f_0 is the beating frequency of axoneme. G) Four eigenvectors corresponding to the four largest eigenvalues of matrix $C(s, s')$. H-I) Superposition of four eigenmodes presented in part G with coefficients $a_1(t)$ to $a_4(t)$, can reproduce shape of the axoneme with high accuracy.

shows an exemplary axoneme with a symmetric waveform in which the static curvature is reduced to $0.01 \mu\text{m}^{-1}$ by addition of 1 mM CaCl_2 . This axoneme with nearly ten times reduced static curvature swims in a straight line. We emphasize that beat frequency, static curvature and amplitude of curvature waves are three important factors which determine the swimming

trajectory of an axoneme in the ambient fluid, and variations in these parameters directly affect the swimming dynamics (see Appendix A.2 (1)).

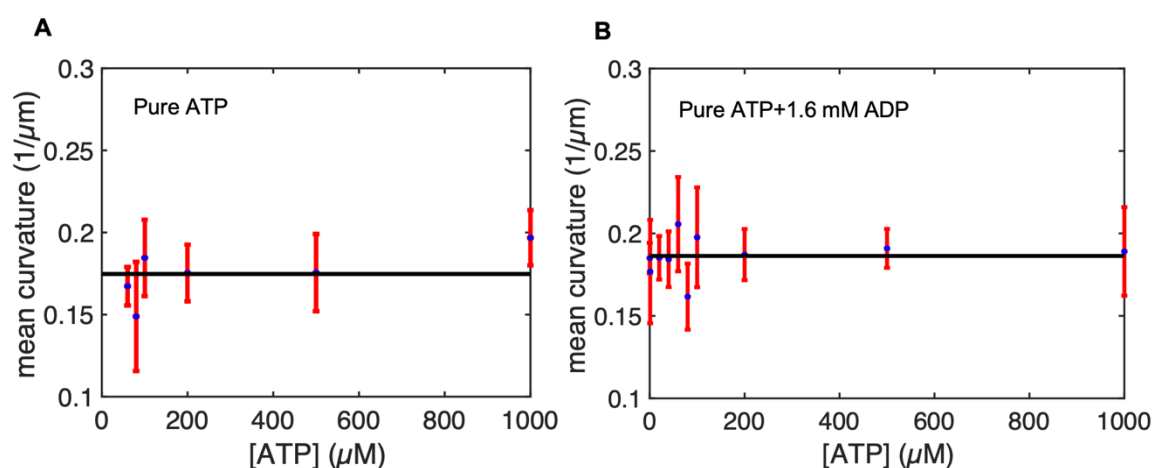


Figure 3.11: Mean curvature of axonemes reactivated using pure commercial ATP plotted versus ATP concentration. In panel A, no ADP is added, while in panel B, the reactivation buffer is supplemented with 1.6 mM ADP. The black solid lines show the mean values of $0.17 \mu\text{m}^{-1}$ (A) and $0.186 \mu\text{m}^{-1}$ (B), which is comparable to the value of $0.16 \mu\text{m}^{-1}$ in energy module experiments shown in Figure 3.7E. The corresponding frequency trends in pure ATP experiments with and without ADP are shown in Figure 3.8C and Figure 3.6E, respectively.

3.2 Light-driven contraction of MTs/Kinesin-1 network

We further tested the suitability of a light-switchable energy module for encapsulation of *in vitro* motility assays constituted of MTs and force-generating molecular motors. This assembly under illumination provides an energetically autonomous system that has the potential to advance the development of synthetic cells (Figure 3.12A). We verified the activity of the motor-driven filamentous network by characterizing its activity in water-in-oil droplets of various diameters. Figure 3.12 shows the contraction of MTs/kinesin-1 network mixed with the preilluminated photosynthetic energy module and encapsulated in a microfluidic device (see Chapter 2, section 2.11.1 and Figure 3.12). We observed a relatively uniform distribution of the network immediately after encapsulation, as shown in Figure 3.12B. Over time, ATP produced in preilluminated energy module drives the activity of molecular motors allowing them to cross-link and slide neighboring MTs against each other. This results in a net force that contracts the network.¹⁸⁴ A snapshot of the contracted network after 40 min is shown in Figure 3.12C. Microtubule–microtubule sliding also causes rotational flows¹⁸⁵ within droplets,

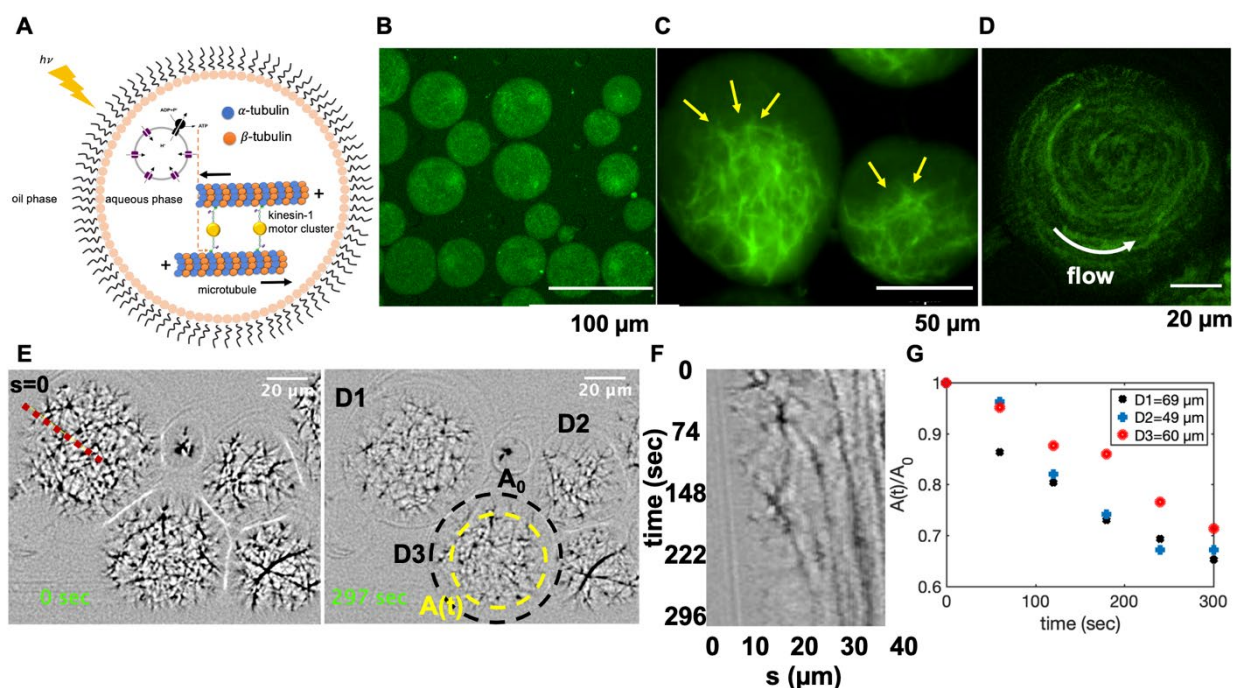


Figure 3.12: Cell-like confinement of MTs, kinesin-1 molecular motors and light-switchable energy module. Kinesin-1 is a dimer with two heads which forms cluster through streptavidin. A) Schematic representation of the MTs/kinesin-1 network coencapsulated with functionalized vesicles inside water-in-oil droplets. Upon illumination, synthesized ATP provides fuel for the kinesin-1 molecular motors, which are plus-end directed motors that exert contractile stresses by sliding MTs relative to each other. B) MTs/kinesin-1 network shows a relatively uniform distribution shortly after encapsulation. C) Snapshots of network contraction after 40 min. The yellow arrows indicate network contraction. D) Rotational flows observed in some of the droplets during network contracts. E) Snapshots of contractile active network at two different time points. The yellow circle shows the area covered by the network after ~ 5 min. F) Space-time plot showing network contraction along the red dashed line in panel E. G) Relative reduction of network area over time for three droplets shown in panel E. A_0 is the initial area of the network before contraction, as marked with a black circle in panel D.

which were occasionally observed in our experiments, as shown in Figure 3.12D and discussed in the ref¹⁸⁵. We quantified the contractile activity of the system by analyzing the relative reduction in the network area over time. Figure 3.12E–G shows that network contraction within droplets of different diameters occurs at similar time-scales. We note that discontinuous illumination of the sample by microscope light every 5 sec during imaging produces ATP, which compensates consumption of ATP by molecular motors. We verified this circulating energy-production and consumption in the system by a separate experiment where we confined the MTs/kinesin-1 network in a millifluidic device (see chapter 2, section 2.11 for device fabrication)

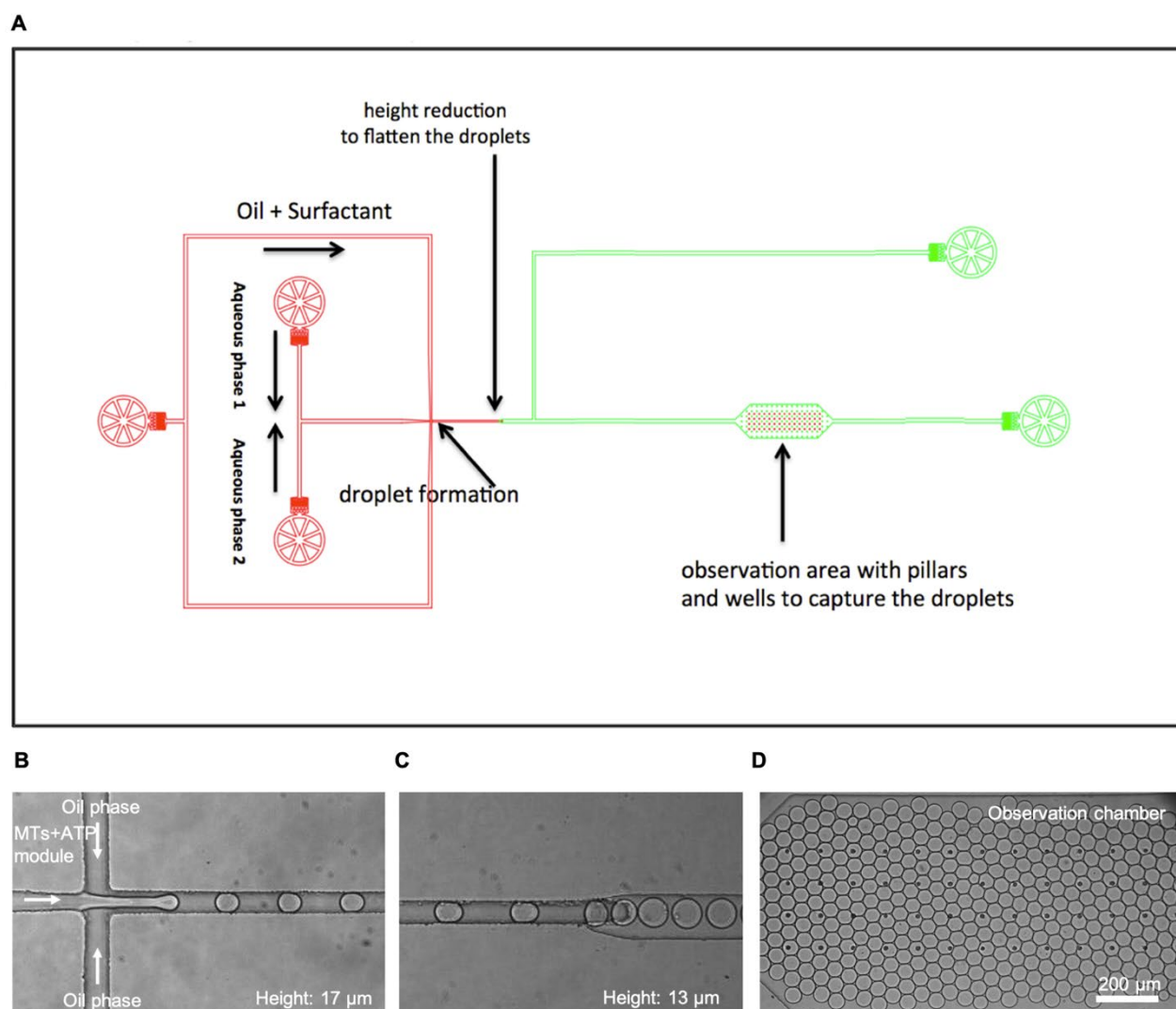


Figure 3.13: Droplet microfluidic setup. A) Schematic diagram showing the encapsulation of MTs/kinesin-1 network (aqueous phase 1) with light-driven ATP module (aqueous phase 2). B) Mono-disperse water-in-oil droplets containing MTs/kinesin-1 solution and light-driven ATP module are formed at the T-junction. C) Droplets enter the green area where height is decreased from 17 μm to 13 μm . D) Observation chamber with entrapped droplets where the flow into the chamber was stopped by guiding the flow to the side channel. The following flow rates were adjusted: aqueous phase 1, 200 $\mu\text{L/hr}$; aqueous phase 2, 200 $\mu\text{L/hr}$; oil phase, 400 $\mu\text{L/hr}$.

with rectangular cross-section (30 mm X 1.5 mm X 0.1 mm). The aim is to compare the contractility of the network in areas illuminated by discontinuous microscope light, where ATP is consumed and produced, versus nonilluminated areas, where ATP is only consumed but not replenished by light. Figure 3.14 shows that initially the active network fills the entire 3D

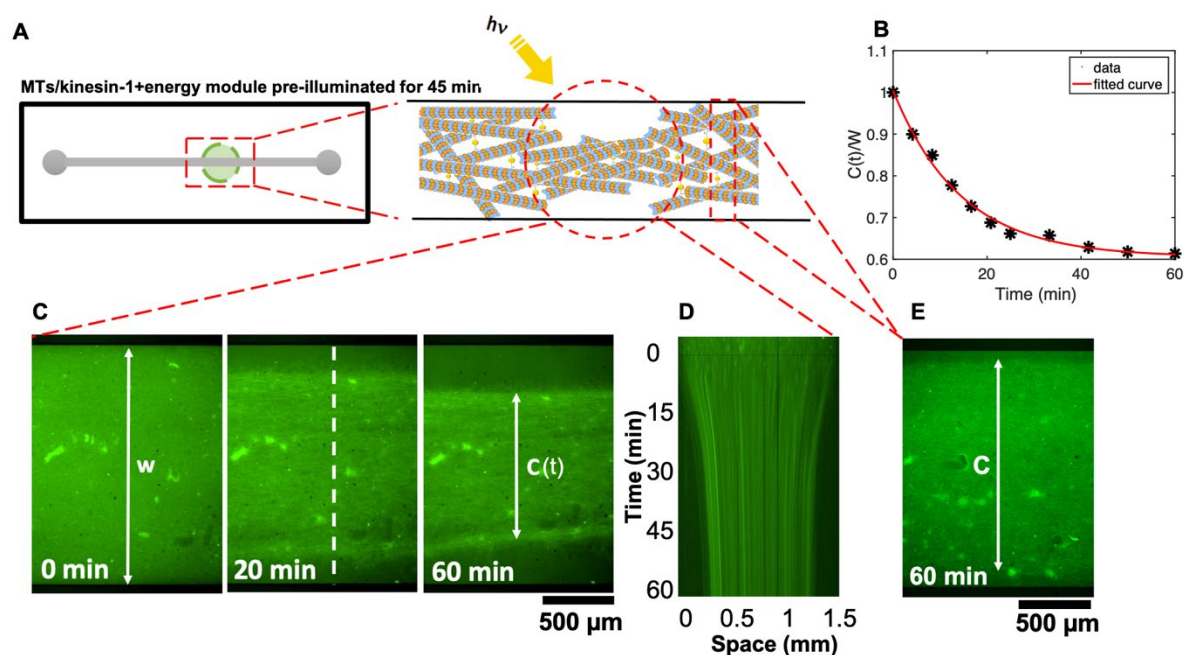


Figure 3.14: Photostimulated contraction of MTs/kinesin-1 network inside a millifluidic device. A) Schematic representation of the millifluidic device highlighting the area illuminated with discontinuous microscope light. Taxol-stabilized MTs are mixed with kinesin-1 motors and a preilluminated energy module prior to injection into a millifluidic channel. B,C) Over time, as available ATP in the energy module is consumed by force-generating kinesin-1 motors, discontinuous microscope illumination compensates for ATP consumption and filamentous network contracts up to 38%. Quantitative analysis of the width of the contracted network in the illuminated region shows an exponential decay over time. The initial width of the network is $W = 1.5$ mm. D) Space-time plot demonstrating the network contraction along the white dashed line drawn in part C. E) In the nonilluminated areas, where ATP is only consumed but not replenished, we monitored a reduced contractility of up to 10% after 1 h.

volume of the channel. Kinesin-1 motors consume ATP synthesized in preilluminated energy module, generating active stresses which result in network contraction (Figure 3.14B–D). As kinesin-1 motors consume ATP, discontinuous microscope illumination compensates ATP consumption and motor-driven network contraction reaches its maximum value of 38.6% within 60 min, as displayed in Figure 3.14B–D.

ATP production is maintained only in areas illuminated by the microscope light, causing stronger network contraction compared to nonilluminated regions in the channel. We observed a reduced contractility of about 10% in the adjacent volume near the region illuminated by the microscope light, as shown in Figure 3.14E. These experiments suggest that the application of patterned illumination in a filamentous network can impose different contraction-maps with spatial gradient. It also demonstrates the efficiency of the light-driven energy module for controlled and localized ATP production and highlights the potential

application of this system in the field of synthetic biology with the ultimate goal of building an artificial cell.

3.3 Discussion

Our experiments demonstrate that light-switchable photosynthetic liposomes can drive ATP dependent activity of axonemal dyneins, which serve as tiny protein machinery to convert chemical energy into mechanical work in the form of a rhythmic beating pattern. We used light energy to dynamically synthesize ATP, allowing us to control beating frequency of axonemes as a function of illumination time. We illuminated the functionalized vesicles at two different light intensities: a 5W microscope lamp and a 50W white LED lamp, which can generate up to 213 μM and 330 μM ATP, respectively, after 45 min of illumination (compare Figure 3.7B and C). We note that bR has a purple color and therefore absorbs green light (500–650 nm) most efficiently. Since bR has a broad excitation spectrum, proton pumping is also possible using white light or red light for excitation. Our results indicate a nonlinear dependence of ATP synthesis rate on light intensity. To generate ATP, ADP is phosphorylated via the F_0F_1 -ATP synthase reaction:



where $n_A \sim 2-3$ the number of protons transported from the inside to the outside of the vesicle each time the reaction of ATP formation takes place, and H^+ indicates hydrogen ions transferred across the vesicle membrane (Figure 3.1A). The rate of ATP formation according to ref¹⁸⁶ can be expressed as

$$r \propto \exp\left(\frac{-\Delta G_{0,ATP} - n_A \Delta G_H}{RT}\right) \frac{K_{Mg-ADP}}{K_{Mg-ATP}} [mADP][P_i] - (1M)[mATP], \quad [3.2]$$

where R is the universal gas constant, T is the temperature, $[mADP]$, $[P_i]$ and $[mATP]$ are the concentrations of magnesium-bound ADP, P_i and magnesium-bound ATP and the factor $(1M)$ is used to balance the units, K_{Mg-ADP} and K_{Mg-ATP} are the equilibrium dissociation constants

for ATP and ADP binding with Mg^{2+} , and $\Delta G_{0,ATP} = -36.03$ kJ/mol is the standard Gibbs free energy for ATP formation. Finally, $\Delta G_H = F\Delta\psi + RT\ln \frac{[H^+]_{out}}{[H^+]_{in}}$, where $\frac{[H^+]_{out}}{[H^+]_{in}}$ is the ratio of external to internal hydrogen ion concentration, $\Delta\psi$ is the membrane potential and F is the Faraday's constant. The concentration of protons inside the vesicles depends on proton pumping by bR, but also on proton pumping by ATP synthase, proton leak across the membrane and buffer capacity inside the vesicles. Only the rate of proton pumping by bR can be considered to be approximately linearly dependent on light intensity,¹⁸⁷ but in general the rate of ATP production r will be nonlinearly dependent on the light intensity. Some experimental studies on similar systems^{140, 188} have confirmed nonlinear dependence of ATP synthesis rate on light intensity and have even shown saturation at higher light intensities, reminiscent of Michaelis–Menten-type kinetics.

In our reactivation experiments with the energy module, we observed that the minimum ATP concentration required to reactivate axonemes is much smaller than the critical value in control experiments with pure commercial ATP (compare Figure 3.6E and Figure 3.7D). Multiple factors potentially account for this discrepancy: (1) ATP is known to be one of the inhibitors of ATP synthase activity, and local consumption of ATP by axonemes can enhance the conversion rate of ADP to ATP, resulting in locally higher ATP concentrations near axonemes. To verify the inhibitory effect of ATP, we coupled the light driven ATP module with a metabolic module by combining the light-driven ATP production with the consumption of glucose, as schematically shown in Figure 3.15. As a proof of concept, a relatively simple metabolic reaction was chosen: Hexokinase converts glucose (G) to glucose-6-phosphate (G-6-P) under the consumption of one molecule of ATP.¹³⁶ Our measurements confirm that in the metabolically coupled system, the ATP production rate is 18% higher than the detected ATP production rate in the control experiments; see Figure 3.15.B,C. (2) The attachment of functionalized vesicles to the demembrated axonemes can generate higher ATP concentrations around the axonemes. Although we did not observe vesicle accumulation along the entire contour length of axonemes, we occasionally observed vesicles attaching to some parts of axonemes. (3) The most important factor which explains the discrepancy is the presence of ADP.

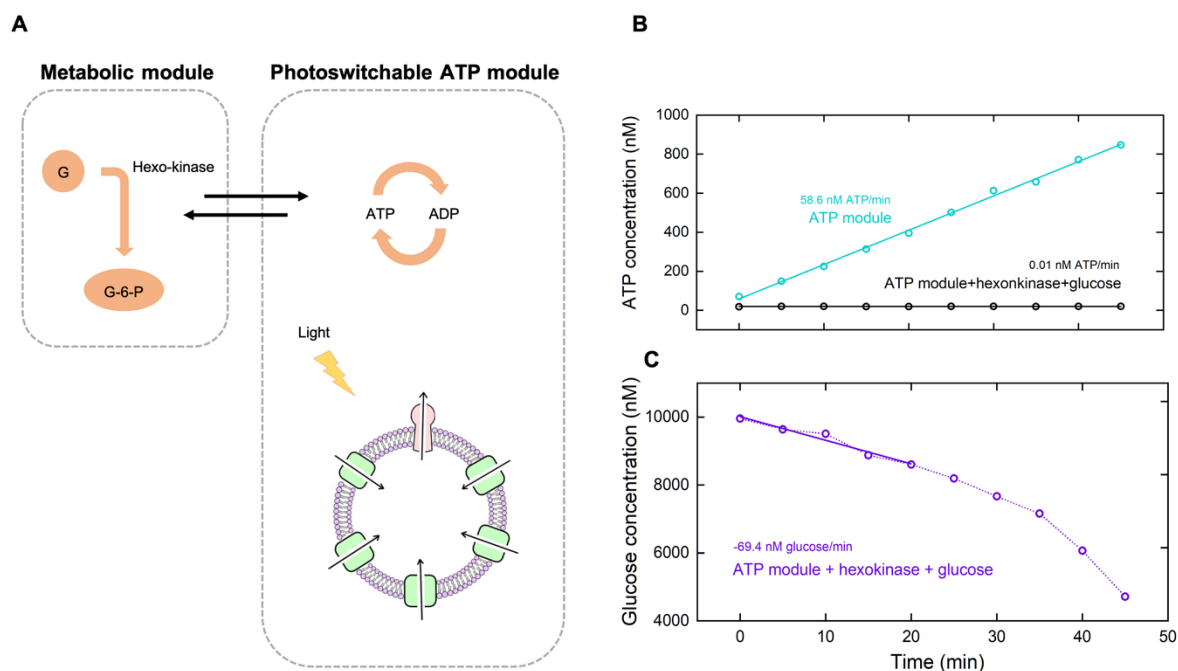


Figure 3.15: ATP and glucose concentration over time under green light illumination. A) Scheme of coupling the ATP regeneration module with a metabolic module for glucose consumption triggered by light. B-C) Measurements were performed in 20 mM tricine-NaOH, 20 mM succinate, 0.6 mM KCl, 80 mM NaCl (inner solution) and 200 mM tricine-NaOH, 5 mM NaH₂PO₄, 160 mM KOH, pH 8.8 (outer solution) in the presence of 20 μ M valinomycin at room temperature. [ADP]= 180 μ M, [P_i]= 5 mM, [lipid]= 0.022 mg/mL, [EF_oF₁] = 1.3 nM, [bR]= 88 nM, $\Delta\Psi$ = 143 mV. Proteins were reconstituted with 0.8 % Triton. For measurement of glucose consumption 10 μ M glucose and 2.7 μ g/mL hexokinase (2400 U/mL) was added to the outer solution. Glucose concentration was determined using a highly sensitive glucose assay (Sigma). Measurements were performed by Dr. Christin Kleineberg, MPI Magdeburg.

In contrast to the experiments with pure ATP, the experimental system with light-to-ATP energy module was additionally supplemented with ADP at a concentration of 1.6 mM. Remarkably, our experiments with pure ATP supplemented with 1.6 mM ADP confirm the activation role of ADP in reactivation of axonemes at low ATP concentrations below 60 μ M (see Figure 3.8C). We observed beating activity even at 0.1 μ M ATP which is much smaller than critical value of 60 μ M in pure ATP experiments without ADP. According to the literature, ADP plays a crucial role in axonemal motility.^{1, 180, 189, 190} For example, Inoue and Shingyoji¹ investigated the influence of ADP and ATP on regulation of dynein activity to produce inter-microtubule sliding in flagella. Dynein motors have four ATP binding sites in each of their heavy chains (Figure 3.8A,B). Only one of these sites is catalytic and responsible for the conversion of ATP to ADP while the other three sites are noncatalytic. According to this study,¹ one of these sites can be occupied by ADP. In the absence of ADP, the mean flagellar velocity was lower

than with ADP. Moreover, in the presence of ADP, the mean velocity reaches its steady state value faster than in the absence of ADP, suggesting that ADP increases the efficiency of energy transduction. This is consistent with our experiments with ADP in which much lower ATP concentrations were required for axonemal beating. In addition, beating frequency with ATP and ADP reaches saturation at very low ATP concentrations, whereas kinetics with pure ATP is much slower (compare Figure 3.6E with Figure 3.7D and Figure 3.8C). Now, considering that very low ATP concentrations around or below 1 μM ATP (active form is actually ATP-Mg) are required to observe axonemal beating, the question arises whether ADP can bind to more than one of the noncatalytic binding sites in dynein (see Figure 3.8B).

Self-sustained motility systems that rely on light energy as a primary source of energy (or for *in vivo* applications, chemical energy such as glucose¹³³), may have potential applications in the area of synthetic micro-swimmers and targeted drug delivery. In our preliminary experiments, to build a sperm-like swimmer, we attached a cargo (1 μm beads) to the distal end of an axoneme that can be propelled by external illumination (Figure 3.16A,B). In light-to-ATP or chemical-to-ATP energy modules, enhanced attachment of functionalized vesicles to the contour length of axonemes could be beneficial to this system¹⁹¹ because ATP will be produced locally around axonemes and consumed subsequently by dynein molecular motors (Figure 3.16C). These functionalized vesicles attached to an axoneme can also be used as drug carriers.¹⁹²⁻¹⁹⁴ Extensive experiments in the future are necessary to investigate the feasibility of these ideas for biomedical applications. Lastly, we have shown that functionalized artificial liposomes capable of continuous production of ATP in response to light as an external stimulus, can serve as an efficient energy source for *in vitro* MTs motility assays in which kinesin-1 molecular motors are actively engaged in generating and sustaining active stresses in the network. In these experiments, preillumination of the energy module for 45 min generates sufficient ATP needed for motor-driven network contraction. Discontinuous microscope illumination every 5 sec replenishes the consumed ATP and the MTs/kinesin-1 network confined in a millifluidic device contracts by up to 38% within 60 min, following an exponential trend (Figure 3.14B). The encapsulated MTs/kinesin-1 network contracts similarly, but in a much faster time scale

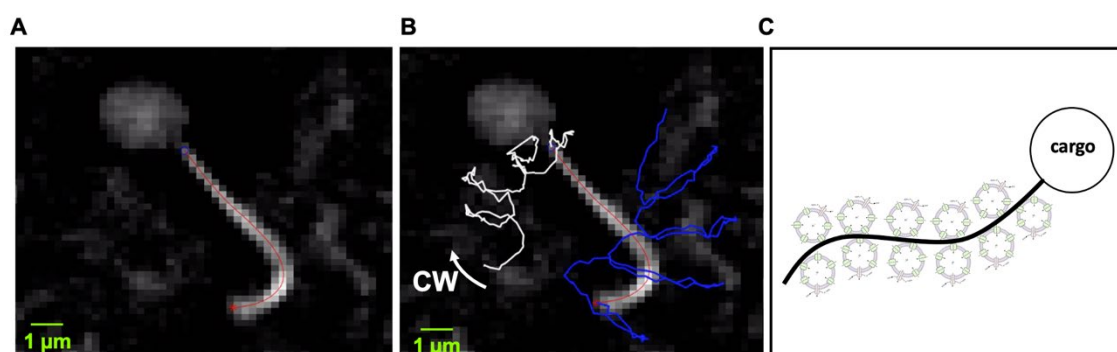


Figure 3.16: Bead as a cargo. A) A bead of diameter $1\ \mu\text{m}$ is attached to the distal end of an axoneme. B) Upon illuminations, the reactivated axoneme propels the bead. Blue line shows the trace of the basal end and the white line is the trace of the distal tip which is attached to a bead. C) A cartoon showing that an enhanced vesicle-axoneme attachment, e.g., via electrostatic interactions, could be beneficial for the local production of ATP in the vicinity of axonemes.

of ~ 5 min. Once contracted, the network which is highly cross-linked by kinesin-1 motors and randomly oriented, remains contracted even after the microscope light is turned off and the ATP is depleted. Thus, a light-controllable reversible switch between contracted and relaxed states does not occur in our experiments. We also performed control experiments with commercial ATP, to confirm that a contracted network does not relax back once ATP is completely consumed (Figure 3.17) for a 19 hr long experiment with 1 mM pure ATP. Further, the preillumination of the energy module is a requirement for the network contraction. Indeed, a MTs/kinesin-1 network mixed with a non-preilluminated energy module does not contract, indicating that ATP produced by discontinuous microscope illumination is insufficient to generate critical contractile stresses in the network.

Our developed scheme of circulating energy consumption and production could serve as a potential platform to encapsulate constituent elements such as actin, microtubules and various regulatory components inside functionalized lipid vesicles to provide ATP in an optically controllable self-sustained manner. ATP-driven motor activity in filamentous biopolymer networks is expected to generate active forces that drive morphological deformation in

liposomes and further contributes to the challenging goal of bottom-up creation of an artificial cell.

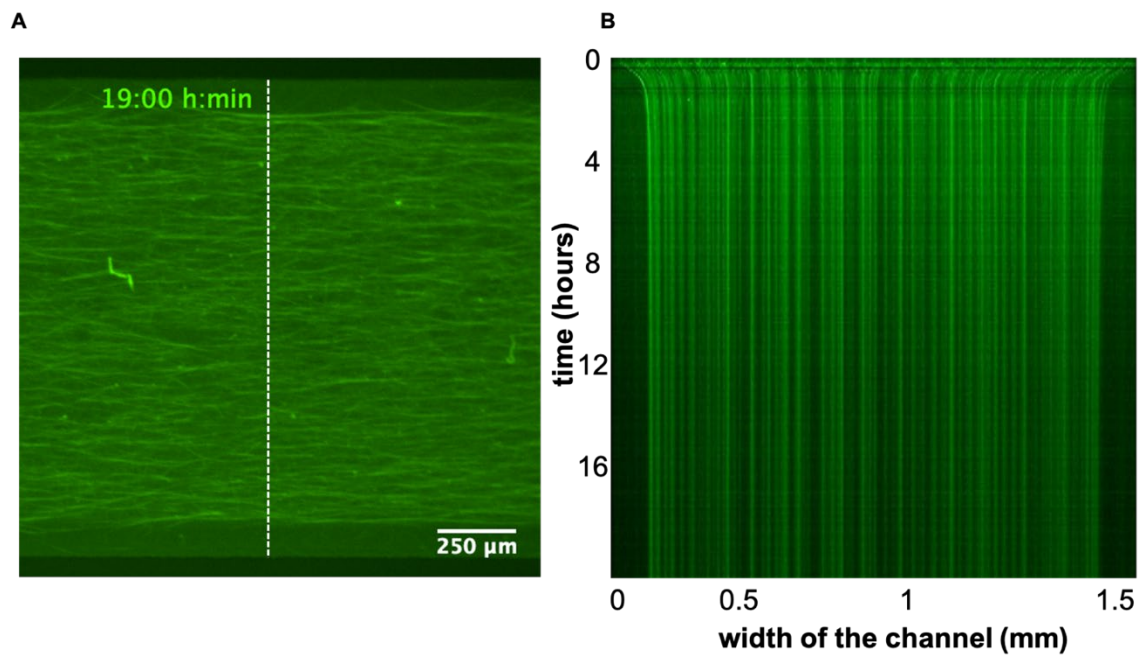


Figure 3.17: A control experiment with 1 mM pure commercial ATP to confirm that a contracted MTs/kinesin1 network does not relax back to its initial state once the ATP is depleted. A) Snapshot of the millifluidic set up filled with MTs/kinesin1 network after 19 hr. B) The space-time plot along the white dashed line in panel A showing the network contraction. Note that the cross-linked network remains contracted for a long period of time.

Chapter 4 Waveform of Free, Hinged and Clamped Axonemes Isolated from *C. reinhardtii*: Influence of Calcium

Chapter 4 is adapted from:

Azam Gholami, [Raheel Ahmad](#), Albert J bae, Alain Pumir and Eberhard Bodenschatz, "Waveform of Free, Hinged and Clamped Axonemes Isolated from *C. reinhardtii*: Influence of Calcium, *New Journal of Physics*, 2022, 24, 053025.

Raheel Ahmad contributions: Isolation of flagella, experiments with calcium, data analysis, discussion and revision.

In this work, to understand the effect of the boundary conditions experimentally in a model system that is close to the real flagellum, we combined high-precision and high-speed phase contrast microscopy (1000 fps) with image processing and analytical analysis to quantitatively describe the wave patterns of beating axonemes isolated from *C. reinhardtii*. Our analysis of the motion using principal component analysis (PCA) shows that the motion of axonemes is very accurately captured by the four dominant modes, consistent with the previous works^{105, 195, 196}. Our experimental data analyzed with PCA shows that the main base-to-tip propagating wave coexists with standing waves. We found that the amplitude of the standing wave depends on the boundary conditions and was higher in non-rotating clamped axonemes that are attached from the distal region to the substrate and can reflect the dominant base-to-tip traveling wave. To investigate how the wave components depend on calcium, we performed experiments at different calcium concentrations. When increasing the calcium concentration from 10^{-4} mM to 1 mM, the static mode drops around 85% triggering a transition from a circular to a straight swimming trajectory. Finally, the analysis of a few cases of freely beating flagella in intact *C. reinhardtii* cells (see Figure 4.1A-B) demonstrates the coexistence of the main dominant wave with standing waves.

4.1 Results

We used established protocols to isolate flagella from *C. reinhardtii* wild type cells, and demembrated them using non-ionic detergents^{125, 197} (see Chapter 2, section 2.7). These naked flagella (axonemes), can be reactivated at various ATP concentrations (see Chapter 2, section 2.7.3). ATP powers dynein molecular motors that convert chemical energy into mechanical work by sliding adjacent MTDs relative to each other, as illustrated in Figure 4.1C-D¹⁹⁸⁻²⁰⁰. However, structural constraints do not allow MTDs to slide freely. Instead, sliding is converted into rhythmic bending deformations that travel along the contour length of axonemes in the base-to-tip direction. To quantify these curvature waves, we tracked the axonemes over time using the GVF technique^{103, 104} (see Chapter 2, Figure 2.6). In our experiments, we vary two parameters, namely ATP and Ca^{2+} concentration, as discussed below. We are focused on the examples where axonemes swim effectively in 2D in the vicinity of the substrate. This greatly facilitates the tracking of flagella and the data analysis.

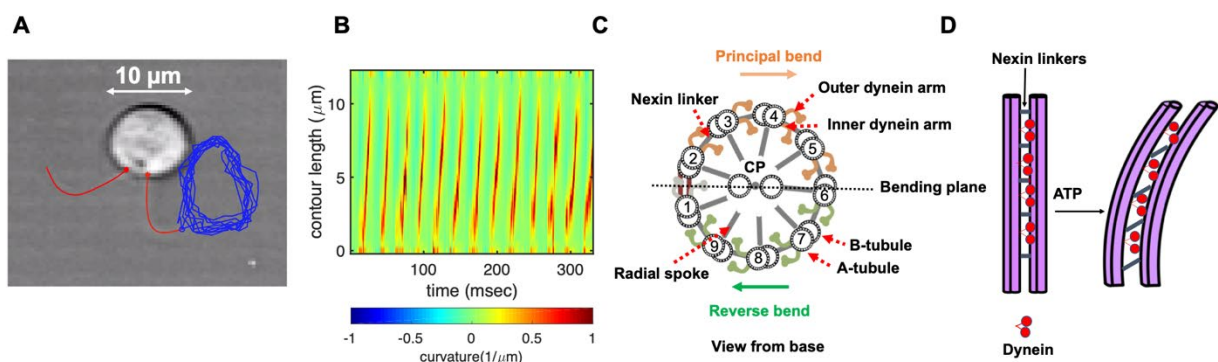


Figure 4.1: A) Snapshot of a *C. reinhardtii* cell with the cell body attached to the substrate, while its two flagella are free to beat. The blue trajectory shows the trace of the distal tip of the tracked flagellum in red. B) Curvature waves initiate at the basal region close to the cell body and travel toward the distal tip at the frequency of around 40 Hz. C-D) A flagellum has an MTs-based structure consisting of nine MTDs at the periphery and two MT singlets at the center.¹³ To actuate a flagellum, dynein molecular motors which are bound periodically in two rows to the MTDs, convert efficiently chemical energy from ATP hydrolysis into mechanical work. Due to the structural constraints which resist sliding, axonemal bending occurs. One row of the motors are the outer dynein arms (ODAs) which provide power output, and the other row is the inner dynein arms (IDAs) which determine the flagellar beat pattern^{14,15}.

4.1.1 Illustration of the motion

Figure 4.2A-D illustrates planar swimming motion of an exemplary axoneme reactivated at 80 μM ATP without calcium (Ca^{2+}). Bending waves initiate at the basal end (shown in blue in Figure

4.3A and B) and travel toward the distal tip of the axoneme (shown in white in Figure 4.3A and B) periodically in time with a beating frequency of $f_0 = 18.17 \pm 0.01$ Hz. The static component of the axonemal waveform, defined as the average angle over one beat cycle at each position along the axonemal length, highlights the existence of an intrinsic curvature of axonemes around the value of $\sim 0.2 \mu\text{m}^{-1}$. To bend an axoneme to a circular arc, tangential axial forces generated by an asymmetric distribution of dynein motors are required to induce a dynamic instability.²⁰¹ Active axonemes show an asymmetric waveform predominantly in 2D which mostly resembles the forward swimming motion of flagella in intact cells. The traveling periodic curvature waves provide the necessary thrust to propel the axoneme in the surrounding water like fluid.²⁰²

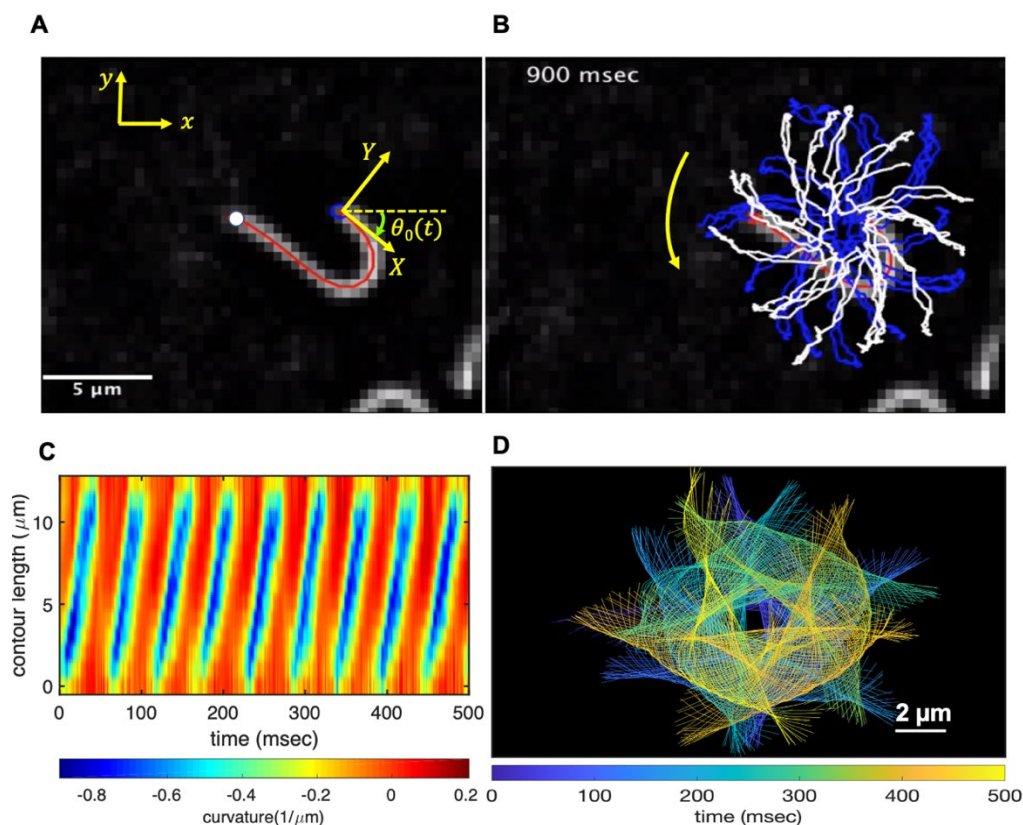


Figure 4.2: An isolated axoneme beating freely. A) An instantaneous shape. The tangent vector $\mathbf{t}(s)$ at $s = 0$ defines the X -direction and the corresponding normal vector $\mathbf{n}(s)$ defines the Y -direction of the swimmer fixed frame. B) Traces of the basal end (originally connected to the intact *C. reinhardtii* cell, blue trace) and the distal tip (white trace) of the axoneme tracked for 900 msec. C) Curvature waves initiate at the basal end of the axoneme and propagate toward the distal tip at a frequency of $f_0 = 18.17 \pm 0.01$ Hz. D) The color-coded time projection of the axoneme shows a circular swimming trajectory. Here $[\text{ATP}] = 80 \mu\text{M}$ and $[\text{Ca}^{2+}] = 0$.

This thrust force is balanced with the viscous drag exerted by the fluid on the swimmer.²⁰² The swimming dynamics of axonemes differ from sperm flagellar propulsion primarily in that axonemes are shorter in length (10 μm in comparison to 50 μm of human spermatozoa) and beat with a non-zero static curvature (Figure 4.3A) resulting in circular swimming trajectory as shown in Figure 4.2B,D. To quantify the static curvature, we translate and rotate the axonemal configurations such that the basal end ($s = 0$) is at the origin of the coordinate system and the tangent vector at $s = 0$ is oriented along the \mathbf{x} –direction (Figure 4.2A). The filament in cyan color in Figure 4.3A shows the time-averaged axonemal shape with mean curvature of $\kappa_0 \sim 0.21 \mu\text{m}^{-1}$. The negative sign of κ_0 indicate a clockwise bend when moving from the basal end at $s = 0$ toward the distal tip at $s = L$ (Figure 4.3A). The base-to-tip bending deformations superimposed on this negative intrinsic curvature cause a counter-clockwise rotation of the axoneme (Figure 4.2B). The wavelength λ of these bending waves is larger than the contour length. To calculate λ , we performed a Fourier transformation of $\theta(s, t)$ in time at each position s along the contour length of the axoneme and obtained the phase $\phi(s)$ (Figure 4.3B). The wavelength can be calculated as $\lambda \sim 2\pi L / (\phi(L) - \phi(0)) \sim 15.95 \mu\text{m}$ ²⁰³, which is $\sim 30\%$ larger than the axonemal contour length $L = 12.35 \mu\text{m}$. We notice that the phase $\phi(0)$ is undefined since $\theta(s = 0, t) = 0$. This is immaterial for the present purpose, as we are only interested in the phase gradient, which we determined by fitting the phase dependence along the axoneme, as indicated by the red line in Figure 4.3B. The beating frequency of axonemes depends on the ATP concentration following a Michaelis-Menten-type kinetics^{41, 175} (Chapter 3, Figure 3.6E). It starts with a linear trend at small concentrations of ATP and saturates at higher ATP concentrations around 1 mM (Figure. 4.3C). In our experiments, we measured a critical minimum of ATP concentration around 60 μM ⁴¹ necessary to reactivate axonemes (see Chapter 3, Figure 3.6E). Reactivated axonemes swim on circular trajectories effectively in 2D (see ref²⁰⁴). Active axonemes undergo planar shape deformations over time, but at any instant of time, it may be considered as a solid body with translational and rotational velocities U_x , U_y and Ω_z which we measure in the swimmer-fixed frame (Figure 4.3D-F)²⁰⁵. These velocities oscillate in time, reflecting the fundamental beat frequency of the axoneme (~ 18 Hz) and its higher harmonics.

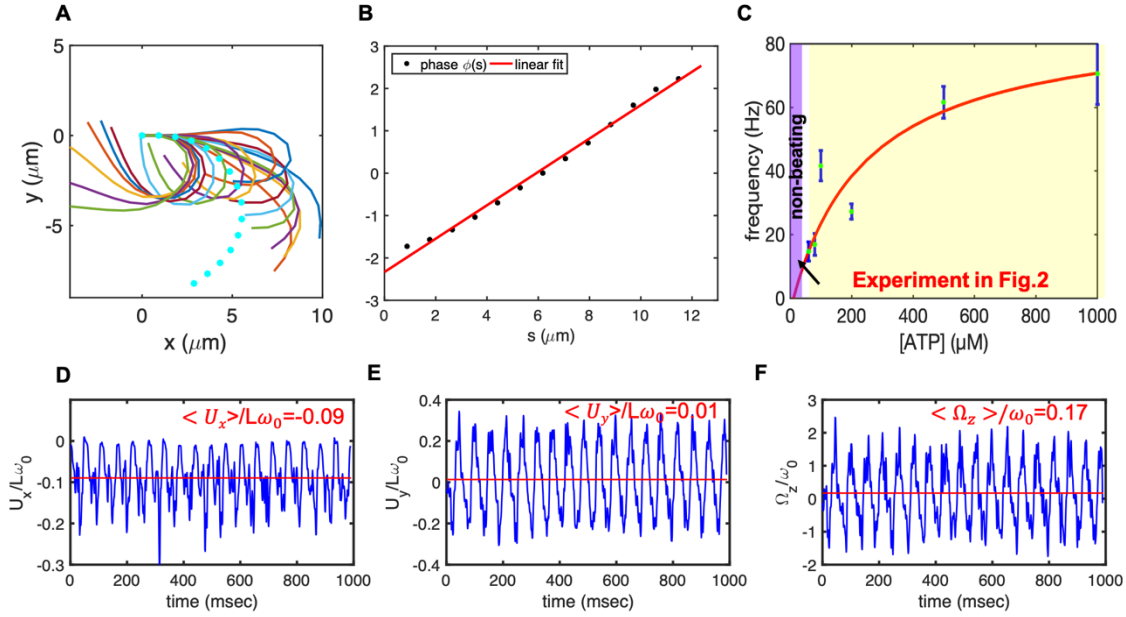


Figure 4.3: Experimental shape of *C. reinhardtii* isolated axoneme. A) The basal end of the tracked axoneme in Figure 4.2 is translated to the origin and rotated such that the tangent vector at $s = 0$ is along the x -axis. Semicircular arc in cyan color with mean curvature of $\kappa_0 \sim 0.21 \mu\text{m}^{-1}$ shows the time averaged shape of the axoneme. This averaged intrinsic curvature makes the waveform asymmetric. B) The phase $\phi(s)$ of traveling curvature waves obtained by performing Fourier transform of $\theta(s, t)$ in time at each position s . The wavelength is then calculated as $\lambda \sim 2\pi L / (\phi(L) - \phi(0)) = 15.95 \mu\text{m}$. Since $\theta(s = 0, t) = 0$. The phase $\phi(0)$ cannot be defined directly, and is instead obtained by extrapolation of $\phi(s)$, as indicated by the red line. C) Axonemal beating frequency depends on the ATP concentration and is higher at higher ATP concentrations. Axonemes ceased to beat at ATP concentrations below $60 \mu\text{M}$ $[\text{ATP}]_{\text{critical}}$. Red curve shows the least square fit to the Michaelis-Menten relation $[\text{ATP}]: f = f_{\text{critical}} + f_{\text{max}} ([\text{ATP}] - [\text{ATP}_{\text{critical}}]) / (K_m + ([\text{ATP}] - [\text{ATP}_{\text{critical}}]))$. The fitting parameters are $f_{\text{max}} = 73.75$ Hz and $K_m = 298.5$ Hz (see Chapter 3, section 3.1.2). The black arrow indicates the ATP concentration that is fixed for the axoneme in Figure 4.2. D-F) Translational and rotational velocities of the axoneme in Figure 4.2, measured in the swimmer fixed frame. The red lines mark the mean values.

4.1.2 Principal component analysis of the curvature waves demonstrates the existence of the back-propagating waves in free axonemes

We performed principal component analysis (PCA) to describe the time-dependent shape deformation of the isolated axonemes.^{50, 105} This analysis is based on the method introduced by Stephens et al.¹⁰⁵ which was initially used to characterize waveforms in *C. elegans* (see Chapter 2.9). Using the x and y coordinates of the tracked flagellum (see Chapter 2, section 2.8), we calculate $\theta(s, t)$, which is defined as the angle between the local tangent vector of the centerline of the tracked flagellum and the x -axis (Figure 4.3A). We then average the

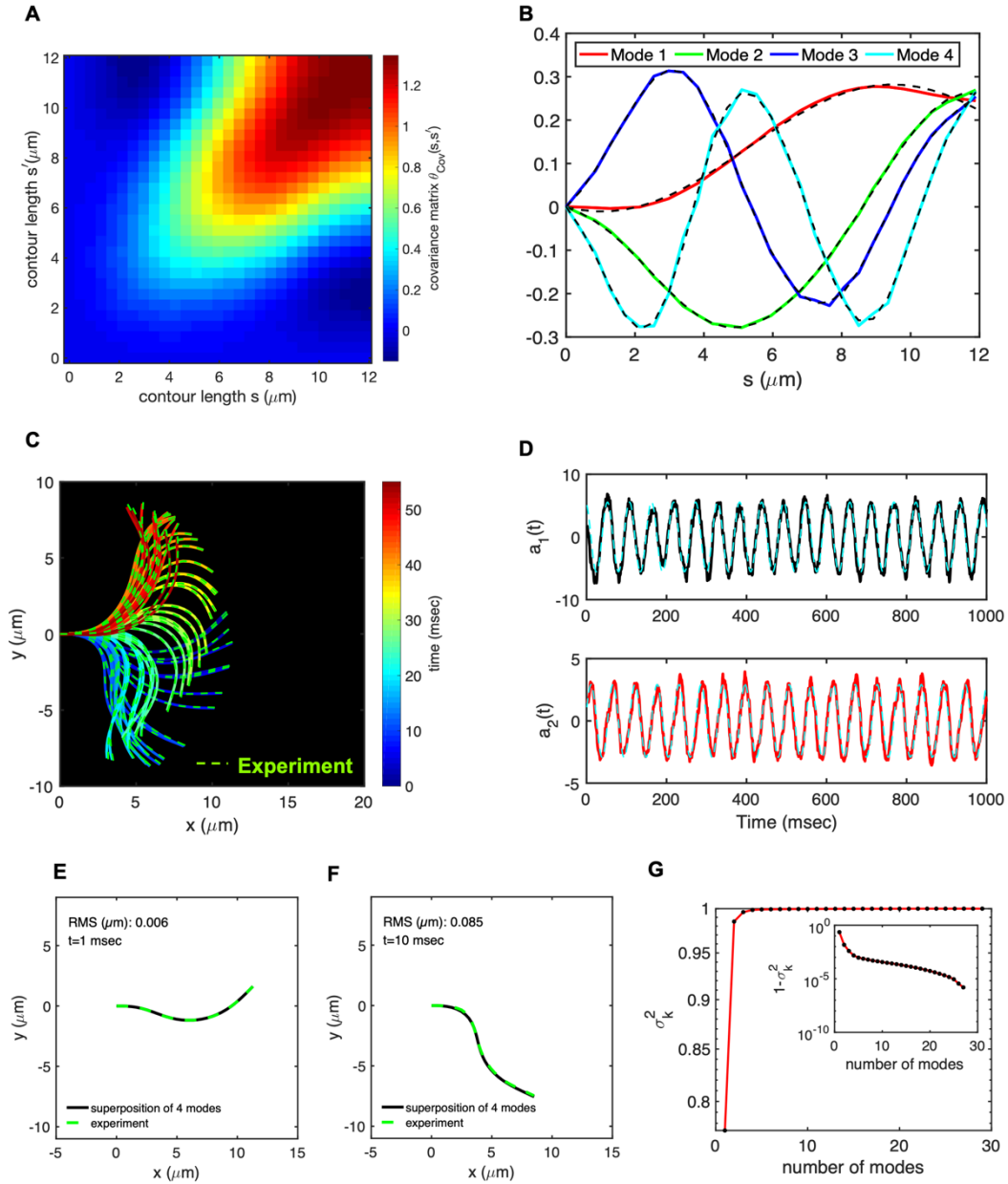


Figure 4.4: PCA analysis of the axoneme in Figure 4.2. A) The covariance matrix $\theta_{Cov}(s, s')$ of fluctuations in $\theta(s, t) - \langle \theta(s, t) \rangle_t$. B) Four eigenvectors corresponding to the four largest eigenvalues of $\theta_{Cov}(s, s')$. C) The time-projection of the mean-shape subtracted experimental data and the corresponding shapes reconstructed using the four eigenmodes presented in panel B. D) The time-dependent coefficients $a_1(t)$ and $a_2(t)$ as defined in Eq. 4.1. The cyan dashed lines present the Fourier fits as defined in Appendix A.2(2), Eqs. A.2.4-5. E-F) To compare the experimental data with reconstructed shape, two exemplary configurations with the lowest and highest root mean square (RMS) errors are presented. G) The fraction of the total variance σ_k^2 plotted versus the number of PCA modes n . The figure in the inset illustrates $1 - \sigma_k^2$ versus n on a semi-log scale. See Chapter 2, section 2.9 for the definition σ_k^2 . Note that already two modes already capture 98.52% of the total variance and four modes capture 99.85%.

axonemal shapes over one beat cycle to obtain the mean shape of the axoneme $\langle \theta(s, t) \rangle_t$, which corresponds to the arc-shaped filament colored in cyan in Figure 4.3A. Next, we compute the covariance matrix $\theta_{cov}(s, s')$ of the fluctuations of the mean subtracted angle $\theta(s, t) - \langle \theta(s, t) \rangle_t$. Figure 4.4A shows the color map of the flagellum covariance matrix, which has an effectively reduced dimensionality with a small number of non-zero eigenvalues. We note that four eigen modes $M_n(s)$ ($1, \dots, 4$) corresponding to the first four largest eigenvalues of $\theta_{cov}(s, s')$ capture the shape of the flagellum with very high accuracy. These four eigenvectors are plotted in Figure 4.4B. We reconstruct the axonemal shapes using the four dominant modes and the corresponding time-dependent motion amplitudes $a_n(t)$ as

$$\theta(s, t) - \langle \theta(s, t) \rangle_t \approx \sum_{n=1}^4 a_n(t) M_n(s) \quad [4.1]$$

The reconstructed axonemal shapes are presented in Figure 4.4C, where the green dashed lines show the experimental data. The time-dependent coefficients $a_1(t)$ and $a_2(t)$ are shown in Figure 4.4D ($a_3(t)$ and $a_4(t)$ are shown in Appendix, Figure A.2.13 and Figure A.2.14). In order to compare the experimental data with the reconstructed shapes, Figure 4.4E-F shows two exemplary configurations with the lowest and the highest root mean square errors of 0.006 and 0.085, respectively. Let us focus on the first two modes $M_1(s)$ and $M_2(s)$, which in combination with the first two time-dependent motion amplitudes $a_1(t)$ and $a_2(t)$ capture 98.52% of the total variance (Figure 4.4G). The black dashed lines in Figure 4.4B represent the Fourier fits of the mode (see Appendix A.2(2)). To distinguish the role of different modes in reconstructing the axonemal shapes, we compared the original experimental data (without the mean-shape subtraction) with the shapes reconstructed using the combination of different modes as $\theta(s, t) = \sum_i \alpha'_i(t) M_i(s)$. Please note that, in contrast to the coefficients $\alpha_i(t)$ in Eq. 4.1, the time-average of $\alpha'_i(t)$ is not zero and $\sum_i \alpha'_i(t) M_i(s)$ gives the axonemal mean shape (cyan filament in Figure 4.3A). The coefficients α'_i and α_i are related by the simple relation $\alpha'_i(t) = \alpha_i(t) + \langle \alpha'_i(t) \rangle_t$. This comparison for different number of modes is presented in Figure 4.5. It is interesting that in the eigenmodes $M_2(s)$, $M_3(s)$ and $M_4(s)$, higher spatial modes $2k$ and $3k$ corresponding to the smaller wavelengths $\lambda/2$ and $\lambda/3$

become important. Finally, we repeated our PCA analysis for 20 different axonemes. After re-scaling the contour length s by the axonemal length L , although each axoneme has a different set of eigenmodes, the individual modes collapse and show a common trend (see Appendix, Figure A.2.15-16).

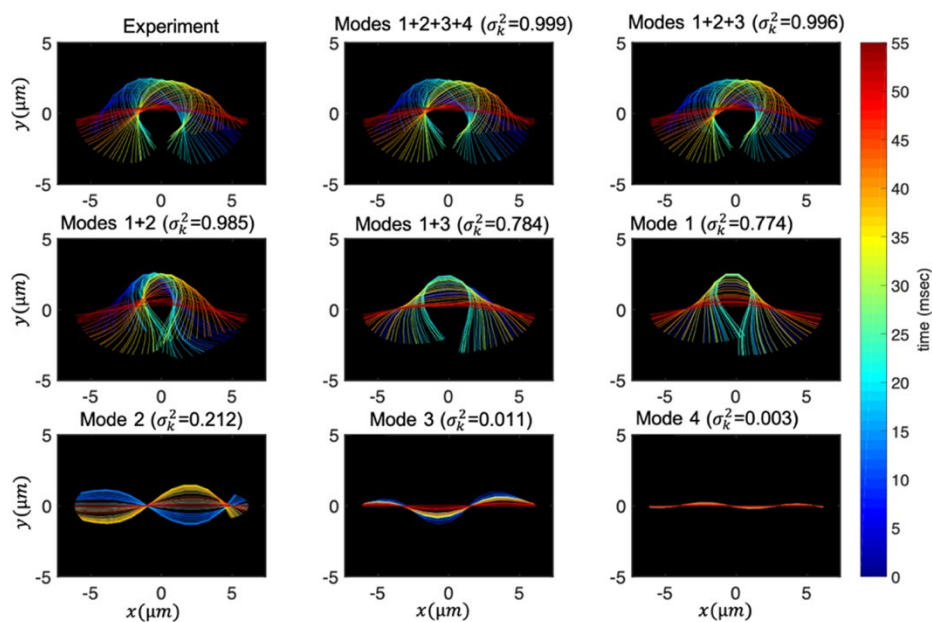


Figure 4.5: Experimental shapes over one beat cycle are compared with the free axonemal shapes, shown in Figure 4.2, reconstructed using combination of the PCA modes, $\sum_i \alpha'_i(t) M_i(s)$, as discussed in the text. For each panel, fraction of total variance is calculated, see Chapter 2, section 2.8 for the definition of σ_k^2 . Please note that in contrast to Figure 4.4C, here the mean axonemal shape (cyan filament in Figure 4.3A) is not subtracted.

4.1.3 Implication for the motion of free axonemes: an analytical study

To understand the effect of various modes on the rotational and translational velocities of a freely beating axoneme, we analyzed analytically a simplified waveform. For detail, see Appendix A.2(4).

4.1.4 Calcium reduces the static curvature of the free axonemes

To investigate the effect of calcium ions on the flagellar waveform, we performed experiments at different calcium concentrations and systematically measured the static and the dynamic components of the axonemal waveform. As shown in Figure 4.6, we changed the calcium concentration from 10^{-4} mM to 1 mM and quantified the curvature waves of the reactivated

axonemes as explained in section 4.1 . Our analysis confirms that static component of the curvature waves C_0 decreases by $\sim 85\%$, as we increase $[Ca^{2+}]$ from 10^{-4} mM to 1 mM. The

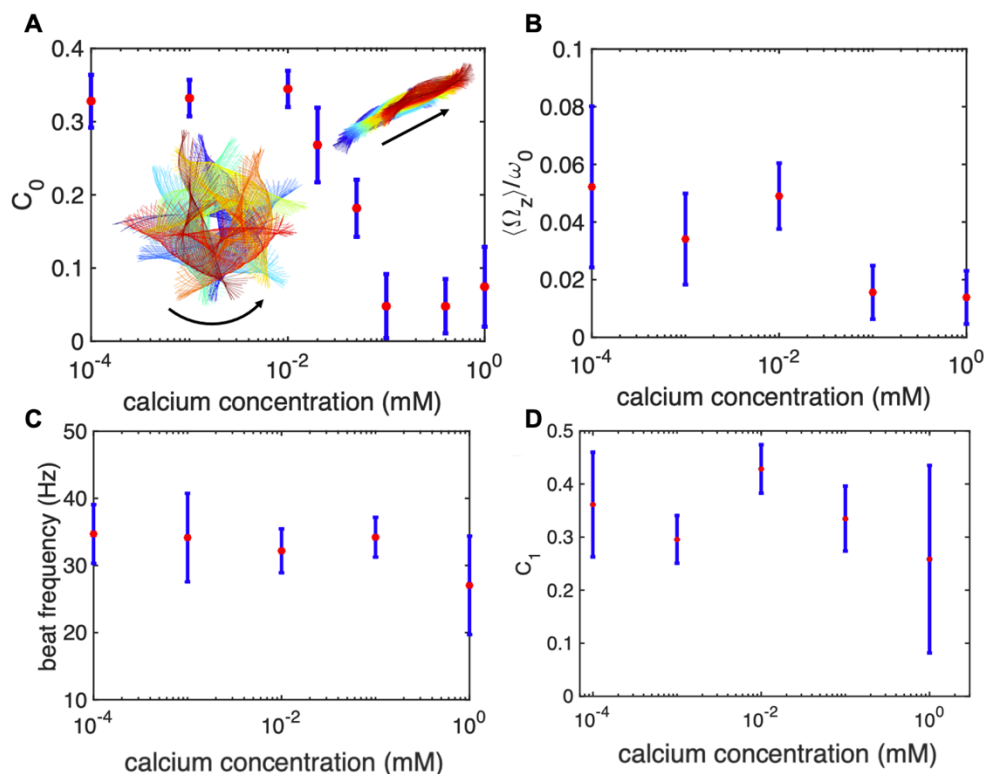


Figure 4.6: Experiments with free axonemes reactivated with the calcium-supplemented buffer at different calcium concentrations. A) The static curvature C_0 show a sudden drop from 0.3 to 0.05 at $[Ca^{2+}]$ around 0.02 mM which induces a switch from circular to straight swimming path. B) Mean rotational velocity of axonemes decreases at $[Ca^{2+}]$ above 0.02 mM, consistent with the observation that axonemes switch from circular to straight swimming trajectories. C) Beat frequency of axonemes drops slightly at $[Ca^{2+}]$ around 1 mM. D) The amplitude C_1 slightly with $[Ca^{2+}]$. In all the experiments, the ATP concentration was fixed to 200 μ M.

drop is relatively sharp at $[Ca^{2+}]$ around 0.02 mM, indicated by a vertical dashed line in Figure 4.6A. This decrease in C_0 causes a transition from a circular swimming trajectory to a straight trajectory (Figure 4.6A-B), as expected based on Appendix, Eq. A.2.10. We also observed that the beat frequency of axonemes drops slightly at high calcium concentrations at ~ 1 mM (Figure 4.6C). In addition, calcium ions affect the amplitude of the main travelling wave component. To quantify this effect, we examined the wave amplitudes (C_1) inferred from our PCA analysis. These results, which are plotted in Figure 4.6D-E, show a small decrease in C_1 at high $[Ca^{2+}]$. We notice that calcium concentrations lower than ~ 0.02 mM do not qualitatively

affect the picture drawn in the absence of calcium, as summarized in section 4.1.1. However, at high calcium concentrations, the rotational velocities of axonemes $\Omega_z(t)$ are small and

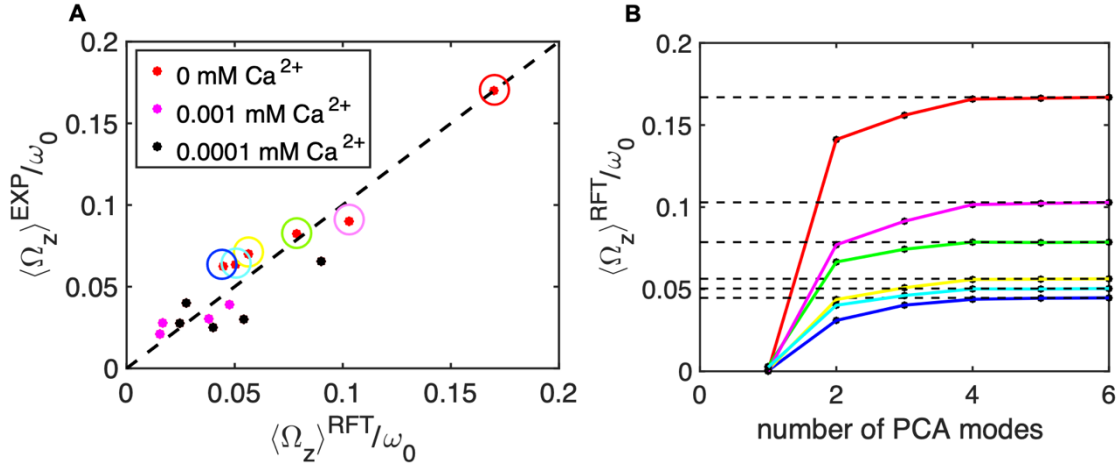


Figure 4.7: A) Comparison of the experimental rotational velocities of free axonemes with the corresponding values obtained by RFT simulations with full experimental shapes, i.e. infinite number of modes. The black line has the slope of 1 and passes through the origin. Each data point corresponds to one axoneme at a given calcium concentration. Circles show the data points which are used in panel B. B) The dependence of $\langle \Omega_z \rangle^{RFT} / \omega_0$ on the number of PCA modes considered for the shape reconstructions for the six axonemes, indicated by colored circles in panel A.

highly noisy, and direct measurement of $\langle \Omega_z \rangle$ is difficult. Therefore, in Figure 4.6B, $\langle \Omega_z \rangle$ are calculated using the full experimental shapes based on RFT simulations with $\eta = \zeta_{\parallel} / \zeta_{\perp} = 1.8$. To check the validity of RFT in our system, we used our experimental data at zero or very low concentrations of calcium, where axonemes swim on circular paths and a direct measurement of $\langle \Omega_z \rangle$ is possible. The comparison between the experimental measurements and RFT simulations is shown in Figure 4.7A. The black dashed line has the slope of 1 and passes through the origin, which provides strong evidence for the validity of RFT in our experimental system. Furthermore, with regard to our PCA analysis as discussed in section 4.1.2, we mention that in our RFT simulations, the mean rotational velocity of axonemes depends on the number of modes which are considered for the shape reconstruction. Figure 4.7B shows that $\langle \Omega_z \rangle / \omega_0$ obtained using RFT simulations, converges for $n \geq 4$. The black dashed lines in Figure 4.7B are the values of $\langle \Omega_z \rangle^{RFT} / \omega_0$ obtained using full experimental shapes, i.e. infinite number of modes. Finally, similar to Figure 4.5, we performed PCA analysis to reconstruct axonemal shapes for an exemplary axoneme at a calcium concentration of 0.1 mM. As shown in Figure 4.8, the first four modes recapitulate the beat pattern of the axonemes with high accuracy.

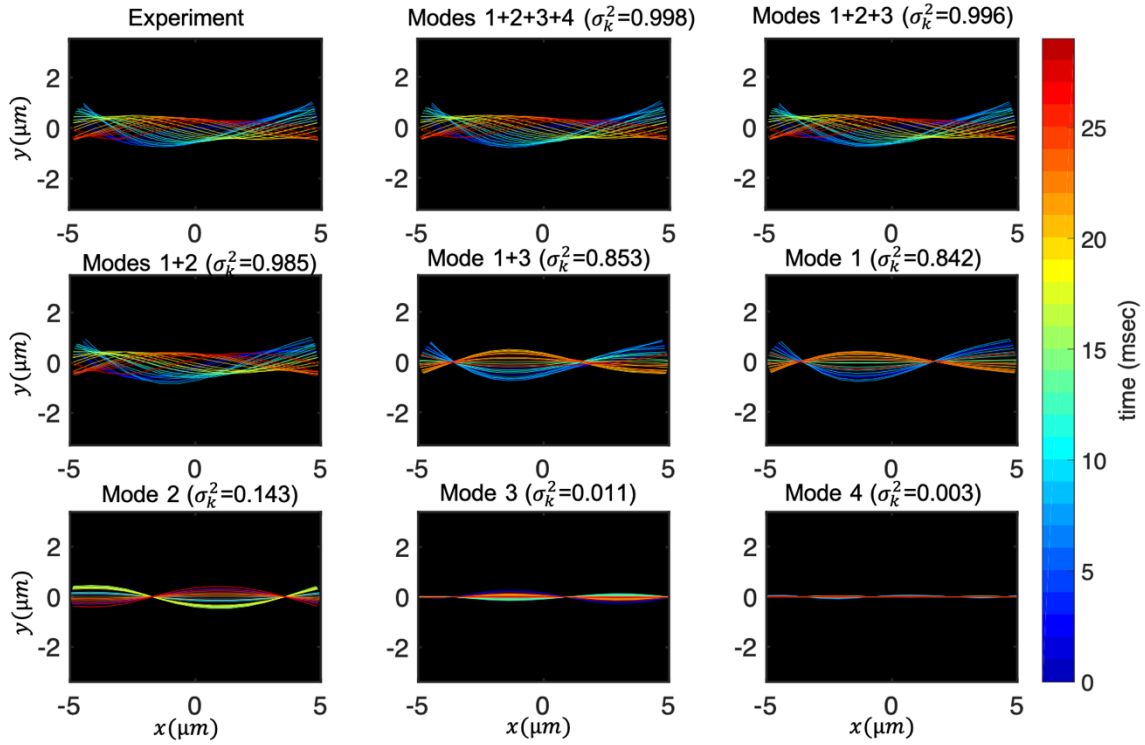


Figure 4.8: Experimental shapes and different combinations of the four dominant eigenmodes used to reconstruct the axonemal shapes. For each panel, fraction of total variance σ_k^2 is calculated (see Chapter 2, section 2.9). Here $[ATP] = 0.2$ mM and $[Ca^{2+}] = 0.1$ mM.

4.1.5 Hinged and clamped boundary conditions

In our experiments, attachment of axonemes to the substrate occurred either from the basal end or the distal tip due to the non-specific axoneme-substrate interactions. These axonemes were either hinged from the basal or the distal side and rotate freely around the hinging point, as shown in Figure 4.9, or they were clamped from the either side to the substrate and were unable to rotate, as shown in Figure 4.10.

Let us first focus on the hinged boundary condition and consider an exemplary case where the axoneme was attached from the basal end and rotates CCW at the mean rotational velocity of $\langle \Omega_z \rangle \sim 15$ rad/sec around the pinning point. Curvature waves initiate at the surface-attached proximal region ($s = 0$) and travel at the frequency of 44.34 ± 0.02 Hz toward the distal tip ($s = L$), see Figure 4.9C. This axoneme has an intrinsic curvature of $\sim -0.17 \mu\text{m}^{-1}$, which

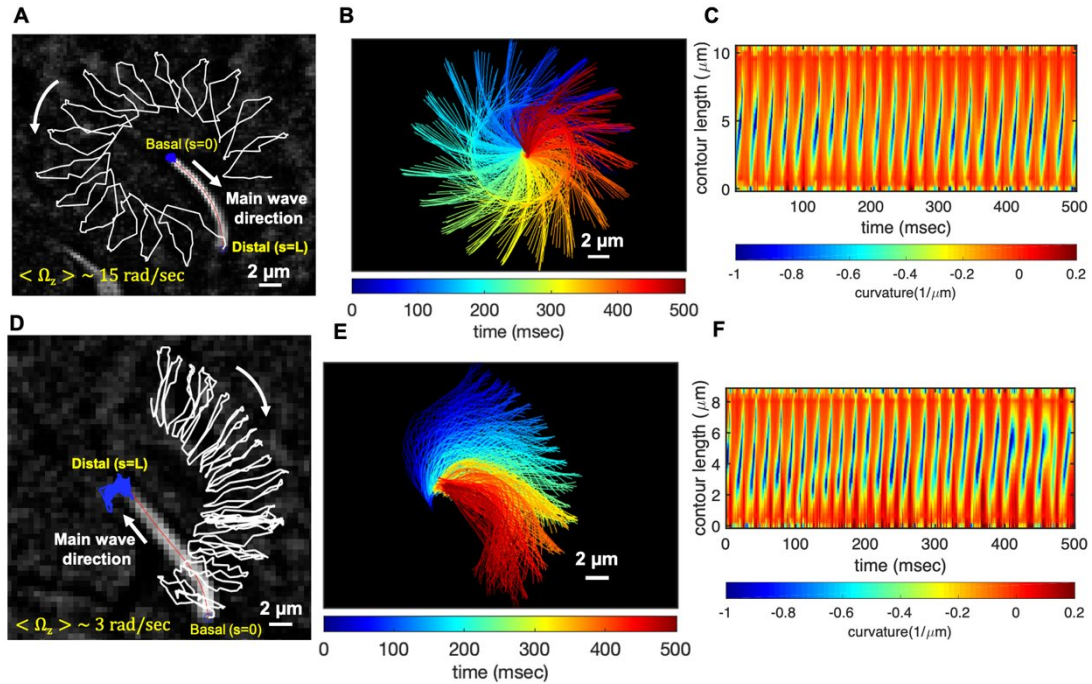


Figure 4.9: Hinged axoneme boundary condition. A-C) A basal-hinged axoneme with the beat frequency of 44.34 ± 0.02 Hz rotates CCW around the pinning point while the bending waves propagate from the basal toward the distal tip. The wavelength is $14.15 \mu\text{m}$, the mean curvature $\kappa_0 = -0.17 \mu\text{m}^{-1}$, $[\text{ATP}] = 200 \mu\text{M}$ and $[\text{Ca}^{2+}] = 0$. In Appendix, Table A.2.3 in blue color shows that the amplitude of the base-to-tip traveling wave (C_1) is around five times larger than the backward tip-to-base traveling wave (C'_1). D-F) A distal-hinged axoneme with $f_0 = 55.65 \pm 0.05$ Hz rotates CW around the pinning point (Figure 4.). The parameters are: $\kappa_0 = -0.19 \mu\text{m}^{-1}$, $[\text{ATP}] = 1 \text{ mM}$ and $[\text{Ca}^{2+}] = 0$. In this case, (C_1) is almost six times larger than (C'_1), which is comparable to the basal-hinged axoneme; see the value in black color in Appendix, Table A.2.3.

is comparable to the corresponding value for the free axoneme presented in Figure 4.2. The amplitude of the traveling wave components, which are inferred from the PCA analysis, are listed in the Appendix, Table A.2.3, (shapes reconstructed from the PCA analysis are illustrated in Appendix, Figure A.2.18). A comparison of the wave amplitudes shows that the main wave amplitude C_1 is almost 5 times larger than the wave component C'_1 , see also Appendix, Table A.2.4 for wave amplitudes of two other basal-clamped exemplary axonemes. For comparison, we also present a distal hinged axoneme which rotates CW around the hinging point, as shown in Figure 4.9D-F. The hinging of axonemes from the distal tip to the substrate was rarely occurred in our experiments. For this exemplary case, C_1 and C'_1 coefficients extracted from the PCA analysis show that $C_1 \sim 6C'_1$ (Appendix, Table A.2.3, see values in black color), which is comparable with the values obtained for the basal-hinged axoneme in panels A-C.

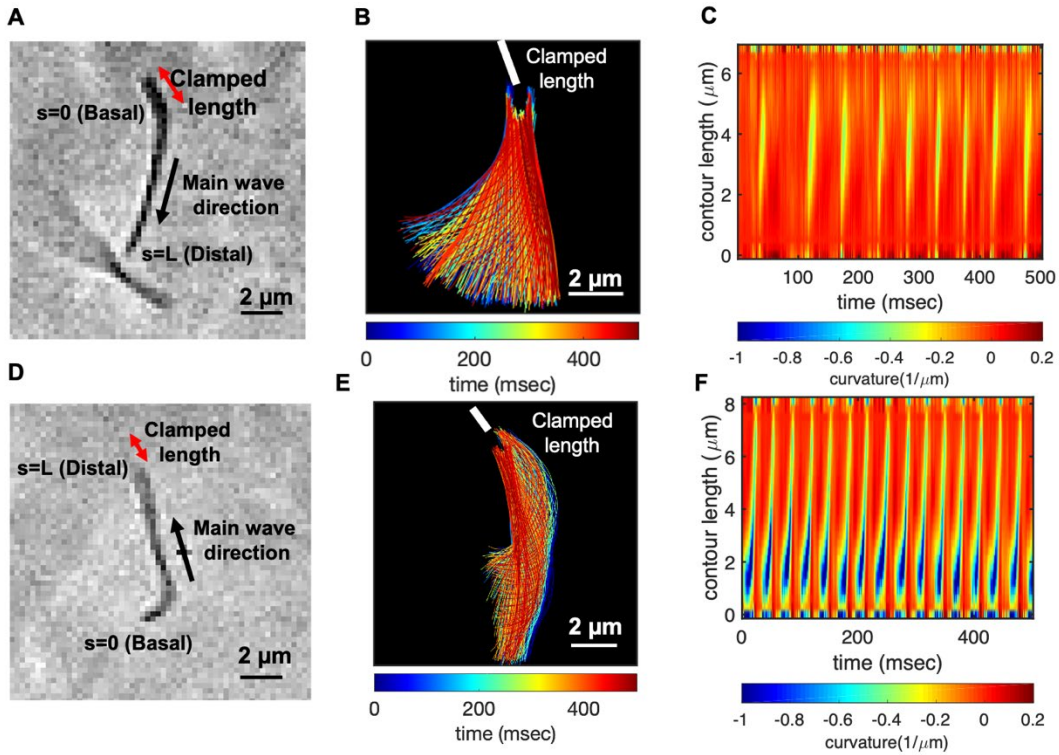


Figure 4.10: Clamped boundary condition. A) A clamped axoneme attached firmly from the basal region to the substrate. B) Time-projection of the axonemal shapes in the time interval of 500 msec. Note that only the oscillating part of the axonemal length ($\sim 7 \mu\text{m}$) is included in this image. The thick white line highlights the position of the surface-attached segment of the axoneme. C) Curvature waves propagating at the frequency of $f_0 = 20.31 \pm 0.29 \text{ Hz}$ from the clamped region toward the distal tip. The mean curvature of axoneme is $\kappa_0 = \sim -0.05 \mu\text{m}^{-1}$. D-F) Similar to the panels A-C with the important difference that the axoneme is clamped from the distal tip. This axoneme has a higher wave amplitude C_1 which is two time larger than C'_1 and it beats at $f_0 = 30.73 \pm 0.06 \text{ Hz}$ with a mean curvature of $\kappa_0 = \sim -0.18 \mu\text{m}^{-1}$. For both experiments $[\text{ATP}] = 80 \mu\text{M}$ and $[\text{Ca}^{2+}] = 0$.

To calculate the mean rotational velocity of a modelled hinged axoneme, we used RFT and the simplified waveform. For detail, see Appendix, A.2.(6). Finally, we present the experimental data of two exemplary non-rotating clamped axonemes where part of the axonemal length, either at the basal or the distal tip, was firmly attached to the substrate. Figure 4.10A-C shows a base-clamped axoneme that beats at the frequency of $f_0 = 20.31 \pm 0.29 \text{ Hz}$ with a reduced intrinsic curvature $\kappa_0 = -0.05 \mu\text{m}^{-1}$ compared to the free and hinged axonemes. The amplitude of the main base-to-tip traveling wave component, extracted from PCA analysis, is also reduced in comparison to the free and the hinged axonemes. Moreover, the amplitude of the backpropagating wave (C'_1) is three times smaller than the main base-to-tip propagating wave component (C_1) (see Appendix, Table A.2.4). Notably, for the case that the axoneme is

clamped from the distal tip, the magnitude of the distal-to-basal back-traveling wave becomes larger ($C_1/C'_1 \sim 2$), indicating a possible wave reflection from the clamped side of the axoneme (see Figure 4.10 D-F and the values in black color of Appendix, Table A.2.5). In intact *C. reinhardtii* cells, the attachment of the flagellum to the cell body is close to a basal-clamped boundary condition, so we repeated our PCA analysis for a flagellum in an intact cell (see Figure 4.1A-B, Appendix, Figure A.2.19). This analysis gives ($C_1/C'_1 \sim 3$), which is comparable to the values mentioned above for the basal-clamped isolated axonemes.

4.2 Discussion

In this work, we have isolated flagella from green algae *C. reinhardtii* using dibucaine and removed the membrane by treatment of detached flagella with non-ionic detergents^{125, 197}. The remaining structure, without membrane and basal bodies, can be reactivated by an ATP-supplemented buffer. Active axonemes show an asymmetric waveform predominantly in 2D which mostly resembles the forward swimming motion of flagella in intact cells^{206, 207}. These asymmetrical beating patterns cause the axoneme to rotate stably around a position in the microscope's field of view. We extracted the shape of axonemes by GVF^{103, 104} and quantitatively described the flagellar beating patterns by dimensionless local curvature $C(s, t)$ at time t and arc-length s along the axonemal length. The results presented in this Chapter, are focused on the examples where axonemes swim effectively in 2D in the vicinity of the substrate. This greatly facilitates the tracking of flagella and the data analysis. However, we also observed examples where the axonemes swim in 3D and undergo tumbling motion. This out of plane swimming dynamics complicates the tracking process of the axonemes. In future studies, 3D microscopy techniques^{102, 208} are necessary to capture the full 3D swimming dynamics of the isolated axonemes.

The static component of the axonemal waveform, defined as the average angle over one beat cycle at each position along the axonemal length, highlights the existence of an intrinsic curvature of axonemes around the value of $\sim -0.2 \mu\text{m}^{-1}$. To bend an axoneme to a circular arc, shear forces along the axonemal centreline generated by asymmetric distribution of dynein motors are required to induce a dynamic instability²⁰⁹⁻²¹². Among different dynein motors, IDAb (inner dynein arm b) is possibly the only dynein which has an asymmetric

distribution, both radially and longitudinally. Bui et al.⁹⁵ have shown that IDAb is absent in the proximal region without being replaced by another dynein, and is predominantly localized at the distal tip with radially asymmetric distribution. The depletion of IDAb from the proximal area might suggest its specific function in bending the axoneme. Future experiments with IDAb mutants are necessary to investigate the possible role of IDAb in inducing an intrinsic curvature in axonemes.

In our experiments with calcium, we observed that among the constituting modes of the flagellar waveform, the static component (C_0) is the most sensitive mode which reduces significantly (~ 10 times) at calcium concentrations above 0.02 mM. The main traveling wave components C_1 is calcium sensitive, especially at high calcium concentration around 1 mM C_1 decreases with a factor of less than two. The reduction of the static mode, triggers a switch from circular to straight swimming path, as previously observed in the refs^{26, 213}. Based on high-resolution structural information obtained by electron cryotomography, Gui et al.⁶⁷ have proposed that RS (radial spoke) heads and CP (central pair) projections interact via electrostatic forces. In this model, an increase in the electrostatic force with decreasing distance as the axoneme bends causes a tilt of the radial spoke. This tilt is the mechanosignal that is transmitted to the IDAs (inner dynein arms), the N-DRC (nexin-dynein regulatory complex) and finally, to the ODAs (outer dynein arms). These electron cryotomography data support the idea that calcium may regulate the transmission of these mechanosignals by inducing a conformational change in calmodulin, which is a calcium responsive protein at the interface between RS1 (radial spoke 1) and IDAa (inner dynein arm a, see Figure 4.1). This conformational change in calmodulin can alter directly the wave pattern by affecting RS1-IDAa interaction. An alternative plausible mechanism is that calcium affects a calmodulin-like subunit (LC4) of the ODAs, and consequently influences the dynein behavior [56]. Further experiments are required to clarify the mechanism of dynein regulation and the precise role of calcium in shaping the flagellar waveform.

The Fourier analysis of PCA modes in the case of free, hinged and clamped axonemes shows that the leading traveling wave component coexists with standing waves at the wavelength of the leading mode and at higher spatial modes. Remarkably, applying the Fourier analysis to flagella of intact *C. reinhardtii* cells yields results (see Appendix, Figure A.2.19 and Table A.2.6)

that are very similar to those presented here. As discussed in the Appendix section the description in terms of a dominant propagation wave superimposed by standing waves does not lead to an immediate biological interpretation and an alternative explanation for the observed wave patterns could be an arc-length dependent amplitude of axonemal bending waves. It would be interesting to see if our analysis leads to qualitatively similar results when applied to numerical solutions of simplified models of cilia.^{210, 214} In these models, the dynein regulation mechanism affects the wave propagation direction: while in curvature-feedback mechanism^{27, 215, 216}, there is an inherent direction in wave propagation which is determined by the coupling between molecular motors and the local axonemal curvature^{102, 217}, in sliding control mechanisms wave direction is not fixed intrinsically, but strongly depends on the boundary condition. This mechanism can be described by considering a model axoneme composed of two polar elastic filaments coupled by passive cross-linkers, and dynein motors exert sliding forces in opposite direction on the two facing filaments, generating an active stress along the long axis of the filament. The unbinding of dynein motors is controlled by the sliding motion between the neighboring MTDs^{102, 217-219}. As the motor activity increases, a Hopf bifurcation leading to sustained oscillations are observed. As mentioned above, the direction of deformation waves depends on the boundary conditions: for hinged filaments, the waves propagate from base-to-tip while for clamped boundary conditions, the waves propagate in the opposite direction. At higher motor activity, a second bifurcation occurs and non-linearities cause a reversal in the direction of wave propagation^{210, 220}. This transition from tip-to-base to base-to-tip wave propagation occurs through a narrow transitional region of intermediate states²²¹. The wave dynamics in the corresponding intermediate regime is reported to be chaotic and is a superposition of standing waves with waves switching quasi-periodically their direction of propagation²²¹. Moreover, the analysis by Camalet et al.^{209, 222} shows that in an internally-driven filament, with a coarse-grained oscillatory force density acting in opposite directions tangentially on two filaments, traveling wave solution can be induced via a dynamic instability. The resulting wave patterns do not depend on the microscopic mechanism of the instability but only of the hydrodynamic forces and the filament rigidity. In this approach, which rests on a coarse-graining of the molecular motors, the direction of wave propagation depends critically on the boundary condition.

We emphasize that, in all these models, the dynein regulation mechanism affects the wave propagation direction: while in sliding-control mechanisms wave direction is not fixed by the equation of motion and strongly depends on the boundary condition, in curvature-feedback mechanism^{27, 215, 216}, there is an inherent direction in wave propagation which is determined by the coupling between molecular motors and the local axonemal curvature^{205, 217}. Lastly, we note that other approximations, such as time-delay variations of the contractile tensions also lead to spontaneous oscillations of the filament^{223, 224}, although a non-linear relation between length variation and tension is needed to keep the wave amplitude finite. For such a non-linear response, the traveling wave can exist only in one direction and a traveling wave solution in both directions is an unstable solution^{223, 224}. In this context, it is interesting to emphasize that the Fourier analysis of the PCA modes of our experimental results shows that the nature of the standing waves is not qualitatively affected by the boundary conditions. To explain this striking difference, one could hypothesise that the discrete structure of the axoneme at the microscopic level, as shown in Figure 4.1C and D, leads to significant deviations at the macroscopic level, especially by changing the boundary conditions at both ends of the cilium. In future studies, it would be an interesting challenge to attribute the formation of these standing waves to the underlying biology and to understand the contribution of different molecular dynein motors in the formation of the standing waves, as well as determine the mechanism of dynein regulation in cilia and flagella.

Chapter 5 Bio-hybrid Micro-swimmers Propelled by Flagella Isolated from *C. reinhardtii*

Chapter 5 is adapted from:

Raheel Ahmad, Albert J Bae, Yu-Jung Su, Samira Goli Pozveh, Alain Pumir, Eberhard Bodenschatz and Azam Gholami, "Bio-hybrid Micro-swimmers Propelled by Flagella Isolated from *C. reinhardtii*", *Soft Matter*, Accepted, 2022.

Raheel Ahmad contributions: Isolation of flagella experiments with calcium and beads, data analysis, discussion and revision.

In this work, we demonstrate the feasibility of using isolated and demembrated flagella from *C. reinhardtii* as a bio-actuator to carry and manoeuvre micron-sized particles. Figure 5.1 demonstrates the existence of two different regimes of propulsion. At low calcium concentration, see Figure 5.1A-B, the micro-swimmer is propelled on a highly curved trajectory. At higher calcium concentration, on the other hand, the bead is propelled along an almost straight path, at a velocity $\sim 20 \mu\text{m}/\text{sec}$, comparable to the velocity of human sperm *in vivo*, see Figure 5.1C-D. The possibility to externally modifying flagellar wave components and beating frequency with light or chemical stimuli (such as calcium ions, as in Figure 5.1B,D)¹⁸³ opens an interesting perspective to control such a bio-hybrid micro-swimmers. The micro-swimmers, propelled by isolated and reactivated flagella, are potentially attractive to develop minimally invasive devices for medical applications, such as *in vivo* active cargo transport^{225, 226}. In this context, understanding the propulsion mechanism as a function of the flagellar beat pattern and flagella-bead attachment geometry appears as an important pre-requisite.

Here, we combine experiments, numerical simulations and analytical approximations to investigate the effect of (i) external calcium ions, (ii) various wave components, (iii) the cargo size and (iv) symmetric versus asymmetric bead-axoneme attachment on the swimming dynamics of a bead that is propelled by an ATP reactivated axoneme. We used calcium ions to reduce the static curvature of axonemes by one order of magnitude, thereby^{26, 227} inducing a

transition from circular to straight swimming trajectories of axonemal-propelled beads (see Figure 5.1). Furthermore, we describe the axonemal waveform as a combination of a static curvature and a traveling wave component and use resistive force theory^{54, 228} to obtain analytical approximations for the translational and rotational velocities of an axonemal-propelled bead in the limit of the small amplitude of curvature waves, and simulated the swimming trajectories. Our analysis reveals a surprising nonmonotonic behavior of the mean translational and rotational velocities of the axonemal-driven bead as a function of the bead radius. Finally, we showed that for a freely swimming axoneme, which rotates predominantly with its static component of the axonemal waveform, sideways bead attachment is sufficient to generate mean rotational velocities comparable to the rotation rates induced by the static curvature.

Note that numerical simulations and analytical approximations were performed by Dr. Azam Gholami (MPI Göttingen) and Dr. Albert J Bae (University of Rochester, USA).

5.1 Results

We fabricated axonemally-based propelled beads, by incubating isolated axonemes from *C. reinhardtii* ($\sim 10 \mu\text{m}$ in length) with beads of diameter $1 \mu\text{m}$, as described in Chapter 2, section 2.7.4. Out of $N = 195$ bead-axoneme attachments, a single bead attaches to the basal end of the axonemes, in 60.5% of the cases. Attachment of beads to the distal tip occurs less frequently in 22.6% of cases, and in even less frequent events (16.9%) we observed more than one bead attached either to the tips or along the axonemal length. The attachment of the beads to the basal or the distal region of the axonemes is either symmetric, i.e. the tangent vector of the axoneme at the bead-axoneme contact point passes through the bead center, or asymmetric. We emphasize that a limitation of our 2D phase-contrast microscopy is that it is not possible to precisely distinguish a symmetric bead attachment from an asymmetric one and 3D microscopy techniques²⁰⁴ are required to fully determine the bead-axoneme attachment geometry. This symmetric versus asymmetric attachment has consequences on the swimming dynamics, as we will in Appendix, section A.2(11).

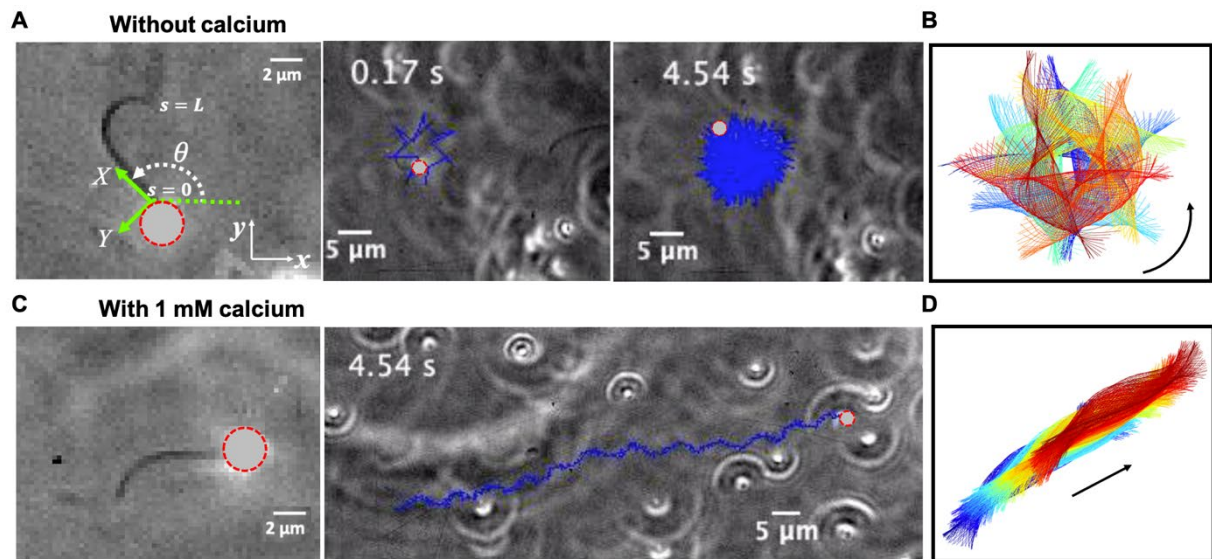


Figure 5.1: Axonemally-driven beads and the effect of calcium ions. A) An exemplary axoneme at $[\text{Ca}^{2+}] = 0 \text{ mM}$ is attached at the basal end ($s = 0$) to a bead of diameter $1 \mu\text{m}$. The blue trajectory of the bead center shows a curved swimming path at two different time points. B) The time-projection of the axonemal shapes highlights the counter-clockwise (CCW) rotation of the axoneme as bending deformations propagate along the contour length. C) In the presence of 1 mM calcium, the bead is propelled on average along a straight path at the propulsion speed of around $20 \mu\text{m}/\text{sec}$, which is comparable to the human sperm propulsion speed in mucus. D) Calcium ions trigger a transition from an 'asymmetric' flagellar waveform that rotates CCW to a 'symmetric' waveform that swims along a straight path. In both experiments, the ATP concentration is $200 \mu\text{M}$.

The propulsion of axonemally-driven beads is highly sensitive to the axonemal waveform. In our experiments, we use calcium ions at different concentrations to change the axonemal waveform and study the propulsion dynamics. In the following subsection, we summarize our results without and with calcium ions and show that calcium ions play a crucial role to achieve a directed cargo transport.

5.1.1 Overview of the results: two modes of propulsion

Returning to Figure 5.1, we recall the existence of two regimes of propagation. While in the first regime, the axonemal-driven bead is propelled on a curved trajectory, in the second regime, the bead is propelled (on average) along a straight path. These two distinct modes of propulsion correspond to two different concentrations of calcium ions in the reactivation buffer (0 mM versus 1 mM), which directly affects the axonemal waveform^{26, 229}. As shown in

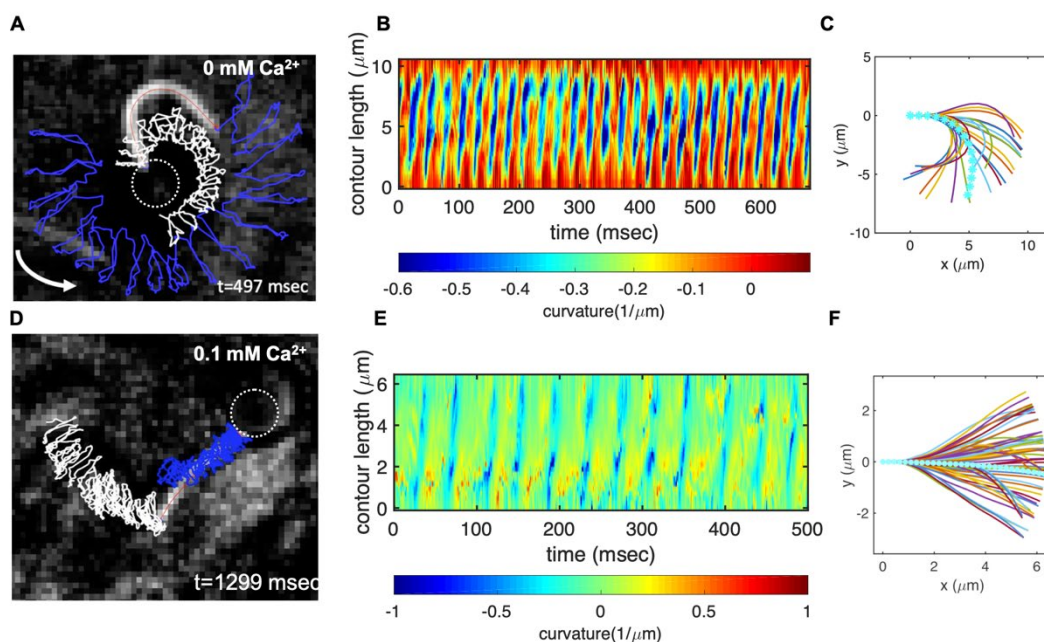


Figure 5.2: Experiments to show the effect of calcium. A) An axonemally-driven bead reactivated at $[\text{ATP}] = 80 \mu\text{M}$ and $[\text{Ca}^{2+}] = 0 \text{ mM}$. Tracked axoneme and trajectories of its distal (blue lines) and basal (white lines) ends. Axoneme-bead swimmer rotates counter-clockwise while the bead center follows a spiral-like path (Figure 5.3B). B) Curvature waves as they travel at the frequency of $38.25 \pm 0.25 \text{ Hz}$ from the proximal region toward the distal tip. C) Mean shape of the axoneme in cyan color averaged over one beat cycle showing a circular arc with static curvature of $\sim -0.19 \mu\text{m}^{-1}$. At different time points, the axoneme is translated and rotated such that the basal end is at $(0,0)$ and the tangent vector at $s = 0$, which defines the X -axis in the swimmer-fixed frame, is along the x -axis of the laboratory-fixed frame (see Figure 5.1A). D) An axonemally-driven bead reactivated at $[\text{ATP}] = 80 \mu\text{M}$. The reactivation buffer is supplemented with 0.1 mM calcium to reduce the static curvature. The axoneme beats at $24.42 \pm 0.18 \text{ Hz}$ and the bead-axoneme attachment appears to be symmetric. F) The axonemal mean shape with static curvature of $\sim -0.03 \mu\text{m}^{-1}$ (filament with cyan color). The mean curvature of axoneme has dropped around ten times in comparison to axonemal shapes in panel C. This reduction in C_0 causes a transition from a circular to a straight swimming trajectory.

Figure 5.2B, in the absence of calcium ions, the time-projection of the 'asymmetric' axonemal shapes indicate a counter-clockwise rotation of the axoneme causing a circular swimming trajectory of the bead. However, in the presence of calcium ions, we observe a significant change in the flagellar waveform (Figure 5.1D) that appears to be 'symmetric' and results in directed bead transport.

Figure 5.2 characterizes in more detail the flagellar waveform of the axonemes in the two regimes observed in Figure 5.1. Figure 5.2C shows a representative example of the first regime, where we have tracked the axoneme over time and quantified the curvature waves that propagate along the axonemal length. These bending waves start from the basal end (at $s = 0$), which is attached to the bead, and propagate at the frequency of $f_0 \sim 38.25 \pm 0.25 \text{ Hz}$

toward the distal tip. Please note that the beat frequency of axonemes depends on the ATP concentration, following Michaelis-Menten kinetics with a linear trend at a low amount of ATP and saturation at higher ATP concentrations around 1 mM (see Chapter 3, Figure 3.5E). An interesting property of these curvature waves is that if we average the flagellar shapes over one beat cycle, we obtain a circular arc with the mean curvature of κ_0 around $-0.19 \mu\text{m}^{-1}$ (see the cyan filament in Figure 5.2C). The negative sign of κ_0 indicates a clockwise bend when moving from the basal end at $s = 0$ toward the distal tip at $s = L$. In other words, we can think of the axonemal waveform as a superposition of a traveling wave component which propagates along this circular arc, causing a counter-clockwise rotation of the axoneme and the cargo (Figure 5.1A-B). However, as shown in Figure 5.3, the mean curvature of axonemes κ_0 is highly sensitive to the concentration of calcium ions and almost vanishes above a calcium concentration of 0.1 mM. This mean axonemal curvature appears to be linearly related to the curvature of the path of the bead, as shown in Figure 5.3B. The proportionality factor is estimated to be around $2^{41, 205}$.

Figure 5.2D-F illustrates how the axonemes beat at higher calcium concentration (0.1 mM). In this case, the axonemal waveform is composed of a propagating wave that travels along an almost straight filament, thereby propelling the axoneme and the cargo along a straight path. This reduction in κ_0 decreases the rotational velocity of the axoneme compared to the experiment presented in Figure 5.2A in the absence of calcium ions. As we will show in our analytical analysis, see Appendix A.2(11), up to the leading order, $\langle \Omega_z \rangle$ scales linearly with the dimensionless mean curvature $C_0 = \kappa_0 L / 2\pi$. At such low values of the mean curvature of the axoneme, we achieve directional cargo transport with a mean velocity of about $20 \mu\text{m}/\text{sec}$ (Figure 5.1C), which is slightly slower than the migration speed of the human sperm in mucus (typically $25\text{-}45 \mu\text{m}/\text{sec}$)²³⁰.

Furthermore, we note that in most of our experiments without calcium, the axonemes rotate counter-clockwise in the microscope's field of view with an effective 2D beat pattern, facilitating the tracking procedure. This motion is characterized by a circular swimming trajectory and a translation in the laboratory frame of reference. The combination of rotation and translation results in a spiral-like swimming path of the axoneme and the bead

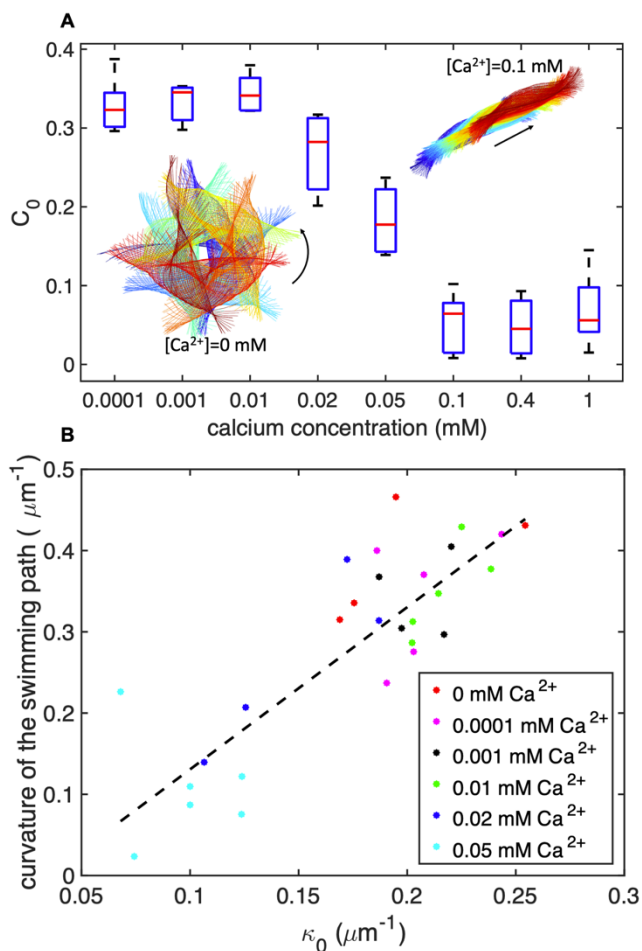


Figure 5.3: A) The dimensionless mean curvature of axonemes defined as $C_0 = \kappa_0 L / 2\pi$ drops almost ten times at $[Ca^{2+}]$ around 0.01 mM. This reduction in C_0 causes a transition in C_0 from a circular to a straight swimming trajectory. The time-projection of experimental shapes of two exemplary axonemes at 0 mM and 0.1 mM $[Ca^{2+}]$ are also shown to illustrate the transition in the swimming path. At each calcium concentration, $N=5$ axonemes (without any bead attached) are tracked to obtain C_0 and the corresponding median and standard deviation. B) The curvature of the swimming path of the axonemes in panel A, plotted versus the mean curvature κ_0 . The slope of the linear least-square fit is around 2.

(see Figure 5.4). Note that for the exemplary experiment in Figure 5.2A, the $x - y$ positions of the bead center exhibit tiny oscillations at the fast beat frequency of $f_0 = 38.25$ Hz and a secondary slow global rotational frequency around 1.5 Hz (see Figure 5.4B). As the axoneme undergoes planar shape deformations over time, at any instant of time, it may be considered as a solid body with translational and rotational velocities U_x , U_y and Ω_z which we measure in the swimmer-fixed frame (Appendix, Figure A.2.22)²⁰⁵. These velocities oscillate in time,

reflecting the fundamental beat frequency of the axoneme shown in Figure 5.2A (~ 38.21 Hz) and its higher harmonics. In contrast, in our experiments with calcium, axonemal movement often occurs in 3D, making tracking of axoneme nearly impossible. Finally, we also performed

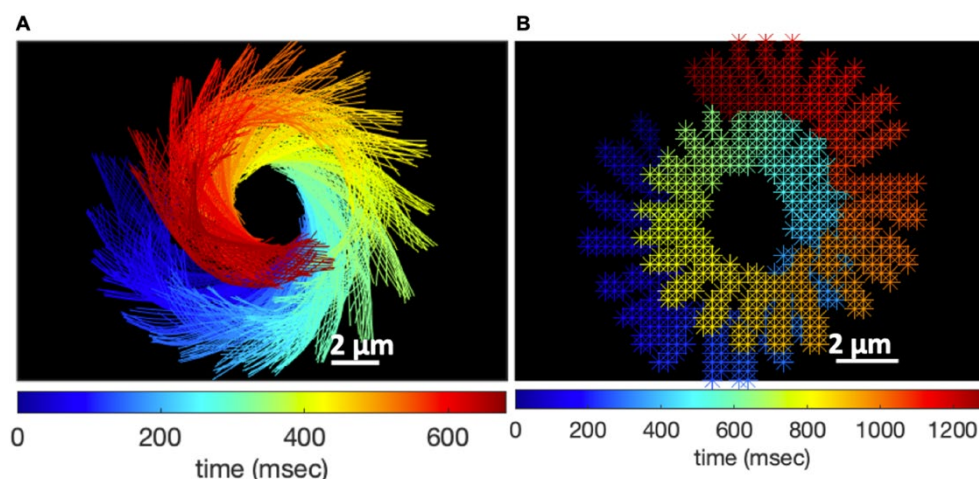


Figure 5.4: A) Color-coded time projection of the axonemal shapes of the axoneme presented in Figure 5.2A. B) Color-coded trajectory of the bead center from Figure 5.2A showing a spiral-like trajectory. The global rotational frequency of the swimmer is around 1.5 Hz (~ 1 full rotation in around 650 msec).

Table 5.1: Frequencies and intrinsic curvature values of 12 different axonemes propelling beads of diameters $D=1, 2$ and $3 \mu\text{m}$. Mean and standard deviations are also presented. All axonemes are reactivated at $[\text{ATP}]=200 \mu\text{M}$.

Axoneme	1	2	3	4	1	2	3	4	1	2	3	4
$D (\mu\text{m})$	1	1	1	1	2	2	2	2	3	3	3	3
f_0 (Hz)	48.50	43.55	53.46	48.5	33.65	38.60	61.15	63.36	46.06	43.55	58.41	23.75
$\langle f_0 \rangle \pm \text{std}$	48.50 ± 4.0				49.19 ± 15.25				42.94 ± 14.35			
$\kappa_0 (\mu\text{m}^{-1})$	0.21	0.22	0.26	0.20	0.25	0.17	0.17	0.19	0.15	0.16	0.15	0.19
$\langle \kappa_0 \rangle \pm \text{std}$	0.22 ± 0.03				0.19 ± 0.04				0.16 ± 0.02			

experiments with larger diameter beads to explore how bead size affects beating frequency and mean curvature of the axonemes. A summary of the beat frequency and intrinsic curvature of axonemes (all reactivated at $[\text{ATP}] = 200 \mu\text{M}$ and $[\text{Ca}^{2+}] = 0 \text{mM}$) propelling beads of diameter 2 and 3 microns are given in Table 5.1. In these experiments, as we increased the bead diameter from $1 \mu\text{m}$ to $3 \mu\text{m}$, we observed a reduction in both the averaged beat frequency ($\sim 12\%$) and the intrinsic curvature ($\sim 31\%$) of the axonemes.

5.1.1.1 Description of the flagellar shapes

Having described the two modes of propulsion with and without calcium, we now focus on the principal component analysis (PCA) of the flagellar waveform as described in Chapter 2, section 2.9. In our flagella-driven beads, the propulsive force and torque exerted on the bead depends on the axonemal waveform. Using the x and y coordinates of the tracked flagellum (see Chapter 2, section 2.8), we calculate $\theta(s, t)$ which is defined as the angle between the local tangent vector of the centerline of the tracked flagellum and the x -axis (see Figure 5.1A). We then average the axonemal shapes over one beat cycle to obtain the mean shape of the axoneme, which corresponds to the arc-shaped filament colored in cyan in Figure 5.2C. Figure 5.5A shows the color map of the covariance matrix of the axoneme shown in Figure 5.2A, which has an effective reduced dimensionality with a small number of non-zero eigenvalues. We note that four eigenmodes $M_n(s)$ ($n = 1, \dots, 4$) corresponding to the first four largest eigenvalues of $\theta_{cov}(s, s')$ capture the axonemal shapes with very high accuracy. These four eigenvectors are plotted in Figure 5.2B. We reconstruct the axonemal shapes using the four dominant modes and the corresponding time-dependent motion amplitudes $a_n(t)$ ($n = 1, \dots, 4$) using Eq. 2.19 (see Chapter 2, section 2.9). The reconstructed shapes are presented in Figure 5.2C, where the green dashed lines show the experimental data. The contribution of different modes in reconstructing the axonemal shapes is shown in Appendix, Figure A.2.23. Please note that higher spatial modes in combination with the corresponding time-dependent motion amplitudes, i.e. $a_2(t)M_2(s)$, $a_3(t)M_3(s)$ and $a_4(t)M_4(s)$, are approximately standing waves. The motion amplitudes $a_1(t)$ and $a_2(t)$, which oscillate at the axonemal beat frequency f_0 , are shown in Figure 5.2D; see also Appendix, Figure A.2.24 for a plot of motion amplitudes $a_1(t)$ to $a_4(t)$ versus each other.

5.1.2 Analytical approximations of rotational and translational velocities of an axonemal-propelled bead

In this section, we discuss analytical approximations for the mean translational and rotational velocities of a flagellar-propelled bead in the regime of small wave amplitude. For detail, see Appendix A.2(11).

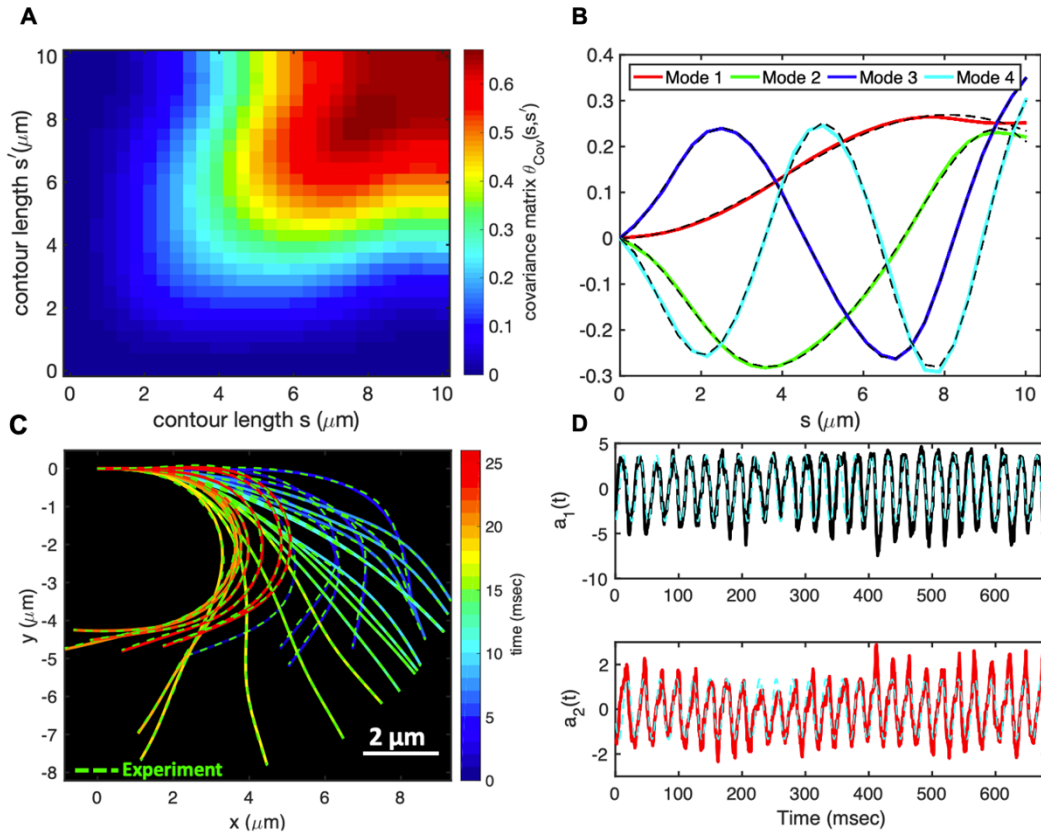


Figure 5.5: PCA analysis of the axoneme presented in Figure 5.1. A) The covariance matrix $\theta_{Cov}(s, s')$ of fluctuations in angle $\theta(s, t)$. B) The four eigenvectors corresponding to the first four largest eigenvalues of $\theta_{Cov}(s, s')$. C) The time-projection of the experimental data and the corresponding shapes reconstructed using the four eigenmodes presented in panel B. D) The time-dependent motion amplitudes $a_1(t)$ and $a_2(t)$ as defined in Chapter 2, sec 2.9. The black and cyan dashed lines in panel B and D show the Fourier fits.

5.1.3 Analysis with the experimental waveform

To confirm that anomalous propulsion regime and the rotation induced by asymmetric cargo attachment are general and not limited to the simplified waveform introduced in Appendix Eq. A.2.62, we also used the experimental beat patterns of the exemplary axoneme in Figure 5.2A. We performed RFT simulations to compute the mean translational and rotational velocities of an axonemal-propelled bead using the experimental waveform as an input for both asymmetric and symmetric bead-axoneme attachment. As shown in Figure 5.6, the anomalous propulsion regime exists for both symmetric and asymmetric attachments.

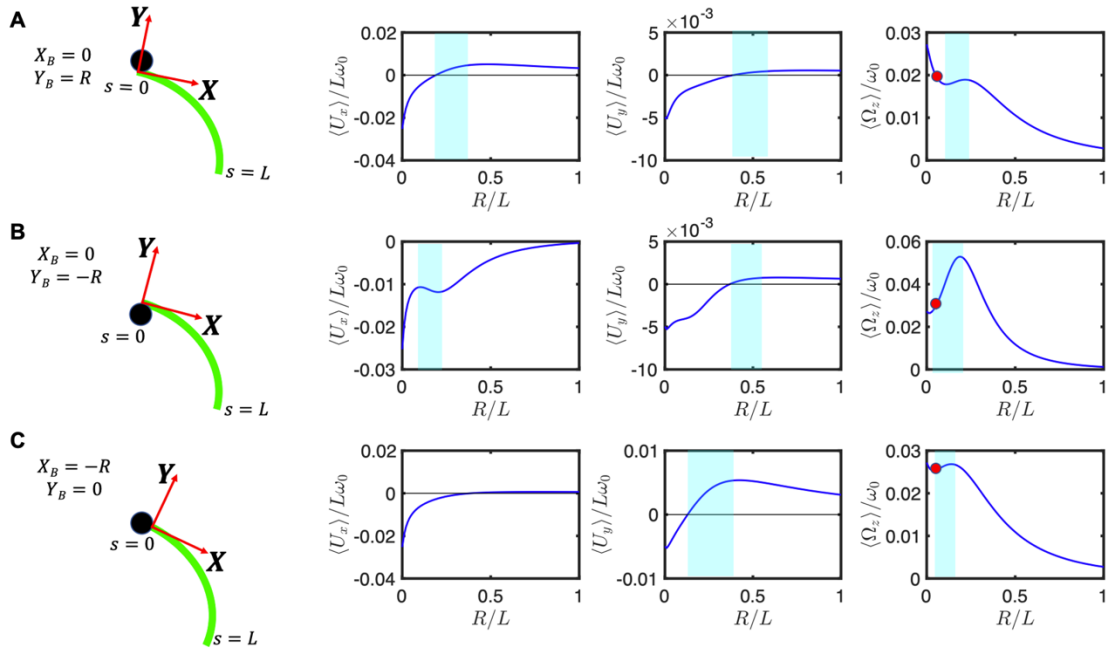


Figure 5.6: Experimental beat pattern in Figure 5.2A are used to calculate translational and rotational velocities of an axonemal-propelled bead attached. A) Asymmetrically at $Y_B = R$, $X_B = 0$. B) Asymmetrically at $Y_B = -R$, $X_B = 0$. C) Symmetrically at $Y_B = 0$, $X_B = -R$. Anomalous propulsion regimes are highlighted in cyan color. Red circles mark the experimental bead size of $R/L \sim 0.05$ and the corresponding rotational velocities. Note that the trend observed in panel C is consistent with the trend predicted by our analytical calculations with a simplified waveform for a symmetric bead-axoneme as shown in Appendix, Figure A.2.12.

Depending on the sign of the static curvature of the axoneme C_0 and the position at which the bead is attached, the asymmetric attachment may contribute to an increase or decrease in the overall mean rotational velocities. For the axoneme in Figure 5.6, C_0 is negative and the sideways bead attachment at $Y_B = R$ (Figure 5.6A) acts against the rotation induced by the intrinsic curvature C_0 . The opposite happens in Figure 5.6B where the bead attachment at $Y_B = -R$ amplifies the rotational velocity of the axoneme. We also note that the anomalous propulsion regime is more pronounced in panel B where the bead is attached sideways at $Y_B = -R$. Note that for the symmetric bead-axoneme attachment, the general trend shown in Figure 5.6C is consistent with our analytical approximations presented in Appendix, Figure A.2.11. An experimental confirmation of our theory is provided by the explicit comparison between the measured rotational velocity, $\langle \Omega_z \rangle / \omega_0$, with the predictions using RFT theory. To this end, we have indicated by a red circle in the right most panels of Figure 5.6A- C the measured values as a function of the bead size used, $R = 0.5 \mu\text{m}$ (so the ratio $R/L \sim 0.05$).

The value of $\langle \Omega_z \rangle / \omega_0 = 0.026$, reported in Figure 5.6C, was documented in Appendix, Figure A.2.22C (see the red line). In this case, the axoneme, as shown in Figure 5.4A, globally rotates around 2π in the time interval of ~ 650 msec, which with $f_0 = 38.21$ Hz, results to $\langle \Omega_z \rangle / \omega_0 = 0.04$. This value is closest to the value of 0.029 in panel B with an asymmetric bead-axoneme attachment. Overall, we observe a good agreement between the predicted and the experimentally measured values of $\langle \Omega_z \rangle / \omega_0$.

We also considered the beat pattern from our experiments at higher calcium concentration, corresponding to Figure 5.2D, to study the propulsion of a model bead at different radii with symmetric versus asymmetric bead-axoneme attachment. Figure 5.7 also shows the existence of anomalous propulsion regimes as highlighted by the bands in cyan color in the three graphs on the right.

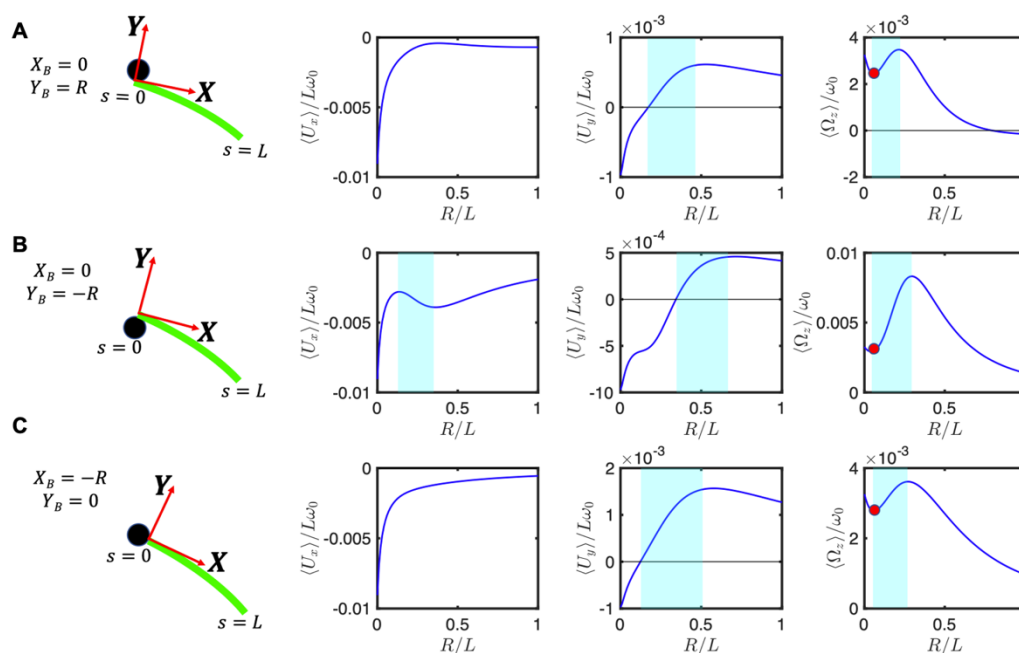


Figure 5.7: Experimental beat pattern shown in Figure 5.2D with 0.1 mM $[\text{Ca}^{2+}]$ and $[\text{ATP}] = 80 \mu\text{M}$ are used to calculate the mean translational and rotational velocities of an axonemal-driven bead attached. A) Asymmetrically at $Y_B = R, X_B = 0$. B) Asymmetrically at $Y_B = -R, X_B = 0$. C) Symmetrically at $Y_B = 0, X_B = -R$. Anomalous propulsion regimes are highlighted in cyan color. Red circles mark the experimental bead radius of $R/L \sim 0.05$ and the corresponding values of $\langle \Omega_z \rangle / \omega_0$. Note that the general trend in panel C is consistent with the analytical analysis presented in Appendix, Figure A.2.12 for a symmetric bead attachment.

The experimental value of $\langle \Omega_z \rangle / \omega_0 = 0.004$ (total rotation of $\pi/4$ in 1299 msec) is slightly larger than the values 0.0024, 0.0029 and 0.0028 in panels A-C, respectively, which are highlighted by the red circles in Figure 5.7A-C. Finally, comparing Figure 5.7 and 5.6 shows that, as expected, the dependence of the mean translational and rotational velocities on the bead size is highly sensitive to the flagellar waveform.

5.2 Conclusions

In this work, we have characterized the motion of a bead (a cargo) propelled by an ATP-reactivated axoneme isolated from the green algae *C. reinhardtii*. We observed two distinct regimes of bead propulsion depending on the calcium concentration. The first regime describes the bead motion along a curved trajectory which is observed in experiments at zero or very small concentration of calcium ions (less than 0.02 mM). A directed bead propulsion along straight trajectories occurs at higher calcium concentrations where the cargo is propelled at an averaged velocity of around 20 $\mu\text{m}/\text{sec}$. This is comparable to the typical human sperm migration speed in mucus²³⁰. High-resolution structural information obtained by electron cryotomography⁶⁷, strongly supports the idea that calcium could regulate the transmission of mechanosignals. Gui et al.⁶⁷ have shown the presence of calmodulin, a calcium responsive protein, at the interface between RS1 (radial spoke 1) and IDAa (inner dynein arm a). Calcium may induce a conformational change in calmodulin, which may directly alter the wave pattern by affecting RS1-IDAa interaction. An alternative plausible mechanism is that calcium affects a calmodulin-like subunit (LC4) of the outer dynein arm (ODA) and consequently, influence the dynein behavior⁶⁷. Further experiments are required to clarify the mechanism of dynein regulation and the precise role of calcium in shaping the flagellar waveform. Since the beads in our experiments were incubated with demembrated axonemes, the quantity, spacing and location of beads attached to the axonemes were not controlled. Normally, a small fraction of the beads (less than 10%) adheres to the axonemes at random sites preferably at the basal or the distal ends.

The axonemes beat with an asymmetric waveform, which resembles the forward swimming motion of flagella in intact cells²⁰⁷. We extracted the axonemal shapes using GVF technique^{103, 104} (see Appendix, Figure A.2.20) and quantitatively described the beating patterns by the

dimensionless curvature $C(s, t)$ at time t and at arc-length s along the axonemal length. Our PCA analysis shows that the axonemal motion is described with a high degree of accuracy, taking into account only the first four dominant eigenmodes corresponding to the first four largest eigenvalues. In this work, we are focusing on the examples where an axoneme-bead swimmer swims effectively in 2D in the vicinity of the substrate. This greatly facilitates the tracking of axonemes and data analysis. However, we also observed examples where the axoneme-bead swimmer undergoes a tumbling motion in 3D. This out of plane swimming dynamics complicates the tracking process of the axonemes. In future studies, 3D microscopy techniques²⁰⁴ are necessary to capture the full 3D swimming dynamics of the isolated axonemes.

We used a simplified waveform to describe the axonemal shapes which is composed of a traveling wave component propagating along a circular arc (Appendix, Eq.A.2.62). This simplified waveform allows us to obtain analytical expressions for translational and rotational velocities of an axonemal-propelled bead in the limit of small amplitudes of curvature waves. The rotational velocity of an axoneme is predominately controlled by its static curvature C_0 . Remarkably, our analysis with the simplified waveform predicts an anomalous propulsion regime where the rotational and/or some of the translational velocity components of an axonemal-propelled bead increase with the bead radius (Appendix, Figure A.2.11). We also used the experimental beat patterns to demonstrate that this counter-intuitive regime is not limited to the simplified waveform and also exists for waveforms closer to the experimental ones. This anomalous propulsion regime has also been predicted for a model sperm-like swimmer which has a zero mean curvature, and is propelled by a traveling wave motion, as illustrated by Appendix, Figure A.2.12F. Consistent with this, we also observed anomalous regimes in our experiments with an increased calcium concentration (0.1 mM instead of 0 mM), which result in a significant reduction (approximately 10 times) in the mean curvature of the axonemes, see Figure 5.3.

An anomalous cargo transport regime was also predicted in biofilm forming bacteria *Pseudomonas aeruginosa* (PA14)^{231, 232}, where swimming is driven by multiple (on average two) rotating helical flagella (length $\sim 4 \mu\text{m}$) that can bundle to propel the bacterium in a corkscrew-like motion or unbundle to change direction, exhibiting a run-and-tumble swimming pattern²³³.

This anomalous behavior is expected to exist for a hypothetical mutant of PA14 which has a larger (around three times) bacteria size in comparison to the wild type. This up-scaling of bacteria size results in a larger rotational drag coefficient of flagella than bacterial body, which in the ref²³¹ is found to be the criteria for the anomalous propulsion. Whether such a hypothetical largescale bacterium exists is an open question. However, this anomalous propulsion regime could be important in bacterial swimming in polymeric solutions, where due to steric interactions between flagella and polymers, the rotational drag coefficient of the flagella can become larger than the bacterial body, fulfilling the criteria for anomalous propulsion. Thus, as experimentally observed and contrary to our expectations, the swimming speed of bacteria in the polymeric solutions can increase^{234, 235}. In our system, however, we are not able to obtain a simple analytical criterion for the anomalous propulsion as it results from the full calculations which include inverting the 3X3 drag matrix of the bead axoneme swimmer. From a general physics perspective, we remark that the anomalous regime corresponds to a change in the partitioning between translation (in the two physical directions) and rotation as R increases, so that some components may increase with R over a range while other components decrease, as dictated by the overall increase in the drag of the bead.

Finally, our analysis shows that asymmetric cargo-axoneme attachment contributes at the same order of magnitude as the mean curvature to the rotational velocity. In other words, a sperm like beating flagellum without mean curvature and second harmonic swims in a curved trajectory if it is attached sideways to a cargo. In our experiments, since we image the sample in 2D, we are not able to precisely distinguish symmetric versus asymmetric bead-axoneme attachments. In a 2D-projected image, a symmetric bead-axoneme attachment could in reality be an asymmetric one. Moreover, as the bead-axoneme swimmer goes slightly out of focus, the attachment in some frames seems to be symmetric and in other frames asymmetric. The 3D microscopy techniques, similar to the one used in the ref²⁰⁴ are necessary to fully characterize symmetric versus asymmetric axoneme-bead attachment in 3D. This 3D characterization is absolutely essential to experimentally prove the anomalous behavior predicted by our analysis with a simplified waveform as well as with the experimental beat patterns. Although we have performed a few experiments using beads of diameters of 1, 2 and 3 μm (see Table 5.1), we are unable to verify the validity of the predicted anomalous trend

because our 2D microscopy does not allow us to distinguish between symmetric and asymmetric bead-axoneme attachment. Future experiments with a multi-plane phase contrast microscope²⁰⁴ is a promising step to resolve the full 3D geometry.

The design and fabrication of synthetic micro-swimmers is a challenging task in the growing field of smart drug delivery, and has recently become a multidisciplinary effort involving physicists, biologists, chemists and materials scientists. Flagella isolated from biological micro-organisms show a variety of waveforms and are promising candidates to provide a reliable power source for motility by an effective conversion of chemical energy from ATP hydrolysis into mechanical work. The *C. reinhardtii* flagellar-propelled micro-swimmers investigated here have the unique advantage that the beat frequency can be controlled via illumination, as we have described in our previous work²³⁶ and chemical stimuli (e.g. calcium ions) can be used to trigger a transition from a circular to a straight swimming trajectories^{227, 229}. They also serve as an ideal model-swimmer to investigate both experimentally and theoretically the contribution of different wave components in cargo propulsion dynamics. Our theoretical analysis as well as numerical simulations reveal the existence of an anomalous cargo transport regime, where contrary to expectation, the flagellar-propelled cargo swims faster as we increase the cargo size. This counter-intuitive behavior may play a crucial role in the design of future artificial flagellar-based propulsion systems. Finally, our analysis also highlights the contribution of the asymmetric cargo-flagellum attachment in the rotational velocity of the micro-swimmer. This turning mechanism should be also taken into account in manufacturing bio-inspired synthetic swimmers where a directional targeted motion is critical for delivery of drug-loaded cargoes.

Chapter 6 Conclusions and Outlook

This final chapter concludes the work of this dissertation and broadens the results of assembling biological and non-biological components in context to control the motility of *C. reinhardtii* isolated axonemes, and the construction of an artificial cell and a bio-hybrid micro-swimmer.

First, a light-driven ATP regeneration system was built in collaboration with the research groups of Dr. Tanja Vidaković-Koch and Prof. Kai Sundmacher (MPI Magdeburg). The artificial ATP regeneration system consisted of three main building blocks: Bacteriorhodopsin (a proton pump), EF_oF_1 -ATP synthase (ADP-to-ATP conversion unit), and a lipid vesicle. As a first step, the functional activity of bR was confirmed by reconstitution into liposomes and encapsulation of pH-sensitive dye (pyranine). The driving force (called the electrochemical potential gradient) for ATP synthesis involves both the proton gradient ΔpH and the potential gradient $\Delta\psi$. Therefore, the next step was to demonstrate that both gradients are required as driving forces for ATP synthesis by measuring the kinetics of ATP synthase in an acid-base transition experiment with valinomycin. After confirming the functionality of both transmembrane proteins, we performed a coreconstitution of ATP synthase and bR into lipid vesicles. In our system, we determined a higher ATP synthesis rate ($4.5 \mu M \text{ ATP (mg ATP synthase)}^{-1} \text{ min}^{-1}$) as compared to the literature^{135, 136, 138, 140} which we explained on the following basis, (i) 1 ATP synthase and 96 bR molecules per liposome, (ii) bR was used in the form of patches that oriented more efficiently in liposomes than the solubilized form, (iii) the method of liposomes preparation also contributed to the reconstitution efficiency¹³⁴, (iv) the effect of DTT in energizing the liposomes and (v) the higher amount of ADP in the system. The functional module was preshined with two light sources at different time points. This showed that higher light intensity increased the activity of the light-driven ATP module (5W microscope light and 50W LED lamp generated $213 \mu M$ and $313 \mu M$, respectively). However, imaging of the

axoneme was performed in the microscope integrated with a 5W light source, so further ATP measurements were performed under the microscope light. We observed that illumination with the microscope light for 1 min produced 1 μM ATP, which was found sufficient to reactivate axonemes at a beat frequency of around 22 Hz. This is in contrast to our experiments with pure commercial ATP, in which the minimum critical ATP concentration to reactivate axonemes was 60 μM ¹³⁰. We explained this discrepancy as follows: (I) ATP inhibitory activity verified in a simple metabolic reaction: Hexokinase convert glucose (G) to glucose-6-phosphate (G-6-P) using 1 ATP molecule. From this experiment, it was concluded that ATP production rate is 18% higher than the control experiment. (II) Attachment of functionalized vesicles to demembrated axonemes can lead to higher ATP concentrations around the axonemes. We used dye-labeled photosynthetic vesicles to monitor the attachment of vesicles, however, we observed the attachment of vesicles to some parts of axonemes along their entire length, but not the accumulation. (III) The presence of ADP in our system. According to literature, ADP plays a critical role in axonemal motility^{1, 179, 190}. In addition, there is evidence that ADP can occupy the non-catalytic sites in the dynein motor. We tested different concentrations of ATP with fixed ADP (1.6 mM) and found that axonemes started to beat at 0.1 μM ATP with 1.6 mM ADP, which we explained on the basis of binding of ADP to non-catalytic sites of dynein^{1, 179}. We observed that the mean flagellar velocity was lower in the absence of ADP. Moreover, in the presence of ADP, the mean velocity reaches its steady-state value faster than in the absence of ADP, suggesting that ADP increases the binding affinity of dynein to the MTs and the efficiency of energy transduction. Therefore, in the presence of ADP binding to a non-catalytic site, dynein is more efficient in generating the sliding force. However, it is questionable whether ADP can occupy one or more sites. Further studies will help to understand this mechanism at the nanoscale.

To create a cell-like compartment, we encapsulated MTs/kinesin-1 with a light-driven ATP module using droplet microfluidics. Light-to-ATP production drives kinesin-1 motility, generates active stresses and contracts MTs networks. In addition, energy production, consumption and regeneration cycling were studied in a millifluidic device in which MTs/kinesin-1 were enclosed with a preshined ATP functional module and a specific area was illuminated with a discontinuous microscope light to replenish the depleted ATP. This showed

that the proposed strategy has the potential for on-demand ATP regeneration with optical stimulus.

On the one hand, this artificial ATP regeneration system opens a new horizon for controlling motility in an optically controllable manner, but on the other hand, it is not very feasible for setting up an *in vitro* motility assay because a larger amount of ATP is needed to start the reaction. As in our system, for the contraction of the MTs/kinesin network, we need to pre-illuminate the ATP module for 45 minutes before encapsulation. In contrast, the enzymatic ATP production system^{41, 237}, creatine kinase and phosphocreatine, is capable of synthesizing a larger amount of ATP, but has limited application when on-demand ATP synthesis is required. Further studies will lead to more insights if we can improve the ATP production rate and develop an *in vitro* motility assay that does not require pre-illumination

Next, we analyzed the waveform of the axoneme generated by the interaction of active motor forces. To do this, we tracked the axoneme using the GVF technique^{103, 104}, and quantitatively described the beat patterns by the dimensionless curvature $C(s, t)$ at time t and the arc length s along the axonemal length. Our PCA analysis showed that axoneme motion can be reconstructed with a high degree of accuracy by taking into account the first four dominant eigenmodes and the corresponding eigenvalues. Our analysis suggests that the wave motion can alternatively be described with Fourier modes whose wavelength λ is larger than the length of the filament L ($\lambda/L \approx 1.3$). Axonemes can have both an asymmetric (curved swimming pathway) and a symmetric (straight swimming) pathway, which depends on the chemical stimuli (calcium concentration). In the absence of calcium, the axoneme showed an asymmetric waveform consisting of the superposition of the static component (C_0), a dynamic wave component moving from the base to the tip (C_1), and higher harmonics. In contrast, we performed reactivation experiments with different calcium concentrations, from 10^{-4} mM to 1 mM. We found that at calcium concentrations above 0.03 mM, the axoneme exhibited a symmetrical waveform, triggered a transition from curved to straight swimming, and its static mode (C_0), was reduced by 85% (see Chapter 4). This calcium-triggered mechanism allowed us to build a bio-hybrid micro-swimmer, by attaching synthetic micron-sized cargo to axonemes, that consume ATP to propel the cargo along straight trajectories. Our experiments

showed that by increasing the cargo diameter from 1 μm to 3 μm , the average beat frequency and the intrinsic curvature of axonemes decreased to ($\sim 12\%$) and ($\sim 31\%$), respectively.

Our theoretical analysis as well as numerical simulations show that there is an anomalous cargo transport regime in which the velocity of the axoneme-driven bead increases with increasing bead size (theoretical and numerical analysis were performed by Dr Azam Gholami (MPI Göttingen) and Dr Albert J Bae (University of Rochester, USA)), which was also confirmed by experimental beat patterns. In addition, our analysis has also revealed the asymmetric attachment of the cargo to the axonemes contributed to the rotational velocity of the micro-swimmer (see Chapter 5).

In summary, scientists in the field of biomedical research have introduced various sophisticated micro-swimmers, such as artificial bacterial flagella²³⁸ and hydrogel-based microrobots²³⁹, for which there are already many fascinating examples in cargo transport for drug delivery, micro-surgery and imaging.²⁴⁰ In this context, micro/nanomotors have been gaining attention specifically for on-demand transportation of cargo. The design strategy depends on the propulsion mechanisms and external stimuli, such as light, electric, magnetic, acoustic and ultrasonic drives.^{240, 241} In addition, *C. reinhardtii* has recently been used as a micro-swimmer for the transport of nanoparticles loaded with chemotherapeutic agents (doxorubicin) for the treatment of breast cancer.²⁴²

In this line of study, we have successfully integrated the ATP functional module to control the motility of axonemes in an optically controllable manner and demonstrated the feasibility of constructing axonemally-driven micro-swimmers for directional cargo transport. Therefore, the study presented here has the potential to open up the possibility of designing and manufacturing more efficient synthetic micro-robots for on-demand targeted drug delivery by attaching the drug-loaded cargo to axonemes through affinity interaction and integrating it with the ATP functional module that provides on-demand energy to the micro-swimmers.

Appendix

A. 1 Buffer, Media and Solutions

Table A. 1: Composition of LB culture media for *E.coli* cell cultivation.

Trypton	10 g/L
Yeast extract	5 g/L
NaCl	5g/L
pH	7.4, adjusted with NaOH

Table A. 2: Composition of French press buffer for EF₀F₁ isolation.

Tris-HCl, pH 7.77	200 mM
KCl	100 mM
MgCl ₂	5 mM
EDTA	0.1 mM
Glycerol	2.5 %

Table A. 3 : Composition of extraction buffer for EF₀F₁ purification.

Tris-HCl, pH 7.5	50 mM
KCl	100 mM
Sucrose	250 mM
MgCl ₂	5 mM
ε-aminocaproic acid	40 mM
p-amino benzamidine	15 mM
EDTA	0.1 mM
DTT	0.2 mM

Phosphatidylcholine	0.8 %
Octyl glucoside	1.5 %
Sodium cholate	0.5 %
Glycerol	2.5 %
Imidazole	30 mM

Table A. 4: Composition of gel sample buffer for SDS-PAGE.

Tris-HCl, pH 7.5	100 mM
SDS	10 %
DTT	5 mM
Glycerin	50 %
Bisphenol B (BPB)	0.2 %

Table A. 5: Composition of staining solution.

Ethanol	25 %
Acetic acid	10 %
Coomassie Blue R250	0.1 %

Table A. 6 Composition of decolorizing solution for SDS-PAGE.

Ethanol	100 mM
EDTA	0.1 mM
DTT	0.5 mM
Cholic acid	7.2 g/L
Deoxycholic acid	3.6g/L

Table A. 7: Composition sonication buffer for liposomes synthesis.

Tricine-NaOH, pH 8	100 mM
EDTA	0.1 mM
DTT	0.5 mM

Cholic acid	7.2 g/L
Deoxycholic acid	3.6 g/L

Table A. 8: Composition dialysis buffer for liposomes purification.

Tricine-NaOH, pH 8	150 mM
MgCl ₂	37.5 mM
EDTA	3 mM
DTT	3.75 mM

Table A. 9: Composition of reconstitution buffer for liposomes.

Tricine-NaOH, pH 8	20 mM
Succinate	20 mM
KCl	0.6 mM
NaCl	80 mM

Table A. 10 : Composition of basic medium for ATP synthesis.

Tricine-NaOH, pH 8.8	200 mM
MgCl ₂	2.5 mM
Sodium phosphate	5 mM
KOH	160 mM

Table A. 11: Composition of acidic medium for ATP synthesis.

Succinate acid-HCl, pH 4.4	20 mM
MgCl ₂	2.5 mM
NaH ₂ PO ₄	5 mM
KOH	0.6 mM

Table A. 12: Composition of cell culture medium for Halobacterium Salinarium.

NaCl	250 g/L
MgSO ₄	20 g/L

Trisodium citrate	3 g/L
KCl	2 g/L
Peptone	10 g/L

Table A. 13: Composition of membrane resuspension buffer for isolation of bR.

NaCl	250 g/L
MgSO ₄	20 g/L
Trisodium citrate	3 g/L
KCl	2 g/L
DNAase	0.02 mg/mL

Table A. 14: Composition of HMDEKP buffer for axonemes reactivation.

HEPES	30 mM
MgSO ₄	5 mM
DTT	1 mM
EGTA	1 mM
K-Acetate	50 mM
PEG (Mw 20 kg mol ⁻¹)	1 %

Table A. 15: Composition of Laemmli buffer (10X) for SDS-PAGE.

Tris	30 g/L
Glycine	144 g/L
SDS	10 g/L

Table A. 16: Composition of salt solution for *C. reinhardtii* growth media (1-Liter).

NH ₄ Cl	15 g/L
MgSO ₄ .7H ₂ O	4 g/L
CaCl ₂ .2H ₂ O	2 g/L

Table A. 17: Composition of potassium phosphate solution for *C. reinhardtii* growth media (1-Liter).

K ₂ HPO ₄	288 g/L
K ₂ HPO ₄ ·2H ₂ O	144 g/L
pH	7.4 adjusted with

Table A. 18: Composition of Hunter's trace element solution (1-Liter) for *C. reinhardtii* growth media.

ZnSO ₄ ·7H ₂ O	22 g/L
H ₃ BO ₃	11.40 g/L
MnCl ₂ ·4H ₂ O	5.06 g/L
CoCl ₂ ·6H ₂ O	1.61 g/L
CuSO ₄ ·5H ₂ O	1.57 g/L
(NH ₄) ₆ Mo ₇ O ₂₄ ·4H ₂ O	1.10 g/L
EDTA disodium salt	50 g/L
FeSO ₄ ·7H ₂ O	4.99 g/L

Table A. 19: Composition of TAP+P stock solution (*C. reinhardtii* growth media).

Tris	2.42 g/L
Salt solution (Table A.16)	25 mL
Potassium phosphate solution (Table A.17)	1.5 mL
Hunter's trace element solution (Table A.18)	1 mL
Glacial acetic acid	~ 1.8 mL

Table A. 20: Composition of HMDS 4 % buffer for axoneme isolation.

HEPES	30 mM
MgSO ₄	5 mM
EGTA	1 mM
Sucrose	4 %
Pefabloc	0.2 mM

Table A. 21: Composition of HMDS-EGTA 4 % buffer for axoneme isolation.

HEPES	30 mM
MgSO ₄	5 mM
DTT	1 mM
EGTA	1 mM
Sucrose	4 %
Pefabloc	0.2 mM

Table A. 22: Composition of HMDS 25 % buffer for axoneme isolation.

HEPES	30 mM
MgSO ₄	5 mM
DTT	1 mM
Sucrose	25 %
Pefabloc	0.2 mM

Table A. 23: Composition of HMDEK + Pefabloc buffer for axoneme isolation.

HEPES	30 mM
MgSO ₄	5 mM
DTT	1 mM
EGTA	1 mM
K-Acetate	50 mM
Pefabloc	0.2 mM

Table A. 24: Composition of HMDEKP + Pefabloc buffer for axoneme isolation.

HEPES	30 mM
MgSO ₄	5 mM
DTT	1 mM
EGTA	1 mM
K-Acetate	50 mM
PEG (Mw 20 kg mol ⁻¹)	1 %

Pefabloc	0.2 mM
Sucrose	20%

Table A. 25: M2B buffer for MTs polymerization

PIPES	80 mM, pH 7.4 (adjusted with KOH)
MgCl ₂	2 mM
EGTA	1 mM

A. 1.1 List of chemicals and materials

Name	Manufacturer/company
Adenosine triphosphate (ATP)- disodium salt ($\geq 99\%$)	Sigma-Aldrich
Adenosine triphosphate (ATP)- disodium salt ($\geq 99\%$)	Sigma-Aldrich
ATP bioluminescence assay kit CLSII	Roche Life Science
ADP ultrapure ($\geq 99.9\%$)	Cell technology
Ammonium paramolybdate tetrahydrate	Sigma-Aldrich
Bio-Beads SM-2	Bio-Beads SM-2
Chloroform ($\geq 99.9\%$)	Sigma-Aldrich
Coomassie blue R-250	Sigma-Aldrich
Cobalt (II) chloride	Sigma-Aldrich
Casein, bovine milk	Sigma-Aldrich
Cover slip	Deckgläser (VWR)
Dithiothreitol (DTT)	Sigma-Aldrich
Ethylenediaminetetraacetic acid (EDTA) (99.5%)	Sigma-Aldrich
Ethyleneglycoltetraacetic acid (EGTA) ($\geq 99\%$)	Sigma-Aldrich
Fluorebrite YG microsphere (1 μ m)	Polysciences

Fluo-oil 7500	Emulseo
Glycerine (≥99%)	Roth
Glycerol (Bio-Reagent)	Bio-Rad
Glycine	Merck
Glacial acetic acid	Sigma-Aldrich
Glass slides (24X60 mm and 18 X 18 mm)	VWR
G25 size exclusion column (PD Mini Trap™ G-25)	GE Healthcare
HEPES	Sigma-Aldrich
Imidazole (Bio Ultra)	Sigma-Aldrich
Iron(II) sulfate hydrate	Sigma-Aldrich
Low range molecular weight standard (PageRuler™ 10-180 kDa) and (PageRuler™ 4.6-42 kDa)	Thermo Scientific
Magnesium chloride (MgCl ₂) hexahydrate	Sigma-Aldrich
Methanol (99.9%)	Sigma-Aldrich
Milli-Q Water (ddH ₂ O)	Sartorius
Manganese(II) chloride	Sigma-Aldrich
Microfilter candle with narrow tube	DWK life sciences
Ni-NTA column His Trap™ FF crude	GE Healthcare
NP-40, protein grade (10%)	Merck
Potassium chloride (KCl)	Sigma-Aldrich
Polycarbonate membrane (100 nm)	Whatman
Proteinase K	Sigma-Aldrich

Pefabloc	Sigma-Aldrich
SYLGARD™ 184 Silicone Elastomer Kit	Dow
SU-8 Photoresist	Microresist
Sucrose (≥99.5%)	Sigma-Aldrich
Soy L-α _phosphatidylcholine (PC) (95%)	Avanti Polar Lipids
Sterile filter (0.22 μm)	Sartorius
Sodium Dodecyl sulfate (SDS) 20%	Sigma-Aldrich
Tetracycline	Sigma-Aldrich
Trichloroacetic Acid (TCA) (≥99%)	Sigma-Aldrich
Tricine (≥99%)	Sigma-Aldrich
Tris (Ultrapure)	Sigma-Aldrich
Tris-acetate (Bio Ultra)	Sigma-Aldrich
Triton X-100 (10%) (Triton)	Sigma-Aldrich
Valinomycin (≥98%)	Sigma-Aldrich
Zinc sulfate	Sigma-Aldrich
ε - Aminocaproic acid	Sigma-Aldrich
4-20% Tris-HCl Criterion Precast Gels	Bio-Rad

A. 1.2 List of equipment

Name	Manufacturer/company
Leica microscope (phase-contrast), DMI8	Leica
Epi-fluorescence microscope (Olympus IX 71)	Olympus life sciences
Cetoni nemesys syringe pumps	Cetoni

Mask aligner UV-KUB 3	Kloe
pH electrode	WTW
Gel apparatus	Bio-Rad
Glomax 20/20 luminometer	Bio-Rad
Mini Extruder	Avanti Polar Lipids
Zetasizer Nano ZS	Malvern, Worcestershire
Zetasizer Nano ZS	Malvern, Worcestershire
Multifuge X1R (centrifuge)	Thermo scientific
50 W LED lamp	SMD RGB Floodlight, V-TAC
Orbital shaker	WVR
Microcentrifuge 54178 R	Eppendorf
French Press	SLM Amino French cell press
Sonicator	VWR
Plasma cleaner PDC-002-CE	Harrick Plasma
Film mask	Micro Lithography service
Incubator	Memmert

A. 2 Supporting Information

(1) Simulation with simplified wave form

Superposition of dynamic mode (cosine wave) and static mode (a circular arc) of axoneme shape provided the information of swimming trajectory. To investigate the influence of

frequency, static curvature and amplitude of curvature wave on swimming trajectory, simulation was performed with simplified wave equation,¹³⁰ as follow:

$$C(s, t) = C_0 + C_1 \cos(2\pi(s/\lambda - f_0 t)), \quad [\text{A.2.1}]$$

where C_0 is the static curvature, C_1 is the amplitude of the dynamic mode, λ is the wave length and f_0 is the beating frequency. Minus sign with term f_0 shows that wave propagate from basal end ($s = 0$) to distal ($s = L$) tip. For a non-zero static curvature ($C_0 \neq 0$), axoneme followed circular path, which was in consistence with the experimental results of *C. reinhardtii* isolated axonemes (Figure A.2.1). On the other hand, in the absence of static curvature ($C_0 = 0$), axoneme swims in a straight as and travelled a longer distance (Figure A.2.1B, C). For the proof of concept, axoneme swims in a straight path with zero static curvature, reactivation of axoneme was performed with ATP functional module supplemented with 1mM CaCl_2 which led to almost zero curvature, axoneme swims in a straight path.

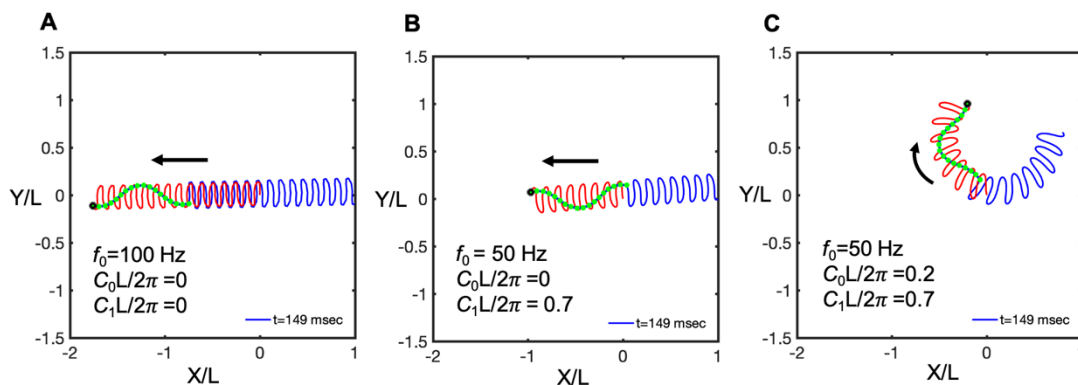


Figure A.2.1: Simulations in the frame work of RFT. A-B) A flagellum swimming in the absence of static curvature (C_0) at two different frequencies of 100 and 50 Hz. Faster beating flagella swims a longer distance. C) Flagellum follows a circular path if C_0 is non-zero. Amplitude of the dynamic mode C_1 is kept the same for all three simulations. L is the contour length of flagellum.

In these simulations, drag force density was calculated using resistive force theory (RFT), inspired by low Reynold number micro-swimmer.⁵³

(2) Principle component analysis (PCA) of the curvature waves – Fourier fits

The black dashed lines in Chapter 4, Figure 4.4, represents Fourier fits of the mode, imposing the boundary condition $\theta(s = 0, t) = 0$.

$$M_1(s) = -b_1 + b_1 \cos(ks) + b_2 \sin(ks), \quad [\text{A.2.2}]$$

$$M_2(s) = -(c_1 + c_3 + c_5) + \sum_{m=1}^3 (c_{2m-1} \cos(mks) + c_{2m} \sin(mks)), \quad [\text{A.2.3}]$$

where $k = 2\pi/\lambda$ and the parameters are: $\lambda = 16.87 \mu\text{m}$, $b_1 = 0.136$, $b_2 = -0.055$, $c_1 = 2.3 \times 10^{-5}$, $c_2 = -0.239$, $c_3 = 0.003$, $c_4 = 0.061$, $c_5 = 0.011$, and $c_6 = 0.012$. In addition, the cyan dashed lines in Chapter 4, Figure 4.4D, fitting the time-dependent coefficients $a_1(t)$ and $a_2(t)$ in Chapter 4 Eq. 4.1 are given by the Fourier modes as:

$$a_1(t) = a_{11} \cos(\omega_0 t) + a_{12} \sin(\omega_0 t), \quad [\text{A.2.4}]$$

$$a_2(t) = a_{21} \cos(\omega_0 t) + a_{22} \sin(\omega_0 t), \quad [\text{A.2.5}]$$

where $a_{11} = 5.29$, $a_{12} = -1.67$, $a_{21} = 0.78$, $a_{22} = 2.81$ and $\omega_0 = 2\pi f_0 = 114.23$ Hz. Please note that since the mean-shape $\langle \theta(s, t) \rangle_t$ is subtracted, the time average of both $a_1(t)$ and $a_2(t)$ is zero. Moreover, we note that, as show in the ref⁵⁰, the second harmonic can play a crucial role in the rotational speed of the axonemes, but at the level of our approximation, Eqs. A.2.4-5 provides a reasonable fit (see Chapter 4, Figure 4.4). The spatial Fourier decomposition of the modes $M_1(s)$ and $M_2(s)$, as presented in Eq. A.2.2-3, in combination with the time dependent coefficients $a_1(t)$ and $a_2(t)$ in in Eq. A.2.4-5 describe the axonemal shapes with good accuracy, the representation propose here also accurately capture the boundary conditions at $s = L$. At the distal region of the axoneme, both $\theta(s = L, t)$ and its derivative oscillate at the beat frequency f_0 , as shown in Figure A.2.2. Having described the angle $\theta(s, t)$ in terms of the eigenmodes $M_1(s)$ and $M_2(s)$, we calculate next the curvatures waves as:

$$\kappa(s, t) = \frac{d\theta(s, t)}{ds} = \frac{d\langle \theta(s, t) \rangle_t}{ds} + a_1(t) \frac{dM_1(s)}{ds} + a_2(t) \frac{dM_2(s)}{ds}. \quad [\text{A.2.6}]$$

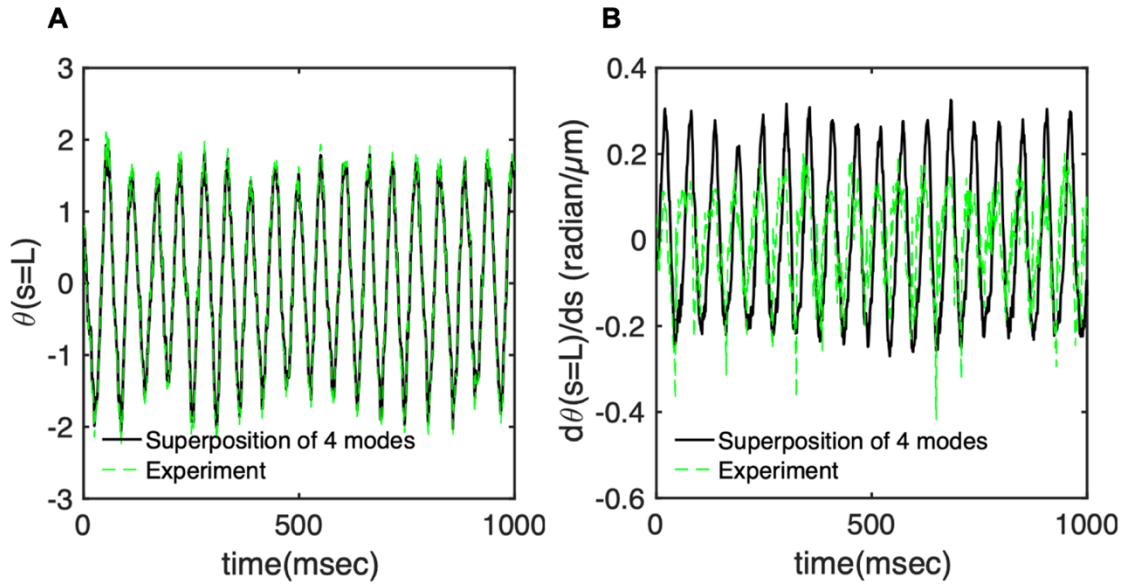


Figure A.2.2: Experimental shape of an axonemes reconstructed using PCA. At the distal tip $s = L$ of the free axoneme in Chapter 4, Figure 4.2, both the θ and its time derivative oscillate at the beat frequency $f_0 = 18$ Hz. The green dashed lines show the results obtained using the four PCA modes, as presented in Chapter 4, Eq. 4.1.

The mean angle $\langle \theta(s, t) \rangle_t$ shows a linear trend with contour length s , indicating a constant static curvature κ_0 (cyan filament in Chapter 4, Figure 4.3A). Next, we define the dimensionless curvature as $C = \kappa\lambda/(2\pi)$ using Eq. A.2.2-5 to express the deviation of $C(s, t)$ from its averaged value C_0 as a sum of propagating waves of wavenumber mk propagating forward and backward, respectively, with an amplitude C_m and C'_m . The expressions for C_m and C'_m can be readily derived from Eqs. A.2.2-5, and the resulting explicit expressions are given in the Table A.2.1. Interestingly, combining the Fourier decomposition in space of M_1 (Eq. A.2.2) or M_2 (Eq. A.2.3) with the temporal dependence of a_1 (Eq. A.2.4) or a_2 (Eq. A.2.5) results in standing waves. Specifically, only M_2 contributes to standing waves of wavenumbers $2k$ and $3k$, resulting in $C_2 = C'_2$ and $C_3 = C'_3$. On the other hand, both M_1 and M_2 generate a standing wave at wavenumber k , which implies that the coefficients $C_1 \neq C'_1$. The expression for the spatial and temporal dependence of the curvature can then be arranged as:

$$C(s, t) - C_0(s) \approx (C_1 - C'_1) \cos(ks - \omega_0 t + \alpha_1) + \sum_{m=1}^3 C'_m [\cos(mks - \omega_0 t + \alpha_m) + \cos(mks - \omega_0 t + \alpha'_m)], \quad [\text{A.2.7}]$$

where $C_0(s) = \kappa_0(s)\lambda/2\pi$ is the dimensionless mean-curvature, κ_0 is the mean curvature of the cyan filament in Chapter 4, Figure 4.3A. For our exemplary axoneme in Chapter 4, Figure 4.2 the values of these coefficients are listed in the first row of Table A.2.2. We summarize the important properties of Eq. A.2.7. (i) To construct the axonemal shape with high precision, in addition to main spatial mode k , higher modes $2k$ and $3k$, must be included. (ii) The Fourier analysis of PCA modes shows that a tip-to-base backpropagating wave component (with amplitude $C_1 - C'_1$) co-exists with standing wave at wavenumbers mk , with amplitude C'_m .

Table A.2.1: The general form of the coefficients, C'_n and C_n as defined in Eq. A.2.7. The coefficients $C_{n,p}$, $C_{n,m}$, $S_{n,p}$ and $S_{n,m}$, correspond to a description of the waves as: $C_{n,p} = \cos(nks - \omega t) + S_{n,p} = \sin(nks - \omega t) + C_{n,m} = \cos(nks + \omega t) + S_{n,m} = \sin(nks + \omega t)$. The expression for C_n and C'_n are identical for $n = 2$ and $n = 3$.

$C_1^2 = (C_{1,p}^2 + S_{1,p}^2)/4$ $\alpha_1 = \tan^{-1}(-S_{1,p}/C_{1,p})$	$C_2^2 = (C_{2,p}^2 + S_{2,p}^2)/4$ $\alpha_1 = \tan^{-1}(-S_{2,p}/C_{2,p})$	$C_3^2 = (C_{3,p}^2 + S_{3,p}^2)/4$ $\alpha_1 = \tan^{-1}(-S_{3,p}/C_{3,p})$
$C_{1,p} = -a_{12}b_1 + a_{11}b_2 - a_{22}c_1 + a_{21}c_2$	$C_{2,p} = -2(a_{22}c_3 - a_{21}c_4)$	$C_{3,p} = -3(a_{22}c_5 - a_{21}c_6)$
$S_{1,p} = -(a_{11}b_1 + a_{12}b_2 + a_{21}c_1 + a_{22}c_2)$	$S_{2,p} = -2(a_{21}c_3 + a_{22}c_4)$	$S_{3,p} = -3(a_{21}c_5 + a_{22}c_6)$
$C_1'^2 = (C_{1,m}^2 + S_{1,m}^2)/4$ $\alpha_1' = \tan^{-1}(-S_{1,m}/C_{1,m})$	$C_2'^2 = (C_{2,m}^2 + S_{2,m}^2)/4$ $\alpha_2' = \tan^{-1}(-S_{2,m}/C_{2,m})$	$C_3'^2 = (C_{3,m}^2 + S_{3,m}^2)/4$ $\alpha_2' = \tan^{-1}(-S_{3,m}/C_{3,m})$
$C_{1,m} = a_{12}b_1 + a_{11}b_2 + a_{22}c_1 + a_{21}c_2$	$C_{2,m} = 2(a_{22}c_3 + a_{21}c_4)$	$C_{3,m} = 3(a_{22}c_5 + a_{21}c_6)$
$S_{1,m} = -(a_{11}b_1 - a_{12}b_2 + a_{21}c_1 - a_{22}c_2)$	$S_{2,m} = -2(a_{21}c_3 - a_{22}c_4)$	$S_{3,m} = -3(a_{21}c_5 - a_{22}c_6)$

We note that these standing waves may result from modulations of the wave amplitude, as discussed in A.2.(3). (iii) For the standing waves at modes k , $2k$ and $3k$, the waveform reduces to $2C'_j \cos(\omega t + (\alpha'_j - \alpha_j)/2) \cos(jk_s + (\alpha_j + \alpha'_j)/2)$, with nodes occur at $s_{node}^j = (jk)^{-1}[(2n + 1)\pi/2 - (\alpha_j + \alpha'_j)/2]$, n being an integer. We stress that the representation of the wavy motion provided by Eq. A.2.7 is only an approximation, and that deviations due to higher order PCA modes M_n with $n > 2$, among others, are expected to lead to $C_m \neq C'_m$ for $m = 2$ and 3 . Still, given that the two modes considered here account for $\sim 98.52\%$ of the total variance of the signal, the corrections to Eq. A.2.7 are expected to be small.

Table A.2.2: Values of the coefficient's, defined in Eq. A.2.7 calculated for the free axoneme in Chapter 4, Figure 4. 2 (first row) and five other axonemes reactivated at $[ATP] = 200 \mu\text{M}$. The calcium concentration is zero.

$C_1 = 0.74$	$C_2 = 0.18$	$C_3 = 0.07$	$\alpha_1 = 0.34 \pi$	$\alpha_2 = 0.43 \pi$	$\alpha_3 = -0.35 \pi$
$C'_1 = 0.14$	$C'_2 = 0.18$	$C'_3 = 0.07$	$\alpha'_1 = 0.16 \pi$	$\alpha'_2 = -0.40 \pi$	$\alpha'_3 = -0.18 \pi$
$C_1 = 0.62$	$C_2 = 0.23$	$C_3 = 0.1$	$\alpha_1 = -0.49 \pi$	$\alpha_2 = -0.08 \pi$	$\alpha_3 = 0.12 \pi$
$C'_1 = 0.08$	$C'_2 = 0.23$	$C'_3 = 0.1$	$\alpha'_1 = -0.19 \pi$	$\alpha'_2 = 0.30 \pi$	$\alpha'_3 = 0.49 \pi$
$C_1 = 0.59$	$C_2 = 0.17$	$C_3 = 0.07$	$\alpha_1 = -0.22 \pi$	$\alpha_2 = -0.16 \pi$	$\alpha_3 = 0.36 \pi$
$C'_1 = 0.07$	$C'_2 = 0.17$	$C'_3 = 0.07$	$\alpha'_1 = 0.14 \pi$	$\alpha'_2 = -0.16 \pi$	$\alpha'_3 = 0.03 \pi$
$C_1 = 0.51$	$C_2 = 0.18$	$C_3 = 0.05$	$\alpha_1 = 0$	$\alpha_2 = -0.16 \pi$	$\alpha_3 = 0.4 \pi$
$C'_1 = 0.08$	$C'_2 = 0.18$	$C'_3 = 0.05$	$\alpha'_1 = 0.14 \pi$	$\alpha'_2 = -0.23 \pi$	$\alpha'_3 = -0.16 \pi$
$C_1 = 0.56$	$C_2 = 0.18$	$C_3 = 0.06$	$\alpha_1 = 0.11 \pi$	$\alpha_2 = -0.4 \pi$	$\alpha_3 = -0.42 \pi$
$C'_1 = 0.05$	$C'_2 = 0.18$	$C'_3 = 0.06$	$\alpha'_1 = 0.46 \pi$	$\alpha'_2 = -0.22 \pi$	$\alpha'_3 = -0.27 \pi$
$C_1 = 0.64$	$C_2 = 0.19$	$C_3 = 0.09$	$\alpha_1 = 0.36 \pi$	$\alpha_2 = -0.05 \pi$	$\alpha_3 = 0.22 \pi$
$C'_1 = 0.04$	$C'_2 = 0.19$	$C'_3 = 0.09$	$\alpha'_1 = 0.42 \pi$	$\alpha'_2 = 0.50 \pi$	$\alpha'_3 = -0.23 \pi$

We insist that the description in terms of a dominant base-to-tip propagating wave, modulated by a set of standing waves, is a convenient way of describing the dynamics of the system, whose biological implications remain to be discussed.

(3) PCA analysis of a model filament: a traveling wave with amplitude variations

Let us consider a model beating filament with (fictitious) boundary conditions $\theta(s = 0, t) = \theta(s = L, t) = 0$, with the following waveform:

$$\theta(s, t) = \sin(\pi s/L) \cos(\omega_0 t - 2\pi s/L), \quad [\text{A.2.8}]$$

where the wavelength is assumed to be the contour length L and the tangent angle at both ends ($s = 0$ and $s = L$) is forced to be zero (see Figure A.2.3A). Our PCA analysis of this idealized waveform with amplitude modulations results in the following coefficients defined in Eq. A.2.7: Note that to satisfy the boundary conditions at both ends, the PCA analysis (see

Figure A.2.3B-D) picks up the main traveling wave component with standing waves at wavelengths L , $L/2$ and $L/3$.

We note that the decomposition from our PCA analysis sharply differs from what one may expect by re-expressing Eq.A.2.9 using elementary trigonometric identity, which leads to:

$$\theta(s, t) = \frac{1}{2}\sin(\omega_0 t - \pi s/L) - \frac{1}{2}\sin(\omega_0 t - 3\pi s/L). \quad [\text{A.2.9}]$$

This decomposition clearly indicates that waves are propagating from $s = 0$ to $s = L$. This prompts some questions in interpreting the results of the above example and indicates that special care should be taken in attributing these results to the underlying biology.

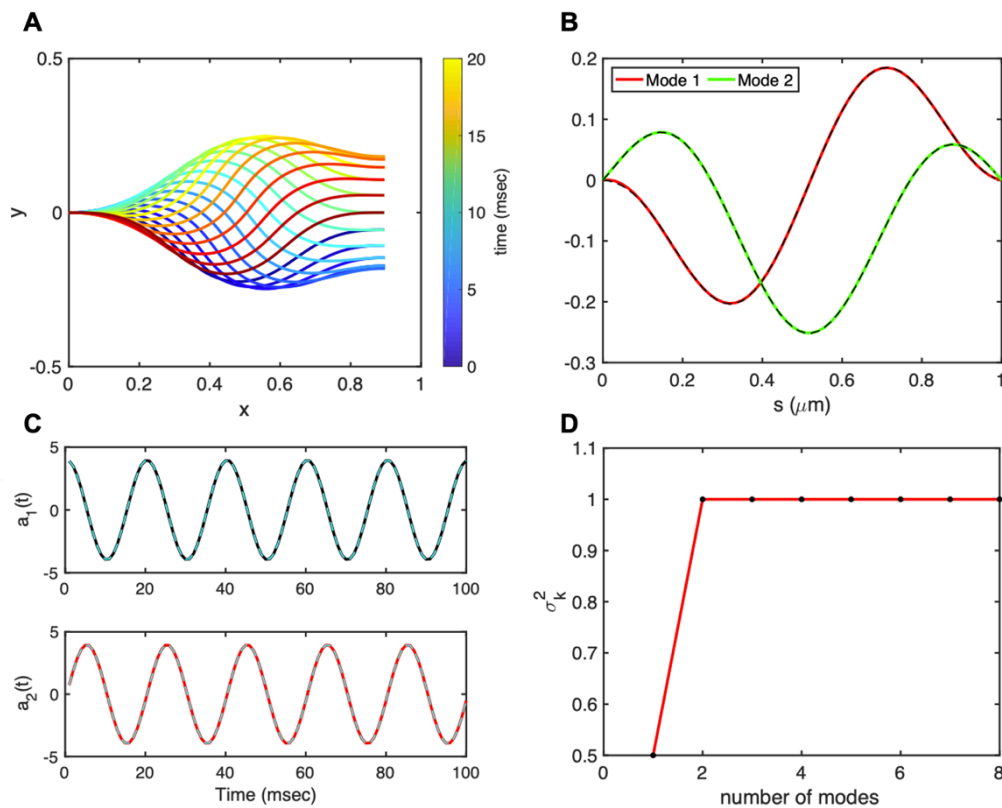


Figure A.2.3: A) Time projection of the shapes of a model filament with a traveling wave as defined by Eq. A.2.8. The beat frequency is 50 Hz. B) The first two PCA modes $M_1(s)$ and $M_2(s)$. The dashed lines are the Fourier fits as defined in Eqs. A.2.2-3. C) Time-dependent motion amplitudes $a_1(t)$ and $a_2(t)$. The dashed lines in cyan show the Fourier fits as defined by Eqs. A.2.4-5. The first two PCA modes describe the shape of the filament with full accuracy.

(4) Implication for the motion of free axonemes: an analytical study

We set the Fourier coefficients c_3 , c_4 , c_5 and c_6 in Eq. A.2.3 to zero. These coefficients capture the effect of the higher spatial modes 2κ and 3κ . The green line in Figure A.2.4 shows the deviation between the experimentally extracted mode $M_2(s)$ and the corresponding fitted mode. We note that setting these coefficients to zero results in having zero coefficients C'_2 and C'_3 in Eq. A.2.7, which leads to the simplified expression:

$$C(s, t) \approx C_0 + C_1 \cos(\omega_0 t - k_s + \alpha_1) + C'_1 \cos(\omega_0 t - k_s + \alpha'_1) \quad [\text{A.2.10}]$$

The total force and torque exerted on a freely swimming axoneme at low Reynolds number regime is zero. Given the prescribed form of curvature waves in Eq. A.2.7, we used resistive force theory (RFT)^{54, 228} to calculate propulsive forces and torques from the tangential and normal velocity components of each axonemal segment (see section A.2(6)). By imposing the force-free and torque-free constraints in 2D, we can uniquely determine the translational and rotational velocities of the axoneme. The resulting expressions for the translational and angular velocities, see section A.2.(5), Eqs. A.2.14-16, reflect an important symmetry property of the system.

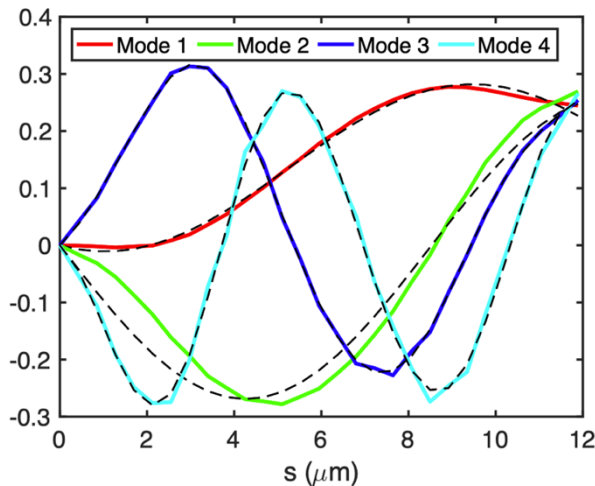


Figure A.2.4: For the second mode $M_2(s)$ of the free axoneme in Chapter 4, Figure 4.2, the coefficients c_3 , c_4 , c_5 and c_6 in Eq. A.2.3 are set to zero which results to the black dashed line in the vicinity of the green curve.

Namely, for the axoneme to rotate, it is necessary to break the mirror symmetry, i.e. $C_0 \neq 0$. If the wave pattern of the axoneme is transformed to its mirror-image after half a period (i.e. $C(s, t) = -C(s, t + T/2)$), then the flagella will swim on average in a straight trajectory. This is the case if only odd harmonics are kept in the waveform of Eq. A.2.10, i.e. $C_1, C'_1 \neq 0$ but $C_0 = 0$. The reason is that the mean rotations achieved in the first and second half-periods, have the same magnitude but opposite signs and the net rotation sums up to zero. Eqs. A.2.14-16 also show that in the absence of even harmonics, $\langle U_y \rangle = 0$ and $\langle U_x \rangle$ depends on the square of C_1 and C'_1 .^{205, 208, 228} One notices that in case of standing wave $C_1 = C'_1$ waves, the net propulsion vanishes.

Finally, in the case $\lambda = L$ and with the value of $\eta = \zeta_{||} / \zeta_{\perp} = 1.8^{54}$, Eqs. A.2.14-16 simplify to:

$$\frac{\langle \Omega_z \rangle}{f_0} \approx -2.23 C_0 (C_1^2 - C'^2_1), \quad [\text{A.2.11}]$$

$$\frac{\langle U_x \rangle}{f_0} \approx -0.93 C_0 (C_1^2 - C'^2_1), \quad [\text{A.2.12}]$$

$$\frac{\langle U_y \rangle}{f_0} \approx 0.26 C_0 (C_1^2 - C'^2_1). \quad [\text{A.2.13}]$$

(5) Translational and rotational velocities of a free and hinged axoneme

We consider a model axoneme with the waveform presented in Eq. A.2.10 to calculate the mean translational and rotational velocities in the regime that wavelength is not the same as contour length. Following the procedure described in the section A.2(6), we obtain:

$$\begin{aligned} \frac{\langle \Omega_z \rangle}{f_0} \approx & (2\eta\pi^5)^{-1} C_0 (C_1^2 - C'^2_1) \lambda'^3 (36\eta(2\eta - 1)\lambda'^6 + 3(1 + \eta(20\eta - 9))\lambda'^2\pi^4 + \\ & 2(\eta - 1)\pi^6 + \lambda'^2(36(1 - 2\eta)\eta\lambda'^4 + 3(-1 + \eta(28\eta - 15))\lambda'^2\pi^2 - 2(\eta^2 - 1)\pi^4) \times \\ & \cos[2\pi/\lambda'] + 3\lambda'^3\pi(24(1 - 2\eta)\eta\lambda'^2 + (-2 + \eta(7\eta - 3))\pi^2)\sin[2\pi/\lambda'], \end{aligned} \quad [\text{A.2.14}]$$

$$\frac{\langle U_x \rangle}{f_0} \approx (4\eta\pi^4)^{-1}(C_1^2 - C_1'^2)\lambda'^3 \left((3 - 6\eta)\lambda'^4 - 4(\eta - 1)\lambda'^2\pi^2 - 2\pi^4 + \lambda'^2((6\eta - 3)\lambda'^2 + 2(1 - 4\eta)\pi^2)\cos[2\pi/\lambda'] - 2\lambda'\pi((3 - 6\eta)\lambda'^2 + \eta\lambda'^2)\sin[2\pi/\lambda'] \right), \quad [\text{A.2.15}]$$

$$\frac{\langle U_y \rangle}{f_0} \approx (4\pi^5)^{-1}C_0(C_1^2 - C_1'^2)\lambda'^5(4(9(1 - 2\eta)\lambda'^4 + 3(2 - 5\eta)\lambda'^2\pi^2 + (4\eta - 1)\pi^4) + 2(18(2\eta - 1)\lambda'^4 + 6(4 - 7\eta)\lambda'^2\pi^2 - (1 - \eta)\pi^4)\cos[2\pi/\lambda'] + 3\lambda'\pi(24(2\eta - 1)\lambda'^2 + (5 - 7\eta)\pi^2)\sin[2\pi/\lambda']). \quad [\text{A.2.16}]$$

Here $\lambda' = \lambda/L$ and $\eta = \zeta_{\parallel} / \zeta_{\perp}$, where ζ_{\perp} and ζ_{\parallel} are transversal and parallel friction coefficient of cylindrical segments of the axoneme, see A.2(6).

For a hinged axoneme, we follow the procedure described in A.2(7), to obtain:

$$\frac{\langle \Omega_z \rangle}{f_0} \approx (8\pi^5)^{-1}C_0(C_1^2 - C_1'^2)\lambda'^3(9(2\eta - 1)\lambda'^6 + 9((4\eta - 1))\lambda'^4\pi^2 + 15(1 - 2\eta)\lambda'^2\pi^4 + 4(\eta - 1)\pi^6 + 3\lambda'^2((3 - 6\eta)\lambda'^4 - 3\lambda'^2\pi^2 + \pi^4)\cos[2\pi/\lambda'] - 3\lambda'^3\pi(6(2\eta - 1)\lambda'^2 + (3 + \eta)\pi^2)\sin[2\pi/\lambda']). \quad [\text{A.2.17}]$$

A hinged axoneme was free to rotate but not to translate, thus the total torque exerted on the axoneme is zero while the total force is non-zero. Following the procedure outlined in section A.2(7), we calculate the mean rotational velocity of the axoneme up to the first order in C_0 and second order in C_1 and C_1' we arrive at Eq. A.2.17, where in the limit of $\lambda = L$ and with the value of $\eta = \zeta_{\parallel} / \zeta_{\perp} = 1.8^{54}$, it simplifies to:

$$\frac{\langle \Omega_z \rangle}{f_0} \approx -0.63C_0(C_1^2 - C_1'^2). \quad [\text{A.2.18}]$$

Comparison with the pre-factor in Eq. A.2.9 shows that with the same intrinsic curvature C_0 and wave amplitudes C_1 and C_1' , the hinged axoneme rotates on average slower than a free one.

(6) Resistive force theory and calculation of translational and rotational velocities of a free axoneme

Biological microorganisms swim with flagella and cilia in the world of "low Reynolds number" where they experience viscous forces many orders of magnitude larger than inertial forces.^{53, 202, 243} In this world where inertia is negligible, Newton's law becomes an instantaneous balance between external and fluid forces and torques exerted on the swimmer, i.e. $\mathcal{F}_{ext} + \mathcal{F}_{fluid} = 0$ and $\mathcal{T}_{ext} + \mathcal{T}_{fluid} = 0$. The fluid force (\mathcal{F}_{fluid}) and torque (\mathcal{T}_{fluid}) exerted by the fluid on axoneme can be written as

$$\mathcal{F}_{fluid} = \int_0^L ds \mathcal{F}_{Axoneme}(s, t), \quad [\text{A.2.19}]$$

$$\mathcal{T}_{fluid} = \int_0^L ds \mathbf{r}(s, t) \times \mathcal{F}_{Axoneme}(s, t), \quad [\text{A.2.20}]$$

where the integrals over the contour length L of the axoneme calculate the total hydrodynamic force and torque exerted by the fluid on the axoneme. ATP-reactivated axonemes show oscillatory shape deformations. At any given time, we consider an axoneme as a solid body with unknown translational and rotational velocities $U(t)$ and $\Omega(t)$, yet to be determined. $U(t)$ and $\Omega(t)$, yet to be determined. \mathcal{F}_{fluid} and \mathcal{T}_{fluid} can be separated into propulsive due to the relative shape deformation of the axoneme in body-fixed frame and drag part²⁴⁴

$$\begin{pmatrix} \mathcal{F}_{fluid} \\ \mathcal{T}_{fluid} \end{pmatrix} = \begin{pmatrix} \mathcal{F}^{prop} \\ \mathcal{T}^{prop} \end{pmatrix} - \mathcal{D}_A \begin{pmatrix} U \\ \Omega \end{pmatrix}, \quad [\text{A.2.21}]$$

where 6×6 geometry-dependent drag matrix of the axoneme \mathcal{D}_A is symmetric and nonsingular (invertible). We also note that a freely swimming axoneme experiences no external forces and torques, thus \mathcal{F}_{fluid} and \mathcal{T}_{fluid} must vanish. Further, since swimming effectively occurs in 2D, \mathcal{D}_A is reduced to a 3×3 matrix and Eq. A.2.21 can be reformulated

$$\begin{pmatrix} U_x \\ U_y \\ \Omega_z \end{pmatrix} = \mathcal{D}_A^{-1} \begin{pmatrix} \mathcal{F}_x^{prop} \\ \mathcal{F}_y^{prop} \\ \mathcal{T}_z^{prop} \end{pmatrix} = \begin{pmatrix} a_{11} & a_{12} & a_{13} \\ a_{21} & a_{22} & a_{23} \\ a_{31} & a_{32} & a_{33} \end{pmatrix}^{-1} \begin{pmatrix} \mathcal{F}_x^{prop} \\ \mathcal{F}_y^{prop} \\ \mathcal{T}_z^{prop} \end{pmatrix}, \quad [\text{A.2.22}]$$

which we used to calculate the translational and rotational velocity of the swimmer after determining the drag matrix \mathcal{D}_A and the propulsive forces torque $(\mathcal{F}_x^{prop}, \mathcal{F}_y^{prop}, \mathcal{J}_z^{prop})$. We calculate $\mathcal{F}_x^{prop}, \mathcal{F}_y^{prop}, \mathcal{J}_z^{prop}$ which are propulsive forces and torque due to the shape deformations of the axoneme in the swimmer-fixed frame by selecting the basal end of the axoneme as the origin of the swimmer-fixed frame. As shown in Chapter 4, Figure 4.2, we define local tangent vector at contour length $s = 0$ as \hat{X} direction, the local normal vector \hat{n} as \hat{Y} direction and assumed that vector \hat{z} and \hat{Z} are parallel. Let us define $\theta_0(t) = \theta(s = 0, t)$ as the angle between \hat{x} and \hat{X} gives the velocity of the basal in the laboratory frame as $U_x^{Basal-Lab} = \cos \theta_0(t) U_x + \sin \theta_0(t) U_y$ and $U_y^{Basal-Lab} = -\sin \theta_0(t) U_x + \cos \theta_0(t) U_y$. Furthermore, we note that the instantaneous velocity of the axoneme in the lab frame is given by $\mathbf{u} = \mathbf{U} + \boldsymbol{\Omega} \times \mathbf{r}(s, t) + \mathbf{u}'$, where, \mathbf{u}' is the deformation of axoneme in body-fixed frame, $\mathbf{U} = (U_x, U_y, 0)$ and $\boldsymbol{\Omega} = (0, 0, \Omega_z)$ with $\Omega_z = d\theta_0(t)/dt$.

To calculate $\mathcal{F}_x^{prop}, \mathcal{F}_y^{prop}, \mathcal{J}_z^{prop}$ for a given beating pattern of axoneme in the body-fixed frame, we used classical framework of RFT which neglects long-range hydrodynamic interactions between different parts of the axoneme.^{54, 228} In this theory, axoneme is divided into small cylindrical segments with velocity $\mathbf{u}'(s, t)$ and propulsive force \mathcal{F}^{prop} is proportional to local center line velocity component of each segment in parallel and perpendicular directions,

$$\begin{aligned} \mathcal{F}^{prop}(s, t) &= \zeta_{\parallel} \mathbf{u}'_{\parallel} + \zeta_{\perp} \mathbf{u}'_{\perp}(s, t), \\ \mathbf{u}'_{\parallel}(s, t) &= [\dot{\mathbf{r}}(s, t) \cdot \mathbf{t}(s, t)] \mathbf{t}(s, t), \\ \mathbf{u}'_{\perp}(s, t) &= \dot{\mathbf{r}}(s, t) - \mathbf{u}'_{\parallel}(s, t), \end{aligned} \tag{A.2.23}$$

where, \mathbf{u}'_{\parallel} and \mathbf{u}'_{\perp} are the projection of local velocity on the directions parallel and perpendicular to the axoneme. The friction coefficient in parallel and perpendicular direction are defined as, $\zeta_{\parallel} = 4\pi\mu/(\ln(2L/a) + 0.5)$ and $\zeta_{\perp} = 2\zeta_{\parallel}$, respectively.

This anisotropy indicates that to obtain the same velocity, one would need to apply a force in the perpendicular direction twice as large as that in the parallel direction.^{54, 202} Axoneme is a

filament of length $L \sim 10 \mu\text{m}$ and radius $a = 100 \text{ nm}$. For a water-like environment with viscosity $\mu = 0.96 \text{ pN msec}/\mu\text{m}^2$, we obtained $\zeta_{\parallel} \sim 2.1 \text{ pN msec}/\mu\text{m}^2$.

(7) Approximation of the mean rotational velocity of a hinged axoneme

Consider an axoneme which is attached from the basal end to the substrate and rotates around the hinging point (see Chapter 4, Figure 4.9A). We select the hinging point of the axoneme as the origin of the swimmer-fixed frame, and define tangent and normal vectors at $s = 0$ as the coordinate system in the swimmer-fixed frame. Since the axoneme is free to rotate but not to translate, the total torque (\mathcal{T}_z^A) exerted on the axoneme is zero but the total force (\mathcal{F}_x^A) and (\mathcal{F}_y^A) is non-zero. Reformulation in term of Eq. A.2.21, we have:

$$\begin{pmatrix} \mathcal{F}_x^A \\ \mathcal{F}_y^A \\ \mathcal{T}_z^A \end{pmatrix} = \begin{pmatrix} \mathcal{F}_x^{prop} \\ \mathcal{F}_y^{prop} \\ \mathcal{T}_z^{prop} \end{pmatrix} + \begin{pmatrix} d_{11} & d_{12} & d_{13} \\ d_{21} & d_{22} & d_{23} \\ d_{31} & d_{32} & d_{33} \end{pmatrix} \begin{pmatrix} U_x \\ U_y \\ \Omega_z \end{pmatrix} \quad [\text{A.2.24}]$$

Which by imposing the constraints $U_x = 0$, $U_y = 0$ and $\mathcal{T}_z^A = 0$, simplifies to

$$\begin{pmatrix} \mathcal{F}_x^A \\ \mathcal{F}_y^A \\ 0 \end{pmatrix} = \begin{pmatrix} \mathcal{F}_x^{prop} \\ \mathcal{F}_y^{prop} \\ \mathcal{T}_z^{prop} \end{pmatrix} + \begin{pmatrix} d_{11} & d_{12} & d_{13} \\ d_{21} & d_{22} & d_{23} \\ d_{31} & d_{32} & d_{33} \end{pmatrix} \begin{pmatrix} 0 \\ 0 \\ \Omega_z \end{pmatrix}. \quad [\text{A.2.25}]$$

$$\mathcal{T}_z^{prop} = -d_{33} \Omega_z, \quad [\text{A.2.26}]$$

where

$$\mathcal{T}_z^{prop}(t) = \int_0^L ds \mathbf{r}(s, t) \times \mathbf{f}(s, t). \quad [\text{A.2.27}]$$

Here, $\mathbf{f}(s, t)$ is calculated from Eq. A.2.21 based on the simplified wave equation as defined Eq. A.2.10. To calculate mean rotational velocity for pinned axoneme, we averaged over one beating cycle,

$$\langle \Omega_z / \omega_0 \rangle = -\frac{1}{2\pi} \int_0^{1/f_0} dt \frac{\mathcal{J}_z^{prop}(t)}{d_{33}(t)}. \quad [\text{A.2.28}]$$

Please note that for a clamped boundary condition, since the mean translational and rotational velocities of the axoneme are zero, the total torque (\mathcal{J}_z^A) and the total force (\mathcal{F}_x^A) and (\mathcal{F}_y^A) are non-zero, and are equal to the propulsive force and torque:

$$\begin{pmatrix} \mathcal{F}_x^A \\ \mathcal{F}_y^A \\ \mathcal{J}_z^A \end{pmatrix} = \begin{pmatrix} \mathcal{F}_x^{prop} \\ \mathcal{F}_y^{prop} \\ \mathcal{J}_z^{prop} \end{pmatrix}. \quad [\text{A.2.29}]$$

(8) Resistive-force theory and calculations of mean translational and rotational velocities of bio-hybrid micro-swimmer

The fluid flow generated by the swimming of small objects is characterized by very small Reynolds numbers. In this regime, viscous forces dominate over inertia and non-reciprocal motion is necessary to break the time-symmetry and generate propulsion (scallop theorem)^{53, 202}. The micro-swimmer in our system is formed of an axoneme (a filament of characteristic length $L \sim 10 \mu\text{m}$ and radius $0.1 \mu\text{m}$), which is attached from one end to a micron-sized bead and swims in a aqueous solution of viscosity $\mu = 10^{-3} \text{ Pa s}$ and density $\rho = 10^3 \text{ kg m}^{-3}$. Given the characteristic axonemal wave velocity $V = \lambda/T \approx 0.5 \text{ mms}^{-1}$ (calculated for a typical axonemal beat frequency of 50 Hz and a wavelength which is comparable to the axonemal contour length L), the Reynolds number $Re = \rho LV / \eta$ will be a small number around 0.005. An important feature of swimming at low Reynolds numbers is its reversibility, which is a consequence of the linearity of the Stokes equation²⁰². In this physical regime, Newton's laws then consist of an instantaneous balance between external and fluid forces and torques exerted on the swimmer, i.e. $\mathbf{F}_{ext} + \mathbf{F}_{fluid} = 0$ and $\boldsymbol{\tau}_{ext} + \boldsymbol{\tau}_{fluid} = 0$. The force \mathbf{F}_{fluid} and torque $\boldsymbol{\tau}_{fluid}$ exerted by the fluid on the axoneme-bead swimmer can be written as:

$$\mathbf{F}_{fluid} = \mathbf{F}_{bead} + \int_0^L ds \mathbf{F}_{Axoneme}(s, t), \quad [\text{A.2.30}]$$

$$\boldsymbol{\tau}_{fluid} = \boldsymbol{\tau}_{bead} + \int_0^L ds \mathbf{r}(s, t) \times \mathbf{F}_{Axoneme}(s, t), \quad [\text{A.2.31}]$$

where \mathbf{F}_{bead} and $\boldsymbol{\tau}_{bead}$ are the hydrodynamic drag force and torque acting on the bead and the integrals over the contour length L of the axoneme calculate the total hydrodynamic force and torque exerted by the fluid on the axoneme. The bead is propelled by oscillatory shape deformations of the ATP-reactivated axoneme. At any given time, we consider axoneme-bead swimmer as a solid body with unknown translational and rotational velocities $\mathbf{U}(t)$ and $\boldsymbol{\Omega}(t)$, yet to be determined. \mathbf{F}_{fluid} and $\boldsymbol{\tau}_{fluid}$ can be separated into propulsive part due to relative shape deformations of the axoneme in body-fixed frame and drag part.²⁴⁴

$$\begin{pmatrix} \mathbf{F}_{fluid} \\ \boldsymbol{\tau}_{fluid} \end{pmatrix} = \begin{pmatrix} \mathbf{F}^{prop} \\ \boldsymbol{\tau}^{prop} \end{pmatrix} - \mathbf{D} \begin{pmatrix} \mathbf{U} \\ \boldsymbol{\Omega} \end{pmatrix} = \begin{pmatrix} \mathbf{F}^{prop} \\ \boldsymbol{\tau}^{prop} \end{pmatrix} - (\mathbf{D}_A + \mathbf{D}_B) \begin{pmatrix} \mathbf{U} \\ \boldsymbol{\Omega} \end{pmatrix}, \quad [\text{A.2.32}]$$

where 6X6 geometry-dependent drag matrix \mathbf{D} is symmetric and non-singular (invertible) and is composed of drag matrix of the axoneme \mathbf{D}_A and drag matrix of the bead \mathbf{D}_B . We also note that a freely swimming axoneme-bead experiences no external forces and torques, thus \mathbf{F}_{fluid} and $\boldsymbol{\tau}_{fluid}$ must vanish. Further, since swimming effectively occurs in 2D, \mathbf{D} is reduced to a 3x3 matrix and Eq. A.2.32 can be reformulated as:

$$\begin{pmatrix} U_x \\ U_y \\ \Omega_z \end{pmatrix} = (\mathbf{D}_A + \mathbf{D}_B)^{-1} \begin{pmatrix} F_x^{prop} \\ F_y^{prop} \\ \tau_z^{prop} \end{pmatrix}, \quad [\text{A.2.33}]$$

which we use to calculate translational and rotational velocities of the swimmer after determining the drag matrices \mathbf{D}_A and \mathbf{D}_B (for drag matrix calculation, and the propulsive forces and torque $(F_x^{prop}, F_y^{prop}, \tau_z^{prop})$).

We calculate $F_x^{prop}, F_y^{prop}, \tau_z^{prop}$ in the body-fixed frame by selecting the basal end of the axoneme (bead-axoneme contact point) as the origin of the swimmer-fixed frame. As shown

in Chapter 5, Figure 5.1A and Appendix, Figure A.2.5, we define local tangent vector at the contour length $s = 0$ as X – direction, the local normal vector \mathbf{n} as Y – direction and assumed that vector \mathbf{z} and Z are parallel. Here $(\mathbf{x}, \mathbf{y}, \mathbf{z})$ denote an orthogonal lab-frame basis. We define $\theta_0(t) = \theta(s = 0, t)$ as the angle between \mathbf{x} and \mathbf{X} which gives the velocity of the basal in the laboratory frame as $U_x^{\text{Bead-Lab}} = \cos \theta_0(t) U_x + \sin \theta_0(t) U_y$ and $U_y^{\text{Bead-Lab}} = -\sin \theta_0(t) U_x + \cos \theta_0(t) U_y$. Furthermore, the instantaneous velocity of axoneme in the lab frame is given by $\mathbf{u} = \mathbf{U} + \boldsymbol{\Omega} \times \mathbf{r}(s, t) + \mathbf{u}'$, where \mathbf{u}' is the deformation of flagellum in body-fixed frame, $\mathbf{U} = (U_x, U_y, 0)$ and $\boldsymbol{\Omega} = (0, 0, \Omega_z)$ with $\Omega_z = d\theta_0(t)/dt$.

To calculate F_x^{prop} , F_y^{prop} , τ_z^{prop} for a given beating pattern of axoneme in the body-fixed frame, we use RFT is used, which neglects long-range hydrodynamics interactions between different parts of the flagellum as well as the inter-flagella interactions.^{54, 228} In this theory, the flagellum is discretized as a set of small cylindrical segments moving with velocity $\mathbf{u}'(s, t)$ in the body-fixed frame and the propulsive force \mathbf{F}^{prop} is proportional to local center-line velocity component of each segment in parallel and perpendicular direction, see Eq. A.2.23. Here is a short summary of the steps in our RFT analysis: first, we translate and rotate the axoneme such that the basal end is at position (0,0) and the local tangent vector at ($s = 0$) at any time t is along the \mathbf{x} -axis (see Chapter 5, Figure 5.1A). In this way, we lose the orientation information of the axoneme at all the time points except for the initial configuration at time $t = 0$. Second, we calculate propulsive forces and torque in the body-frame using RFT (Eq. A.2.23), and then use Eq. A.2.33 to obtain translational velocities U_x , U_y as well as rotational velocity Ω_z of the axoneme. Now the rotational matrix can be calculated as:

$$d\mathbf{\Gamma}(t) = \begin{pmatrix} \cos(\Omega_z(t)dt) & -\sin(\Omega_z(t)dt) & U_x(t)dt \\ \sin(\Omega_z(t)dt) & \cos(\Omega_z(t)dt) & U_y(t)dt \\ 0 & 0 & 1 \end{pmatrix}, \quad [\text{A.2.34}]$$

which we use to update rotation matrix as $\mathbf{\Gamma}(t + dt) = \mathbf{\Gamma}(t)d\mathbf{\Gamma}(t)$, considering $\mathbf{\Gamma}(t = 0)$ to be the unity matrix. Having the rotation matrix at time t , we obtain the configuration of the axoneme at time t from its shape at body-fixed frame by multiplying the rotation matrix as $\mathbf{r}_{\text{lab-frame}}(s, t) = \mathbf{\Gamma}(t)\mathbf{r}_{\text{body-frame}}(s, t)$, which can then be compared with experimental

data. Please note that $\mathbf{r}_{\text{body-frame}}(s, t)$ is an input from experimental data presenting the beating patterns in the body-fixed frame.

(9) Drag matrix of a bead in 2D

Let us consider the two-dimensional geometry defined in Figure A.2.5A. Note that the origin of the swimmer-fixed frame is not at the bead center and is selected to be at the bead-axoneme contact point, as shown in Figure A.2.5A. In general, the tangent vector at position $s = 0$ of the axoneme, which defines the X – axis, does not pass through the bead center located at (X, Y) . This asymmetric bead-axoneme attachment is also observed in our experiments, as shown in Chapter 5, Figure 5.1A. We emphasize that the drag force is actually a distributed force, given by $d\mathbf{f} = \sigma \cdot d\vec{A}$, applied at the surface of the sphere, but symmetry implies that drag force effectively acts on the bead center.

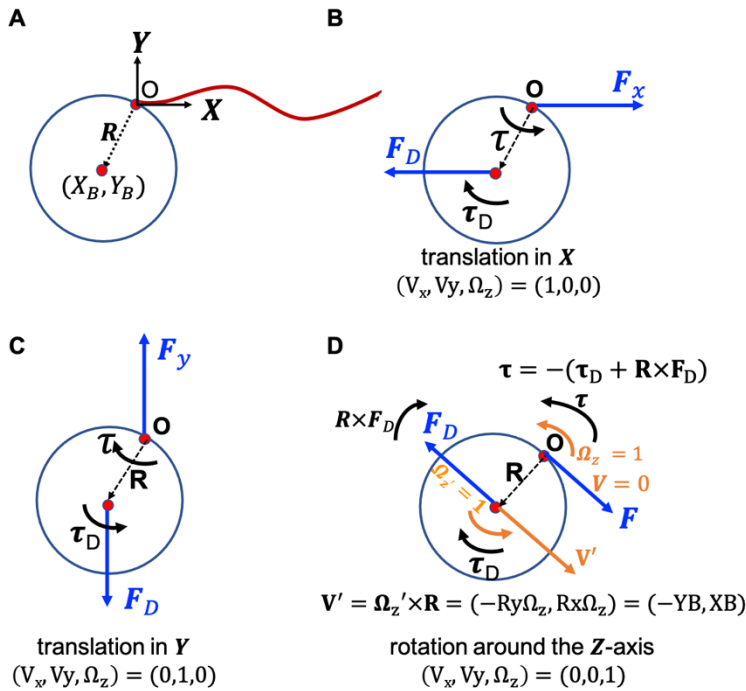


Figure A.2.5: Illustration of bead attached axoneme. A) Illustration of bead orientation with respect to the axoneme and definition of the swimmer-fixed frame. Tangent vector at $s = 0$ (basal end) defines the X -direction. B-D) Schematic drawing of the forces and torques that counteract the hydrodynamic drag force and torque.

We define the translational and rotational friction coefficients of the bead as $v_T = 6\pi\alpha_t\mu R$ and $v_R = 8\pi\alpha_t\mu R^3$, where $\mu = 10^{-3}$ pa is the dynamic viscosity of water and factors

$\alpha_t = 1/(1 - 9(R/h)/16 + (R/h)^3/8)$ and $\alpha_r = 1/(1 - (R/h)^3/8)$ are corrections due to the fact that axonemal-based bead propulsion occurs in the vicinity of a substrate.²⁴⁵ Here R is the bead radius ($\sim 0.5 \mu\text{m}$), h is the distance between the center of the bead and the substrate. Assuming $R/h \sim 1$, we $\alpha_t = 16/9$ and $\alpha_r = 8/7$. We now look at each component of velocity and ask what force do we need to apply to counteract the viscous force and torque?

(i) Translation in \mathbf{X} – direction. In this case, we have U_x, U_y, Ω_z as shown in Figure A.2.5B. We need to apply a force in $+\mathbf{X}$ direction to counteract the drag force as:

$$F_x = 6\pi\alpha_t\mu R = v_T. \quad [\text{A.2.35}]$$

But we must also apply a torque in a $+\mathbf{Z}$ for the case illustrated in Figure A.2.5B (where $Y_B < 0$) to prevent rotation from occurring:

$$\tau = -\tau_D = -Y_B F_x = -v_T Y_B, \quad [\text{A.2.36}]$$

so we get:

$$(F_x, F_x, \tau_z) = (v_T, 0, -v_T Y_B) U_x. \quad [\text{A.2.37}]$$

(ii) Translational in \mathbf{Y} – direction This case corresponds to $(U_x, U_y, \Omega_z) = (0,0,1)$ as shown in Figure A.2.5B. We have $F_x = 0$ and $F_y = +6\pi\alpha_t\mu R = v_T$. Note that we need to apply a negative torque, and since $X_B < 0$, we have $\tau = +X_B v_T$ which gives

$$(F_x, F_x, \tau) = (0, v_T, v_T X_B) U_y. \quad [\text{A.2.38}]$$

(iii) Rotation around \mathbf{Z} – direction. For this case, we have $(U_x, U_y, \Omega_z) = (0,0,1)$ as shown in Figure A.2.5D. Before looking at the forces, let us examine the motion. The rotation Ω'_z of the bead center around the origin O also generates translational velocity $\mathbf{U}' = (-R_y, R_x)\Omega_z = (-X_B, Y_B)$. Note that for $Y_B < 0$ and $X_B < 0$ we get $V'_x > 0$ and $V'_y < 0$ which is consistent. Around the center of the bead, drag exerts force and torque \mathbf{F}_D and τ_D , as depicted in Figure A.2.5D:

$$\mathbf{F}_D = -v_T \mathbf{U}' = (v_T Y_B, -v_T X_B) \quad \text{and} \quad (\boldsymbol{\tau}_D)_z = -v_R. \quad [\text{A.2.39}]$$

To counteract the drag force, we must apply

$$\mathbf{F}_D = (-v_T Y_B, -v_T X_B) \quad \text{and} \quad \tau_z = v_R + FR = v_R + v_T R^2, \quad [\text{A.2.40}]$$

$$\text{so we obtain } (F_x, F_y, \tau_z) = (-v_T Y_B, v_T X_B, v_R + v_T R^2) \Omega_z. \quad [\text{A.2.41}]$$

This can be expressed as:

$$\begin{pmatrix} F_x \\ F_y \\ \tau_z \end{pmatrix} = \begin{pmatrix} v_T & 0 & -v_T Y_B \\ 0 & v_T & v_T X_B \\ -v_T Y_B & v_T X_B & v_R + v_T R^2 \end{pmatrix} \begin{pmatrix} U_x \\ U_y \\ \Omega_z \end{pmatrix}. \quad [\text{A.2.42}]$$

For the special case that center of the bead is at $(X_B, Y_B) = (-R, 0)$ which corresponds to the situation that tangent vector of the flagella at $s = 0$ goes through the bead center, Eq. A.2.42 simplifies to:

$$\begin{pmatrix} F_x \\ F_y \\ \tau_z \end{pmatrix} = \begin{pmatrix} v_T & 0 & 0 \\ 0 & v_T & -v_T R \\ 0 & -v_T X_B & v_R + v_T R^2 \end{pmatrix} \begin{pmatrix} U_x \\ U_y \\ \Omega_z \end{pmatrix}. \quad [\text{A.2.43}]$$

Note that Eq. A.2.42 present the force and torque exerted by the bead on the fluid which has opposite sign of the force generated by fluid on the bead, so drag matrix of the bead \mathbf{D}_B is the given by

$$\mathbf{D}_B = \begin{pmatrix} -v_T & 0 & v_T X_B \\ 0 & -v_T & -v_T X_B \\ v_T Y_B & -v_T X_B & -v_R - v_T R^2 \end{pmatrix}. \quad [\text{A.2.44}]$$

The general form of the drag matrix in 3D is given in the next section.

(10) Drag matrix of a bead in 3D

Let us fix a couple points P and P' on or in a rigid body (see Figure A.2.6) The distance between these points remains constant. Furthermore, if we attach two parallel vectors at P and P' , they would remain parallel under movement. Since this is the case, it follows that $\boldsymbol{\Omega}_P = \boldsymbol{\Omega}_{P'}$, so we will drop the subscript and call it $\boldsymbol{\Omega}$.

Let us denote the positions of P and P' by \mathbf{R}_P and $\mathbf{R}_{P'}$ (see Figure A.2.6B). The distance $|\mathbf{R}_P - \mathbf{R}_{P'}|$ is constant, but the orientation changes:

$$U_{P'} - U_P = \frac{d}{dt}(\mathbf{R}_{P'} - \mathbf{R}_P) = -(\mathbf{R}_{P'} - \mathbf{R}_P) \times \boldsymbol{\Omega}. \quad [\text{A.2.45}]$$

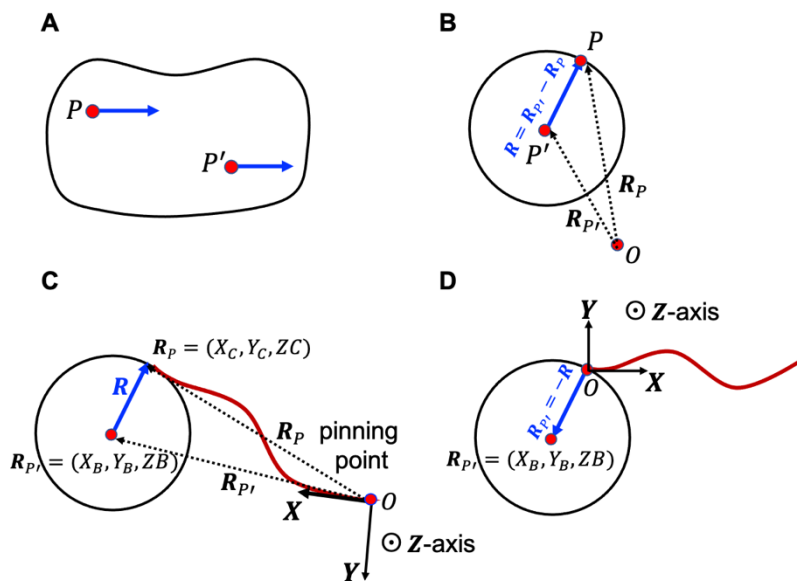


Figure A.2.6: Schematic presentation of the setup and the coordinate system.

Next, suppose we apply a distribution of forces f_i at \mathbf{R}_i as $\mathbf{F} = \sum_i f_i$ which does not depend on P and P' . The torques depend on P and P'

$$\boldsymbol{\tau}_P = \sum_i (\mathbf{R}_i - \mathbf{R}_P) \times f_i, \quad \text{and} \quad \boldsymbol{\tau}_{P'} = \sum_i (\mathbf{R}_{P'} - \mathbf{R}_P) \times f_i \quad [\text{A.2.46}]$$

and the difference gives:

$$\boldsymbol{\tau}_{P'} - \boldsymbol{\tau}_P = -(\mathbf{R}_{P'} - \mathbf{R}_P) \times \mathbf{F}. \quad [\text{A.2.47}]$$

Now let us define the problem we wish to solve: What is the force $\mathbf{F} = (F_x, F_y, F_z)^T$ and torque $\boldsymbol{\tau} = (\tau_x, \tau_y, \tau_z)^T$ must we apply at point P on the bead's surface to counteract the drag force and make the bead move with translational velocity $\mathbf{U} = U_P$ and angular velocity $\boldsymbol{\Omega}$. This amounts to asking what is the drag force and drag torque one needs to overcome. Let us denote the center of the bead as P' and define $\mathbf{R} = \mathbf{R}_P - \mathbf{R}_{P'}$ (Figure A.2.6B). This problem would have been much simpler if we were asked what force \mathbf{F}' and torque $\boldsymbol{\tau}'$ needs to be applied at the bead's center to counteract drag:

$$\begin{pmatrix} \mathbf{F}' \\ \boldsymbol{\tau}' \end{pmatrix} = \begin{pmatrix} V_T \mathbf{I} & \mathbf{0} \\ \mathbf{0} & V_R \mathbf{I} \end{pmatrix} \begin{pmatrix} \mathbf{U}' \\ \boldsymbol{\Omega}' \end{pmatrix}. \quad [\text{A.2.48}]$$

Here $V_T = 6\pi R\mu$ and $V_R = 8\pi R^3\mu/3$ and

$$\mathbf{I} = \begin{pmatrix} 1 & 0 & 0 \\ 0 & 1 & 0 \\ 0 & 0 & 1 \end{pmatrix}, \quad \text{and} \quad \mathbf{0} = \begin{pmatrix} 0 & 0 & 0 \\ 0 & 0 & 0 \\ 0 & 0 & 0 \end{pmatrix}. \quad [\text{A.2.49}]$$

Now we use what we learned about rigid body motion in Eq. A.2.43:

$$\begin{pmatrix} \mathbf{U}' \\ \boldsymbol{\Omega}' \end{pmatrix} = \begin{pmatrix} \mathbf{U} - (\mathbf{R}_{P'} - \mathbf{R}_P) \times \boldsymbol{\Omega} \\ \boldsymbol{\Omega} \end{pmatrix} = \begin{pmatrix} \mathbf{U} + \mathbf{R} \times \boldsymbol{\Omega} \\ \boldsymbol{\Omega} \end{pmatrix} = \begin{pmatrix} \mathbf{I} & \mathcal{R} \\ \mathbf{0} & \mathbf{I} \end{pmatrix} \begin{pmatrix} \mathbf{U} \\ \boldsymbol{\Omega} \end{pmatrix}, \quad [\text{A.2.50}]$$

$$\mathcal{R} = \begin{pmatrix} 0 & R_Z & R_y \\ R_Z & 0 & -R_x \\ -R_y & R_x & 0 \end{pmatrix} = \begin{pmatrix} 0 & -Z_C + Z_B & Y_C + Y_B \\ -Z_C + Z_B & 0 & -X_C + X_B \\ -Y_C + Y_B & X_C + X_B & 0 \end{pmatrix}. \quad [\text{A.2.51}]$$

Recall that $\mathbf{R}_P = (X_C, Y_C, Z_C)$ are the coordinates point of the flagella-bead contact point and $\mathbf{R}_{P'} = (X_B, Y_B, Z_B)$ are the coordinates of the bead center (Figure A.2.6C). Similarly, we have that

$$\begin{pmatrix} \mathbf{F}' \\ \boldsymbol{\tau}' \end{pmatrix} = \begin{pmatrix} \mathbf{F} \\ \boldsymbol{\tau} - (\mathbf{R}_{P'} - \mathbf{R}_P) \times \mathbf{F} \end{pmatrix} = \begin{pmatrix} \mathbf{F} \\ \boldsymbol{\tau} + \mathbf{R} \times \mathbf{F} \end{pmatrix} = \begin{pmatrix} \mathbf{I} & \mathbf{0} \\ \mathcal{R} & \mathbf{I} \end{pmatrix} \begin{pmatrix} \mathbf{F} \\ \boldsymbol{\tau} \end{pmatrix}, \quad [\text{A.2.52}]$$

So, the Eq. A.2.48 becomes:

$$\begin{pmatrix} \mathbf{I} & \mathbf{0} \\ \mathcal{R} & \mathbf{I} \end{pmatrix} \begin{pmatrix} \mathbf{F}' \\ \boldsymbol{\tau}' \end{pmatrix} = \begin{pmatrix} V_T \mathbf{I} & \mathbf{0} \\ \mathbf{0} & V_R \mathbf{I} \end{pmatrix} \begin{pmatrix} \mathbf{I} & \mathbf{0} \\ \mathcal{R} & \mathbf{I} \end{pmatrix} \begin{pmatrix} \mathbf{U} \\ \boldsymbol{\Omega} \end{pmatrix}, \quad [\text{A.2.53}]$$

Multiply both sides by $\begin{pmatrix} \mathbf{I} & \mathbf{0} \\ -\mathcal{R} & \mathbf{I} \end{pmatrix}$ and calculating the products of matrices yields

$$\begin{pmatrix} \mathbf{F} \\ \boldsymbol{\tau} \end{pmatrix} = \begin{pmatrix} V_T \mathbf{I} & V_T \mathcal{R} \\ -V_T \mathcal{R} & V_R \mathbf{I} - V_T \mathcal{R}^2 \end{pmatrix} \begin{pmatrix} \mathbf{U} \\ \boldsymbol{\Omega} \end{pmatrix} \quad [\text{A.2.54}]$$

where

$$\mathcal{R}^2 = \begin{pmatrix} 0 & -R_z & R_y \\ R_z & 0 & -R_x \\ -R_y & R_x & 0 \end{pmatrix} \begin{pmatrix} 0 & -R_z & R_y \\ R_z & 0 & -R_x \\ -R_y & R_x & 0 \end{pmatrix} \quad [\text{A.2.55}]$$

$$= \begin{pmatrix} -R_y^2 - R_z^2 & R_x R_y & R_x R_z \\ R_x R_y & -R_x^2 - R_z^2 & R_y R_z \\ R_x R_z & R_y R_z & -R_x^2 - R_y^2 \end{pmatrix}. \quad [\text{A.2.56}]$$

Possibly noteworthy is that:

$$\mathcal{R}^2 + R\mathbf{I} = \begin{pmatrix} -R_y^2 - R_z^2 & R_x R_y & R_x R_z \\ R_x R_y & -R_x^2 - R_z^2 & R_y R_z \\ R_x R_z & R_y R_z & -R_x^2 - R_y^2 \end{pmatrix} + \begin{pmatrix} R^2 & 0 & 0 \\ 0 & R^2 & 0 \\ 0 & 0 & R^2 \end{pmatrix} \quad [\text{A.2.57}]$$

$$= \begin{pmatrix} R_x^2 & R_x R_y & R_x R_z \\ R_x R_y & R_y^2 & R_y R_z \\ R_x R_z & R_y R_z & R_z^2 \end{pmatrix} = \mathbf{R} \mathbf{R}^T. \quad [\text{A.2.58}]$$

For the motion in 2D ($x - y$) plane, we are only interested in F_x , F_y and τ_z as a function of U_x , U_y and Ω_z . Here we also assume $R_z = 0$, so we are only interested in components 1,2 and 6

$$\begin{pmatrix} F_x \\ F_y \\ \tau_z \end{pmatrix} = \begin{pmatrix} V_T & 0 & V_T \mathcal{R}_{13} \\ 0 & V_T & V_T \mathcal{R}_{23} \\ -V_T \mathcal{R}_{31} & -V_T \mathcal{R}_{32} & V_R - V_T \mathcal{R}_{32}^2 \end{pmatrix} \begin{pmatrix} U_x \\ U_y \\ \Omega_z \end{pmatrix} \quad [\text{A.2.59}]$$

$$= \begin{pmatrix} V_T & 0 & V_T R_y \\ 0 & V_T & V_T R_x \\ -V_T R_y & -V_T R_x & V_R + R^2 V_T \end{pmatrix} \begin{pmatrix} U_x \\ U_y \\ \Omega_z \end{pmatrix}. \quad [\text{A.2.60}]$$

Up until now, we haven't actually specified where our origin is. Let's set the origin to be at point P on the surface of the bead ($\mathbf{R}_P = \mathbf{0}$). We will choose \mathbf{X} to point tangent to the flagella at the point of attachment, and let the coordinates of the center of the bead be located at $\mathbf{R}_{P'} = (X_B, Y_B, 0)$. Note that $X_B \leq 0$ and $-R \leq Y_B \leq R$ (Figure A.2.6D). Also note that $\mathbf{R} = -\mathbf{R}_{P'}$, so the force equation reads:

$$\begin{pmatrix} F_x \\ F_y \\ \tau_z \end{pmatrix} = \begin{pmatrix} V_T & 0 & -V_T Y_B \\ 0 & V_T & V_T X_B \\ -V_T Y_B & V_T X_B & V_R + V_T R^2 \end{pmatrix} \begin{pmatrix} U_x \\ U_y \\ \Omega_z \end{pmatrix}, \quad [\text{A.2.61}]$$

Which was previously extracted in Eq. A.2.42. Note that setting $Y_B \neq 0$ allows us to handle the case where the flagella is not attached normal to the bead.

(11) Analytical approximations of rotational and translational of an axonemal-propelled bead

In this part, we discuss analytical approximations for the mean translational and rotational velocities of a flagellar-propelled bead in the regime of small wave amplitude. To describe the

traveling curvature waves analytically, we use the following simplified waveform which is composed of a traveling wave component with amplitude C_1 superimposed on a circular arc with the mean curvature of C_0

$$C(s, t) \approx C_0 + C_1 \cos(\omega_0 t - \kappa s), \quad [\text{A.2.62}]$$

where $\omega_0 = 2\pi f_0$, $\kappa = 2\pi/\lambda$ is the wave number. For our exemplary axoneme in Chapter 5, Figure 5.2, following the method described in the ref.⁴¹, we calculate the wavelength to be $\lambda \sim 13.19 \mu\text{m}$ (see Figure A.2.7), which is $\sim 27\%$ larger than the axonemal contour length $L \sim 10.38 \mu\text{m}$.

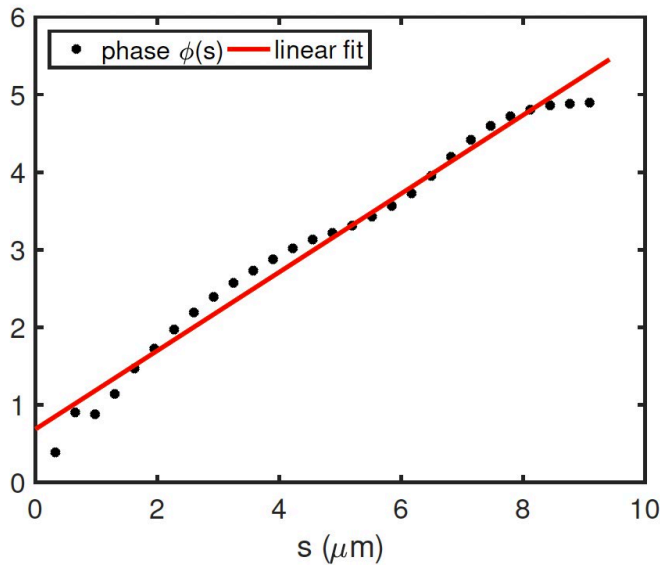


Figure A.2.7: Calculation of phase of travelling wave. The phase $\phi(s)$ of traveling curvature waves of the axoneme presented in Chapter 5, Figure 5.1, obtained by performing Fourier transform in time at each position s along the axonemal length. The wavelength is then calculated as $\lambda = 2\pi L / (\phi(L) - \phi(0)) = 13.19 \mu\text{m}$.

Next, we obtain analytical expressions for the mean translational and rotational velocities of the swimmer in the regime of small C_0 and C_1 . For our analytical approximations and simulations, we used the RFT which is presented in section A.2(8). To check the validity of RFT, we extracted rotational and translational velocities of another exemplary axonemal-driven

bead and compared the results with velocities obtained by RFT simulations using experimental beat patterns. This comparison is presented in Figure A.2.8, which demonstrates a semi-qualitative agreement between RFT simulations and experimental data (see section A.2(8)). In the rest of section, we will use the simplified waveform, as defined in Eq. A.2.62 to perform analytical analysis as well as numerical simulations for two cases: first, for a symmetric bead-axoneme attachment, and second, for an asymmetric attachment.

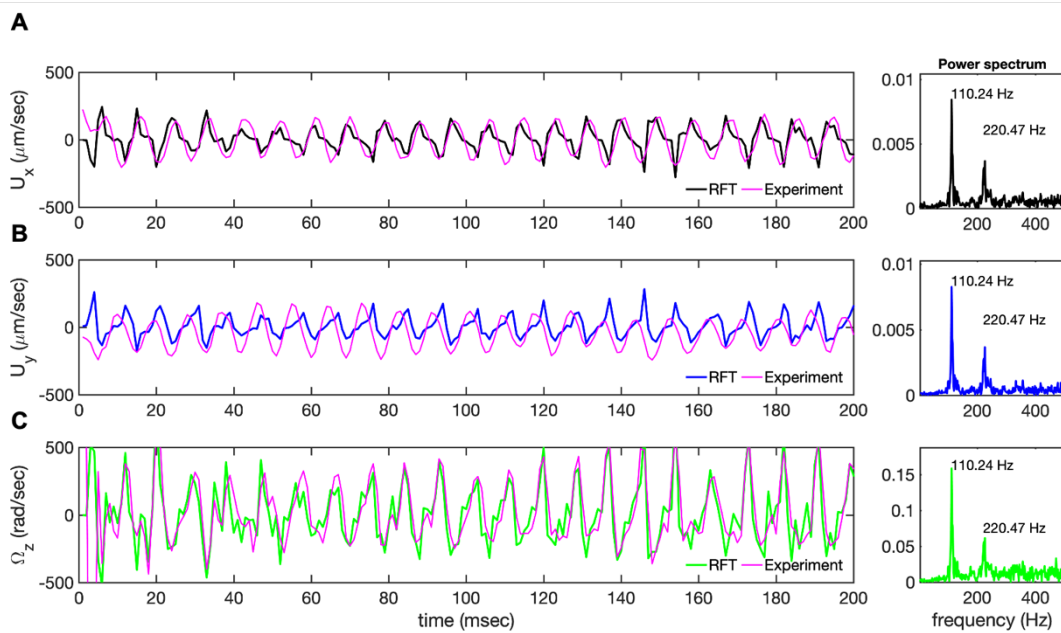


Figure A.2.8: Velocity components of the bead's center. $U_x(t)$ and $U_y(t)$ and the rotational velocity of the bead $\Omega_z(t)$ measured in the body-fixed frame of the exemplary axoneme. Comparison with results obtained in the frame work of resistive-force theory shows a good agreement. The power spectra show a dominant peak at the beat frequency of 110.24 Hz and its second harmonic.

(10.1) Symmetric bead-axoneme attachment

Let us first consider the example where an axoneme is attached from the basal side to a bead, so that the tangent vector at $(s = 0)$ passes through the bead center. To determine the translational and rotational velocities of the swimmer in dependence of the dimensionless bead radius $r = R = L$, we used the prescribed form of curvature waves in Eq. A.2.62 and imposed the force-free and torque-free constraints in 2D. The drag matrices of bead and

axoneme are calculated with respect to the reference point, which is defined as the bead-axoneme contact point (see section A.2.(9)).

We approximate analytically the averaged angular and linear velocities in the swimmer-fixed frame, as defined in Chapter 5, Figure 5.1A, in the limit where the wavelength of the beat-pattern, λ , is equal to the size of the axoneme, L , and up to the first order in C_0 and C'_0 and the second order in C_1 to obtain:

$$\frac{\langle \Omega_z \rangle}{\omega_0} \approx \beta_1(r, \zeta'_\perp, \eta) C_0 C_1^2, \quad [\text{A.2.63}]$$

$$\frac{\langle U_x \rangle}{L\omega_0} \approx \beta_2(r, \zeta'_\perp, \eta) C_1^2, \quad [\text{A.2.64}]$$

$$\frac{\langle U_y \rangle}{L\omega_0} \approx \beta_3(r, \zeta'_\perp, \eta) C_0 C_1^2. \quad [\text{A.2.65}]$$

The full expressions of functions β_1 , β_2 and β_3 are presented in, Eqs. A.2.66- 68.

$$\begin{aligned} \frac{\langle \Omega_z \rangle}{\omega_0} \approx & \frac{7C_0 C_1^2 \zeta'_\perp}{5\pi^3(7\eta \zeta'_\perp + 96\pi r) (73728\pi^2 r^4 + 2688\zeta'_\perp \pi(r(5r+3)+1)r + 49\zeta'^2_\perp)^2} (5(24461180928 \\ & \times (\eta-1)\pi^8 r^7 + 42467328\pi^6(-720\eta + 32(9\eta-11)\pi^2 + 7(\eta-1)(2\eta+9)\zeta'_\perp \pi + 240)r^6 \\ & + 3096576\zeta'_\perp \pi^5(-24\eta(26\eta+67) + 16(\eta(8\eta+31) - 47)\pi^2 + 35(\eta-1)\zeta'_\perp \pi + 552)r^5 \\ & + 258048\zeta'_\perp \pi^4(288\pi(4\pi^2\eta - 21\eta - 4\pi^2 + 9) + 7\zeta'_\perp(-3\eta(65\eta+23) + (\eta(8\eta+67) \\ & - 83)\pi^2 + 24))r^4 + 2688\zeta'_\perp \pi^3(-735(\eta(9\eta-4) + 1)\zeta'^2_\perp + 14112(\eta-1)\pi^3\zeta'_\perp - 6048 \\ & \times (\eta+3)(3\eta-1)\pi\zeta'_\perp + 18432(\eta-1)\pi^4 + (245(2\eta^2 + \eta - 3)\zeta'^2_\perp - 27648(5\eta-3))\pi^2 \\ & + 82944(2\eta-1)r^3 + 56448\zeta'^2_\perp \pi^2(112\pi^4(\eta-1) + 7(\eta+2)\zeta'_\perp \pi^3(\eta-1) - 24(\eta(4\eta+31) \\ & - 17)\pi^2 + 288(\eta+2)(2\eta-1) + 21\eta(1-5\eta)\zeta'_\perp \pi)r^2 + 32928\zeta'^3_\perp \pi(7\pi^4(\eta-1) - 3(\eta(13\eta \\ & + 5) - 6)\pi^2 + 36(4\eta^2 - 1))r - 2401\zeta'^4_\perp(9(-8 + \pi^2)\eta^2 - (-36 + \pi^4)\eta + \pi^4 - 3\pi^2)), \end{aligned} \quad [\text{A.2.66}]$$

$$\begin{aligned}
\frac{\langle U_y \rangle}{L\omega_0} \approx & -\frac{7C_0C_1^2\zeta'_\perp}{30\pi^3(7\eta\zeta'_\perp + 96\pi r)(73728\pi^2r^4 + 2688\zeta'_\perp\pi(r(5r+3)+1)r + 49\zeta_\perp'^2)} (45) \quad [\text{A.2.67}] \\
& \times (7\zeta'_\perp(-4718592\pi^5(4\pi^2(5r+2)-39)r^6 + 516096\zeta'_\perp\pi^2(\pi^2(r(35r-6)+1)-6)r^3 \\
& + 3136\zeta_\perp'^2\pi(4\pi^4(5r+2)r - 72r - 3\pi^2(r(90r+29)+6)+36)r - 1029\zeta_\perp'^3(-8+\pi^2))\eta^2 \\
& + (-1358954496\pi^6(\pi^2(20r+6)-15)r^7 - 16515072\zeta'_\perp\pi^3(-3\pi^2(33r^2+6r+5) \\
& + 2\pi^4(r(r(70r+39)+12)+1)+18)r^4 - 301056\zeta_\perp'^2\pi^2(36(r-1)+3\pi^2(r(80r^2+74r+39) \\
& + 10)+2\pi^4(r(2r(5r(20r+19)+46)+25)+4))r^2 - 10976\zeta_\perp'^3\pi(-36(2r+1) \\
& + 2\pi^4(4r+1)(5r+2)-3\pi^2(4r(25r+6)+1))r + 2401\zeta_\perp'^4(-12+\pi^2))\eta + 32\pi r(14155776\pi^5 \\
& \times (\pi^2(60r+22)-15)r^6 + 516096\zeta'_\perp\pi^2(-3\pi^2(r(13r+6)+3)+2\pi^4(r(r(90r+49)+9)+1)+9) \\
& \times r^3 + 9408\zeta_\perp'^2\pi(36r+3\pi^2(20r^3+2r^2+r+2))+2\pi^4(r(2r(5r(20r+17)+31)+15)+2)-18)r \\
& + 343\zeta_\perp'^3(\pi^4(6r+2)-3\pi^2(4r+1)(10r+1)-36))) .
\end{aligned}$$

$$\begin{aligned}
\frac{\langle U_x \rangle}{L\omega_0} \approx & -\frac{21C_0^2\zeta'_\perp}{6\pi^2(49\zeta_\perp'^2 + 2688\pi\zeta'_\perp(r(5r+3)+1)r + 73728\pi^2r^4)(7\eta\zeta'_\perp + 96\pi r)} (49(6\eta \\
& + \pi^2 - 3)\zeta_\perp'^2 - 672\pi\zeta'_\perp r(2\eta(\pi^2(r(20r+9)+2)-3) - \pi^2(2r(20r+9)+5)+3) - 221184\pi^4(\eta-1)r^4), \quad [\text{A.2.68}]
\end{aligned}$$

Here $\zeta'_\perp = \zeta_\perp/\mu = 2\zeta_\parallel/u \sim 8\pi/(\log(2L/a) + 0.5) \sim 4.33$ where $a = 100$ is the radius, $L \sim 10\mu\text{m}$ is the contour length of axoneme and we have assumed $\eta = \zeta_\parallel/\zeta_\perp = 0.5$. Note that in the absence of the bead ($r = 0$) and with $\eta = 0.5$, Eqs. A.2.66-68 simplify to:

$$\frac{\langle \Omega_z \rangle}{\omega_0} \approx -0.42C_0C_1^2, \quad [\text{A.2.69}]$$

$$\frac{\langle U_x \rangle}{L\omega_0} \approx -0.16C_1^2, \quad [\text{A.2.70}]$$

$$\frac{\langle U_y \rangle}{L\omega_0} \approx +0.038C_0C_1^2. \quad [\text{A.2.71}]$$

The results for a bead of size $r = 0.1$ with drag anisotropy $\eta = \zeta_{\parallel} / \zeta_{\perp} = 0.5$, Eqs. A.2.63-65 simplifies to

$$\frac{\langle \Omega_z \rangle}{\omega_0} \approx -0.24 C_0 C_1^2 \quad [\text{A.2.72}]$$

$$\frac{\langle U_x \rangle}{L\omega_0} \approx -0.04 C_1^2 \quad [\text{A.2.73}]$$

$$\frac{\langle U_y \rangle}{L\omega_0} \approx 0.006 C_0 C_1^2 \quad [\text{A.2.74}]$$

We note that in Eqs. A.2.63-65, without the even harmonic, i.e intrinsic curvature $C_0 = 0$, the axoneme swims in a straight path with $\langle U_y \rangle = 0$, $\langle U_x \rangle$ proportional to the square of traveling wave component C_1 ^{205, 246, 247} and the mean rotational velocity $\langle \Omega_z \rangle$ vanishes (see the solid lines in Figure A.2.9A-F and Figure A.2.10).

In parallel to our analytical approximations, we also performed numerical simulations given the simplified waveform in Eq. A.2.62 and using RFT with the realistic value of $\eta = \zeta_{\parallel} / \zeta_{\perp} = 0.5$. As shown in Figure A.2.9A-F, the comparison between numerical simulations and the full analytical approximations presented in Eqs. A.2.66-68, shows a good agreement at small values of C_0 and C_1 and deviations at larger values. In addition, three exemplary simulations in Figure A.2.9G-I highlight the dependency of the mean rotational velocity $\langle \Omega_z \rangle$ of the model swimmer on the square of the traveling wave component C_1 . To investigate the dependency of the mean translational and rotational velocities of our model swimmer on the bead size, we plotted Eqs. A.2.63-65 as a function of r (Figure A.2.11). We also performed numerical simulations at different bead radii. As shown in Figure A.2.11, there is a good agreement between our numerical simulations and analytical approximations at small values of C_1 (panels A-C) but deviations at larger values (panels D-F). Furthermore, it is remarkable that while $\langle U_x \rangle$ reduces monotonically with the bead radius r , both $\langle \Omega_z \rangle$ and $\langle U_y \rangle$ exhibit a non-monotonic dependence. This anomalous behavior is counter-intuitive, since rotational and translational speeds are expected to decrease with increasing the bead radius. To examine this anomalous

behavior, we looked at the asymptotic expressions of Eqs. A.2.63- 65 in two opposite limits of small and large bead radii.

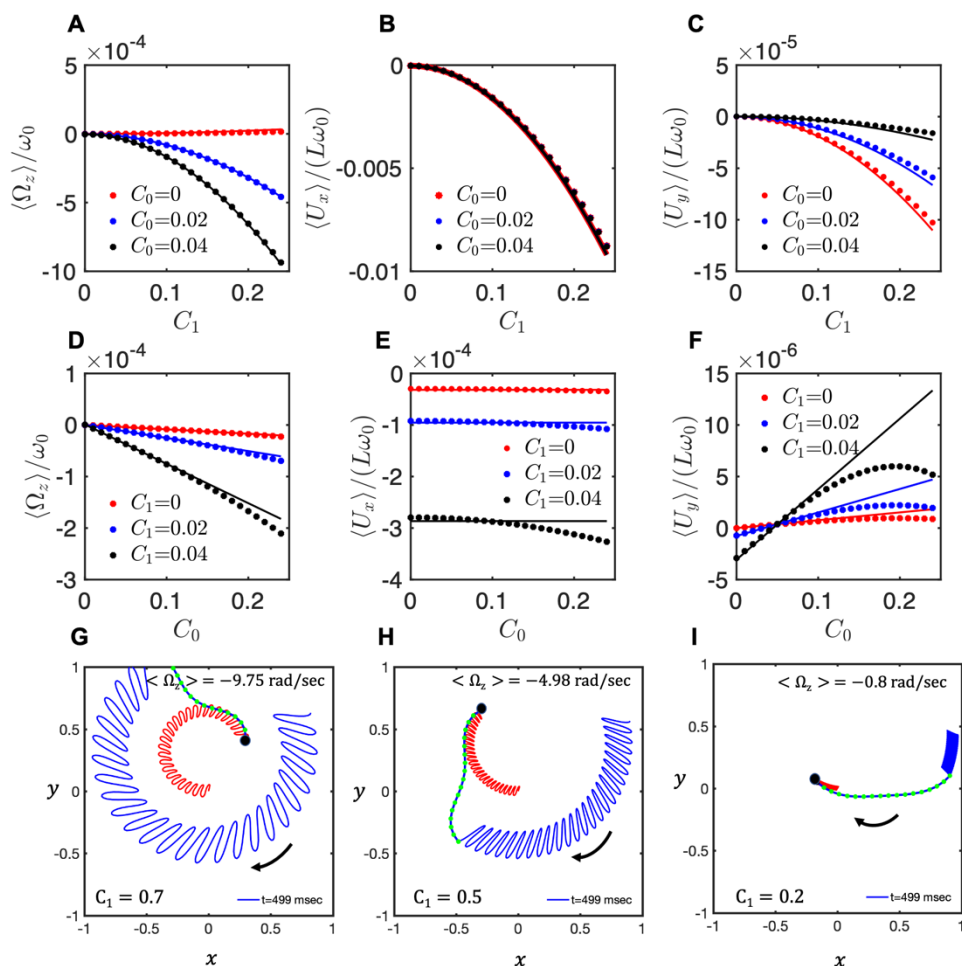


Figure A.2.9: Comparison of analytical approximations of rotational and translational velocities with numerical simulations at bead radius of $R = 0$. Solid lines present the analytical approximations summarized in Eqs. A.2.61-63 and dots show the numerical simulations. G-I) Numerical simulations performed with the simplified waveform to show the effect of C_1 . A bead of radius $R/L = 0.1$ is attached symmetrically to a model flagellum. The mean rotational velocity decreases as the amplitude of dynamic mode C_1 decreases from G) $C_1 = 0.7$ to H) $C_1 = 0.5$ and further to I) $C_1 = 0.2$. The static curvature is fixed at $C_0 = 0.2$.

For the case where the bead radius R is much larger than the flagellar length L (small $1/r$), we obtain up to the second order in r^{-1}

$$\frac{\langle \Omega_z \rangle}{\omega_0} \approx \frac{21C_0C_1(\eta-1)\zeta'_\perp r^{-2}}{64}, \quad [\text{A.2.75}]$$

$$\frac{\langle U_x \rangle}{\omega_0} \approx \frac{7C_1^2(\eta-1)\zeta'_\perp r^{-1}}{36864\pi^2} (576\pi - 7(6\eta + 5)\zeta'_\perp r^{-1}), \quad [\text{A.2.76}]$$

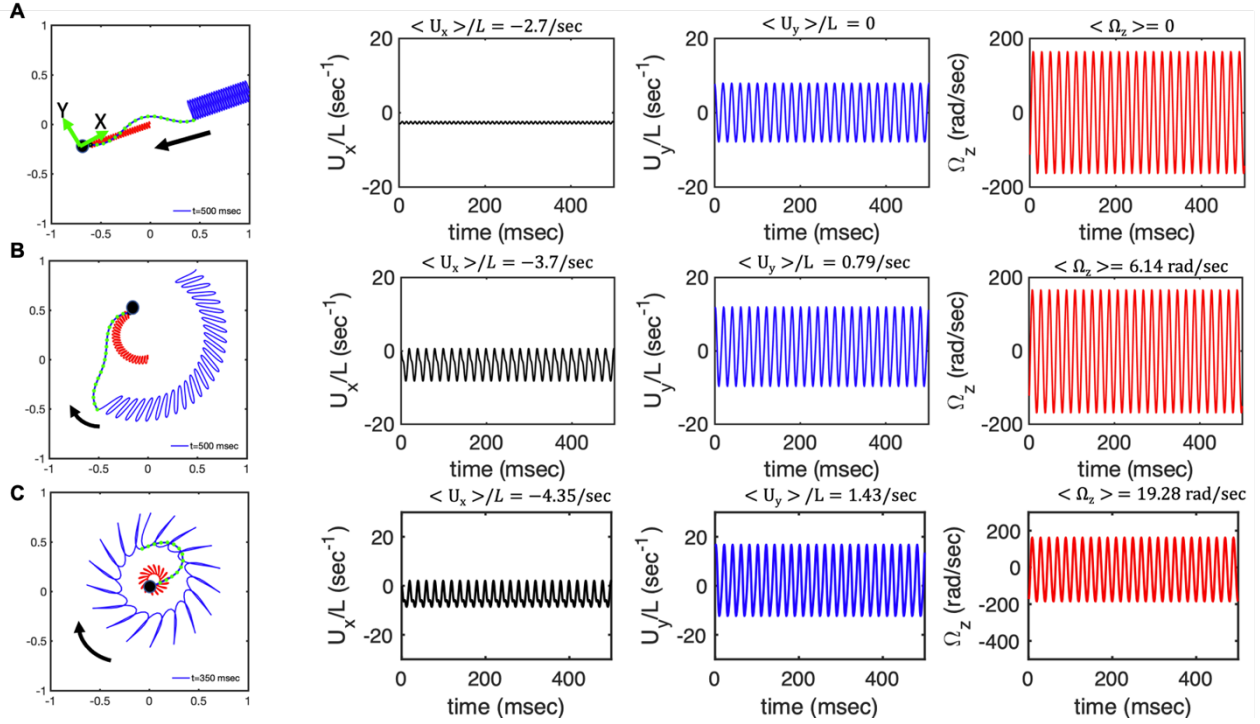


Figure A.2.10: Simulations to show the effect of C_0 at a fixed amplitude of dynamic mode $C_1 = 0.5$. A bead of radius $R/L = 0.1$ is attached to the basal end. A-C) Swimming trajectory and mean translational and rotational velocities of the swimmer in the body-fixed frame. Parameters are $f_0 = 50$ Hz, $\eta = \zeta_{\parallel} / \zeta_{\perp} = 0.5$, A) $C_0 = 0$, B) $C_0 = 0.25$, and C) $C_0 = 0.5$.

$$\frac{\langle U_y \rangle}{\omega_0} \approx \frac{7C_0C_1^2r^{-1}}{36864\pi^2} (35\pi(\eta - 1)(4\eta + 21)\zeta'_\perp r^{-1} + 720(3\eta - 1)r^{-1} - 96\pi^2(\eta(9r^{-1} + 30) - 11r^{-1} - 30)). \quad [\text{A.2.77}]$$

In the opposite limit of small r (i.e. $R \ll L$), up to the second order in r , we set $\eta = 0.5$ and $\zeta'_\perp = \zeta_\perp / \mu = 4\pi / (\ln(2L/a) + 0.5) \sim 4.33$ to get:

$$\frac{\langle \Omega_z \rangle}{L\omega_0} \approx -0.42C_0C_1^2(1 - 19.15r + 513.77r^2), \quad [\text{A.2.78}]$$

$$\frac{\langle U_x \rangle}{L\omega_0} \approx -0.6C_1^2(1-29.85r + 960.23r^2), \quad [\text{A.2.79}]$$

$$\frac{\langle U_y \rangle}{L\omega_0} \approx 0.038C_0C_1^2(1+39.8r - 3941.65r^2). \quad [\text{A.2.80}]$$

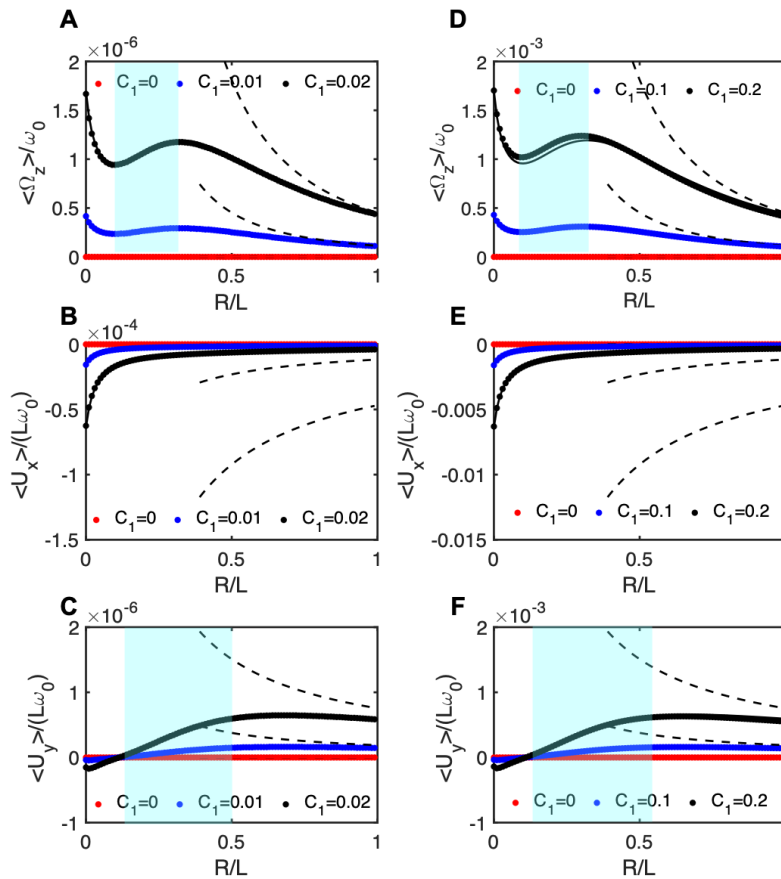


Figure A.2.11: Anomalous flagella-based propulsion speed of a symmetrically attached bead as a function of its dimensionless radius R/L . Contrary to expectations, in the cyan region the mean translational and rotational velocities increase with increasing the bead radius. Analytical approximations (continuous lines calculated from Eqs. A.2.64-66) and simulations (dotted points) are performed at different values of C_1 , while the intrinsic curvature of the axoneme is fixed at $C_0 = -0.01$ in (A-C), and $C_0 = -0.1$ in (D-F). The black dashed curves show the trend expected in the limit of large bead radius ($r = R/L > 1$), as presented in Eqs. A.2.73-75. The black dashed lines with stars in magenta illustrate the opposite limit of the small r , as given in Eqs. A.2.76-78.

The black dashed lines (with and without stars in pink color) in Figure A.2.11 show these asymptotic results. The transition from r^2 dependency at small values of bead radius to r^{-2} trend at large values of r manifests itself in an anomalous behavior. Finally, we note that in the

absence of the bead ($r = 0$), Eqs. A.2.78-80 reduce to Eqs. A.2.69-71 as discussed in the Refs.^{50,}

195

(10.2) Rotational velocity of a bead attached asymmetrically to a freely-swimming axoneme

To mimic a sperm-like swimmer, we consider a model flagellum with only the main traveling wave component C_1 , setting the other modes to zero ($C'_0 = C'_1 = C_1 = 0$). We calculate the mean rotational velocity of an axoneme attached sideways to a bead using the matrix introduced Eq. A.2.61 and drag matrix of flagellum to obtain:

$$\begin{aligned}
 \langle \Omega_z \rangle / \omega_0 \approx & - \left(8064C_1^2 \zeta'_\perp r y_b \left(7\eta^2 \zeta'_\perp (343\zeta'^3_\perp (6 + \pi^2) - 2352\zeta'^2_\perp \pi r (-24 + \pi^2) \right. \right. \\
 & \times (-3 + 40r^2 - 12x_b) - 5308416\pi^5 r^3 (5r^2 - 3x_b^2) - 129024\zeta'_\perp \pi^2 r^2 \\
 & \times (-3 + \pi^2 (-1 + 25r^2 - 12x_b^2)) + 288\pi r (-343\zeta'^3_\perp + 21504\zeta'_\perp \pi^2 r^2 \\
 & \times (-3 + \pi^2 (-1 + 50r^2 - 24x_b^2 - 30y_b^2)) + 784\zeta'^2_\perp \pi r (-12 + \pi^2 (1 + 40r^2 \\
 & - 12x_b - 24y_b^2)) + 3538944\pi^5 r^5 + 3\eta (-2401\zeta'^4_\perp + 5488\zeta'^3_\perp \pi^3 r \\
 & \times (3 + 40r^2 - 12x_b) - 4128768\zeta'_\perp \pi^3 r^3 (-3 + \pi^2 (-1 + 10r^2 - 3x_b^2 - 15y_b^2)) \\
 & - 339738624\pi^6 r^6 + 75264\zeta'^2_\perp \pi^2 r^2 \times (18 + \pi^2 (1 + 60r^2 + 12(1 - 4x_b)x_b \\
 & \left. \left. + 24y_b^2)) \right) \right) / \left(2\pi^2 \left((7\eta \zeta'_\perp + 96\pi r)(49\zeta'^2_\perp + 2688\zeta'_\perp \pi r (1 + 5r^2 - 3x_b) \right. \right. \\
 & \left. \left. + 36864\pi^2 r^2 (5r^2 - 3x_b^2) - 110592\pi^2 r^2 (7\zeta'_\perp + 96\pi r)y_b^2 \right)^2 \right) \quad [A.2.81]
 \end{aligned}$$

where $x_b^2 + y_b^2 = r^2$, $\zeta'_\perp = \zeta_\perp / \mu = 4.3$ and $\zeta_\parallel / \zeta_\perp = 0.5$.

(10.3) The sideways bead-axoneme attachment contributes to the rotational velocity of the swimmer

In our experiments, we frequently observed an asymmetric attachment of a bead to an axoneme, i.e. the tangent vector of the axoneme at $s = 0$ does not pass through the bead center. This case is schematically shown in Figure A.2.5 and Figure A.2.12 B. Care needs to be

taken since, as mentioned previously, a bead that appears to be symmetrically attached to an axoneme in our 2D phase-contrast images, could in reality be attached asymmetrically and 3D imaging techniques are necessary to distinguish these two scenarios. Interestingly, our analytical approximations and simulations confirm that this asymmetric bead-axoneme attachment is enough to rotate the axoneme and presence of static curvature and second harmonic are not necessary for rotation to occur. For this analysis, we consider the 2D case where the center of the bead is at position X_B and Y_B which is measured with respect to the coordinate system defined at the bead-axoneme contact point (Figure A.2.5 and Chapter 5, Figure 5.1A). The drag matrix of the bead is given by Eq.A.2.44. To focus on the effect of the sideways bead attachment on the axonemal rotational velocity, we set both modes C_0 and C'_0 to zero and consider a model sperm-like axoneme with only the traveling wave component $C_1 \neq 0$ in Eq. A.2.62. We calculate the mean rotational velocity of the axonemal-driven bead by combining the drag matrix of the bead and the axoneme (see section A.2.(9) to arrive at:

$$\langle \Omega_z \rangle / L\omega_0 \approx \alpha(\eta, \zeta'_\perp, y_b, r) C_1^2, \quad [\text{A.2.82}]$$

where dimensionless quantities are $r = R/L$, $y_b = Y_B/L$, $\eta = \zeta_\parallel / \zeta_\perp$ and $\eta = \zeta_\parallel / \zeta_\perp$ and $\zeta'_\perp = \zeta_\perp / \mu = 4\pi / (\log(2L/a) + 0.5)$.

Here μ is the viscosity of the ambient water-like fluid and $a = 100$ nm is the axonemal radius. Note that variable $x_b^2 = r^2 - y_b^2$ is not an independent variable. For the complete form of the function, see Eq. A.2.81.

Some important characteristics of Eq. A.2.82 are as follows: First, since intrinsic C_0 curvature even harmonics are set to zero, $\langle \Omega_z \rangle$ is zero for the case of a symmetric bead attachment, i.e. $x_b = R/L$ and $y_b = 0$. The effect of sideways bead attachment on rotational velocity of the axoneme is highlighted in Figure A.2.12A-C. In these simulations, the model axoneme has only the traveling wave component C_1 and it swims in a straight path if the bead is attached symmetrically (Figure A.2.12A). An asymmetric bead-axoneme attachment causes the axoneme to rotate (Figure A.2.12B-C). Second, a comparison between the effect of the intrinsic

curvature (Eq. A.2.68 with $r = 0$) versus asymmetric bead attachment (Eq. A.2.82 with $\eta = 0.5$, $\zeta_{\parallel}' = 4.33$ and $r = 0.2$) on rotational velocity shows that the contribution of the asymmetry in

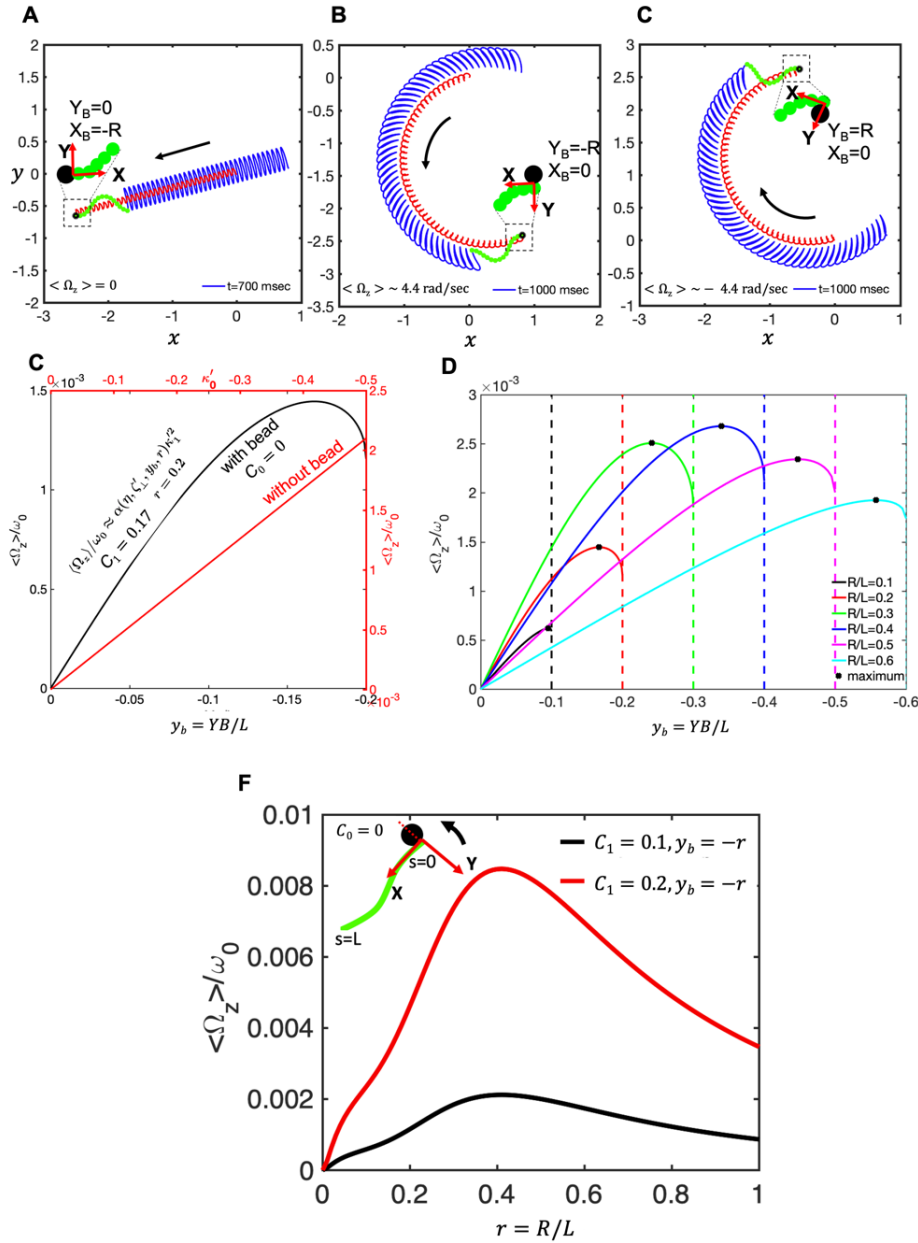


Figure A.2.12: Comparison of symmetric vs asymmetric bead attachment with axoneme. A-C) Asymmetric versus symmetric bead attachment to an axoneme with a beat pattern consisting only of the traveling wave component C_1 . While the axoneme in panel A, to which the bead is symmetrically attached, swims on a straight path, the axonemes in panel B and C, with asymmetric bead attachment, swim on curved paths. D) Comparison of the effect of the asymmetric bead attachment (in black) as a function of y_b versus the effect of the intrinsic curvature C_0 (in red) on $\langle \Omega_z \rangle$. E) The averaged angular velocity $\langle \Omega_z \rangle$ changes non monotonically with y_b for different bead radii. X_B and Y_B are the coordinates of the bead center in the swimmer-fixed reference frame. Parameters are $\eta = 0.5$, $\zeta_{\parallel}' = 4.33$ and $C_0 = 0.1$. F) The mean rotational velocity of a bead which is asymmetrically attached to an axoneme with $y_b = -r$ and $x_b = 0$ for two different values of C_1 . The mean curvature C_0 is set to zero.

the attachment to $\langle \Omega_z \rangle$ is comparable to that of the intrinsic curvature, C_0 , see Figure A.2.12D. Third, as shown Figure A.2.12E, the maximum rotational velocity occurs in the vicinity of $y_b = -r$. the maximum $\langle \Omega_z \rangle$ occurs around $r = 0.4$.

(12) Supporting Figures

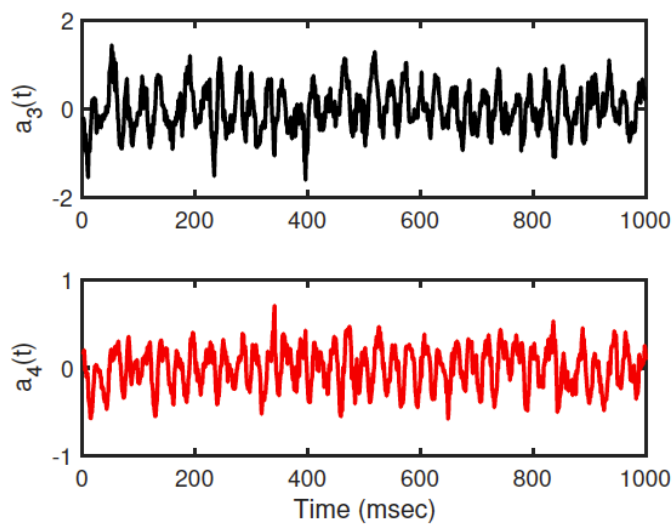


Figure A.2.13: Time -dependent coefficients $a_3(t)$ and $a_4(t)$ calculated using the PCA for freely beating axoneme presented in Chapter 4, Figure 4.2.

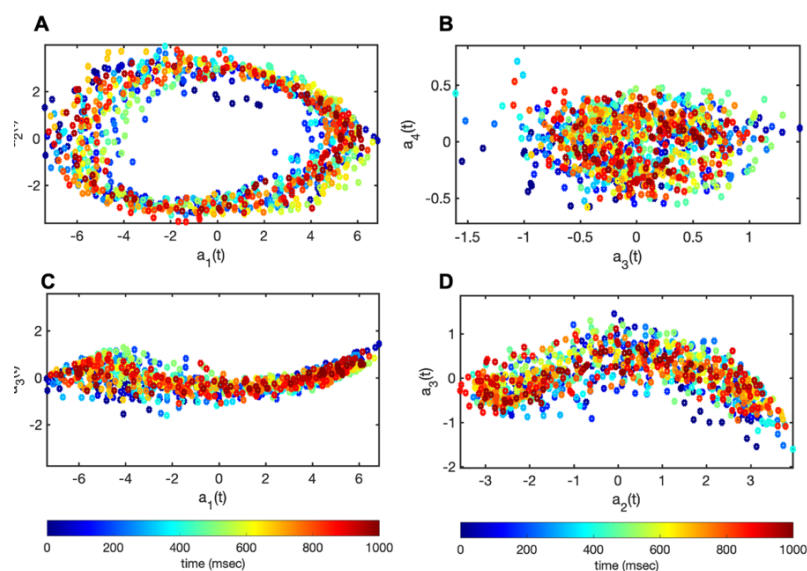


Figure A.2.14: Comparison of time-dependent coefficients calculated using PCA. A) Two time-independent coefficients $a_1(t)$ and $a_2(t)$ are plotted versus each other showing a limit cycle. B-C) For comparison, $a_4(t) - a_3(t)$, $a_3(t) - a_1(t)$ and $a_3(t) - a_1(t)$ plots are also presented. These coefficients are calculated using the PCA for the freely beating axoneme presented in chapter 4, Figure 4. 2.

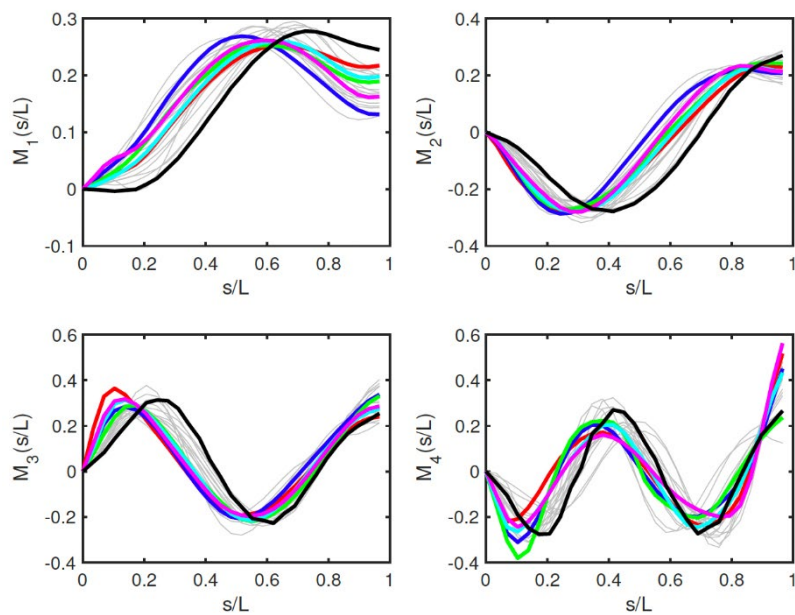


Figure A.2.15: PCA analysis of the flagellar beat of free axonemes. Four main eigenmodes corresponding to the four largest eigenvalues for 21 freely beating axonemes are presented. Each trace corresponds to a different axoneme from different experiments. The modes show a common trend after being re-scaled by the contour length L . The black, red, blue, green, cyan and magenta curves correspond to the six axonemes described in the first through sixth rows of the Appendix, Table A.2.2, respectively. Note that the x -axis is scaled by the axonemal contour length L (see Figure A.2.15 for the case that s is scaled by the wavelength λ). A scatter plot showing the wavelength and the contour length of these axonemes is shown in Figure A.2.16.

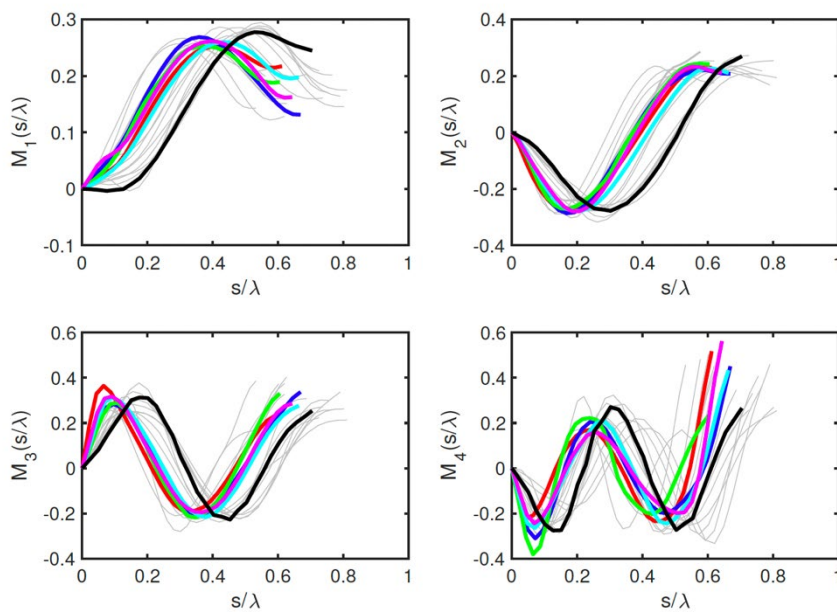


Figure A.2.16: Traces of the four PCA modes of 21 different free axonemes presented in Figure 4.6, re-scaled by s/λ . See the caption of Figure A.2.15 for the color-code and Figure A.2.16 for the ATP concentrations.

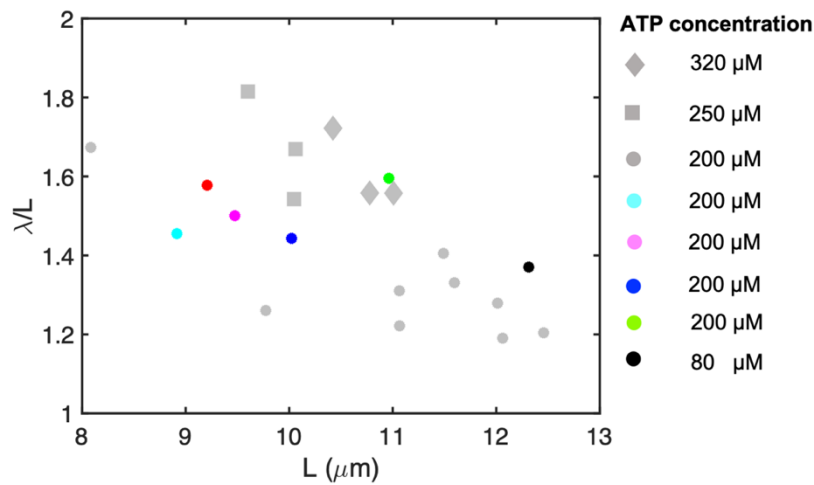


Figure A.2.17: A scatter plot showing the wavelength and the contour length of 21 different free axonemes used in the analysis of Figure 4.6 and 4.7. Each data point presents one axoneme. The black circle corresponds to the axoneme presented in Figure 4.2. For the color code, which is the same as Figure 4.7, see the caption of Figure 4.6.

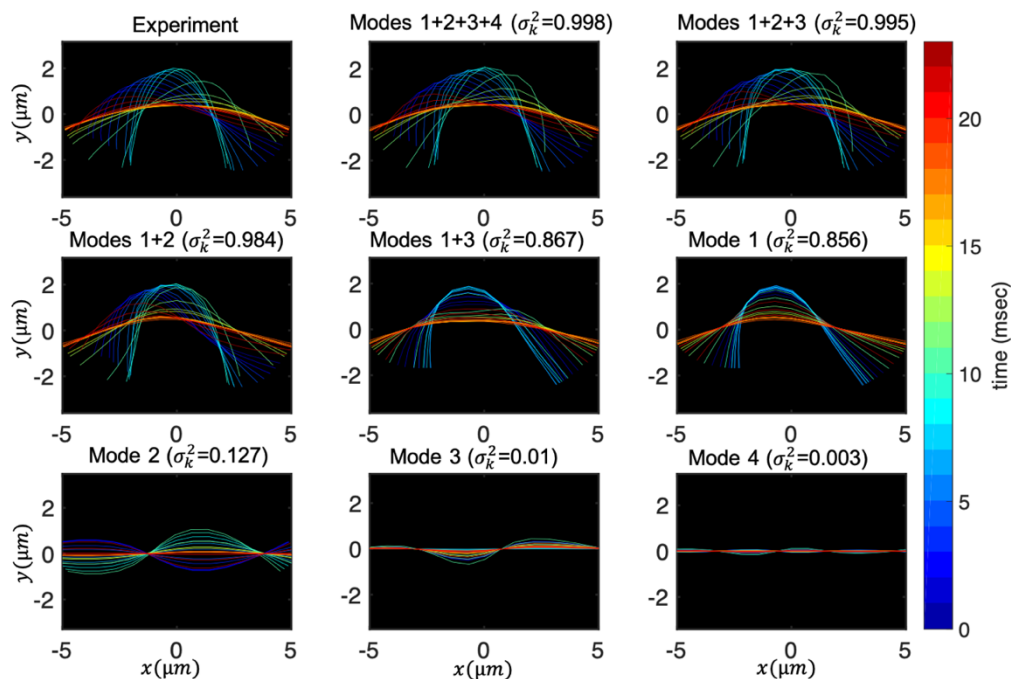


Figure A.2.18: Experimental shapes of the hinged axoneme in Figure 4.12 plotted over one beat cycle ($T = 22.55$ msec), are compared with the axonemal shapes reconstructed using different combination of the modes. For each panel, fraction of the total variance σ_k^2 is calculated (see Chapter 2, section 2.9).

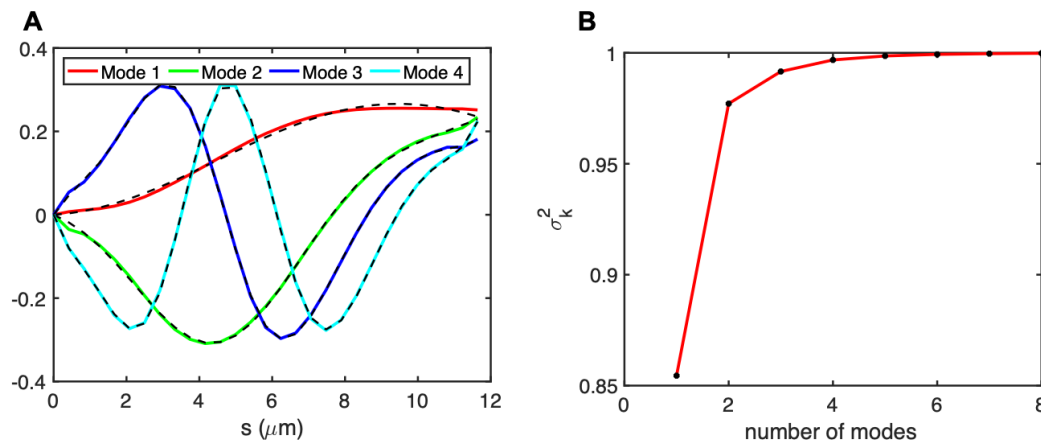


Figure A.2.19: PCA analysis of the flagella in the intact *C. reinhardtii* cell presented in Figure 4.1A-B. The table in Appendix A.2.5 shows the wave amplitudes and the phase values as defined in Appendix Eq. A.2.7.

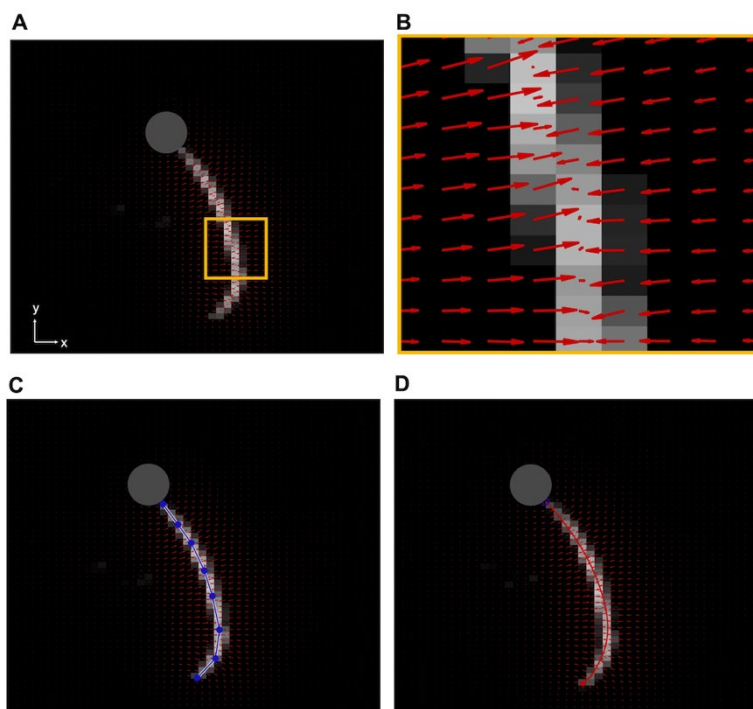


Figure A.2.20: Gradient vector flow method implemented to track the flagellum. A) High intensity of the bead interferes with tracking; therefore, it is removed by applying a threshold. B) The vector field calculated for small yellow region shown in panel A, converging toward pixels with maximum intensity. C) A polygonal line with eight nodes along the axonemal contour to initiate the snake. D) The tracking algorithm yields a discrete approximation of the axoneme's contour represented by a set of $N = 30$ positions $\mathbf{r}(s, t) = ((s_i, t), y(s_i, t))$, $i = 1, \dots, N$.

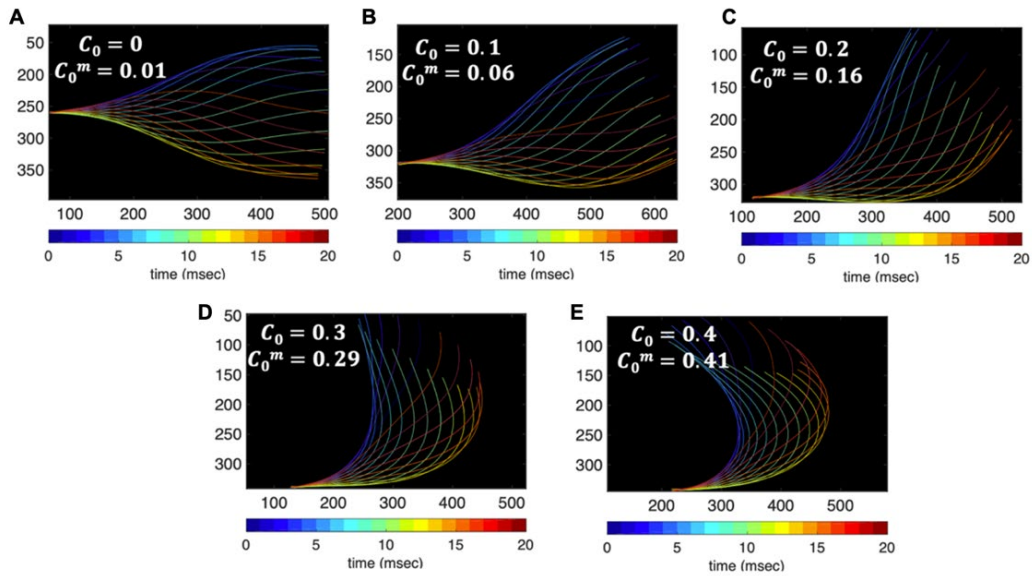


Figure A.2.21: To measure the systematic error of our tracking GVF algorithm, we generated artificial data with known values of dimensionless mean curvature $C_0 = \kappa_0 L / 2\pi$, and tracked the filaments using GVF. The measured values of mean curvatures of tracked filaments is given by C_0^m . As it is shown in the panels A-E, the measured values deviate from the real values at small C_0 , but approaches the real values at higher. In other words, our algorithm has a smaller systematic error (less than 4%) for curved filaments with $C_0 > 0.3$.

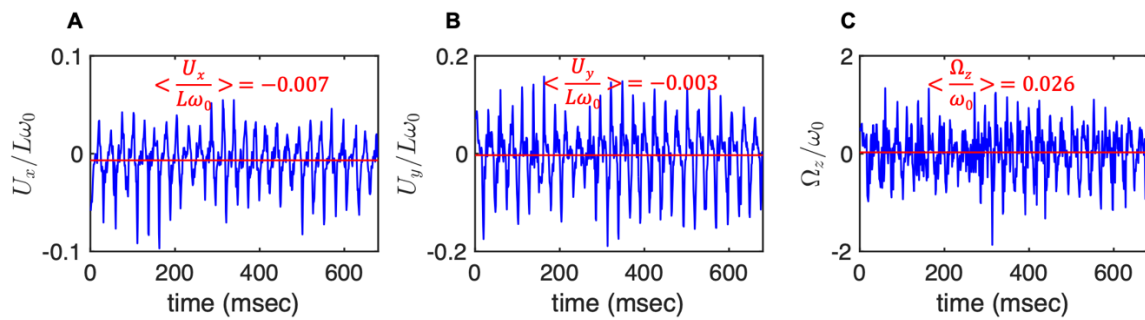


Figure A.2.22: The translational and rotational velocities of the axoneme presented in Chapter 5, Figure 5.1A, measured in the swimmer-fixed frame, obtained with RFT simulations using the experimental beat pattern as input. The red lines mark the mean values.

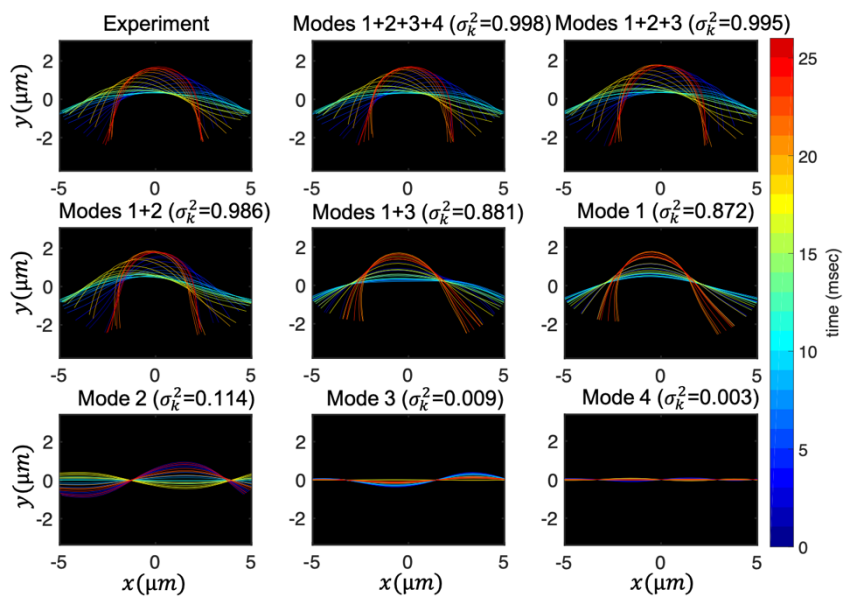


Figure A.2.23: Experimental shapes over one beat cycle of the axoneme in Chapter 5, Figure 5.1A are compared with the axonemal shapes reconstructed using different combination of PCA modes as $\theta(s, t) = \langle \theta(s, t) \rangle_t + \sum_i a_i(t) M_i(s)$. For each panel, the fraction of the total variance σ^2 is also calculated; see Chapter 2, section 2.10 for the definition of σ^2 . Note that shapes reconstructed using modes 2, 3 and 4 are approximately standing waves.

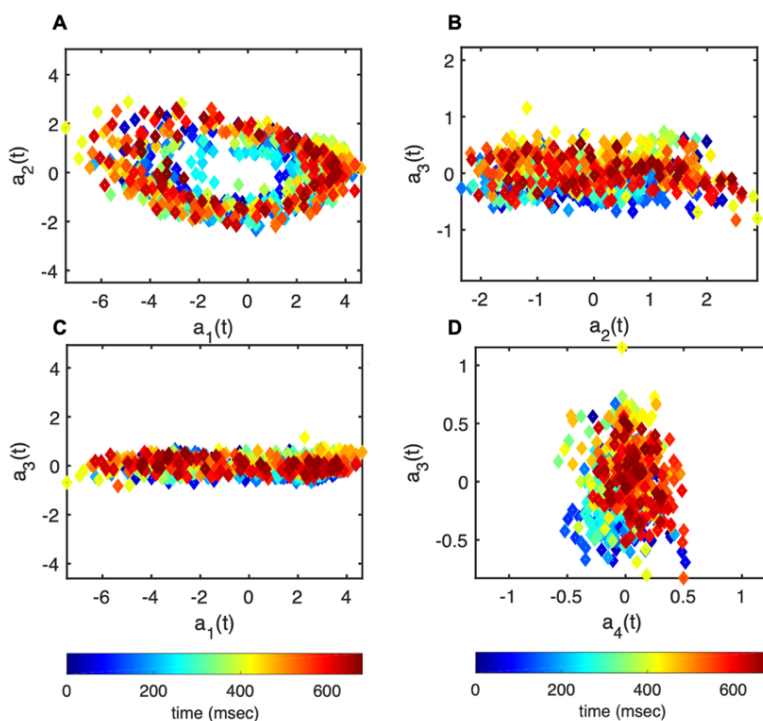


Figure A.2.24: The time-dependent motion amplitudes $a_1(t)$ to $a_4(t)$ are plotted versus each other for the exemplary axoneme shown in Chapter 5, Figure 5.3A.

(13) Supporting tables

Table A.2.3: The coefficient as defined Appendix, Eq. A.2.7 for exemplary basal-hinged and distal hinged axonemes shown in Chapter 4, Figure 4.9. The calcium concentration is zero.

$C_1 = 0.48$	$C_2 = 0.05$	$C_3 = 0.09$	$\alpha_1 = -0.19\pi$	$\alpha_2 = -0.34\pi$	$\alpha_3 = -0.22\pi$
$C'_1 = 0.10$	$C'_2 = 0.05$	$C'_3 = 0.09$	$\alpha'_1 = -0.14\pi$	$\alpha'_2 = -0.22\pi$	$\alpha'_3 = -0.1\pi$
$C_1 = 0.25$	$C_2 = 0.006$	$C_3 = 0.06$	$\alpha_1 = 0.003\pi$	$\alpha_2 = -0.06\pi$	$\alpha_3 = 0.47\pi$
$C'_1 = 0.04$	$C'_2 = 0.006$	$C'_3 = 0.06$	$\alpha'_1 = -0.2\pi$	$\alpha'_2 = -0.4\pi$	$\alpha'_3 = -0.06\pi$

Table A.2.4: The coefficient as defined Appendix, Eq. A.2.7 for two exemplary basal-hinged axonemes. The calcium concentration is zero.

$C_1 = 0.55$	$C_2 = 0.10$	$C_3 = 0.10$	$\alpha_1 = 0.15\pi$	$\alpha_2 = 0.10\pi$	$\alpha_3 = 0.21\pi$
$C'_1 = 0.05$	$C'_2 = 0.10$	$C'_3 = 0.10$	$\alpha'_1 = 0.06\pi$	$\alpha'_2 = 0.02\pi$	$\alpha'_3 = 0.12\pi$
$C_1 = 0.56$	$C_2 = 0.08$	$C_3 = 0.06$	$\alpha_1 = 0.07\pi$	$\alpha_2 = -0.33\pi$	$\alpha_3 = -0.09\pi$
$C'_1 = 0.04$	$C'_2 = 0.08$	$C'_3 = 0.06$	$\alpha'_1 = 0.26\pi$	$\alpha'_2 = -0.28\pi$	$\alpha'_3 = -0.04\pi$

Table A.2.5: The coefficient as defined Appendix, Eq. A.2.7 for exemplary basal-clamped and distal-clamped axonemes shown in Chapter 4, Figure 4.10. The calcium concentration is zero.

$C_1 = 0.13$	$C_2 = 0.05$	$C_3 = 0.03$	$\alpha_1 = -0.19\pi$	$\alpha_2 = 0.13\pi$	$\alpha_3 = -0.33\pi$
$C'_1 = -0.04$	$C'_2 = 0.05$	$C'_3 = 0.03$	$\alpha'_1 = -0.17\pi$	$\alpha'_2 = -0.18\pi$	$\alpha'_3 = -0.36\pi$
$C_1 = 0.50$	$C_2 = 0.15$	$C_3 = 0.09$	$\alpha_1 = 0.34\pi$	$\alpha_2 = 0.03\pi$	$\alpha_3 = 0.17\pi$
$C'_1 = 0.26$	$C'_2 = 0.15$	$C'_3 = 0.09$	$\alpha'_1 = -0.13\pi$	$\alpha'_2 = 0.29\pi$	$\alpha'_3 = 0.43\pi$

Table A.2.6: Amplitude and phase of travelling waves of flagella in the intact *C. reinhardtii* cell.

$C_1 = 0.54$	$C_2 = 0.10$	$C_3 = 0.10$	$\alpha_1 = 0.31\pi$	$\alpha_2 = -0.33\pi$	$\alpha_3 = 0.35\pi$
$C'_1 = 0.18$	$C'_2 = 0.10$	$C'_3 = 0.10$	$\alpha'_1 = -0.41\pi$	$\alpha'_2 = 0.29\pi$	$\alpha'_3 = -0.03\pi$

Nomenclature

C. reinhardtii

Axoneme

ODA

IDA

IFT

MTs

RS

 α β γ

GTP

GDP

ATP

ADP

MTBD

PCA

KIFs

LC

HC

NADH

PCr

CK

hv

bR

EF_oF₁-ATP synthase

Chlamydomonas reinhardtii

Demembrated flagella

Outer dynein arm

Inner dynein arm

Intra flagellar transport

Microtubules

Radial spokes

Alpha tubulin

Beta tubulin

Gamma tubulin

Guanosine-5'-triphosphate

Guanosine diphosphate

Adenosine-5'-triphosphate

Adenosine diphosphate

Microtubule binding domain

Principle component analysis

Kinesin super family proteins

Light chain

Heavy chain

Nicotinamide adenine dinucleotide hydrid

Phosphocreatine

Creatine kinase

Light energy

Bacteriorhodopsin

F-type ATP synthase from *E. coli*

P_i	Inorganic phosphate
PC	Phosphatidylcholine
SDS	Sodium dodecyl sulfate
Triton	Triton X-100
<i>E. coli</i>	Escherichia coli
HPTS	Pyranine/8-hydroxyprrene-1,3,6-trisulfonic acid
P	Permeability coefficient
PDI	Polydispersity index
SDS-PAGE	Sodium dodecyl sulfate polyacrylamide gel electrophoresis
DLS	Dynamic light scattering
R_{eff}	Reconstitution efficiency
RLU	Relative light units
ΔpH	pH difference
pH_{in}	pH inside the vesicle
pH_{out}	pH outside of the vesicle
pH_{mean}	Average value of pH
pH_0	pH at $t_0 = 0$
$\Delta\mu_H$	Electrochemical potential difference
$\Delta\psi$	Electrical potential difference
A_x	Absorption at x nm
C_x	Concentration of x
ϵ_x	Extinction coefficient at x nm
I_x	Luminescence signal of x
n_x	Amount of substance x
N_x	Number of x per ml
M_x	Molar mass of x
V_x	Volume of x

$[E]$	Enzyme concentration
k_{cat}	Catalytic constant of ATP synthesis
C_{ATP}	ATP concentration change
$C_{ATP,cor}$	Corrected ATP concentration changes ($t_0=0$)
v_0	Initial reaction velocity
C_{bR}	Concentration of bacteriorhodopsin
CE_{FoF_1}	Concentration of ATP synthase
κ	Curvature
$\mathbf{t}(s)$	Tangent vector
$\mathbf{n}(s)$	Normal vector
$C(s, s')$	Covariance matrix
λ_n	Eigenvalues
$V_n(s)$	Eigenvectors
$a_n(t)$	Amplitude of motion
$d\phi/dt$	Phase angle
C_0	Static curvature
C_1	Dynamic curvature
C_1'	Backward traveling waves
C_2	Second harmonic
$f_{critical}$	Minimum beating frequency
f_{max}	Maximum beating frequency
$[ATP]_{critical}$	Minimum ATP concentration
K_m	Michaelis-Menten constant
$\zeta_{ }$	Parallel drag coefficient
ζ_{\perp}	Perpendicular drag coefficient
$\langle \Omega_z \rangle$	Rotational velocity
CCW	Counterclockwise
CW	Clockwise
σ^2	Variance

PEG	Polyethylene glycol
EGTA	Ethylene glycol tetraacetic acid
K-acetate	Potassium acetate
Np-40	Nonyl phenoxy polyethoxy ethanol
CaCl ₂	Calcium chloride
DTT	Dithiothreitol
PEG	Polyethylene glycol
MgSO ₄	Magnesium acetate
ddH ₂ O	Double distilled water

References

1. Inoue, Y.; Shingyoji, C., The roles of noncatalytic ATP binding and ADP binding in the regulation of dynein motile activity in flagella. *Cell Motil Cytoskeleton* **2007**, *64* (9), 690-704.
2. Lesich, K. A.; Pelle, D. W.; Lindemann, C. B., Insights into the mechanism of ADP action on flagellar motility derived from studies on bull sperm. *Biophys J* **2008**, *95* (1), 472-82.
3. Gilpin, W.; Bull, M. S.; Prakash, M., The multiscale physics of cilia and flagella. *Nature Reviews Physics* **2020**, *2* (2), 74-88.
4. Ringers, C.; Olstad, E. W.; Jurisch-Yaksi, N., The role of motile cilia in the development and physiology of the nervous system. *Philos. Trans. R. Soc. Lond. B Biol. Sci.* **2020**, *375* (1792), 20190156.
5. Marshall, W. F.; Nonaka, S., Cilia: tuning in to the cell's antenna. *Curr. Biol.* **2006**, *16* (15), R604-14.
6. Bustamante-Marin, X. M.; Ostrowski, L. E., Cilia and Mucociliary Clearance. *Cold Spring Harb Perspect Biol* **2017**, *9* (4).
7. Tilley, A. E.; Walters, M. S.; Shaykhiev, R.; Crystal, R. G., Cilia dysfunction in lung disease. *Annu Rev Physiol* **2015**, *77*, 379-406.
8. Günther, A.-K. Transport of lipid vesicles via the cilia logistic network in the brain of mice. PhD Thesis, Georg-August-Universität Göttingen, Göttingen, 2019.
9. Suarez, S. S.; Wolfner, M. F., Cilia take the egg on a magic carpet ride. *Proc. Natl. Acad. Sci. U. S. A.* **2021**, *118* (27).
10. Nonaka, S.; Tanaka, Y.; Okada, Y.; Takeda, S.; Harada, A.; Kanai, Y.; Kido, M.; Hirokawa, N., Randomization of left-right asymmetry due to loss of nodal cilia generating leftward flow of extraembryonic fluid in mice lacking KIF3B motor protein (vol 95, pg 829, 95). *Cell* **1999**, *99* (1).
11. Richard D. Amelar, L. D., Cy Schoenfeld, Sperm Motility. *Fertil Steril* **1980**, *34* (3), 197-215.
12. Sasso, S.; Stibor, H.; Mittag, M.; Grossman, A. R., From molecular manipulation of domesticated *Chlamydomonas reinhardtii* to survival in nature. *Elife* **2018**, *7*.
13. Milisav, I., Dynein and dynein-related genes. *Cell Motil Cytoskel* **1998**, *39* (4), 261-272.
14. Yagi, T.; Uematsu, K.; Liu, Z.; Kamiya, R., Identification of dyneins that localize exclusively to the proximal portion of *Chlamydomonas* flagella. *J Cell Sci* **2009**, *122* (9), 1306-1314.

15. Pazour, G. J.; Agrin, N.; Leszyk, J.; Witman, G. B., Proteomic analysis of a eukaryotic cilium. *J Cell Biol* **2005**, *170* (1), 103-13.
16. Lin, J.; Tritschler, D.; Song, K.; Barber, C. F.; Cobb, J. S.; Porter, M. E.; Nicastro, D., Building blocks of the nexin-dynein regulatory complex in Chlamydomonas flagella. *J Biol Chem* **2011**, *286* (33), 29175-29191.
17. Ogawa, K.; Mohri, H., Studies on flagellar ATPase from sea urchin spermatozoa. I. Purification and some properties of the enzyme. *Biochim Biophys Acta* **1972**, *256* (1), 142-55.
18. Hyman, A. A.; Salser, S.; Drechsel, D. N.; Unwin, N.; Mitchison, T. J., Role of GTP hydrolysis in microtubule dynamics: information from a slowly hydrolyzable analogue, GMPCPP. *Mol Biol Cell* **1992**, *3* (10), 1155-67.
19. Bashirzadeh, Y.; Liu, A. P., Encapsulation of the cytoskeleton: towards mimicking the mechanics of a cell. *Soft Matter* **2019**, *15* (42), 8425-8436.
20. Nedelec, F. J.; Surrey, T.; Maggs, A. C.; Leibler, S., Self-organization of microtubules and motors. *Nature* **1997**, *389* (6648), 305-8.
21. Biner, O.; Fedor, J. G.; Yin, Z.; Hirst, J., Bottom-Up Construction of a Minimal System for Cellular Respiration and Energy Regeneration. *ACS Synth Biol* **2020**, *9* (6), 1450-1459.
22. Bastos-Arrieta, J.; Revilla-Guarinos, A.; Uspal, W. E.; Simmchen, J., Bacterial Biohybrid Microswimmers. *Front Robot AI* **2018**, *5*, 97.
23. Shchelik, I. S.; Molino, J. V. D.; Gademann, K., Biohybrid microswimmers against bacterial infections. *Acta Biomater* **2021**, *136*, 99-110.
24. Stanton, M. M.; Park, B. W.; Miguel-Lopez, A.; Ma, X.; Sitti, M.; Sanchez, S., Biohybrid Microtube Swimmers Driven by Single Captured Bacteria. *Small* **2017**, *13* (19).
25. Wang, W.; Duan, W. T.; Ahmed, S.; Mallouk, T. E.; Sen, A., Small power: Autonomous nano- and micromotors propelled by self-generated gradients. *Nano Today* **2013**, *8* (5), 531-554.
26. Bessen, M.; Fay, R. B.; Witman, G. B., Calcium control of waveform in isolated flagellar axonemes of Chlamydomonas. *J Cell Biol* **1980**, *86* (2), 446-55.
27. Sartori, P.; Geyer, V. F.; Scholich, A.; Julicher, F.; Howard, J., Dynamic curvature regulation accounts for the symmetric and asymmetric beats of Chlamydomonas flagella. *Elife* **2016**, *5*.
28. Koonin, E. V., The origins of cellular life. *Antonie Van Leeuwenhoek* **2014**, *106* (1), 27-41.
29. Schrum, J. P.; Zhu, T. F.; Szostak, J. W., The origins of cellular life. *Cold Spring Harb Perspect Biol* **2010**, *2* (9), a002212.
30. Walker, S. I.; Packard, N.; Cody, G. D., Re-conceptualizing the origins of life. *Philos Trans A Math Phys Eng Sci* **2017**, *375* (2109).
31. Payne, M. C. a. S., *Cell Structure and Biochemical Reactions*. 2015; Vol. 13, p 1-176.

32. Schmoller, K. M.; Skotheim, J. M., The Biosynthetic Basis of Cell Size Control. *Trends Cell Biol* **2015**, *25* (12), 793-802.
33. Przytycka, T. M.; Andrews, J., Systems-biology dissection of eukaryotic cell growth. *BMC Biol* **2010**, *8*, 62.
34. Vega-Cabrera, L. A.; Pardo-Lopez, L., Membrane remodeling and organization: Elements common to prokaryotes and eukaryotes. *IUBMB Life* **2017**, *69* (2), 55-62.
35. Favor, R. G. M. a. L. J., *How Eukaryotic and Prokaryotic Cells Differ*. Britannica Educational Publishing: New York, 2015.
36. Blount, Z. D., THE NATURAL HISTORY OF MODEL ORGANISMS The unexhausted potential of *E. coli*. *Elife* **2015**, *4*.
37. Vitova, M.; Bisova, K.; Hlavova, M.; Kawano, S.; Zachleder, V.; Cizkova, M., *Chlamydomonas reinhardtii*: duration of its cell cycle and phases at growth rates affected by temperature. *Planta* **2011**, *234* (3), 599-608.
38. Lehti, M. S.; Sironen, A., Formation and function of sperm tail structures in association with sperm motility defects. *Biol Reprod* **2017**, *97* (4), 522-536.
39. Harris, E. H., *Chlamydomonas as a Model Organism*. *Annu Rev Plant Phys* **2001**, *52*, 363-406.
40. Cross, F. R.; Umen, J. G., The *Chlamydomonas* cell cycle. *Plant J* **2015**, *82* (3), 370-392.
41. Veikko F, G., Characterization of the flagellar beat of the single cell green alga *Chlamydomonas Reinhardtii*. *Ph.D Dissertation 2013, TU Dresden Germany*.
42. Khan, S.; Scholey, J. M., Assembly, Functions and Evolution of Archaeella, Flagella and Cilia. *Curr. Biol.* **2018**, *28* (6), R278-R292.
43. Magdanz, V.; Boryshpolets, S.; Ridzewski, C.; Eckel, B.; Reinhardt, K., The motility-based swim-up technique separates bull sperm based on differences in metabolic rates and tail length. *PLoS One* **2019**, *14* (10), e0223576.
44. Gibbons, B. H., Intermittent swimming in live sea urchin sperm. *J Cell Biol* **1980**, *84* (1), 1-12.
45. Doro, E.; Jacobs, S. H.; Hammond, F. R.; Schipper, H.; Pieters, R. P.; Carrington, M.; Wiegertjes, G. F.; Forlenza, M., Visualizing trypanosomes in a vertebrate host reveals novel swimming behaviours, adaptations and attachment mechanisms. *Elife* **2019**, *8*.
46. Helinski, M. E.; Knols, B. G., Sperm quantity and size variation in un-irradiated and irradiated males of the malaria mosquito *Anopheles arabiensis* Patton. *Acta Trop* **2009**, *109* (1), 64-9.
47. Katerina A. Turner , A. R., Samantha Schon, Ashok Agarwal ,; Stephen A. Krawetz, J. M. D. a. T. A.-R., Male Infertility is a Women’s Health Issue—Research and Clinical Evaluation of Male Infertility Is Needed. *Cels* **2020**, *9* (4), 2-14.

48. Salome, P. A.; Merchant, S. S., A Series of Fortunate Events: Introducing Chlamydomonas as a Reference Organism. *Plant Cell* **2019**, *31* (8), 1682-1707.
49. Gompper, R. G. W. a. G., *Hydrodynamics in Motile Active Matter*. Springer: 2020.
50. Saggiorato, G.; Alvarez, L.; Jikeli, J. F.; Kaupp, U. B.; Gompper, G.; Elgeti, J., Human sperm steer with second harmonics of the flagellar beat. *Nat Commun* **2017**, *8* (1), 1415.
51. Gadelha, H.; Hernandez-Herrera, P.; Montoya, F.; Darszon, A.; Corkidi, G., Human sperm uses asymmetric and anisotropic flagellar controls to regulate swimming symmetry and cell steering. *Sci Adv* **2020**, *6* (31), eaba5168.
52. Bennett, R. R.; Golestanian, R., A steering mechanism for phototaxis in Chlamydomonas. *J R Soc Interface* **2015**, *12* (104), 20141164.
53. Purcell, E. M., Life at low Reynolds number. *American Journal of Physics* **1976**, *45* (3), 1-11.
54. Johnson, R. E.; Brokaw, C. J., Flagellar hydrodynamics. A comparison between resistive-force theory and slender-body theory. *Biophys J* **1979**, *25* (1), 113-27.
55. Drescher, K.; Dunkel, J.; Cisneros, L. H.; Ganguly, S.; Goldstein, R. E., Fluid dynamics and noise in bacterial cell-cell and cell-surface scattering. *Proc. Natl. Acad. Sci. U. S. A.* **2011**, *108* (27), 10940-5.
56. Hu, J.; Yang, M.; Gompper, G.; Winkler, R. G., Modelling the mechanics and hydrodynamics of swimming E. coli. *Soft Matter* **2015**, *11* (40), 7867-76.
57. Brown, A. T.; Vladescu, I. D.; Dawson, A.; Vissers, T.; Schwarz-Linek, J.; Lintuvuori, J. S.; Poon, W. C., Swimming in a crystal. *Soft Matter* **2016**, *12* (1), 131-40.
58. Singh, A. V.; Kishore, V.; Santomauro, G.; Yasa, O.; Bill, J.; Sitti, M., Mechanical Coupling of Puller and Pusher Active Microswimmers Influences Motility. *Langmuir* **2020**, *36* (19), 5435-5443.
59. Carvalho-Santos, Z.; Azimzadeh, J.; Pereira-Leal, J. B.; Bettencourt-Dias, M., Evolution: Tracing the origins of centrioles, cilia, and flagella. *J Cell Biol* **2011**, *194* (2), 165-75.
60. Satir, P.; Christensen, S. T., Overview of structure and function of mammalian cilia. *Annu Rev Physiol* **2007**, *69*, 377-400.
61. Linck, R. W., Cilia and Flagella. *eLS. JohnWiley & Sons, Ltd: Chichester.* **2015**, 1-17.
62. Nicastro, D.; Schwartz, C.; Pierson, J.; Gaudette, R.; Porter, M. E.; McIntosh, J. R., The molecular architecture of axonemes revealed by cryoelectron tomography. *Science* **2006**, *313* (5789), 944-8.
63. De Jesus-Rojas, W.; Reyes De Jesus, D.; Nieves, A. M.; Mosquera, R. A.; Martinez-Cruzado, J. C., Primary Ciliary Dyskinesia: Ancestral Haplotypes Analysis of the RSPH4A Founder Mutation in Puerto Rico. *Cureus* **2021**, *13* (9), e17673.

64. Milisav, I., Dynein and dynein-related genes. *Cell Motil Cytoskeleton* **1998**, *39* (4), 261-72.
65. Lin, J.; Heuser, T.; Carbajal-Gonzalez, B. I.; Song, K.; Nicastro, D., The structural heterogeneity of radial spokes in cilia and flagella is conserved. *Cytoskeleton (Hoboken)* **2012**, *69* (2), 88-100.
66. Becker-Heck, A.; Loges, N. T.; Omran, H., Dynein Dysfunction as a Cause of Primary Ciliary Dyskinesia and Other Ciliopathies. *Dyneins: Structure, Biology and Disease* **2012**, 603-627.
67. Gui, M.; Ma, M.; Sze-Tu, E.; Wang, X.; Koh, F.; Zhong, E. D.; Berger, B.; Davis, J. H.; Dutcher, S. K.; Zhang, R.; Brown, A., Structures of radial spokes and associated complexes important for ciliary motility. *Nat Struct Mol Biol* **2021**, *28* (1), 29-37.
68. King, S. M.; Patel-King, R. S., Identification of a Ca(2+)-binding light chain within Chlamydomonas outer arm dynein. *J Cell Sci* **1995**, *108* (Pt 12), 3757-64.
69. Ishikawa, T., Axoneme Structure from Motile Cilia. *Cold Spring Harb Perspect Biol* **2017**, *9* (1).
70. Sanders, M. A.; Salisbury, J. L., Centrin-mediated microtubule severing during flagellar excision in Chlamydomonas reinhardtii. *J Cell Biol* **1989**, *108* (5), 1751-60.
71. Szymanska, K.; Johnson, C. A., The transition zone: an essential functional compartment of cilia. *Cilia* **2012**, *1* (1), 10.
72. Schmidt, H.; Carter, A. P., Review: Structure and mechanism of the dynein motor ATPase. *Biopolymers* **2016**, *105* (8), 557-67.
73. Sept, D.; Baker, N. A.; McCammon, J. A., The physical basis of microtubule structure and stability. *Protein Sci* **2003**, *12* (10), 2257-61.
74. Ma, M.; Stoyanova, M.; Rademacher, G.; Dutcher, S. K.; Brown, A.; Zhang, R., Structure of the Decorated Ciliary Doublet Microtubule. *Cell* **2019**, *179* (4), 909-922 e12.
75. Barton, N. R.; Goldstein, L. S., Going mobile: microtubule motors and chromosome segregation. *Proc. Natl. Acad. Sci. U. S. A.* **1996**, *93* (5), 1735-42.
76. Hyman, A. A.; Karsenti, E., Morphogenetic properties of microtubules and mitotic spindle assembly. *Cell* **1996**, *84* (3), 401-10.
77. Verdier-Pinard, P.; Pasquier, E.; Xiao, H.; Burd, B.; Villard, C.; Lafitte, D.; Miller, L. M.; Angeletti, R. H.; Horwitz, S. B.; Braguer, D., Tubulin proteomics: towards breaking the code. *Anal Biochem* **2009**, *384* (2), 197-206.
78. Horio, T.; Murata, T., The role of dynamic instability in microtubule organization. *Front Plant Sci* **2014**, *5*, 511.
79. Roostalu, J.; Thomas, C.; Cade, N. I.; Kunzelmann, S.; Taylor, I. A.; Surrey, T., The speed of GTP hydrolysis determines GTP cap size and controls microtubule stability. *Elife* **2020**, *9*.

80. Hyman, J. H. a. A. A., Growth, fluctuation and switching at microtubule plus ends. *Nat Rev Mol Cell Bio* **2009**, *10*, 569-574.
81. Carlier, M. F.; Didry, D.; Pantaloni, D., Microtubule elongation and guanosine 5'-triphosphate hydrolysis. Role of guanine nucleotides in microtubule dynamics. *Biochemistry-Us* **1987**, *26* (14), 4428-37.
82. O'Brien, E. T.; Voter, W. A.; Erickson, H. P., GTP hydrolysis during microtubule assembly. *Biochemistry-Us* **1987**, *26* (13), 4148-56.
83. Drechsel, D. N.; Kirschner, M. W., The minimum GTP cap required to stabilize microtubules. *Curr. Biol.* **1994**, *4* (12), 1053-61.
84. Bruce Alberts, A. J., Julian Lewis, Martin Raff, Keith Roberts, and Peter Walter, *Molecular Biology of the Cell*. New York: Garland Science: 2002.
85. Kato, Y.; Miyakawa, T.; Tanokura, M., Overview of the mechanism of cytoskeletal motors based on structure. *Biophys Rev* **2018**, *10* (2), 571-581.
86. Szent-Gyorgyi, A. G., Meromyosins, the subunits of myosin. *Arch Biochem Biophys* **1953**, *42* (2), 305-20.
87. Gibbons, I. R., Studies on the Protein Components of Cilia from Tetrahymena Pyriformis. *Proc. Natl. Acad. Sci. U. S. A.* **1963**, *50*, 1002-10.
88. Paschal, B. M.; Vallee, R. B., Retrograde transport by the microtubule-associated protein MAP 1C. *Nature* **1987**, *330* (6144), 181-3.
89. Helgo Schmidt, E. S. G., and Andrew P. Carter, Insights into dynein motor domain function from a 3.3 Å crystal structure. *Nat Struct Mol Biol* **2012**, *19* (5), 492-51.
90. Burgess, S. A.; Walker, M. L.; Sakakibara, H.; Knight, P. J.; Oiwa, K., Dynein structure and power stroke. *Nature* **2003**, *421* (6924), 715-8.
91. Samsó, M.; Koonce, M. P., 25 Angstrom resolution structure of a cytoplasmic dynein motor reveals a seven-member planar ring. *J Mol Biol* **2004**, *340* (5), 1059-72.
92. Kamiya, R.; Kurimoto, E.; Muto, E., Two types of Chlamydomonas flagellar mutants missing different components of inner-arm dynein. *J Cell Biol* **1991**, *112* (3), 441-7.
93. Kagami, O; Kamiya, R., Translocation and rotation of microtubules caused by multiple species of Chlamydomonas inner-arm dynein *Journal of Cell Science* **1992**, *103*, 653-664.
94. Kotani, N.; Sakakibara, H.; Burgess, S. A.; Kojima, H.; Oiwa, K., Mechanical properties of inner-arm dynein-f (dynein I1) studied with in vitro motility assays. *Biophys J* **2007**, *93* (3), 886-94.
95. Bui, K. H.; Yagi, T.; Yamamoto, R.; Kamiya, R.; Ishikawa, T., Polarity and asymmetry in the arrangement of dynein and related structures in the Chlamydomonas axoneme. *J Cell Biol* **2012**, *198* (5), 913-25.

96. Pigino, G.; Maheshwari, A.; Bui, K. H.; Shingyoji, C.; Kamimura, S.; Ishikawa, T., Comparative structural analysis of eukaryotic flagella and cilia from *Chlamydomonas*, *Tetrahymena*, and sea urchins. *J Struct Biol* **2012**, *178* (2), 199-206.
97. Toshiaki Yagi, K. U., Zhongmei Liu, Ritsu Kamiya, Identification of dyneins that localize exclusively to the proximal portion of *Chlamydomonas* flagella. *J Cell Sci* **2009**, *122*, 1306-1314.
98. Hoops, H. J.; Witman, G. B., Outer doublet heterogeneity reveals structural polarity related to beat direction in *Chlamydomonas* flagella. *J Cell Biol* **1983**, *97* (3), 902-8.
99. Brokaw, C. J., Computer simulation of flagellar movement. I. Demonstration of stable bend propagation and bend initiation by the sliding filament model. *Biophys J* **1972**, *12* (5), 564-86.
100. Brokaw, C. J., Bend propagation by a sliding filament model for flagella. *J. Exp. Biol.* **1971**, *55* (2), 289-304.
101. Lindemann, C. B., A model of flagellar and ciliary functioning which uses the forces transverse to the axoneme as the regulator of dynein activation. *Cell Motil Cytoskel* **1994**, *29*, 141-154.
102. Ingmar H Riedel-Kruse, A. H., Jonathon Howard, Frank Jülicher, How molecular motors shape the flagellar beat. *Frontiers in Life Science* **2007**, *1* (13), 192-208.
103. Xu, C. P., J. L., Gradient Vector Flow- A New External Force for Snakes. *IEEE Proc. CVPR.* **1997**, *7* (359-369).
104. Xu, C.; Prince, J. L., Snakes, shapes, and gradient vector flow. *IEEE Trans Image Process* **1998**, *7* (3), 359-69.
105. Stephens, G. J.; Johnson-Kerner, B.; Bialek, W.; Ryu, W. S., Dimensionality and dynamics in the behavior of *C. elegans*. *PLoS Comput. Biol.* **2008**, *4* (4), e1000028.
106. Hirokawa, H. M. a. N., *Encyclopedia of Biophysics*. Springer: 2013.
107. Lawrence, C. J.; Dawe, R. K.; Christie, K. R.; Cleveland, D. W.; Dawson, S. C.; Endow, S. A.; Goldstein, L. S.; Goodson, H. V.; Hirokawa, N.; Howard, J.; Malmberg, R. L.; McIntosh, J. R.; Miki, H.; Mitchison, T. J.; Okada, Y.; Reddy, A. S.; Saxton, W. M.; Schliwa, M.; Scholey, J. M.; Vale, R. D.; Walczak, C. E.; Wordeman, L., A standardized kinesin nomenclature. *J Cell Biol* **2004**, *167* (1), 19-22.
108. Moores, C. A.; Milligan, R. A., Lucky 13-microtubule depolymerisation by kinesin-13 motors. *J Cell Sci* **2006**, *119* (Pt 19), 3905-13.
109. Endow, S. A., Determinants of molecular motor directionality. *Nat Cell Biol* **1999**, *1* (6), E163-7.
110. Vale, R. D.; Reese, T. S.; Sheetz, M. P., Identification of a novel force-generating protein, kinesin, involved in microtubule-based motility. *Cell* **1985**, *42* (1), 39-50.

111. Brady, S. T., A novel brain ATPase with properties expected for the fast axonal transport motor. *Nature* **1985**, 317 (6032), 73-5.
112. Utton, M. A.; Noble, W. J.; Hill, J. E.; Anderton, B. H.; Hanger, D. P., Molecular motors implicated in the axonal transport of tau and alpha-synuclein. *J Cell Sci* **2005**, 118 (Pt 20), 4645-54.
113. Toleikis, A.; Carter, N. J.; Cross, R. A., Backstepping Mechanism of Kinesin-1. *Biophys J* **2020**, 119 (10), 1984-1994.
114. Seog, D. H.; Lee, D. H.; Lee, S. K., Molecular motor proteins of the kinesin superfamily proteins (KIFs): structure, cargo and disease. *J Korean Med Sci* **2004**, 19 (1), 1-7.
115. Kawaguchi, K., Energetics of kinesin-1 stepping mechanism. *FEBS Lett* **2008**, 582 (27), 3719-22.
116. Langen, P.; Hucho, F., Karl Lohmann and the discovery of ATP. *Angew Chem Int Ed Engl* **2008**, 47 (10), 1824-7.
117. Yellen, M. T. a. G., *Imaging Changes in the Cytosolic ATP-to-ADP Ratio- Methods in Enzymology*. 2014; Vol. 547.
118. Bonora, M.; Patergnani, S.; Rimessi, A.; De Marchi, E.; Suski, J. M.; Bononi, A.; Giorgi, C.; Marchi, S.; Missiroli, S.; Poletti, F.; Wieckowski, M. R.; Pinton, P., ATP synthesis and storage. *Purinergic Signal* **2012**, 8 (3), 343-57.
119. Seelert, H.; Dencher, N. A., ATP synthase superassemblies in animals and plants: two or more are better. *Biochim Biophys Acta* **2011**, 1807 (9), 1185-97.
120. Neupane, P.; Bhujju, S.; Thapa, N.; Bhattarai, H. K., ATP Synthase: Structure, Function and Inhibition. *Biomol Concepts* **2019**, 10 (1), 1-10.
121. Demetrius, L. A.; Magistretti, P. J.; Pellerin, L., Alzheimer's disease: the amyloid hypothesis and the Inverse Warburg effect. *Front Physiol* **2014**, 5, 522.
122. Schlattner, U.; Tokarska-Schlattner, M.; Wallimann, T., Mitochondrial creatine kinase in human health and disease. *Biochim Biophys Acta* **2006**, 1762 (2), 164-80.
123. M. A. J. Roberts, R. M. C., M. P. Stevens and P. C. F. Oyston, Synthetic biology: biology by design. *Microbiology* **2013**, 159, 1219-1220.
124. Kron, S. J.; Spudich, J. A., Fluorescent actin filaments move on myosin fixed to a glass surface. *Proc. Natl. Acad. Sci. U. S. A.* **1986**, 83 (17), 6272-6.
125. Witman, G. B., Isolation of Chlamydomonas flagella and flagellar axonemes. *Methods Enzymol* **1986**, 134, 280-90.
126. Cole, D. G.; Diener, D. R.; Himelblau, A. L.; Beech, P. L.; Fuster, J. C.; Rosenbaum, J. L., Chlamydomonas kinesin-II-dependent intraflagellar transport (IFT): IFT particles contain

- proteins required for ciliary assembly in *Caenorhabditis elegans* sensory neurons. *Journal of Cell Biology* **1998**, *141* (4), 993-1008.
127. Witman, G. B.; Plummer, J.; Sander, G., Chlamydomonas flagellar mutants lacking radial spokes and central tubules. Structure, composition, and function of specific axonemal components. *J Cell Biol* **1978**, *76* (3), 729-47.
128. Witman, G. B.; Carlson, K.; Berliner, J.; Rosenbaum, J. L., Chlamydomonas flagella. I. Isolation and electrophoretic analysis of microtubules, matrix, membranes, and mastigonemes. *J Cell Biol* **1972**, *54* (3), 507-39.
129. Weisenberg, R. C.; Flynn, J.; Gao, B. C.; Awodi, S., Microtubule gelation-contraction in vitro and its relationship to component a of slow axonal transport. *Cell Motil Cytoskeleton* **1988**, *10* (1-2), 331-40.
130. Geyer, V. F.; Sartori, P.; Friedrich, B. M.; Julicher, F.; Howard, J., Independent Control of the Static and Dynamic Components of the Chlamydomonas Flagellar Beat. *Curr. Biol.* **2016**, *26* (8), 1098-103.
131. Chen, H.; Zhang, Y. P. J., Enzymatic regeneration and conservation of ATP: challenges and opportunities. *Crit Rev Biotechnol* **2021**, *41* (1), 16-33.
132. Otrin, L.; Kleineberg, C.; da Silva, L. C.; Landfester, K.; Ivanov, I.; Wang, M. H.; Bednarz, C.; Sundmacher, K.; Vidakovic-Koch, T., Artificial Organelles for Energy Regeneration. *Adv Biosyst* **2019**, *3* (6).
133. Otrin, L.; Marusic, N.; Bednarz, C.; Vidakovic-Koch, T.; Lieberwirth, I.; Landfester, K.; Sundmacher, K., Toward Artificial Mitochondrion: Mimicking Oxidative Phosphorylation in Polymer and Hybrid Membranes. *Nano Lett* **2017**, *17* (11), 6816-6821.
134. Kleineberg, C., Bottom-up Assembly of a Light-driven ATP Regeneration Module in Lipid, Polymer and Hybrid Vesicles. *Ph.D Dissertation* **2021**, OVGU Magdeburg, Germany.
135. Mitchell, P., Coupling of phosphorylation to electron and hydrogen transfer by a chemi-osmotic type of mechanism. *Nature* **1961**, *191*, 144-8.
136. Racker, E.; StoECKENIUS, W., Reconstitution of purple membrane vesicles catalyzing light-driven proton uptake and adenosine triphosphate formation. *J Biol Chem* **1974**, *249* (2), 662-3.
137. Allen, J., Photosynthesis of ATP-electrons, proton pumps, rotors, and poise. *Cell* **2002**, *110* (3), 273-6.
138. Matuschka, S.; Zwicker, K.; Nawroth, T.; Zimmer, G., Atp Synthesis by Purified Atp-Synthase from Beef-Heart Mitochondria after Coreconstitution with Bacteriorhodopsin. *Archives of Biochemistry and Biophysics* **1995**, *322* (1), 135-142.

139. Richard, P.; Graber, P., Kinetics of ATP synthesis catalyzed by the H(+)-ATPase from chloroplasts (CF₀F₁) reconstituted into liposomes and coreconstituted with bacteriorhodopsin. *Eur J Biochem* **1992**, *210* (1), 287-91.
140. Wagner, N.; Gutweiler, M.; Pabst, R.; Dose, K., Coreconstitution of bacterial ATP synthase with monomeric bacteriorhodopsin into liposomes. A comparison between the efficiency of monomeric bacteriorhodopsin and purple membrane patches in coreconstitution experiments. *Eur J Biochem* **1987**, *165* (1), 177-83.
141. Choi, H. J.; Montemagno, C. D., Artificial organelle: ATP synthesis from cellular mimetic polymersomes. *Nano Lett* **2005**, *5* (12), 2538-42.
142. Kleineberg, C.; Wolfer, C.; Abbasnia, A.; Pischel, D.; Bednarz, C.; Ivanov, I.; Heitkamp, T.; Borsch, M.; Sundmacher, K.; Vidakovic-Koch, T., Light-Driven ATP Regeneration in Diblock/Grafted Hybrid Vesicles. *ChemBiochem* **2020**.
143. Nakanishi-Matsui, M.; Sekiya, M.; Futai, M., ATP synthase from Escherichia coli: Mechanism of rotational catalysis, and inhibition with the epsilon subunit and phytopolyphenols. *Biochim Biophys Acta* **2016**, *1857* (2), 129-140.
144. Boyer, P. D., The binding change mechanism for ATP synthase--some probabilities and possibilities. *Biochim Biophys Acta* **1993**, *1140* (3), 215-50.
145. Friedrich, D.; Brunig, F. N.; Nieuwkoop, A. J.; Netz, R. R.; Hegemann, P.; Oschkinat, H., Collective exchange processes reveal an active site proton cage in bacteriorhodopsin. *Commun Biol* **2020**, *3* (1), 4.
146. Hirai, T.; Subramaniam, S., Protein conformational changes in the bacteriorhodopsin photocycle: comparison of findings from electron and X-ray crystallographic analyses. *PLoS One* **2009**, *4* (6), e5769.
147. Dattler, D.; Fuks, G.; Heiser, J.; Moulin, E.; Perrot, A.; Yao, X.; Giuseppone, N., Design of Collective Motions from Synthetic Molecular Switches, Rotors, and Motors. *Chem Rev* **2020**, *120* (1), 310-433.
148. Nummelin, S.; Shen, B.; Piskunen, P.; Liu, Q.; Kostiainen, M. A.; Linko, V., Robotic DNA Nanostructures. *ACS Synth Biol* **2020**, *9* (8), 1923-1940.
149. Pennadam, S. S.; Firman, K.; Alexander, C.; Gorecki, D. C., Protein-polymer nano-machines. Towards synthetic control of biological processes. *J Nanobiotechnology* **2004**, *2* (1), 8.
150. Bao, P.; Paterson, D. A.; Peyman, S. A.; Jones, J. C.; Sandoe, J. A. T.; Gleeson, H. F.; Evans, S. D.; Bushby, R. J., Production of giant unilamellar vesicles and encapsulation of lyotropic nematic liquid crystals. *Soft Matter* **2021**, *17* (8), 2234-2241.
151. Bachler, S.; Haidas, D.; Ort, M.; Duncombe, T. A.; Dittrich, P. S., Microfluidic platform enables tailored translocation and reaction cascades in nanoliter droplet networks. *Commun Biol* **2020**, *3* (1), 769.

152. Shetty, S. C.; Yandrapalli, N.; Pinkwart, K.; Krafft, D.; Vidakovic-Koch, T.; Ivanov, I.; Robinson, T., Directed Signaling Cascades in Monodisperse Artificial Eukaryotic Cells. *ACS Nano* **2021**, *15* (10), 15656-15666.
153. Zheng, Y.; Wu, Z.; Lin, L.; Zheng, X.; Hou, Y.; Lin, J. M., Microfluidic droplet-based functional materials for cell manipulation. *Lab Chip* **2021**, *21* (22), 4311-4329.
154. Ai, Y.; Xie, R.; Xiong, J.; Liang, Q., Microfluidics for Biosynthesizing: from Droplets and Vesicles to Artificial Cells. *Small* **2020**, *16* (9), e1903940.
155. Ishmukhametov, R. R.; Galkin, M. A.; Vik, S. B., Ultrafast purification and reconstitution of His-tagged cysteine-less Escherichia coli F1Fo ATP synthase. *Biochim Biophys Acta* **2005**, *1706* (1-2), 110-6.
156. Laemmli, U. K., Cleavage of structural proteins during the assembly of the head of bacteriophage T4. *Nature* **1970**, *227* (5259), 680-5.
157. Fischer, S.; Graber, P., Comparison of DeltapH- and Delta*** ϕ ***-driven ATP synthesis catalyzed by the H(+)-ATPases from Escherichia coli or chloroplasts reconstituted into liposomes. *FEBS Lett* **1999**, *457* (3), 327-32.
158. Oesterhelt, D.; Stoeckenius, W., Isolation of the cell membrane of Halobacterium halobium and its fractionation into red and purple membrane. *Methods Enzymol* **1974**, *31*, 667-78.
159. Shiu, P. J.; Ju, Y. H.; Chen, H. M.; Lee, C. K., Facile isolation of purple membrane from Halobacterium salinarum via aqueous-two-phase system. *Protein Expr Purif* **2013**, *89* (2), 219-24.
160. Meyer, O.; Ollivon, M.; Paternostre, M. T., Solubilization steps of dark-adapted purple membrane by Triton X-100. A spectroscopic study. *FEBS Lett* **1992**, *305* (3), 249-53.
161. Gerber, G. E.; Gray, C. P.; Wildenauer, D.; Khorana, H. G., Orientation of bacteriorhodopsin in Halobacterium halobium as studied by selective proteolysis. *Proc. Natl. Acad. Sci. U. S. A.* **1977**, *74* (12), 5426-30.
162. NanoSciences, <http://www.liposomes.org/2009/01/number-of-lipid-molecules-per-liposome.html> [online]. **2009**.
163. Gorman, D. S.; Levine, R. P., Cytochrome f and plastocyanin: their sequence in the photosynthetic electron transport chain of Chlamydomonas reinhardi. *Proc. Natl. Acad. Sci. U. S. A.* **1965**, *54* (6), 1665-9.
164. Alper, J.; Geyer, V.; Mukundan, V.; Howard, J., Reconstitution of flagellar sliding. *Methods Enzymol* **2013**, *524*, 343-69.
165. Frenet, J. F. Sur quelque propriete`s des courbes a´ double courbure., Toulouse, 1847.
166. Gilbert, S. P.; Johnson, K. A., Expression, purification, and characterization of the Drosophila kinesin motor domain produced in Escherichia coli. *Biochemistry-Us* **1993**, *32* (17), 4677-84.

167. Young, E. C.; Berliner, E.; Mahtani, H. K.; Perez-Ramirez, B.; Gelles, J., Subunit interactions in dimeric kinesin heavy chain derivatives that lack the kinesin rod. *J Biol Chem* **1995**, *270* (8), 3926-31.
168. Fischer, S. Isolation, Rekonstitution und kinetische Charakterisierung der H⁺-ATPsynthase aus *Escherichia coli*. Universität Stuttgart., 1999.
169. Fischer, S.; Graber, P., Comparison of Delta pH- and Delta phi-driven ATP synthesis catalyzed by the H⁺-ATPases from *Escherichia coli* or chloroplasts reconstituted into liposomes. *Febs Letters* **1999**, *457* (3), 327-332.
170. Steinberg-Yfrach, G.; Rigaud, J. L.; Durantini, E. N.; Moore, A. L.; Gust, D.; Moore, T. A., Light-driven production of ATP catalysed by FOF1-ATP synthase in an artificial photosynthetic membrane. *Nature* **1998**, *392* (6675), 479-82.
171. Pitard, B.; Richard, P.; Dunach, M.; Rigaud, J. L., ATP synthesis by the FOF1 ATP synthase from thermophilic *Bacillus PS3* reconstituted into liposomes with bacteriorhodopsin. 2. Relationships between proton motive force and ATP synthesis. *Eur J Biochem* **1996**, *235* (3), 779-88.
172. Pitard, B.; Richard, P.; Dunach, M.; Girault, G.; Rigaud, J. L., ATP synthesis by the FOF1 ATP synthase from thermophilic *Bacillus PS3* reconstituted into liposomes with bacteriorhodopsin. 1. Factors defining the optimal reconstitution of ATP synthases with bacteriorhodopsin. *Eur J Biochem* **1996**, *235* (3), 769-78.
173. Kirakosyan, G.; Bagramyan, K.; Trchounian, A., Redox sensing by *Escherichia coli*: effects of dithiothreitol, a redox reagent reducing disulphides, on bacterial growth. *Biochem Biophys Res Commun* **2004**, *325* (3), 803-6.
174. Mondal, D.; Adhikari, R.; Sharma, P., Internal friction controls active ciliary oscillations near the instability threshold. *Sci Adv* **2020**, *6* (33), eabb0503.
175. Chen, D. T. N.; Heymann, M.; Fraden, S.; Nicastro, D.; Dogic, Z., ATP Consumption of Eukaryotic Flagella Measured at a Single-Cell Level. *Biophys J* **2015**, *109* (12), 2562-2573.
176. Chen, D. T. N.; Heymann, M.; Fraden, S.; Nicastro, D.; Dogic, Z., ATP Consumption of Eukaryotic Flagella Measured at a Single-Cell Level. *Biophys J* **2015**, *109* (12), 2562-2573.
177. Brokaw, C. J., Effects of viscosity and ATP concentration on the movement of reactivated sea-urchin sperm flagella. *J. Exp. Biol.* **1975**, *62* (3), 701-19.
178. Kikushima, K.; Yagi, T.; Kamiya, R., Slow ADP-dependent acceleration of microtubule translocation produced by an axonemal dynein. *FEBS Lett* **2004**, *563* (1-3), 119-22.
179. Shiroguchi, K.; Toyoshima, Y. Y., Regulation of monomeric dynein activity by ATP and ADP concentrations. *Cell Motil Cytoskeleton* **2001**, *49* (4), 189-99.
180. Frey, E.; Brokaw, C. J.; Omoto, C. K., Reactivation at low ATP distinguishes among classes of paralyzed flagella mutants. *Cell Motil Cytoskel* **1997**, *38* (1), 91-99.

181. Omoto, C. K.; Yagi, T.; Kurimoto, E.; Kamiya, R., Ability of paralyzed flagella mutants of *Chlamydomonas* to move. *Cell Motil Cytoskeleton* **1996**, *33* (2), 88-94.
182. Yoshimura, A.; Nakano, I.; Shingyoji, C., Inhibition by ATP and activation by ADP in the regulation of flagellar movement in sea urchin sperm. *Cell Motil Cytoskel* **2007**, *64* (10), 777-793.
183. Schmidt, J. A.; Eckert, R., Calcium couples flagellar reversal to photostimulation in *Chlamydomonas reinhardtii*. *Nature* **1976**, *262* (5570), 713-5.
184. Strubing, T.; Khosravanizadeh, A.; Vilfan, A.; Bodenschatz, E.; Golestanian, R.; Guido, I., Wrinkling Instability in 3D Active Nematics. *Nano Lett* **2020**, *20* (9), 6281-6288.
185. Suzuki, K.; Miyazaki, M.; Takagi, J.; Itabashi, T.; Ishiwata, S., Spatial confinement of active microtubule networks induces large-scale rotational cytoplasmic flow. *Proc. Natl. Acad. Sci. U. S. A.* **2017**, *114* (11), 2922-2927.
186. Beard, D. A., A biophysical model of the mitochondrial respiratory system and oxidative phosphorylation. *PLoS Comput. Biol.* **2005**, *1* (4), e36.
187. del Rosario, R. C.; Oppawsky, C.; Tittor, J.; Oesterhelt, D., Modeling the membrane potential generation of bacteriorhodopsin. *Math Biosci* **2010**, *225* (1), 68-80.
188. Krupinski, J.; Hammes, G. G., Steady-State Atp Synthesis by Bacteriorhodopsin and Chloroplast Coupling Factor Co-Reconstituted into Asolectin Vesicles. *Proc. Natl. Acad. Sci. U. S. A.* **1986**, *83* (12), 4233-4237.
189. Hayashi, S.; Shingyoji, C., Mechanism of flagellar oscillation-bending-induced switching of dynein activity in elastase-treated axonemes of sea urchin sperm. *J Cell Sci* **2008**, *121* (Pt 17), 2833-43.
190. Yagi, T., ADP-dependent microtubule translocation by flagellar inner-arm dyneins. *Cell Struct Funct* **2000**, *25* (4), 263-7.
191. Ngweniform, P.; Li, D.; Newton, S. M.; Klebba, P. E.; Mao, C. B., Self-assembly of drug-loaded liposomes on genetically engineered protein nanotubes: a potential anti-cancer drug delivery vector (vol 5, pg 954, 2009). *Soft Matter* **2009**, *5* (24), 5044-5044.
192. Hallan, S. S.; Kaur, P.; Kaur, V.; Mishra, N.; Vaidya, B., Lipid polymer hybrid as emerging tool in nanocarriers for oral drug delivery. *Artif Cell Nanomed B* **2016**, *44* (1), 334-349.
193. Ahmed, K. S.; Hussein, S. A.; Ali, A. H.; Korma, S. A.; Lipeng, Q.; Jinghua, C., Liposome: composition, characterisation, preparation, and recent innovation in clinical applications. *J Drug Target* **2019**, *27* (7), 742-761.
194. Xu, H.; Medina-Sanchez, M.; Magdanz, V.; Schwarz, L.; Hebenstreit, F.; Schmidt, O. G., Sperm-Hybrid Micromotor for Targeted Drug Delivery. *ACS Nano* **2018**, *12* (1), 327-337.

-
195. Gong, A.; Rode, S.; Kaupp, U. B.; Gompper, G.; Elgeti, J.; Friedrich, B. M.; Alvarez, L., The steering gaits of sperm. *Philos. Trans. R. Soc. Lond. B Biol. Sci.* **2020**, *375* (1792), 20190149.
196. Werner, S.; Rink, J. C.; Riedel-Kruse, I. H.; Friedrich, B. M., Shape mode analysis exposes movement patterns in biology: flagella and flatworms as case studies. *PLoS One* **2014**, *9* (11), e113083.
197. Witman, G., *The Chlamydomonas Sourcebook: Cell Motility and Behavior*. 2008; Vol. 3.
198. Heuser, T.; Raytchev, M.; Krell, J.; Porter, M. E.; Nicastro, D., The dynein regulatory complex is the nexin link and a major regulatory node in cilia and flagella. *Journal of Cell Biology* **2009**, *187* (6), 921-933.
199. Bower, R., The N-DRC forms a conserved biochemical complex that maintains outer doublet alignment and limits microtubule sliding in motile axonemes (vol 24, pg 1134, 2013). *Mol Biol Cell* **2013**, *24* (11), 1825-1825.
200. Luck, D.; Piperno, G.; Ramanis, Z.; Huang, B., Flagellar mutants of Chlamydomonas: studies of radial spoke-defective strains by dikaryon and revertant analysis. *Proc. Natl. Acad. Sci. U. S. A.* **1977**, *74* (8), 3456-60.
201. Gadelha, H.; Gaffney, E. A.; Smith, D. J.; Kirkman-Brown, J. C., Nonlinear instability in flagellar dynamics: a novel modulation mechanism in sperm migration? *J R Soc Interface* **2010**, *7* (53), 1689-97.
202. Eric Lauga, T. R. P., The hydrodynamics of swimming microorganisms. *Reports on Progress in Physics* **2009**, *75* (096601).
203. Geyer, V. Characterization of the flagellar beat of the single cell green alga Chlamydomonas reinhardtii. Ph.D. thesis. Sächsische Landesbibliothek-Staats-und Universitätsbibliothek Dresden, 2013.
204. Mojiri, S.; Isbaner, S.; Muhle, S.; Jang, H.; Bae, A. J.; Gregor, I.; Gholami, A.; Enderlein, J., Rapid multi-plane phase-contrast microscopy reveals torsional dynamics in flagellar motion. *Biomed Opt Express* **2021**, *12* (6), 3169-3180.
205. Friedrich, B. M.; Riedel-Kruse, I. H.; Howard, J.; Julicher, F., High-precision tracking of sperm swimming fine structure provides strong test of resistive force theory. *J. Exp. Biol.* **2010**, *213* (Pt 8), 1226-34.
206. Goldstein, R. E., Green Algae as Model Organisms for Biological Fluid Dynamics. *Annu Rev Fluid Mech* **2015**, *47*, 343-375.
207. Wan, K. Y.; Leptos, K. C.; Goldstein, R. E., Lag, lock, sync, slip: the many 'phases' of coupled flagella. *J R Soc Interface* **2014**, *11* (94), 20131160.
208. Jikeli, J. F.; Alvarez, L.; Friedrich, B. M.; Wilson, L. G.; Pascal, R.; Colin, R.; Pichlo, M.; Rennhack, A.; Brenker, C.; Kaupp, U. B., Sperm navigation along helical paths in 3D chemoattractant landscapes. *Nat Commun* **2015**, *6*, 7985.

-
209. Sébastien Camalet, F. J., and Jacques Prost, Self-Organized Beating and Swimming of Internally Driven Filaments. *Physical Review Letters* **1999**, *82* (7).
210. Man, Y.; Ling, F.; Kanso, E., Cilia oscillations. *Philos. Trans. R. Soc. Lond. B Biol. Sci.* **2020**, *375* (1792), 20190157.
211. Bayly, P. V.; Dutcher, S. K., Steady dynein forces induce flutter instability and propagating waves in mathematical models of flagella. *J R Soc Interface* **2016**, *13* (123).
212. De Canio, G.; Lauga, E.; Goldstein, R. E., Spontaneous oscillations of elastic filaments induced by molecular motors. *J R Soc Interface* **2017**, *14* (136).
213. Eshel, D.; Brokaw, C. J., New evidence for a "biased baseline" mechanism for calcium-regulated asymmetry of flagellar bending. *Cell Motil Cytoskeleton* **1987**, *7* (2), 160-8.
214. Oriola, D.; Gadelha, H.; Casademunt, J., Nonlinear amplitude dynamics in flagellar beating. *R Soc Open Sci* **2017**, *4* (3), 160698.
215. Brokaw, C. J., Computer simulation of flagellar movement. VI. Simple curvature-controlled models are incompletely specified. *Biophys J* **1985**, *48* (4), 633-42.
216. Brokaw, C. J., Computer simulation of flagellar movement VIII: coordination of dynein by local curvature control can generate helical bending waves. *Cell Motil Cytoskeleton* **2002**, *53* (2), 103-24.
217. Bayly, P. V.; Wilson, K. S., Analysis of unstable modes distinguishes mathematical models of flagellar motion. *J R Soc Interface* **2015**, *12* (106).
218. Brokaw, C. J., Molecular mechanism for oscillation in flagella and muscle. *Proc. Natl. Acad. Sci. U. S. A.* **1975**, *72* (8), 3102-6.
219. Prost, J. u. F. a., Spontaneous Oscillations of Collective Molecular Motors. *Physical Review Letters* **1997**, *78* (23), 4510.
220. Coy, R.; Gadelha, H., The counterbend dynamics of cross-linked filament bundles and flagella. *J R Soc Interface* **2017**, *14* (130).
221. Saintillan, B. C. a. D., Spontaneous oscillations, beating patterns, and hydrodynamics of active microfilaments. *Physical Review Fluids* **2019**, *4* (4), 043102.
222. Jülicher, S. C. a. F., Generic aspects of axonemal beating. *New Journal of Physics* **2000**, *2*.
223. Machin, K. E., Wave Propagation along Flagella. **1958**, *35* (4), 796–806.
224. Machin, K. E., The control and synchronization of flagellar movement. **1963**, *158* (970).
225. Alapan, Y.; Yasa, O.; Schauer, O.; Giltinan, J.; Tabak, A. F.; Sourjik, V.; Sitti, M., Soft erythrocyte-based bacterial microswimmers for cargo delivery. *Sci Robot* **2018**, *3* (17).

226. Carlsen, R. W.; Sitti, M., Bio-hybrid cell-based actuators for microsystems. *Small* **2014**, *10* (19), 3831-51.
227. Hyams, J. S.; Borisy, G. G., Isolated flagellar apparatus of Chlamydomonas: characterization of forward swimming and alteration of waveform and reversal of motion by calcium ions in vitro. *J Cell Sci* **1978**, *33*, 235-53.
228. J. Gray, G. J. H., The Propulsion of Sea-Urchin Spermatozoa *J. Exp. Biol.* **1955**, *32* (4), 802-814.
229. Omoto, C. K.; Brokaw, C. J., Bending patterns of Chlamydomonas flagella: II. Calcium effects on reactivated Chlamydomonas flagella. *Cell Motil* **1985**, *5* (1), 53-60.
230. Katz, D. F.; Drobnis, E. Z.; Overstreet, J. W., Factors Regulating Mammalian Sperm Migration through the Female Reproductive-Tract and Oocyte Vestments. *Gamete Res* **1989**, *22* (4), 443-469.
231. Prakash, P.; Abdulla, A. Z.; Singh, V.; Varma, M., Tuning the torque-speed characteristics of the bacterial flagellar motor to enhance swimming speed. *Phys Rev E* **2019**, *100* (6-1), 062609.
232. Prakash, P.; Abdulla, A. Z.; Singh, V.; Varma, M., Swimming statistics of cargo-loaded single bacteria. *Soft Matter* **2020**, *16* (41), 9499-9505.
233. Berg, H. C., Motile behavior of bacteria. *Phys Today* **2000**, *53* (1), 24-29.
234. Martinez, V. A.; Schwarz-Linek, J.; Reufer, M.; Wilson, L. G.; Morozov, A. N.; Poon, W. C., Flagellated bacterial motility in polymer solutions. *Proc. Natl. Acad. Sci. U. S. A.* **2014**, *111* (50), 17771-6.
235. Patteson, A. E.; Gopinath, A.; Goulian, M.; Arratia, P. E., Running and tumbling with E. coli in polymeric solutions. *Sci Rep* **2015**, *5*, 15761.
236. Ahmad, R.; Kleineberg, C.; Nasirimarekani, V.; Su, Y. J.; Goli Pozveh, S.; Bae, A.; Sundmacher, K.; Bodenschatz, E.; Guido, I.; Vidakovic-Koch, T.; Gholami, A., Light-Powered Reactivation of Flagella and Contraction of Microtubule Networks: Toward Building an Artificial Cell. *ACS Synth Biol* **2021**.
237. Wallimann, T.; Tokarska-Schlattner, M.; Schlattner, U., The creatine kinase system and pleiotropic effects of creatine. *Amino Acids* **2011**, *40* (5), 1271-96.
238. Zhang, L.; Abbott, J. J.; Dong, L. X.; Kratochvil, B. E.; Bell, D.; Nelson, B. J., Artificial bacterial flagella: Fabrication and magnetic control. *Appl Phys Lett* **2009**, *94* (6).
239. Ceylan, H.; Yasa, I. C.; Yasa, O.; Tabak, A. F.; Giltinan, J.; Sitti, M., 3D-Printed Biodegradable Microswimmer for Theranostic Cargo Delivery and Release. *ACS Nano* **2019**, *13* (3), 3353-3362.
240. Bunea, A. I.; Taboryski, R., Recent Advances in Microswimmers for Biomedical Applications. *Micromachines (Basel)* **2020**, *11* (12).

-
241. Xu, D.; Wang, Y.; Liang, C.; You, Y.; Sanchez, S.; Ma, X., Self-Propelled Micro/Nanomotors for On-Demand Biomedical Cargo Transportation. *Small* **2020**, *16* (27), e1902464.
242. Akolpoglu, M. B.; Dogan, N. O.; Bozuyuk, U.; Ceylan, H.; Kizilel, S.; Sitti, M., High-Yield Production of Biohybrid Microalgae for On-Demand Cargo Delivery. *Adv Sci (Weinh)* **2020**, *7* (16), 2001256.
243. Lighthill, J., Flagellar Hydrodynamics. *Society for Industrial and Applied Mathematics* **1976**, *18* (2), 161-230.
244. Keller, J. B.; Rubinow, S. I., Swimming of flagellated microorganisms. *Biophys J* **1976**, *16* (2 Pt 1), 151-70.
245. Leach, J.; Mushfique, H.; Keen, S.; Di Leonardo, R.; Ruocco, G.; Cooper, J. M.; Padgett, M. J., Comparison of Faxen's correction for a microsphere translating or rotating near a surface. *Phys Rev E Stat Nonlin Soft Matter Phys* **2009**, *79* (2 Pt 2), 026301.
246. Wilczek, A. S. a. F., Self-Propulsion at Low Reynolds Number. *Physical Review Letters* **1987**, *58* (20), 2051-2054.
247. Lauga, E., Floppy swimming: viscous locomotion of actuated elastica. *Phys Rev E Stat Nonlin Soft Matter Phys* **2007**, *75* (4 Pt 1), 041916.

List of Figures

Figure 1.1: A structure of an eukaryotic cell.	3
Figure 1.2: Difference between prokaryotic and eukaryotic cell	4
Figure 1.3: Life cycle of <i>C. reinhardtii</i>	5
Figure 1.4: Schematic illustration of flagellated micro-swimmers	8
Figure 1.5: Schematic illustration of puller and pusher type micro-swimmers.....	8
Figure 1.6: Structure of cilia/flagella	9
Figure 1.7: An arrangement and interconnectivity of axonemal motors and regulators.....	11
Figure 1.8: MTs polymerization and depolymerization.....	12
Figure 1.9: Structure of dynein molecular motor.....	14
Figure 1.10: Schematic illustration of an instantaneous shape of an axoneme	16
Figure 1.11: A schematic illustration of kinesin-1 and its constituent components.....	18
Figure 1.12: Schematic illustration of ATP-ADP energy cycle.....	19
Figure 1.13: An ATP energy transduction cycle.....	20
Figure 1.14: Bottom-up construction of an artificial ATP regeneration module	22
Figure 1.15: A schematic illustration of bacterial EF ₀ F ₁ -ATP synthase and its subunits.....	24
Figure 1.16: A schematic illustration of Boyer's binding change mechanism for EF ₀ F ₁ -ATP synthase.....	24
Figure 1.17: An overview of a bR photo-cycle.....	25
Figure 1.18: Integration of light-switchable ATP regeneration module with two types of motility modules.....	27
Figure 1.19: <i>C. reinhardtii</i> isolated axonemes as an ATP-driven micro-swimmer	28
Figure 1.20: Construction of a bio-hybrid micro-swimmer	29
Figure 2.1: Turnover (k_{cat}) of ATP synthase determined by acid-base transition experiment.....	34
Figure 2.2 : Schematic illustration of lipid vesicles preparation by extrusion method.....	37
Figure 2.3: Proton pumping of bR measured by encapsulation of pH sensitive dye.....	38
Figure 2.4: Schematic illustration of laboratory scale set up for <i>C. reinhardtii</i> cells cultivation.....	43
Figure 2.5: Growth rate of <i>C. reinhardtii</i>	44
Figure 2.6: Axoneme contour tracking.....	48
Figure 3.1: Light-driven ATP production	55
Figure 3.2: SDS-PAGE of purified proteins.....	56
Figure 3.3: Proteolytic cleavage of reconstituted bR with proteinase K	57
Figure 3.4: Size distribution of vesicles before (before) and after reconstitution.....	57
Figure 3.5: ATP production in Tris-HCl buffer in the presence (+DTT) and absence of DTT (-DTT)	58
Figure 3.6: Experiments with commercial ATP.....	60
Figure 3.7: Integration of the motility module with the light-switchable energy module	61
Figure 3.8: Activating role of ADP	63
Figure 3.9: Light-driven reactivation of axonemes with and without calcium	64
Figure 3.10: Mode analysis of the reactivated axoneme presented in Figure 3.9A-F	66
Figure 3.11: Mean curvature of axonemes reactivated using pure commercial ATP.....	67
Figure 3.12: Cell-like confinement	68
Figure 3.13: Droplet microfluidic setup.....	69
Figure 3.14: Photostimulated contraction of MTs/kinesin-1 network inside a millifluidic device.....	70
Figure 3.15: ATP and glucose concentration over time under green light illumination.....	73

Figure 3.16: Bead as a cargo.	75
Figure 3.17: A control experiment with 1 mM pure commercial ATP.....	76
Figure 4.1: A) Snapshot of a <i>C. reinhardtii</i> cell with the cell body attached to the substrate.	78
Figure 4.2: An isolated axoneme beating freely.....	79
Figure 4.3: Experimental shape of <i>C. reinhardtii</i> isolated axoneme.....	81
Figure 4.4: PCA analysis of the axoneme in Figure 4.2.....	82
Figure 4.5: Experimental shapes over one beat cycle are compared with the free axonemal shape	84
Figure 4.6: Experiments with free axonemes reactivated with the calcium	85
Figure 4.7: Validation of Resistive force theory (RFT)	86
Figure 4.8: Experimental shapes and different combinations of the four dominant eigenmodes.....	87
Figure 4.9: Hinged axoneme boundary condition.....	88
Figure 4.10: Clamped boundary condition.....	89
Figure 5.1: Axonemally-driven beads and the effect of calcium ions.....	96
Figure 5.2: Experiments to show the effect of calcium bead-axoneme attachment	97
Figure 5.3: A) The dimensionless mean curvature of axonemes.....	99
Figure 5.4: A) Color-coded time projection of the axonemal shapes of the axoneme.....	100
Figure 5.5: PCA analysis of the axoneme	102
Figure 5.6: Experimental beat pattern	103
Figure 5.7: Experimental beat pattern	104
Figure A.2.1: Simulations in the frame work of RFT.....	123
Figure A.2.2: Experimental shape of an axonemes reconstructed using PCA.....	125
Figure A.2.3: A) Time projection of the shapes of a model filament with a traveling wave.....	128
Figure A.2.4: For the second mode	129
Figure A.2.5: Illustration of bead attached axoneme	138
Figure A.2.6: Schematic presentation of the setup and the coordinate system.	141
Figure A.2.7: Calculation of phase of travelling wave.....	145
Figure A.2.8: Velocity components of the bead's center.	146
Figure A.2.9: Comparison of analytical approximations of rotational and translational	150
Figure A.2.10: Simulations to show the effect.	151
Figure A.2.11: Anomalous flagella-based propulsion speed of a symmetrically.	152
Figure A.2.12: Comparison of symmetric vs asymmetric bead attachment with axoneme	155
Figure A.2.13: Time -dependent coefficients.	156
Figure A.2.14: Comparison of time-dependent coefficients calculated using PCA	156
Figure A.2.15: PCA analysis of the flagellar beat of free axonemes..	157
Figure A.2.16: Traces of the four PCA modes of 21 different free axonemes.....	157
Figure A.2.17: A scatter plot showing the wavelength and the contour length of 21.....	158
Figure A.2.18: Experimental shapes of the hinged axoneme	158
Figure A.2.19: PCA analysis of the flagella in the intact <i>C. reinhardtii</i>	159
Figure A.2.20: Gradient vector flow method implemented to track the flagellum	159
Figure A.2.21: To measure the systematic error of our tracking GVF algorithm.....	160
Figure A.2.22: The translational and rotational velocities of the axoneme presented	160
Figure A.2.23: Experimental shapes over one beat cycle of the axoneme.....	161
Figure A.2.24: The time-dependent motion amplitudes.....	161

List of Tables

Table 1.1: Types of flagellated micro-swimmers.....	7
Table 5.1: Frequencies and intrinsic curvature values of 12 different axonemes.....	100
Table A.2.1: The general form of the coefficients.....	126
Table A.2.2: Values of the coefficient's, defined in Eq. A.2.7.....	127
Table A.2.3: The coefficient as defined Appendix, Eq. A.2.7.....	162
Table A.2.4: The coefficient as defined Appendix, Eq. A.2.7 for two exemplary basal-hinged axonemes.....	162
Table A.2.5: The coefficient as defined Appendix, Eq. A.2.7 for exemplary basal-clamped.....	162
Table A.2.6: Amplitude and phase of travelling waves of flagella in the intact <i>C. reinhardtii</i> cell.....	162